Parametric and Stochastic Characterization of Color Textures

Mohamed Kaseb

THESE

Pour l'obtention du Grade de

DOCTEUR DE L'UNIVERSITE DE POITIERS

(Faculté des Sciences Fondamentales et Appliquées)
(Diplôme National - Arrêté du 25 mai 2016)

Ecole Doctorale : Sciences et Ingénierie des Systèmes, Mathématiques et Informatique

Secteur de Recherche : Traitement du signal et de l'image

Présentée par :

Mohamed KASEB

****

Parametric and Stochastic Characterization of Color Textures

****

Directeurs de Thèse :

Philippe CARRÉ
Hermine BIERMÉ
Guillaume MERCÈRE

Soutenue le 14/12/2021

devant la Commission d'Examen

****

JURY

Anne ESTRADE

Guillaume GILET
Bruno GALERNE
Jean-Christophe PESQUET
José RAMOS

Contents

Résumé

Résumé en français

La thématique générale de cette thèse était la caractérisation paramétrique et stochastique de textures couleur. En traitement d'image, le terme « texture » renvoie de façon générale à toutes les propriétés structurelles d'une image, sa régularité, ses motifs, sa granulosité etc. L'objectif de l'analyse de texture est de caractériser numériquement ces propriétés, notamment à l'aide de modélisations déterministes ou stochastiques. Actuellement, on a souvent recours aux statistiques du second ordre pour caractériser les textures, mais celles-ci se révèlent souvent insuffisantes pour décrire leur structure locale. L'objectif de la thèse était donc une caractérisation plus précise des textures, en s'appuyant sur des techniques issues du traitement du signal, des probabilités et de l'identification des systèmes. Une attention particulière a été portée au traitement de la couleur.

Un premier axe de recherche a consisté en l'utilisation d'algorithmes d'identification de modèle afin de reconstruire les parties manquantes de textures couleur structurellement homogènes. Les paramètres du modèle étaient extraits des zones connues de la texture, puis un morceau de texture d'aspect similaire mais non directement copié des données disponibles était généré à partir de cette estimation afin de combler la zone masquée. Un des atouts essentiels du modèle utilisé était son traitement des trois canaux couleur de l'image comme un vecteur dynamique et non trois signaux scalaires indépendants. En effet, nos résultats ont montré que cette approche vectorielle avait un impact direct sur la qualité de la reconstruction de la couleur.

Si cette approche a fourni des résultats pertinents dans la complétion de texture, elle ne parvenait qu'à capter la dynamique générale de l'image et échouait à en extraire sa structure locale. C'est ce qui a motivé l'utilisation de l'outil monogène, dont les mesures d'énergie, structure et orientation locales avaient déjà fait leurs preuves dans des domaines tels l'interférométrie, la démodulation d'hologramme ou l'imagerie médicale. Avant d'être appliqué à la couleur, le signal monogène a d'abord été étudié dans le cas scalaire, en particulier l'estimation locale de phase et d'orientation qu'il fournit. Nos travaux ont ainsi établi des résultats théoriques garantissant la fiabilité de l'extraction de ces grandeurs, aussi bien dans le cas de textures déterministes que de champs aléatoires. Le modèle utilisé pour générer des champs aléatoire était le bruit de Gabor, choisi pour le controle direct du contenu fréquentiel de la texture qu'il fournit. Dans les deux cas, déterministe et stochastique, l'application à des textures réelles confirmait les attentes de la théorie, à savoir la qualité de la caractérisation monogène de la structure locale dans le cas de textures contenant des motifs d'oscillation clairs.

Après avoir illustré la pertinence de l'outil monogène dans la caractérisation de la structure locale de textures grises, nous avons généralisé ces résultats à des textures couleur. Pour

cela, nous avons utilisé l'approche elliptique des signaux oscillants multivariés, qui a pour avantage de fournir un lien direct entre ses paramètres et le contenu couleur de la texture générée. Un premier objectif était de définir proprement un modèle de synthèse de texture couleur aléatoire, ce qui a été possible en fusionnant l'approche elliptique et les bruits de Gabor. Il en résultait un controle du contenu fréquentiel de l'image générée, mais aussi des couleurs présentes. L'outil monogène a ensuite été appliqué dans un but à la fois d'analyse et d'évaluation de la synthèse. Nous avons alors montré que le signal monogène fournissait un moyen fiable de caractériser la richesse du contenu couleur d'une texture stochastique. Par ailleurs, dans le cadre de la synthèse de texture, la mesure de phase local a permis de définir un critère de qualité de la texture couleur générée, notamment grâce à sa capacité à détecter les artéfacts.

Mot-clés:
Analyse de texture couleur, traitement d'image, modèle de Roesser, signal monogène, phase locale, orientation locale, bruit de Gabor, synthèse de texture couleur, modèle elliptique couleur, détection de singularités

Résumé en anglais

The general topic of this thesis was the parametric and stochastic characterization of color textures. In image processing, the term ''texture" generally refers to all the structural properties of an image, its regularity, its patterns, its graininess, etc. The objective of texture analysis is to characterize these properties numerically, in particular using deterministic or stochastic models. Currently, second-order statistics are often used to characterize textures, but they often prove insufficient to describe their local structure. The objective of the thesis was therefore a more precise characterization of textures, based on techniques from signal processing, probabilities and system identification. Particular attention has been paid to the treatment of color.
A first line of research consisted in the use of model identification algorithms to reconstruct the missing parts of structurally homogeneous color textures. The model parameters were extracted from known areas of the texture, then a piece of texture that looked similar but not directly copied from the available data was generated from this estimate to fill in the masked area. One of the main advantages of the model used was its treatment of the three color channels of the image as a dynamic vector rather than three independent scalar signals. Indeed, our results showed that this vectorial approach had a direct impact on the quality of color reconstruction.
While this approach provided relevant results in texture completion, it only managed to capture the general dynamics of the image and failed to extract its local structure. This is what motivated the use of the monogenic tool, whose measurements of energy, structure and local orientation had already proved their worth in fields such as interferometry, hologram demodulation or medical imaging. Before being applied to color images, the monogenic signal was first studied in the scalar case, in particular the local estimation of phase and orientation that it provides. Our work has thus established theoretical results that guarantee the reliability of the extraction of these quantities, both in the case of deterministic textures and random fields. The model used to generate random fields was the Gabor noise, chosen for the direct control of the frequency content of the texture it provides. In both deterministic and stochastic cases, the application to real textures confirmed the expectations of the theory, namely the quality of the monogeneous characterization of the local structure in the case of textures containing clear oscillation patterns.
After illustrating the relevance of the monogenic tool in the characterization of the local

structure of greyscale textures, we generalized these results to color textures. To do so, we used the elliptical approach of multivariate oscillating signals, which has the advantage of providing a direct link between its parameters and the color content of the generated texture. A first objective was to properly define a random color texture synthesis model, which was possible by merging the elliptical approach and Gabor noises. This resulted in a control of the frequency content of the generated image, but also of the colors present. The monogenic tool was then applied for the purpose of both analysis and evaluation of the synthesis. We then showed that the monogenic signal provided a reliable means of characterizing the richness of the color content of a stochastic texture. Moreover, in the context of texture synthesis, the measure of local phase enabled the definition of a quality criterion for the color texture generated, thanks to its ability to detect artefacts.

Keywords:
Color texture analysis, image processing, Roesser model, monogenic signal, local phase, local orientation, Gabor noise, color texture synthesis, elliptic color model, singularity detection

Remerciements

Je tiens tout d'abord à remercier mes encadrants de thèse, Philippe Carré, Hermine Biermé et Guillaume Mercère, pour ces trois années très enrichissantes. Le sujet qu'ils m'ont proposé était captivant par sa complexité et sa transversalité, et j'ai apprécié la qualité de nos discussions scientifiques. À la fois pointus dans leur domaine et très impliqués dans l'encadrement et le suivi, ils m'ont offert un cadre de travail idéal dans lequel je me suis réellement épanoui. Par ailleurs, je tiens également à remercier le projet MISTIC de l'ANR (ID ANR-19-CE40-0005) pour son soutien financier et les échanges avec des chercheuses et chercheurs de tout le pays qu'il a permis.

Je remercie évidemment les laboratoires XLIM, LMA et LIAS, ainsi que toutes celles et tous ceux qui y travaillent, pour les moyens qu'ils ont mis à ma disposition. Je n'oublie pas celles et ceux qui m'ont aidé quand j'en avais besoin, aussi bien sur des questions scientifiques que techniques, et ils ont donc aussi contribué au bon déroulement de cette thèse.

À titre plus personnel, je remercie ma Marjorie chérie et ses merveilleux enfants Marion et Paul, pour l'amour, le soutien et les rires qu'ils m'apportent au quotidien, ce sont mes vrais trésors et je ne sais pas où je serais sans eux. Je pense aussi très fort à ma maman que j'ai perdu durant ma thèse, je sais qu'elle aurait été fière de moi, et si j'en suis là c'est aussi grâce à elle! Et merci enfin à mon frère Mehdi, mon complice éternel dans les délires les plus surréalistes, et dont je suis fier de la réussite professionnelle.

Introduction

The word "texture", borrowed from Middle French, stems from the Latin verb "texere", which means "to weave". It was originally used to describe the feel or shape of a surface or substance, such as smoothness, roughness, softness, etc. The meaning of the word has widened over time, and now includes visual or sound aspects too. This work focuses on the case of color images, and the characterization of their visual properties. Indeed, when we look at an image, our brain is able to detect lots of its features such as an overall regularity, the presence of particular patterns, or the richness of its color content. This is what enables us to distinguish the two color textures displayed in Figure 1 clearly. However, from a numerical point of view, an image is just a table of pixels, with each pixel containing an intensity value. This makes the link between the values at each pixel and the structural information of the texture perceived by the brain difficult to grasp. The main objective of the parametric texture analysis tackled in this thesis is hence to characterize the visual properties of an image with a small number of parameters that quantify features such as the local regularity, the statistical behavior, the directionality, the color content, etc.

Figure 1: Examples of color textures.

In the recent years, neural-network-based solutions for, *e.g.*, color image denoising (Zhang, Zuo, Chen, Meng & Zhang 2017), segmentation (Zhuang, Low & Yau 2012) and classification (Yin, Wang, Luo, Zhai, Jha & Shi 2019) have been widely used. These techniques usually give satisfactory results thanks to the ability of the neural networks to handle large data, but the parameters and the underlying process often lack explicitness (Hosono, Ono & Miyata 2019). Consequently, it is difficult to get numerical descriptors with a clear physical interpretation in terms of visual features from such techniques. This is what has oriented the scope of this thesis towards parametric texture analysis.

Among the parametric solutions available in the literature, the 2D ARMA models are

particularly widespread (Köppel, Doshkov, Racape, Ndjiki-Nyab & Wiegand 2015). The main idea is to model the texture as a dynamic spatial series characterized by a recursive equation and second order statistics. While interesting in many aspects, such solutions have big limits. The first one is the lack of a proper color formulation. Indeed, 2D ARMA models are usually designed for scalar-valued images, while color images are vector-valued (Soulard 2012). When dealing with color images, these models are either marginally applied to each of the three color channels, or applied to the luminance component of the image (Köppel et al. 2015). In both cases, the interdependency between the color channels is left unmodeled, which leads to the loss of crucial color information (Xu, Yu, Xu, Zhang & Nguyen 2015).

Another limit is that the parameters of 2D ARMA models characterize the statistical behavior and dependency from the past, but fail to extract the local structure of the image. This is already true for 1D signals, as illustrated in Figure 2. The two time series have been generated from the same autoregressive model, but despite their identical statistical behavior (which is reflected in their similar autocorrelation values), they have different trajectories, which the AR parameters cannot differentiate. This suggests that the ARMA framework is not well-suited to characterize the local features of a signal, whether 1D or 2D.

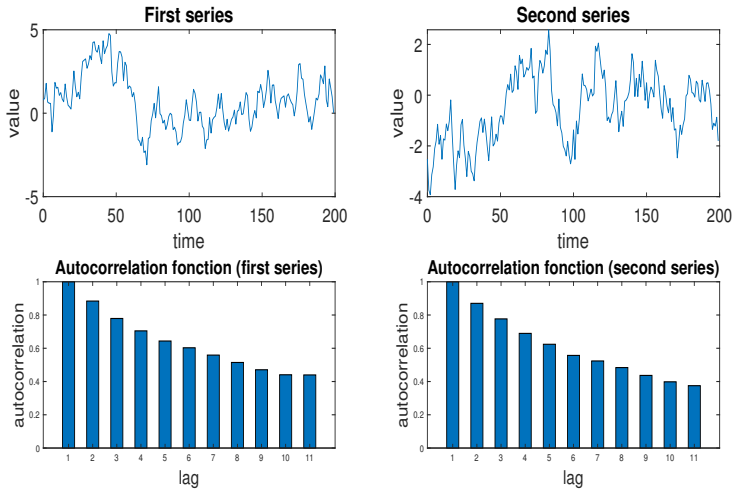

Figure 2: Two examples of times series generated from the same AR(1) model (top), and their respective autocorrelation functions (bottom).

This thesis aims at bypassing these two limits by merging techniques from the fields of signal processing, probabilities and system identification, respectively. Indeed, all three domains have introduced useful tools to characterize the local features of color images (Soulard & Carré 2015, Galerne, Lagae, Lefebvre & Drettakis 2012, Ramos & Mercère 2018), but few works in the current literature focus on bridging the gaps between these different approaches, according to the authors' knowledge. In the whole study, a particular stress is put on the vectorial treatment of the color information. As said previously, the interdependency between the color channels play an important role in the color content of the texture, which suggests favoring vectorial techniques over marginal ones.

A first step consists in applying alternatives to 2D ARMA models that are more suitable

for vectorial signals. Widely used in the field of system identification, the Roesser model, introduced in (Roesser 1975), provides a useful representation of 2D systems in general. Though it was not designed for images specifically, its relevance in the field of image processing has been illustrated in numerous works in the last decades. In the more recent years, efficient algorithms have been introduced to estimate the parameters of the Roesser based on state-space representations (Ramos & Mercère 2016, Ramos & Mercère 2018), with a vectorial treatment of the components that makes them particularly interesting for color image processing. However, the current literature rarely emphasizes the advantages of such approaches in terms of color content, especially the role of the color correlations. In the further developments, the 2D system identification and color image processing frameworks are merged by performing a brand-new colorimetric study of the Roesser model and the state-space-based estimation algorithms.

While 2D state-space representations manage to capture the color information of an image, they still fail to extract some of its local features. Works such as (Kailath, Sayed & Hassibi 2000) have already highlighted the fact that, in both ARMA and Roesser models, the error term contains some structural information, and cannot be fully characterized by its second-order statistics. Additionally, by using spectral analysis, some studies performed in the last 20 years suggest that the information captured by the ARMA and Roesser parameters are linked to the Fourier modulus of the image, while the local structure is encoded in its Fourier phase (Oppenheim & Lim 1981, Leclaire & Moisan 2015). The main issue with the Fourier phase is that it is defined on the frequency domain, which makes it difficult to connect with the local features of the image. This urges the need to define a local notion of phase.

In the 1D case, the Hilbert transform and the analytic signal have been widely used since the early 20th century to characterize the instantaneous behavior of a time signal (Ville 1948, Oswald 1956, Picinbono 2008). By extending the signal to the complex domain, the Hilbert transform yields notions of instantaneous amplitude and phase, which can be directly linked with the energy and structure of the signal at each time, respectively. There have been numerous attempts to generalize the analytic signal to 2D images in the 80s and 90s, but it was not until the early 2000s with the introduction of the monogenic signal that this goal was properly reached (Larkin, Bone & Oldfield 2001, Felsberg & Sommer 2001). Based on the Riesz transform (Riesz 1928), this technique yields notions of local amplitude, phase and orientation, which have since proved their relevance in the characterization of greyscale images in fields such as interferometry (Larkin et al. 2001, Kaseb, Mercère, Biermé, Brémand & Carré 2019), hologram demodulation (Seelamantula, Pavillon, Depeursinge & Unser 2012), medical imaging (Alessandrini, Basarab, Liebgott & Bernard 2013), etc.

Nevertheless, some issues still require further investigations. Despite being used for a wide variety of images, the local measures provided by the monogenic signal are only optimal for 2D unidirectional images. For images with richer content, some works give conditions on the regularity of the amplitude and phase functions to ensure the quality of their respective monogenic estimations, but these conditions often lack precision. Furthermore, because the monogenic signal was originally designed for 2D deterministic oscillating waves, the current literature lacks formal studies of the monogenic extraction of the local features of random textures, according to the authors' knowledge. Finally, the generalization of the monogenic framework to color images is still an open question, though the last

10 years saw the emergence of interesting suggestions (Demarcq, Mascarilla, Berthier & Courtellemont 2011, Soulard & Carré 2015).

In order to introduce new solutions for the aforementioned drawbacks and limits of the solutions available in the literature, this thesis will be divided in 6 chapters. Chapter 1 focuses on the use of the Roesser model to characterize and reconstruct color images. The structure of the model and its main assumptions are first discussed, especially the role of the innovation sequence. Its parameters are then estimated thanks to a reliable subspace-based algorithm introduced in (Ramos & Mercère 2018). This step emphasizes the direct implication of the color covariances in the estimation process, which ensures that the color information is captured by the model. The benefits of this approach are then illustrated by applying it to color texture completion. The purely vectorial subspace-based technique enables a better reconstruction of the color information when compared to marginal solutions, which confirms the importance of the color channel interdependency already highlighted in (Soulard 2012, Xu et al. 2015, Yin et al. 2019, Hosono et al. 2019)

As said previously, the Roesser model fails to extract some of the local features contained in the image, which is left in the innovation sequence. This motivates the use of more suitable tools for local structure characterization, namely, the Riesz transform and the monogenic signal, tackled in Chapter 2. The first part of the chapter recalls classical results of the 1D case, while pointing out some of the main issues regarding phase extraction. Then, the quality of the local measures provided by the monogenic tool is studied both theoretically and numerically in the case of 2D deterministic greyscale waves. Indeed, because the monogenic signal was originally designed for purely monochromatic waves (Felsberg & Sommer 2001), the reliability of its estimates is optimal only for such images (Seelamantula et al. 2012). The main contribution of this chapter is hence the formal study of how the Riesz transform deals with more complex patterns. The monogenic tool is then applied to real interferometric fringes to illustrate these theoretical results.

In practice, real textures may display stochastic features, unlike the purely deterministic images studied in Chapter 2. Consequently, Chapter 3 aims at extending the robustness of the monogenic estimates to random fields, which is a rarely treated subject in the current literature, according to the authors' knowledge. The developments of this chapter provide theoretical conditions to guarantee the quality of the monogenic extraction of both phase and orientation, respectively. The stochastic texture model used in this chapter is the Gabor noise, which is chosen for its ability to generated realistic textures displaying oscillating features (Lagae & Drettakis 2011, Galerne et al. 2012, Gilet, Sauvage, Vanhoey, Dischler & Ghazanfarpour 2014, Tricard, Efremov, Zanni, Neyret, Martinez & Lefebvre 2019). The application of the monogenic tool to real images shows how the underlying oscillating structure, as well the preferred direction of variation, are well extracted. Notice that Chapters 2 and 3 only deal with greyscale images, which is a necessary step before tackling color textures.

A proper color stochastic texture model, the color phasor noise, is introduced in Chapter 4 by merging the elliptic approach of multivariate signals found in (Lilly 2011, Soulard & Carré 2015) with the Gabor noise framework. Though works dealing with Gabor and phasor noises such as (Galerne et al. 2012, Tricard et al. 2019) include color textures, they do not define any formal color model. The main advantage of color phasor noise introduced in this chapter is that the structural and color features are fully encoded in a small number of

explicit parameters. This provides a full control over both the frequency and color content of the synthesized image, respectively. The elliptic representation also enables a useful visualization of color oscillation inside the RGB cube.

Chapter 5 then studies the use of the monogenic signal to characterize both the color and structural information of oscillating color textures. The theoretical and numerical developments show how the monogenic tool manages to extract the elliptic parameters from the image, from which an explicit description of its color content can be obtained. Focusing on the texture synthesis field, this chapter also tackles the occurrence of singularities in synthesized phasor noises. Though already mentioned in (Tricard et al. 2019), this issue was left as an open problem for future works. Thanks to its reliable phase estimation, the monogenic signal successfully detects the singularities in the noise, which yields measures of its quality in terms of local regularity.

The last part of this thesis sums up the main contributions of the previous chapters in the field of parametric texture analysis, and introduces a list of short term and long term perspectives.

CHAPTER 1

Subspace-based model learning

2D ARMA models have become standard techniques in the fields of image parametrization, image restoration and texture synthesis (Ramos & Mercère 2016). The key idea of this approach is to model each part of the image as a linear combination of surrounding pixels and independent errors occurring at each pixel (Kokaram 2004, Köppel et al. 2015). The ARMA parameters can then be explicitly linked with the second-order statistics of the texture, which enables the generation of another piece of texture sharing the same statistical behavior as the original image (Kokaram 2004).

Interestingly, many of the image modeling techniques available in the literature are designed for scalar signals (Xu et al. 2015), and hence do not handle the vectorial nature of color textures. Some works like *e.g.*, (Li, He, Tai, Yin & Chen 2015, Köppel et al. 2015), involve a shift from the RGB encoding to a luminance-chrominance base and apply scalar techniques to the luma and the luminance component, respectively, which puts the color information aside from the model. Other works like (Mairal, Elad & Sapiro 2008) tackle this problem by putting constraints on the three color components, but again, a significant part of the color structure is lost (Xu et al. 2015). In many cases, such scalar approaches lead to the apparition of color artifacts in the synthesized texture, *i.e.*, colors that do not appear in the original texture and damage the visual aspect of the synthesis (Soulard 2012, Xu et al. 2015). Though color regularization algorithms exist to eliminate such artifacts, such as in (Ono & Yamada 2016), this is an *a posteriori* treatment, and the color structure of the image is still not included in the model.

Meanwhile, many works such as (Chierchia, Pustelnik, Pesquet-Popescu & Pesquet 2014, Xu et al. 2015, Yin et al. 2019, Hosono et al. 2019) highlight the benefits of a vectorial treatment of the color components in the context of image processing. This is due to the fact that color textures are 3D objects living inside the RGB cube with correlated components rather than three independent scalar signals (Xu et al. 2015). This is illustrated in Figure 1.1 where a sand texture and its trajectory inside the RGB cube are represented, respectively. The geometrical shape of this trajectory shows that the three color components do not vary independently, which is confirmed by its empirical covariance matrix $\mathbf{\Lambda}$ given by

$$\mathbf{\Lambda} = \begin{pmatrix} 0.0266 & 0.0118 & -0.003 \\ 0.0118 & 0.0084 & 0.0047 \\ -0.003 & 0.0047 & 0.124 \end{pmatrix} \tag{1.1}$$

Many of the non-diagonal coefficients of $\mathbf{\Lambda}$ have the same order of magnitude as the di-

agonal coefficients, and neglecting them necessarily implies a loss of information. Such observations explain why treating the color channels marginally implies losing the color structure of the original texture partially, and suggest that a color model has to take these correlations into account in order to be efficient. Of course vectors are usually more difficult to handle than real numbers, which makes the generalization of greyscale techniques to color textures particularly complex.

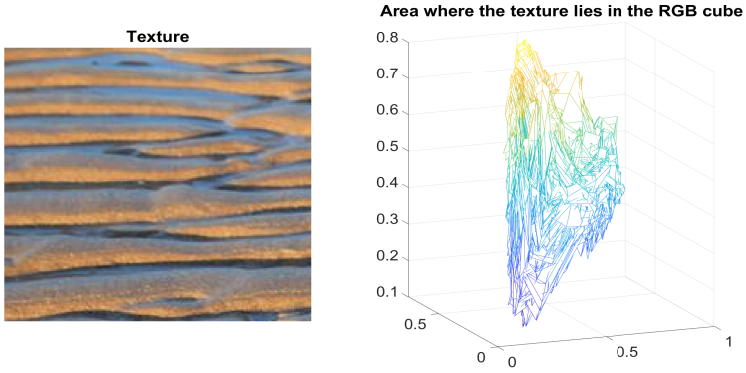

Figure 1.1: A texture (left) and the area where it lies inside the RGB cube (right).

The benefits of 2D ARMA-based parametrical representations (Köppel et al. 2015) can be extended to vectorial signals by relying on state space representations such as the Roesser model introduced in (Roesser 1975). Though not originally designed for color images specifically, this model gives good results in image restoration (Ramos & Mercère 2016), and efficient algorithms exist to estimate its parameters (Ramos & Mercère 2018). Furthermore, like the ARMA models handled in (Kokaram 2004, Köppel et al. 2015) in the greyscale case, it provides a direct link between the statistical behavior of the analyzed 2D signal and the parameters (Ramos & Mercère 2016, Ramos & Mercère 2018). Unlike the previously discussed marginal techniques, one of the main advantages of the algorithm introduced in (Ramos & Mercère 2018) is its purely vectorial treatment of multichannel signals, thanks to the use of Hankel matrices. However, most works related to the Roesser model do not interpret its parameters in terms of color structure, and, as a result, the benefits of its non-marginal treatment of the color components are not highlighted. This chapter hence introduces a brand new colorimetric study of the Roesser model and the estimation algorithm presented in (Ramos & Mercère 2018). The main purpose is to show how the color structure of the image is fully encoded in the Roesser parameters.

The rest of the chapter is organized as follows. The Roesser model and its parameters are first presented in Section 1.1. After the introduction of some useful operators in Section 1.2, the algorithm used to estimate the parameters of the model is detailed in Section 1.3. The colorimetric study of the Roesser model and the estimation algorithm introduced in Section 1.4 then show how the color structure is preserved during the estimation process, which makes this model of particular interest compared to scalar solutions available in the literature. The Roesser model is finally applied to texture completion in Section 1.5, which further illustrates the benefits of its vectorial treatment of the color channels.

1.1 Subspace-based model identification for 2D vectorial signals

This section recalls the basic equations and assumptions of the Roesser model as defined in (Roesser 1975). A brand new colorimetric interpretation of the model is then introduced.

1.1.1 The Roesser model

Let $\mathbf{Y}$ denote a stochastic hypermatrix of $\mathbb{R}^{M\times N\times n_y}$, with $(M,N,n_y)\in(\mathbb{N}^*)^3$. For all $(r,s)\in\{0,\dots,M-1\}\times\{0,\dots,N-1\}$, the vectorial components of $\mathbf{Y}$ are denoted by $\mathbf{y}_{r,s}\in\mathbb{R}^{n_y}$. In practice, if the data matrix $\mathbf{Y}$ is a color image, then $n_y=3$. The case of $n_y=1$ corresponds to greyscale images. The 1D state-space model detailed, *e.g.*, in (Overschee & Moor 1996, Katayama 2005), can then be generalized to 2D systems by use of the Roesser model introduced in (Roesser 1975). This model is defined for all $(r,s)\in\{0,\dots,M-1\}\times\{0,\dots,N-1\}$, $(M,N)\in\mathbb{N}^2$, by

$$\begin{cases} \mathbf{x}^h_{r+1,s} = \mathbf{A}_1\mathbf{x}^h_{r,s} + \mathbf{A}_2\mathbf{x}^v_{r,s} + \mathbf{K}_1\mathbf{e}_{r,s}, & \text{(1.2a)}\\ \mathbf{x}^v_{r,s+1} = \mathbf{A}_3\mathbf{x}^h_{r,s} + \mathbf{A}_4\mathbf{x}^v_{r,s} + \mathbf{K}_2\mathbf{e}_{r,s}, & \text{(1.2b)}\\ \mathbf{y}_{r,s} = \mathbf{C}_1\mathbf{x}^h_{r,s} + \mathbf{C}_2\mathbf{x}^v_{r,s} + \mathbf{e}_{r,s}, & \text{(1.2c)}\end{cases}$$

where $\mathbf{x}^h_{r,s}\in\mathbb{R}^{n_h}$ and $\mathbf{x}^v_{r,s}\in\mathbb{R}^{n_v}$ are the horizontal and vertical state vectors, respectively, $\mathbf{e}_{r,s}\in\mathbb{R}^{n_y}$ is the innovation vector (Ramos & Mercère 2018), while $\mathbf{A}_1$, $\mathbf{A}_2$, $\mathbf{A}_3$, $\mathbf{A}_4$, $\mathbf{C}_1$, $\mathbf{C}_2$, $\mathbf{K}_1$ and $\mathbf{K}_2$ are matrices of appropriate dimensions corresponding to the model parameters to be estimated. In this approach, the image $\mathbf{Y}$ is hence modeled as the output of a system governed by Eq. (1.2) and excited by the input sequence $(\mathbf{e}_{r,s})_{r,s}$ (see Figure 1.2). The state variables $\mathbf{x}^h_{r,s}$ and $\mathbf{x}^v_{r,s}$ can be seen as the memory of the underlying system at the pixel (r,s), *i.e.*, the impact of the previous pixels on the pixel (r,s) (Kailath et al. 2000).

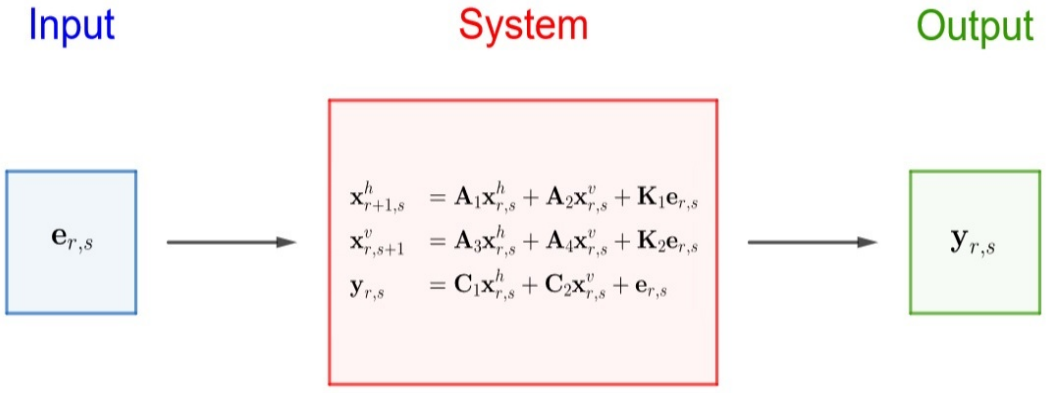

Figure 1.2: Input, system and output of the Roesser model.

1.1.2 2D Recursion

Unlike the case of 1D recursion, defining notions of previous and following pixels, respectively, is not trivial. A notable feature of the Roesser model given in Eq. (1.2) is that the horizontal and vertical state variables do not share the same pixel order. Indeed, for all $(r,s)\in\{0,\dots,M-1\}\times\{0,\dots,N-1\}$, the term coming after $\mathbf{x}^h_{r,s}$ is $\mathbf{x}^h_{r+1,s}$, while the term

coming after $\mathbf{x}^v_{r,s}$ is $\mathbf{x}^v_{r,s+1}$. A first consequence of this feature is that both variables require different types of initial conditions. More precisely, the whole first line of $\mathbf{x}^h$, *i.e.*, $(\mathbf{x}^h_{0,s})_s$, and the whole first column of $\mathbf{x}^v$, *i.e.*, $(\mathbf{x}^v_{r,0})_r$, must be known to perform the recursion. Assuming that the innovation sequence $\mathbf{e}$ is already generated, the state variables are computed as follows. The initial conditions and the innovation terms are displayed in black to distinguish them from the terms calculated during the process, which are displayed in color. Notice however that the colors are chosen randomly and are used to quickly identify the involved terms, but have no link with the color content of the image.

- Step 1 :

$$\begin{aligned}
\mathbf{x}^h_{1,0} &= \mathbf{A}_1\mathbf{x}^h_{0,0} + \mathbf{A}_2\mathbf{x}^v_{0,0} + \mathbf{K}_1\mathbf{e}_{0,0},\\
\mathbf{x}^v_{0,1} &= \mathbf{A}_3\mathbf{x}^h_{0,0} + \mathbf{A}_4\mathbf{x}^v_{0,0} + \mathbf{K}_2\mathbf{e}_{0,0},\\
\mathbf{x}^h_{1,1} &= \mathbf{A}_1\mathbf{x}^h_{0,1} + \mathbf{A}_2\mathbf{x}^v_{0,1} + \mathbf{K}_1\mathbf{e}_{0,1},\\
\mathbf{x}^v_{1,1} &= \mathbf{A}_3\mathbf{x}^h_{1,0} + \mathbf{A}_4\mathbf{x}^v_{1,0} + \mathbf{K}_2\mathbf{e}_{1,0}.
\end{aligned} \tag{1.3}$$

- Step 2 :

$$\begin{aligned}
\mathbf{x}^h_{2,0} &= \mathbf{A}_1\mathbf{x}^h_{1,0} + \mathbf{A}_2\mathbf{x}^v_{1,0} + \mathbf{K}_1\mathbf{e}_{1,0},\\
\mathbf{x}^v_{0,2} &= \mathbf{A}_3\mathbf{x}^h_{0,1} + \mathbf{A}_4\mathbf{x}^v_{0,1} + \mathbf{K}_2\mathbf{e}_{0,1},\\
\mathbf{x}^h_{2,1} &= \mathbf{A}_1\mathbf{x}^h_{1,1} + \mathbf{A}_2\mathbf{x}^v_{1,1} + \mathbf{K}_1\mathbf{e}_{1,1},\\
\mathbf{x}^v_{2,1} &= \mathbf{A}_3\mathbf{x}^h_{2,0} + \mathbf{A}_4\mathbf{x}^v_{2,0} + \mathbf{K}_2\mathbf{e}_{2,0},\\
\mathbf{x}^h_{1,2} &= \mathbf{A}_1\mathbf{x}^h_{0,2} + \mathbf{A}_2\mathbf{x}^v_{0,2} + \mathbf{K}_1\mathbf{e}_{0,2},\\
\mathbf{x}^v_{1,2} &= \mathbf{A}_3\mathbf{x}^h_{1,1} + \mathbf{A}_4\mathbf{x}^v_{1,1} + \mathbf{K}_2\mathbf{e}_{1,1},\\
\mathbf{x}^h_{2,2} &= \mathbf{A}_1\mathbf{x}^h_{1,2} + \mathbf{A}_2\mathbf{x}^v_{1,2} + \mathbf{K}_1\mathbf{e}_{1,2},\\
\mathbf{x}^v_{2,2} &= \mathbf{A}_3\mathbf{x}^h_{2,1} + \mathbf{A}_4\mathbf{x}^v_{2,1} + \mathbf{K}_2\mathbf{e}_{2,1}.
\end{aligned} \tag{1.4}$$

- ...

At each step $r \in \{0, \dots, \min(M, N) - 2\}$, knowing all the values of the square $\{0, \dots, r\}^2$ enables the calculation of the values $\mathbf{x}^\bullet_{r+1,\ell}$ and $\mathbf{x}^\bullet_{\ell,r+1}$, $\bullet \in \{h, v\}$, $\ell \in \{0, \dots, r+1\}^2$. This process is repeated until the two state variables are fully computed inside the square $\{0, \dots, \min(M, N) - 1\}^2$. Assuming for example that $M < N$, the remaining values of the rectangle $\{0, \dots, M-1\} \times \{M, \dots, N-1\}$ can finally be calculated.

1.1.3 Stochastic assumptions

The 2D process $(\mathbf{y}_{r,s})_{r,s}$ is assumed to be stationary. This may seem to be a strong assumption, but in practice, the Roesser model still gives good results when this assumption is mildly violated (Ramos & Mercère 2018). From a more practical point of view, this requires the processed image to display some structural homogeneity (Köppel et al. 2015). The innovation process $(\mathbf{e}_{r,s})_{r,s}$ is assumed to be a zero-mean white noise, with its covariance matrix denoted by $\mathbf{R} \in \mathbb{R}^{n_y \times n_y}$. Section 1.1.4 details the role of this sequence in the model. Given the fact that $\mathbf{e}_{r,s}$ has the same dimension as $\mathbf{y}_{r,s}$ (see Eq. (1.2c)), it can also be interpreted as a color image in the special case of $n_y = 3$. The coefficients of the matrix $\mathbf{R}$ can hence be seen as color covariances that characterize the color content of the innovation term. The horizontal and vertical state processes $(\mathbf{x}^h_{r,s})_{r,s}$ and $(\mathbf{x}^v_{r,s})_{r,s}$ are also

assumed to be stationary and zero-mean, with their covariance matrices denoted by $\mathbf{\Pi}_h$ and $\mathbf{\Pi}_v$, respectively. In (Ramos & Mercère 2018), further assumptions are made on the non-correlation of the state variables, *i.e.*,

$$\mathbb{E}\left[\begin{pmatrix}\mathbf{x}^h_{r,s}\\ \mathbf{x}^v_{r',s'}\end{pmatrix}\begin{pmatrix}\left(\mathbf{x}^h_{r,s}\right)^\top & \left(\mathbf{x}^v_{r',s'}\right)^\top\end{pmatrix}\right] = \begin{pmatrix}\mathbf{\Pi}_h & 0_{n_h\times n_v}\\ 0_{n_v\times n_h} & \mathbf{\Pi}_v\end{pmatrix} \tag{1.5}$$

for all $(r, r', s, s') \in \mathbb{N}^4$. As seen in Section 1.3, this condition is crucial for the estimation of the state sequences. Notice that unlike $\mathbf{R}$, the matrices $\mathbf{\Pi}_h$ and $\mathbf{\Pi}_v$ do not contain color covariances, as the state variables do not necessarily have the same dimension as $\mathbf{y}_{r,s}$ (see Eq. (1.2a) and (1.2b), respectively). If the system orders n_h and n_v are seen as the number of horizontal and vertical inner variables of the image, respectively, the coefficients of $\mathbf{\Pi}_h$ and $\mathbf{\Pi}_v$ then quantify the degree interdependence between these variables.

1.1.4 The innovation sequence

For each $(r, s) \in \{0, \ldots, M-1\} \times \{0, \ldots, N-1\}$, the term $\mathbf{e}_{r,s}$ is called the innovation because it is the part of $\mathbf{y}_{r,s}$ that is not determined by the previous data (see Chapter 4 in (Kailath et al. 2000)). In other words, it is the new information brought at the pixel (r, s). In many works dealing with ARMA models, the innovation sequence $\mathbf{e}_{r,s}$ is only described in terms of second-order statistics (Köppel et al. 2015). However, as shown in (Kailath et al. 2000), knowing the variance of $\mathbf{e}_{r,s}$ is not enough to fully characterize it. Despite being a white noise, the innovation sequence is directly linked with the available data $\mathbf{y}_{r,s}$, which makes it unique, and thus crucial in the reconstruction of $\mathbf{y}_{r,s}$ (Kailath et al. 2000). Consequently, once the parameters of the Roesser model and the second order statistics of the innovation are estimated, generating a white noise from these estimated statistics and using it as an input sequence in the model cannot yield a satisfactory reconstruction of the output sequence $\mathbf{y}_{r,s}$, which is highlighted in Section 1.3.5 with practical examples. While this chapter does not provide a full characterization of the innovation, this suggests that subsequent works dealing with parametric image modeling should put more emphasis on the information contained in this sequence. Before detailing the algorithm developed in (Ramos & Mercère 2016) to identify the parameters of the Roesser model, some useful matrix operators and their properties are introduced in Section 1.2.

1.2 Matrix operators for subspace-based identification

1.2.1 Matrix stacking and Hankel matrices

In subspace-based identification, the basic equations of the model, given by Eq. (1.2), are rewritten as matrix products through recursion (Katayama 2005, Ramos & Mercère 2016). Similarly to what is done in (Ramos & Mercère 2016, Ramos & Mercère 2018), block matrices are introduced to make the equations more compact in the subsequent developments. Let $(\mathbf{u}_{r,s})_{r,s}$ be a 2D vectorial series, where each $\mathbf{u}_{r,s}$, $(r, s) \in \mathbb{N}^2$, is a column vector of $\mathbb{R}^{n_u}$, $n_u \in \mathbb{N}^*$. In the subsequent developments of Section 1.3, $\mathbf{u}$ is equal to $\mathbf{y}$, $\mathbf{x}^h$,$\mathbf{x}^v$ or $\mathbf{e}$, respectively. The finite column stacked vector is defined for all $n \in \mathbb{N}^+_*$ as

$$\text{cstack}\{\mathbf{u}_{k,\ell}, \mathbf{u}_{k+n-1,\ell}\} = \begin{pmatrix}\mathbf{u}^\top_{k,\ell} & \cdots & \mathbf{u}^\top_{k+n-1,\ell}\end{pmatrix}^\top \in \mathbb{R}^{nn_u\times 1}. \tag{1.6}$$

Likewise, the finite row stacked matrix is defined as

$$\text{rstack}\{\mathbf{u}_{k,\ell}, \mathbf{u}_{k+n-1,\ell}\} = \begin{pmatrix} \mathbf{u}_{k,\ell} & \cdots & \mathbf{u}_{k+n-1,\ell} \end{pmatrix} \in \mathbb{R}^{n_u \times n}. \tag{1.7}$$

The Hankel matrix, which is also crucial in subspace-based identification (Katayama 2005, Ramos & Mercère 2016), is defined as

$$\text{hankel}\{\mathbf{u}_{k,\ell}, \mathbf{u}_{k+n+j-2,\ell}, n, j\} = \begin{pmatrix} \mathbf{u}_{k,\ell} & \mathbf{u}_{k+1,\ell} & \cdots & \mathbf{u}_{k+j-1,\ell} \\ \mathbf{u}_{k+1,\ell} & \mathbf{u}_{k+2,\ell} & \cdots & \mathbf{u}_{k+j,\ell} \\ \vdots & \vdots & \ddots & \vdots \\ \mathbf{u}_{k+n-1,\ell} & \mathbf{u}_{k+n,\ell} & \cdots & \mathbf{u}_{k+n+j-2,\ell} \end{pmatrix} \in \mathbb{R}^{nn_u \times j}, \tag{1.8}$$

where n is the number of row blocks and j is the number of columns, respectively. Using matrices $\mathbf{A}$, $\mathbf{B}$, $\mathbf{C}$ and $\mathbf{D}$ of appropriate dimensions, the extended controllability-like matrix is defined for all $\ell \in \mathbb{N}_*^+$ as

$$\text{crtb}\{\mathbf{A}, \mathbf{B}, \ell\} = \begin{pmatrix} \mathbf{A}^{\ell-1}\mathbf{B} & \cdots & \mathbf{AB} & \mathbf{B} \end{pmatrix}, \tag{1.9}$$

the extended observability-like matrix as

$$\text{obsv}(\mathbf{A}, \mathbf{B}, \ell) = \begin{pmatrix} \mathbf{B} \\ \mathbf{BA} \\ \vdots \\ \mathbf{BA}^{\ell-1} \end{pmatrix}, \tag{1.10}$$

and the block lower-triangular Toeplitz matrix as

$$\text{toep}\{\mathbf{A}, \mathbf{B}, \mathbf{C}, \mathbf{D}, \ell\} = \begin{pmatrix} \mathbf{D} & \mathbf{0} & \cdots & \mathbf{0} \\ \mathbf{CB} & \mathbf{D} & \cdots & \mathbf{0} \\ \vdots & \ddots & \ddots & \vdots \\ \mathbf{CA}^{\ell-2}\mathbf{B} & \cdots & \mathbf{CB} & \mathbf{D} \end{pmatrix}. \tag{1.11}$$

1.2.2 Oblique projection

Similarly to what is done in the 1D case, oblique projections are at the core of 2D subspace-based identification (Katayama 2005, Ramos & Mercère 2018). This section aims at presenting some basic properties of oblique projections that are useful in the estimation of the state sequence detailed in Section 1.3.3. Let $\mathbf{M}$, $\mathbf{N}$ and $\mathbf{P}$ be matrices of appropriate dimensions. The oblique projection of the row space of $\mathbf{M}$ on the row space of $\mathbf{P}$ along the row space of $\mathbf{N}$, denoted by $\mathbf{M}/_{\mathbf{N}}\mathbf{P}$, is defined by (Horn & Johnson 1990)

$$\mathbf{M}/_{\mathbf{N}}\mathbf{P} = \mathbf{M}\mathbf{\Pi}_{\mathbf{N}}^{\perp}\mathbf{P}^{\top}\left(\mathbf{P}\mathbf{\Pi}_{\mathbf{N}}^{\perp}\mathbf{P}^{\top}\right)^{-1}\mathbf{P}, \tag{1.12}$$

where the orthogonal projection $\mathbf{\Pi}_{\mathbf{N}}^{\perp}$ is defined by

$$\mathbf{\Pi}_{\mathbf{N}}^{\perp} = \mathbf{I} - \mathbf{\Pi}_{\mathbf{N}} = \mathbf{I} - \mathbf{N}^{\top}\left(\mathbf{N}\mathbf{N}^{\top}\right)^{-1}\mathbf{N}. \tag{1.13}$$

A first property is that the projection of $\mathbf{N}$ on $\mathbf{P}$ along $\mathbf{N}$ is the null matrix. Indeed,

$$\mathbf{N}\mathbf{\Pi}_{\mathbf{N}}^{\perp} = \mathbf{N}\left[\mathbf{I} - \mathbf{N}^{\top}\left(\mathbf{N}\mathbf{N}^{\top}\right)^{-1}\mathbf{N}\right] = \mathbf{N} - \underbrace{\mathbf{N}\mathbf{N}^{\top}\left(\mathbf{N}\mathbf{N}^{\top}\right)^{-1}}_{\mathbf{I}}\mathbf{N} = \mathbf{0}, \tag{1.14}$$

which implies that

$$\mathbf{N}/_{\mathbf{N}}\mathbf{P} = \underbrace{\mathbf{N}\mathbf{\Pi}_{\mathbf{N}}^{\perp}}_{\mathbf{0}}\mathbf{P}^{\top}\left(\mathbf{P}\mathbf{\Pi}_{\mathbf{N}}^{\perp}\mathbf{P}^{\top}\right)^{-1}\mathbf{P} = \mathbf{0}. \tag{1.15}$$

Another property is that $\mathbf{P}$ is invariant with respect to the projection on $\mathbf{P}$. Indeed,

$$\mathbf{P}/_{\mathbf{N}}\mathbf{P} = \underbrace{\mathbf{P}\mathbf{\Pi}_{\mathbf{N}}^{\perp}\mathbf{P}^{\top}\left(\mathbf{P}\mathbf{\Pi}_{\mathbf{N}}^{\perp}\mathbf{P}^{\top}\right)^{-1}}_{\mathbf{I}}\mathbf{P} = \mathbf{P}. \tag{1.16}$$

Now that the oblique projections are introduced, the subspace-based estimation algorithm presented in (Ramos & Mercère 2018) can be detailed, with a special focus on the treatment of the color content of the original image.

1.3 Estimation algorithm

1.3.1 General idea

In practice, only the output sequence $\mathbf{y}$ is available, while the state sequences $\mathbf{x}^h$ and $\mathbf{x}^v$, the innovation sequence $\mathbf{e}$, as well as the parameters $\mathbf{A}_1$, $\mathbf{A}_2$, $\mathbf{A}_3$, $\mathbf{A}_4$, $\mathbf{C}_1$, $\mathbf{C}_2$, $\mathbf{K}_1$ and $\mathbf{K}_2$, have to be estimated. Assuming that the state variables have been estimated, the Roesser model defined in Eq. (1.2) can be seen as a linear regression of the dependent variable $\mathbf{y}$ on the regressors $\mathbf{x}^h$ and $\mathbf{x}^v$. In this case, the parameters of the model can be extracted by using ordinary least squares, the innovation sequence being the residuals of this linear model (Ramos & Mercère 2018). For this to be possible, the state sequences are estimated thanks to oblique projections involving available data only, as done in (Overschee & Moor 1996, Katayama 2005) in the 1D case and (Ramos & Mercère 2016, Ramos & Mercère 2018) in the 2D case. The 2D subspace-based algorithm of (Ramos & Mercère 2018) can thus be summed up as follows.

- Step 1 : express the state sequences $\mathbf{x}^h$ and $\mathbf{x}^v$ as a combination of available data through oblique projections.
- Step 2 : estimate the matrices $\mathbf{A}_1$, $\mathbf{A}_2$, $\mathbf{A}_3$, $\mathbf{A}_4$, $\mathbf{C}_1$ and $\mathbf{C}_2$ by using ordinary least squares.
- Step 3 : estimate the innovation sequence $\mathbf{e}$ as the residuals of the previous linear model.
- Step 4 : estimate the matrices $\mathbf{K}_1$ and $\mathbf{K}_2$ by solving standard Riccati equations (Overschee & Moor 1996).

Each of these steps are detailed in the next sections.

1.3.2 Horizontal and vertical data equations

In order to generalize the algorithm of the 1D case (see (Katayama 2005, Overschee & Moor 1996)) to 2D images, the same processes are applied to each row and each column of the data matrix $\mathbf{Y}$, respectively. Indeed, if $\ell \in \{0, \ldots, N-1\}$ denotes a fixed column index, then the horizontal equations given by

$$\begin{cases} \mathbf{x}^h_{r+1,\ell} &= \mathbf{A}_1\mathbf{x}^h_{r,\ell} + \mathbf{A}_2\mathbf{x}^v_{r,\ell} + \mathbf{K}_1\mathbf{e}_{r,\ell}, \\ \mathbf{y}_{r,\ell} &= \mathbf{C}_1\mathbf{x}^h_{r,\ell} + \mathbf{C}_2\mathbf{x}^v_{r,\ell} + \mathbf{e}_{r,\ell}. \end{cases} \tag{1.17}$$

can be seen as a 1D state-space representation (with respects to r) with two input vectors $\mathbf{x}^v_{r,\ell}$ and $\mathbf{K}_1\mathbf{e}_{r,\ell}$, one state vector $\mathbf{x}^h_{r,\ell}$, one output vector $\mathbf{y}_{r,\ell}$ and an innovation term $\mathbf{e}_{r,\ell}$. From this state-space form, standard recursions encountered in subspace-based identification for 1D models can be applied (see, *e.g.*, (Katayama 2005)). Indeed, by applying Eq. (1.17) successively, $\mathbf{y}_{r,\ell}$ can be expressed for all $r \in \{1, \dots M-1\}$ as

$$\begin{aligned} \mathbf{y}_{r,\ell} &= \mathbf{C}_1\mathbf{x}^h_{r,\ell} + \mathbf{C}_2\mathbf{x}^v_{r,\ell} + \mathbf{e}_{r,\ell}, \\ &= \mathbf{C}_1\mathbf{A}_1\mathbf{x}^h_{r-1,\ell} \\ &\quad + \mathbf{C}_1\mathbf{A}_2\mathbf{x}^v_{r-1,\ell} + \mathbf{C}_2\mathbf{x}^v_{r,\ell} \\ &\quad + \mathbf{C}_1\mathbf{K}_1\mathbf{e}_{r-1,\ell} + \mathbf{e}_{r,\ell}, \\ &= \mathbf{C}_1\mathbf{A}_1^2\mathbf{x}^h_{r-2,\ell} \\ &\quad + \mathbf{C}_1\mathbf{A}_1\mathbf{A}_2\mathbf{x}^v_{r-2,\ell} + \mathbf{C}_1\mathbf{A}_2\mathbf{x}^v_{r-1,\ell} + \mathbf{C}_2\mathbf{x}^v_{r,\ell} \\ &\quad + \mathbf{C}_1\mathbf{A}_1\mathbf{K}_1\mathbf{e}_{r-2,\ell} + \mathbf{C}_1\mathbf{K}_1\mathbf{e}_{r-1,\ell} + \mathbf{e}_{r,\ell}, \\ &= \mathbf{C}_1\mathbf{A}_1^3\mathbf{x}^h_{r-3,\ell} \\ &\quad + \mathbf{C}_1\mathbf{A}_1^2\mathbf{A}_2\mathbf{x}^v_{r-3,\ell} + \mathbf{C}_1\mathbf{A}_1\mathbf{A}_2\mathbf{x}^v_{r-2,\ell} + \mathbf{C}_1\mathbf{A}_2\mathbf{x}^v_{r-1,\ell} + \mathbf{C}_2\mathbf{x}^v_{r,\ell} \\ &\quad + \mathbf{C}_1\mathbf{A}_1^2\mathbf{K}_1\mathbf{e}_{r-3,\ell} + \mathbf{C}_1\mathbf{A}_1\mathbf{K}_1\mathbf{e}_{r-2,\ell} + \mathbf{C}_1\mathbf{K}_1\mathbf{e}_{r-1,\ell} + \mathbf{e}_{r,\ell}, \\ &= \dots, \\ &= \mathbf{C}_1\mathbf{A}_1^r\mathbf{x}^h_{0,\ell} \\ &\quad + \mathbf{C}_1\sum_{k=1}^{r}\mathbf{A}_1^{k-1}\mathbf{A}_2\mathbf{x}^v_{r-k,\ell} + \mathbf{C}_2\mathbf{x}^v_{r,\ell} \\ &\quad + \mathbf{C}_1\sum_{k=1}^{r}\mathbf{A}_1^{k-1}\mathbf{K}_1\mathbf{e}_{r-k,\ell} + \mathbf{K}_1\mathbf{e}_{r,\ell}. \end{aligned} \tag{1.18}$$

The sums can then be rewritten as block matrix products, leading to

$$\begin{aligned} \mathbf{y}_{r,\ell} = \mathbf{C}_1\mathbf{A}_1^r\mathbf{x}^h_{0,\ell} &\\ + \begin{pmatrix}\mathbf{C}_1\mathbf{A}_1^{r-1}\mathbf{A}_2 & \dots & \mathbf{C}_1\mathbf{A}_1\mathbf{A}_2 & \mathbf{C}_2\end{pmatrix} &\begin{pmatrix}\mathbf{x}^v_{0,\ell}\\ \vdots \\ \mathbf{x}^v_{r,\ell}\end{pmatrix} \\ + \begin{pmatrix}\mathbf{C}_1\mathbf{A}_1^{r-1}\mathbf{K}_1 & \dots & \mathbf{C}_1\mathbf{A}_1\mathbf{K}_1 & \mathbf{I}_{n_y}\end{pmatrix} &\begin{pmatrix}\mathbf{e}_{0,\ell}\\ \vdots \\ \mathbf{e}_{r,\ell}\end{pmatrix}. \end{aligned} \tag{1.19}$$

This is exactly where the block matrices introduced in Section 1.2.1 are involved. Let i and j be two integer indices such that $2i + j - 2 = \min\{M-1, N-1\}$. This condition is imposed on the indices i and j in order to include the greatest amount of data in the process. This constraint notably implies that the greater i is, the smaller j becomes, and vice-versa. Applying Eq. (1.19) to all $r \in \{0, \dots, 2i+j-2\}$ and stacking all the equations in block matrices leads for all $\ell \in \{0, \dots, N-1\}$ to the following horizontal data equations (Ramos & Mercère 2016, Ramos & Mercère 2018)

$$\begin{aligned}\mathbf{Y}_p^h(\ell) &= \mathbf{\Gamma}_p^h \mathbf{X}_p^h(\ell) + \mathbf{G}_p^{vh} \mathbf{X}_p^{vh}(\ell) + \mathbf{H}_p^h \mathbf{E}_p^h(\ell),\\ \mathbf{Y}_f^h(\ell) &= \mathbf{\Gamma}_f^h \mathbf{X}_f^h(\ell) + \mathbf{G}_f^{vh} \mathbf{X}_f^{vh}(\ell) + \mathbf{H}_f^h \mathbf{E}_f^h(\ell),\end{aligned} \tag{1.20}$$

where

$$\begin{aligned}\mathbf{Y}_p^h(\ell) &= \text{hankel}\{\mathbf{y}_{0,\ell}, \mathbf{y}_{i+j-2,\ell}, i, j\},\\ \mathbf{X}_p^h(\ell) &= \text{rstack}\{\mathbf{x}_{0,\ell}^h, \mathbf{x}_{j-1,\ell}^h\},\\ \mathbf{X}_p^{vh}(\ell) &= \text{hankel}\{\mathbf{x}_{0,\ell}^v, \mathbf{x}_{i+j-2,\ell}^v, i, j\},\\ \mathbf{E}_p^h(\ell) &= \text{hankel}\{\mathbf{e}_{0,\ell}, \mathbf{e}_{i+j-2,\ell}, i, j\},\\ \mathbf{Y}_f^h(\ell) &= \text{hankel}\{\mathbf{y}_{i,\ell}, \mathbf{y}_{2i+j-2,\ell}, i, j\},\\ \mathbf{X}_f^h(\ell) &= \text{rstack}\{\mathbf{x}_{i,\ell}^h, \mathbf{x}_{i+j-1,\ell}^h\},\\ \mathbf{X}_f^{vh}(\ell) &= \text{hankel}\{\mathbf{x}_{i,\ell}^v, \mathbf{x}_{2i+j-2,\ell}^v, i, j\},\\ \mathbf{E}_f^h(\ell) &= \text{hankel}\{\mathbf{e}_{i,\ell}, \mathbf{e}_{2i+j-2,\ell}, i, j\},\end{aligned} \tag{1.21}$$

while, for $n \in \{f, p\}$,

$$\begin{aligned}\mathbf{\Gamma}_n^h &= \text{obsv}\{\mathbf{A}_1, \mathbf{C}_1, i\},\\ \mathbf{G}_n^{vh} &= \text{toep}\{\mathbf{A}_1, \mathbf{A}_2, \mathbf{C}_1, \mathbf{C}_2, i\},\\ \mathbf{H}_n^h &= \text{toep}\{\mathbf{A}_1, \mathbf{K}_1, \mathbf{C}_1, \mathbf{I}_{n_y}, i\}.\end{aligned} \tag{1.22}$$

Notice that unlike the 1D case where the time variable clearly defines notions of past and future, these notions must be defined arbitrarily in the case of 2D images. Usually, the horizontal space variable is assumed to evolve from top to bottom, while the vertical space variable is assumed to evolve from left to right, which is consistent with the recursive equations that define of the horizontal and vertical states, respectively. With this convention, the first and second lines of Eq. (1.20) are called past and future equations, respectively, hence the indices p and f. The parameter i is an integer that corresponds to the maximal order of the recursions performed to obtain the past and future equations. In theory, this tuning parameter must be chosen so that rank conditions like the one given by Eq. (1.45) is satisfied. In practice, i is chosen large enough to guarantee that $i >> \{n_h, n_v\}$. As shown in Section 1.5, selecting $i = 20$ for the tested images is sufficient to get good results. Notice that, at this stage, the color components of the data vectors $\mathbf{y}_{r,s}$ are only stacked inside block matrices but not mixed yet. Indeed, in the special case of $n_y = 3$, by using Eq. (1.8), the future Hankel matrix $\mathbf{Y}_f^h(\ell)$ can be written for all $\ell \in \{0, \ldots, N-1\}$ as

$$\begin{aligned}\mathbf{Y}_f^h(\ell) &= \begin{pmatrix} \mathbf{y}_{i,\ell} & \mathbf{y}_{i+1,\ell} & \cdots & \mathbf{y}_{i+j-1,\ell} \\ \mathbf{y}_{i+1,\ell} & \mathbf{y}_{i+2,\ell} & \cdots & \mathbf{y}_{i+j,\ell} \\ \vdots & \vdots & \ddots & \vdots \\ \mathbf{y}_{2i-1,\ell} & \mathbf{y}_{2i,\ell} & \cdots & \mathbf{y}_{2i+j-2,\ell} \end{pmatrix} \\ &= \begin{pmatrix} y_{i,\ell}^R & y_{i+1,\ell}^R & \cdots & y_{i+j-1,\ell}^R \\ y_{i,\ell}^G & y_{i+1,\ell}^G & \cdots & y_{i+j-1,\ell}^G \\ y_{i,\ell}^B & y_{i+1,\ell}^B & \cdots & y_{i+j-1,\ell}^B \\ \vdots & \vdots & \ddots & \vdots \\ y_{2i-1,\ell}^R & y_{2i,\ell}^R & \cdots & y_{2i+j-2,\ell}^R \\ y_{2i-1,\ell}^G & y_{2i,\ell}^G & \cdots & y_{2i+j-2,\ell}^G \\ y_{2i-1,\ell}^B & y_{2i,\ell}^B & \cdots & y_{2i+j-2,\ell}^B \end{pmatrix}; \end{aligned} \tag{1.23}$$

where for all $r \in \{i, \ldots, 2i+j-2\}$, the scalars $y_{r,\ell}^R$, $y_{r,\ell}^G$ and $y_{r,\ell}^B$ denote the red, blue and green components of the vector $\mathbf{y}_{r,\ell}$, respectively. Figure 1.3 shows an example of how the future Hankel matrix is built for $\ell = 10$ and $M = N = 180$. This process is repeated for all $\ell \in \{0, \ldots, N-1\}$. In each case, the past Hankel matrix is built from the rectangular zone between the pixels $(0, \ell)$ and $(159, \ell)$, while the future Hankel matrix is built from the rectangular zone between the pixels $(20, \ell)$ and $(179, \ell)$.

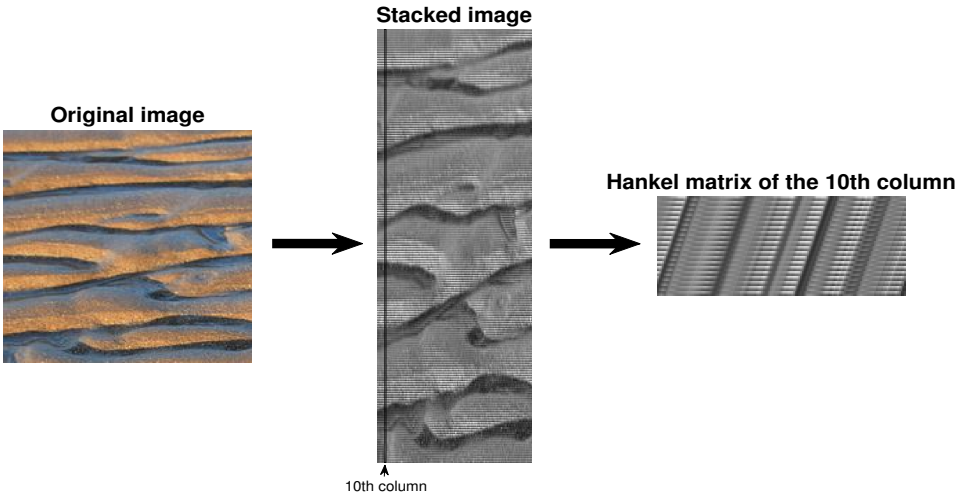

Figure 1.3: Original image (left), stacked image (middle) and future Hankel matrix built from the 10th column (right), with $M = N = 180$, $i = 20$, $j = 141$.

The same procedures are now applied to the rows of the data matrix $\mathbf{Y}$. Indeed, if $\ell \in \{0, \ldots, M-1\}$ denotes a fixed row index, then the vertical equations given by

$$\begin{cases} \mathbf{x}_{\ell,s+1}^v &= \mathbf{A}_3 \mathbf{x}_{\ell,s}^h + \mathbf{A}_4 \mathbf{x}_{\ell,s}^v + \mathbf{K}_2 \mathbf{e}_{\ell,s}, \\ \mathbf{y}_{\ell,s} &= \mathbf{C}_1 \mathbf{x}_{\ell,s}^h + \mathbf{C}_2 \mathbf{x}_{\ell,s}^v + \mathbf{e}_{\ell,s}. \end{cases} \tag{1.24}$$

can be seen as a 1D state-space representation (with respects to s). Applying standard recursions then leads, for all $\ell \in \{0, \ldots, M-1\}$, to the following vertical data equations (Ramos & Mercère 2016, Ramos & Mercère 2018)

$$\begin{aligned}\mathbf{Y}_p^v(\ell) &= \mathbf{\Gamma}_p^v \mathbf{X}_p^v(\ell) + \mathbf{G}_p^{hv} \mathbf{X}_p^{hv}(\ell) + \mathbf{H}_p^v \mathbf{E}_p^v(\ell),\\ \mathbf{Y}_f^v(\ell) &= \mathbf{\Gamma}_f^v \mathbf{X}_f^v(\ell) + \mathbf{G}_f^{hv} \mathbf{X}_f^{hv}(\ell) + \mathbf{H}_f^v \mathbf{E}_f^v(\ell),\end{aligned} \tag{1.25}$$

where

$$\begin{aligned}\mathbf{Y}_p^v(\ell) &= \text{hankel}\{\mathbf{y}_{\ell,0}, \mathbf{y}_{\ell,i+j-2}, i, j\},\\ \mathbf{X}_p^v(\ell) &= \text{rstack}\{\mathbf{x}_{\ell,0}^v, \mathbf{x}_{\ell,j-1}^v\},\\ \mathbf{X}_p^{hv}(\ell) &= \text{hankel}\{\mathbf{x}_{\ell,0}^h, \mathbf{x}_{\ell,i+j-2}^h, i, j\},\\ \mathbf{E}_p^v(\ell) &= \text{hankel}\{\mathbf{e}_{\ell,0}, \mathbf{e}_{\ell,i+j-2}, i, j\},\\ \mathbf{Y}_f^v(\ell) &= \text{hankel}\{\mathbf{y}_{\ell,i}, \mathbf{y}_{\ell,2i+j-2}, i, j\},\\ \mathbf{X}_f^v(\ell) &= \text{rstack}\{\mathbf{x}_{\ell,i}^v, \mathbf{x}_{\ell,i+j-1}^v\},\\ \mathbf{X}_f^{hv}(\ell) &= \text{hankel}\{\mathbf{x}_{\ell,i}^h, \mathbf{x}_{\ell,2i+j-2}^h, i, j\},\\ \mathbf{E}_f^v(\ell) &= \text{hankel}\{\mathbf{e}_{\ell,i}, \mathbf{e}_{\ell,2i+j-2}, i, j\},\end{aligned} \tag{1.26}$$

while, for $n \in \{f, p\}$,

$$\begin{aligned}\mathbf{\Gamma}_n^v &= \text{obsv}\{\mathbf{A}_4, \mathbf{C}_2, i\},\\ \mathbf{G}_n^{hv} &= \text{toep}\{\mathbf{A}_4, \mathbf{A}_3, \mathbf{C}_2, \mathbf{C}_1, i\},\\ \mathbf{H}_n^v &= \text{toep}\{\mathbf{A}_4, \mathbf{K}_2, \mathbf{C}_2, \mathbf{I}_{n_y}, i\}.\end{aligned} \tag{1.27}$$

1.3.3 State sequence estimation and projection of the future on the past

Focusing on the horizontal data equations given by Eq. (1.20), the key idea of subspace-based algorithms is the projection of the future data on the past data to get an estimation of the state sequence, *i.e.*, the values of $\mathbf{x}_{r,s}^h$ and $\mathbf{x}_{r,s}^v$, for $(r,s) \in \{i, \ldots, i+j-1\}^2$. To do so, the future state vector $\mathbf{X}_f^h(\ell)$ is first expressed as a linear combination of the past state vector $\mathbf{X}_p^{vh}(\ell)$ and the past data vector $\mathbf{Y}_p^h(\ell)$, with $\ell \in \{0, \ldots, N-1\}$. The first step consists in expressing the innovation term for all $(r,s) \in \{0, \ldots, M-1\} \times \{0, \ldots, N-1\}$ as

$$\mathbf{e}_{r,\ell} = \mathbf{y}_{r,\ell} - \mathbf{C}_1 \mathbf{x}_{r,\ell}^h - \mathbf{C}_2 \mathbf{x}_{r,\ell}^v. \tag{1.28}$$

Notice how this equation is consistent with the interpretation of the variables given in Section 1.1. Indeed, $\mathbf{e}_{r,\ell}$ is expressed as the difference between the available data at the pixel (r,ℓ), $\mathbf{y}_{r,\ell}$, and the memory of the previous pixels represented by the terms $\mathbf{C}_1 \mathbf{x}_{r,\ell}^h$ and $\mathbf{C}_2 \mathbf{x}_{r,\ell}^v$, which illustrates how $\mathbf{e}_{r,\ell}$ contains the new information brought at the pixel (r,ℓ), *i.e.*, the innovation. Focusing again on the estimation algorithm, the horizontal 1D system given by Eq. (1.24) can then be equivalently rewritten for all $\ell \in \{0, \ldots, N-1\}$ as

$$\left\{ \begin{array}{ll} \mathbf{x}_{r+1,\ell}^h & = \widetilde{\mathbf{A}}_1 \mathbf{x}_{r,\ell}^h + \widetilde{\mathbf{A}}_2 \mathbf{x}_{r,\ell}^v + \mathbf{K}_1 \mathbf{y}_{r,\ell},\\ \mathbf{y}_{r,\ell} & = \mathbf{C}_1 \mathbf{x}_{r,\ell}^h + \mathbf{C}_2 \mathbf{x}_{r,\ell}^v + \mathbf{e}_{r,\ell}, \end{array} \right. \tag{1.29}$$

where

$$\widetilde{\mathbf{A}}_1 = \mathbf{A}_1 - \mathbf{K}_1 \mathbf{C}_1 \quad \text{and} \quad \widetilde{\mathbf{A}}_2 = \mathbf{A}_2 - \mathbf{K}_2 \mathbf{C}_2. \tag{1.30}$$

By applying standard recursions, as done in, *e.g.*, (Peternell, Sherrer & Deistler 1996), $\mathbf{x}^h_{r,\ell}$ can be expressed with the past data as

$$\begin{aligned}\mathbf{x}^h_{r,\ell} &= \widetilde{\mathbf{A}}_1^i \mathbf{x}^h_{r-i,\ell} + \sum_{k=1}^{i} \widetilde{\mathbf{A}}_1^{k-1} \widetilde{\mathbf{A}}_2 \mathbf{x}^v_{r-k,\ell} + \sum_{k=1}^{i} \widetilde{\mathbf{A}}_1^{k-1} \mathbf{K}_1 \mathbf{y}_{r-k,\ell}, \\ &= \widetilde{\mathbf{A}}_1^i \mathbf{x}^h_{r-i,\ell} + \widetilde{\mathbf{\Phi}}^{vh}_p \mathbf{x}^v_p(r,\ell) + \widetilde{\mathbf{L}}^h_p \mathbf{y}_p(r,\ell),\end{aligned} \tag{1.31}$$

where

$$\begin{aligned}\widetilde{\mathbf{\Phi}}^{vh}_p &= \mathrm{crtb}\{\widetilde{\mathbf{A}}_1, \widetilde{\mathbf{A}}_2, i\}, \\ \widetilde{\mathbf{L}}^h_p &= \mathrm{crtb}\{\widetilde{\mathbf{A}}_1, \mathbf{K}_1, i\}, \\ \mathbf{x}^v_p(r,\ell) &= \mathrm{cstack}\{\mathbf{x}^v_{r-i,\ell}, \mathbf{x}^v_{r-1,\ell}\}, \\ \mathbf{y}_p(r,\ell) &= \mathrm{cstack}\{\mathbf{y}_{r-i,\ell}, \mathbf{y}_{r-1,\ell}\}.\end{aligned} \tag{1.32}$$

If $\|\bullet\|_2$ and $|||\bullet|||_2$ denote the vectorial and matricial Euclidian norms, respectively, using the submultiplicativity of $|||\bullet|||_2$ (see (Horn & Johnson 1990) for details about vector and matrix norms) leads to

$$\begin{aligned}\left\|\mathbf{x}^h_{r,\ell} - \widetilde{\mathbf{\Phi}}^{vh}_p \mathbf{x}^v_p(r,\ell) - \widetilde{\mathbf{L}}^h_p \mathbf{y}_p(r,\ell)\right\|_2 &= \left\|\widetilde{\mathbf{A}}_1^i \mathbf{x}^h_{r-i,\ell}\right\|_2, \\ &\leq \left|||\widetilde{\mathbf{A}}_1|||_2^i \left\|\mathbf{x}^h_{r-i,\ell}\right\|_2, \\ &= \lambda_{max}^i \left\|\mathbf{x}^h_{r-i,\ell}\right\|_2,\end{aligned} \tag{1.33}$$

where λ_{max} denotes the greatest eigenvalue of $\widetilde{\mathbf{A}}_1$. By definition of the Kalman gain $\mathbf{K}_1$ (Katayama 2005), the modulus of the greatest eigenvalue of $\widetilde{\mathbf{A}}_1$ is necessarily strictly lower than 1, which implies that the term $\widetilde{\mathbf{A}}_1^i \mathbf{x}^h_{r-i,\ell}$ becomes negligible if i is chosen sufficiently large. Consequently, the distance between $\mathbf{x}^h_{r,\ell}$ and $\widetilde{\mathbf{\Phi}}^{vh}_p \mathbf{x}^v_p(r,\ell) + \widetilde{\mathbf{L}}^h_p \mathbf{y}_p(r,\ell)$ expressed in Eq. (1.33) becomes negligible for large values of i. The state vector $\mathbf{x}^h_{r,\ell}$ can hence be approached for all $(r,\ell) \in \{0,\ldots,M-1\} \times \{0,\ldots,N-1\}$ as

$$\mathbf{x}^h_{r,\ell} \approx \widetilde{\mathbf{\Phi}}^{vh}_p \mathbf{x}^v_p(r,\ell) + \widetilde{\mathbf{L}}^h_p \mathbf{y}_p(r,\ell). \tag{1.34}$$

This can be seen as the optimal linear estimate of $\mathbf{x}^h_{r,\ell}$ (in the least-square error sense) given $\mathbf{x}^v_p(r,\ell)$ and $\mathbf{y}_p(r,\ell)$. Combining this linear estimation of $\mathbf{x}^h_{r,\ell}$ with the horizontal equation given by Eq. (1.20) leads to

$$\mathbf{Y}^h_f(\ell) = \mathbf{\Gamma}^h_f \widetilde{\mathbf{\Phi}}^{vh}_p \mathbf{X}^{vh}_p(\ell) + \mathbf{\Gamma}^h_f \widetilde{\mathbf{L}}^h_p \mathbf{Y}^h_p(\ell) + \mathbf{G}^{vh}_f \mathbf{X}^{vh}_f(\ell) + \mathbf{H}^h_f \mathbf{E}^h_f(\ell). \tag{1.35}$$

Applying this equation to all $\ell \in \{0,\ldots,N-1\}$ and grouping all the obtained equations in block matrices finally leads to

$$\mathbf{Y}^h_f = \mathbf{\Gamma}^h_f \widetilde{\mathbf{\Phi}}^{vh}_p \mathbf{X}^{vh}_p + \mathbf{\Gamma}^h_f \widetilde{\mathbf{L}}^h_p \mathbf{Y}^h_p + \mathbf{G}^{vh}_f \mathbf{X}^{vh}_f + \mathbf{H}^h_f \mathbf{E}^h_f, \tag{1.36}$$

where for all $n \in \{f,p\}$ and all matrix $\mathbf{M} \in \{\mathbf{Y}^h_n, \mathbf{X}^{vh}_n, \mathbf{E}^h_n\}$,

$$\mathbf{M} = \begin{pmatrix}\mathbf{M}(0) & \ldots & \mathbf{M}(N-1)\end{pmatrix}. \tag{1.37}$$

Figure 1.4 illustrates how the past and future data are extracted from the original image to build the horizontal past and future block Hankel matrix $\mathbf{Y}_p^h$ and $\mathbf{Y}_f^h$, respectively. As in Figure 1.3, the size of the image is 180×180, while the tuning parameters are $i = 20$ and $j = 141$. Notice that the constraint $2i + j - 2 = \min\{M - 1, N - 1\}$ fixed in Section 1.3.2 ensures that the greatest amount of pixels are involved in the estimation process.

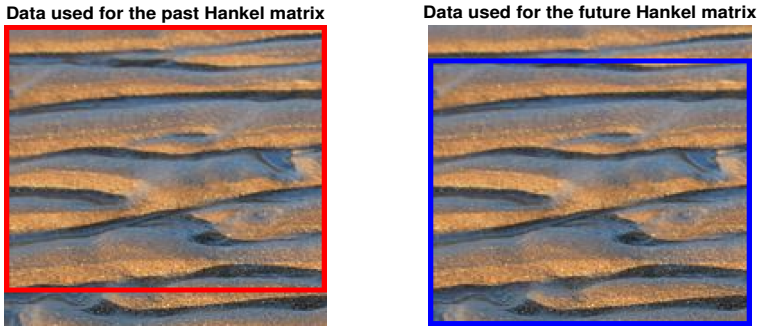

Figure 1.4: Data used for the horizontal past (left) and future (right) block Hankel matrix.

Similar procedures can then be applied to the vertical equations, leading to

$$\mathbf{Y}_f^v = \mathbf{\Gamma}_f^v \widetilde{\mathbf{\Phi}}_p^{hv} \mathbf{X}_p^{hv} + \mathbf{\Gamma}_f^v \widetilde{\mathbf{L}}_p^v \mathbf{Y}_p^v + \mathbf{G}_f^{hv} \mathbf{X}_f^{hv} + \mathbf{H}_f^v \mathbf{E}_f^h, \tag{1.38}$$

where

$$\begin{aligned} \widetilde{\mathbf{A}}_3 &= \mathbf{A}_3 - \mathbf{K}_2 \mathbf{C}_1, \\ \widetilde{\mathbf{A}}_4 &= \mathbf{A}_4 - \mathbf{K}_2 \mathbf{C}_2, \\ \widetilde{\mathbf{\Phi}}_p^{hv} &= \mathrm{crtb}\{\widetilde{\mathbf{A}}_4, \widetilde{\mathbf{A}}_3, i\}, \\ \widetilde{\mathbf{L}}_p^v &= \mathrm{crtb}\{\widetilde{\mathbf{A}}_4, \mathbf{K}_2, i\}, \end{aligned} \tag{1.39}$$

and for all $n \in \{f, p\}$ and all matrix $\mathbf{M} \in \{\mathbf{Y}_n^v, \mathbf{X}_n^{hv}, \mathbf{E}_n^v\}$,

$$\mathbf{M} = \begin{pmatrix} \mathbf{M}(0) & \dots & \mathbf{M}(M-1) \end{pmatrix}. \tag{1.40}$$

Figure 1.5 illustrates how the past and future data are extracted from the original image to build the vertical past and future block Hankel matrix $\mathbf{Y}_p^h$ and $\mathbf{Y}_f^h$, respectively.
In Eq. (1.36) and (1.38), the future data contained in the Hankel matrices $\mathbf{Y}_f^\bullet$, $\bullet \in \{h, v\}$, involve both available and unavailable data. In order to express them with only available data, an oblique projection of the future on the past is performed. More precisely, focusing on the horizontal equation, the row space of $\mathbf{Y}_f^h$ is projected on the row space $\mathbf{Z}_p^h$ along the row space $\mathbf{X}_f^{vh}$ (Ramos & Mercère 2018), where

$$\mathbf{Z}_p^h = \begin{pmatrix} \mathbf{X}_p^{vh} \\ \mathbf{Y}_p^h \end{pmatrix}. \tag{1.41}$$

Eq. (1.15) implies that $\mathbf{X}_f^{vh}$ is projected on the null matrix, while Eq. (1.16) implies that $\mathbf{Z}_p^h$ is invariant, hence

$$\mathbf{Y}_f^h /_{\mathbf{X}_f^{vh}} \mathbf{Z}_p^h = \mathbf{\Gamma}_f^h \begin{pmatrix} \widetilde{\mathbf{\Phi}}_p^{vh} & \widetilde{\mathbf{L}}_p^h \end{pmatrix} \mathbf{Z}_p^h + \mathbf{H}_f^h \mathbf{E}_f^h /_{\mathbf{X}_f^{vh}} \mathbf{Z}_p^h. \tag{1.42}$$

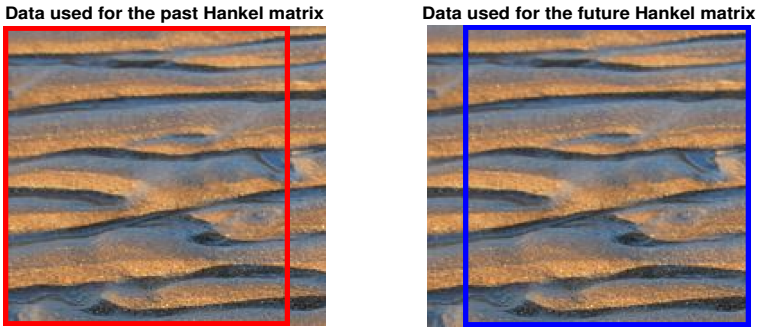

Figure 1.5: Data used for the vertical past (left) and future (right) block Hankel matrix.

Similarly,

$$\mathbf{Y}_f^v/_{\mathbf{X}_f^{hv}}\mathbf{Z}_p^v = \mathbf{\Gamma}_f^v \begin{pmatrix} \widetilde{\mathbf{\Phi}}_p^{hv} & \widetilde{\mathbf{L}}_p^v \end{pmatrix} \mathbf{Z}_p^v + \mathbf{H}_f^v \mathbf{E}_f^v/_{\mathbf{X}_f^{hv}}\mathbf{Z}_p^v, \tag{1.43}$$

where

$$\mathbf{Z}_p^v = \begin{pmatrix} \mathbf{X}_p^{hv} \\ \mathbf{Y}_p^v \end{pmatrix}. \tag{1.44}$$

Because the oblique projection involves the inversion of the matrices $\mathbf{Z}_p^h \mathbf{\Pi}^{\perp}_{\mathbf{X}_f^{vh}} \mathbf{Z}_p^{h\top}$ and $\mathbf{Z}_p^v \mathbf{\Pi}^{\perp}_{\mathbf{X}_f^{hv}} \mathbf{Z}_p^{v\top}$, respectively (see Eq. (1.13) for the definition of $\mathbf{\Pi}^{\perp}_{\mathbf{N}}$), they must be assumed of full rank if M and N are sufficiently large, *i.e.*,

$$\begin{aligned} \operatorname{rank}\left(\lim_{M\to+\infty} \mathbf{Z}_p^h \mathbf{\Pi}^{\perp}_{\mathbf{X}_f^{vh}} \mathbf{Z}_p^{h\top}\right) &= p(n_v + n_y), \\ \operatorname{rank}\left(\lim_{N\to+\infty} \mathbf{Z}_p^v \mathbf{\Pi}^{\perp}_{\mathbf{X}_f^{hv}} \mathbf{Z}_p^{v\top}\right) &= p(n_h + n_y). \end{aligned} \tag{1.45}$$

Furthermore, as shown in (Ramos & Mercère 2018), given the fact that the future innovation terms are uncorrelated with the past state and data terms, respectively, it can be stated that

$$\begin{aligned} \lim_{M\to+\infty} \mathbf{E}_f^h \mathbf{\Pi}^{\perp}_{\mathbf{X}_f^{vh}} \mathbf{Z}_p^{h\top} &= 0, \\ \lim_{N\to+\infty} \mathbf{E}_f^v \mathbf{\Pi}^{\perp}_{\mathbf{X}_f^{hv}} \mathbf{Z}_p^{v\top} &= 0, \end{aligned} \tag{1.46}$$

so that Eq. (1.42) and (1.43) simplify as

$$\begin{aligned} \mathbf{Y}_f^h/_{\mathbf{X}_f^{vh}}\mathbf{Z}_p^h &= \mathbf{\Gamma}_f^h \begin{pmatrix} \widetilde{\mathbf{\Phi}}_p^{vh} & \widetilde{\mathbf{L}}_p^h \end{pmatrix} \mathbf{Z}_p^h, \\ \mathbf{Y}_f^v/_{\mathbf{X}_f^{hv}}\mathbf{Z}_p^v &= \mathbf{\Gamma}_f^v \begin{pmatrix} \widetilde{\mathbf{\Phi}}_p^{hv} & \widetilde{\mathbf{L}}_p^v \end{pmatrix} \mathbf{Z}_p^v, \end{aligned} \tag{1.47}$$

respectively. Remember that, for $\bullet \in \{h, v\}$, the right members correspond to the optimal linear estimates of $\mathbf{X}_f^{\bullet}$ (see Eq. (1.34)), which implies that these equations can be rewritten as

$$\begin{aligned}\mathbf{Y}_f^h/_{\mathbf{X}_f^{vh}}\mathbf{Z}_p^h &= \mathbf{\Gamma}_f^h\mathbf{X}_f^h,\\ \mathbf{Y}_f^v/_{\mathbf{X}_f^{hv}}\mathbf{Z}_p^v &= \mathbf{\Gamma}_f^v\mathbf{X}_f^v,\end{aligned} \tag{1.48}$$

where

$$\begin{aligned}\mathbf{X}_f^h &= \begin{pmatrix}\mathbf{X}_f^h(0) & \dots & \mathbf{X}_f^h(N-1)\end{pmatrix},\\ \mathbf{X}_f^v &= \begin{pmatrix}\mathbf{X}_f^v(0) & \dots & \mathbf{X}_f^v(M-1)\end{pmatrix}.\end{aligned} \tag{1.49}$$

Unfortunately, these equations are not directly usable in practice. Indeed, they involve oblique projections along the row spaces of $\mathbf{X}_f^{vh}$ and $\mathbf{X}_f^{hv}$, which contain the unknown vertical and horizontal state variables, respectively. The solution developed in (Ramos & Mercère 2018) is based on the fact that the above-mentioned oblique projections simplify to orthogonal projections of the future data on the past data assuming that the horizontal and vertical states are uncorrelated, *i.e.*, assuming that Eq. (1.5) holds. If $\bullet \in \{h, v\}$, this yields

$$\mathbf{Y}_f^\bullet\mathbf{\Pi}_{\mathbf{Y}_p^\bullet} = \mathbf{\Gamma}_f^\bullet\mathbf{X}_f^\bullet, \tag{1.50}$$

where, this time, the projections only involve available data. Notice that performing this projection directly involves the color covariances of the image, which is exactly what makes this approach non-marginal. This is discussed in details in Section 1.4.1. Once estimates of $\mathbf{\Gamma}_f^\bullet\mathbf{X}_f^\bullet$, $\bullet \in \{h, v\}$, are computed from the orthogonal projections $\mathbf{Y}_f^\bullet\mathbf{\Pi}_{\mathbf{Y}_p^\bullet}$, estimates of the future horizontal and vertical state variables can be extracted through a singular value decomposition (Horn & Johnson 1990) (see Section 1.3.4 for a description of the implementation).

1.3.4 Singular value decomposition and parameter estimation

As done in any subspace-based algorithm, the orthogonal projection of the future on the past is performed through an RQ factorization (Horn & Johnson 1990), *i.e.*, for $\bullet \in \{h, v\}$,

$$\begin{aligned}\mathbf{\Gamma}_f^\bullet\mathbf{X}_f^\bullet &= \mathbf{Y}_f^\bullet\mathbf{\Pi}_{\mathbf{Y}_p^\bullet},\\ &= \mathbf{R}_{21}^\bullet\left(\mathbf{Q}_1^\bullet\right)^\top,\end{aligned} \tag{1.51}$$

with

$$\begin{pmatrix}\mathbf{Y}_p^\bullet\\ \mathbf{Y}_f^\bullet\end{pmatrix} = \begin{pmatrix}\mathbf{R}_{11}^\bullet & \mathbf{0}_{n_yp\times n_yf}\\ \mathbf{R}_{21}^\bullet & \mathbf{R}_{22}^\bullet\end{pmatrix}\begin{pmatrix}\left(\mathbf{Q}_1^\bullet\right)^\top\\ \left(\mathbf{Q}_2^\bullet\right)^\top\end{pmatrix}. \tag{1.52}$$

Once the projection is available, the extraction of the state sequences is performed by resorting to a Singular Value Decomposition (SVD) (Horn & Johnson 1990), hence,

$$\mathbf{R}_{21}^\bullet\left(\mathbf{Q}_1^\bullet\right)^\top = \begin{pmatrix}\mathbf{U}_\bullet & \mathbf{U}_\bullet^\perp\end{pmatrix}\begin{pmatrix}\mathbf{\Sigma}_\bullet & \mathbf{0}\\ \mathbf{0} & \times\end{pmatrix}\begin{pmatrix}\mathbf{V}_\bullet^\top\\ \left(\mathbf{U}_\bullet^\perp\right)^\top\end{pmatrix}. \tag{1.53}$$

In theory, the product $\mathbf{\Gamma}_f^\bullet\mathbf{X}_f^\bullet$ is of rank $n_\bullet$, $\bullet \in \{h, v\}$, which implies that the matrix $\mathbf{\Sigma}_\bullet$ is of dimension $n_\bullet \times n_\bullet$, $\bullet \in \{h, v\}$, and only contain non-zero singular values (Overschee & Moor 1996). In practice, due to the innovation $\mathbf{e}_{r,s}$ and the finite number of data, the

singular values of $\mathbf{\Gamma}_f^\bullet \mathbf{X}_f^\bullet$ are not exactly zero beyond the order $n_\bullet$, but a quick drop is observed after $n_\bullet$. The orders of the horizontal and vertical systems, denoted by n_h and n_v, respectively, are then determined as the index of the lowest non-negligible singular value. This process is illustrated in Section 1.5.2. Extracting the non-negligible part of the SVD hence leads to

$$\mathbf{R}_{21}^\bullet \left(\mathbf{Q}_1^\bullet\right)^\top = \mathbf{U}_\bullet \mathbf{\Sigma}_\bullet \mathbf{V}_\bullet^\top. \tag{1.54}$$

The state sequence is finally extracted as the right part of the SVD, *i.e.*, for $\bullet \in \{h, v\}$,

$$\begin{aligned} \mathbf{X}_f^\bullet &= \mathbf{\Sigma}_\bullet^{\frac{1}{2}} \mathbf{V}_\bullet^\top, \\ &= \mathbf{\Sigma}_\bullet^{-\frac{1}{2}} \mathbf{U}_\bullet^\top \mathbf{R}_{21}^\bullet \left(\mathbf{Q}_1^\bullet\right)^\top. \end{aligned} \tag{1.55}$$

Remark. *In practice, the SVD is performed on the matrix* $\mathbf{W}_1^\bullet \mathbf{R}_{21}^\bullet \left(\mathbf{Q}_1^\bullet\right)^\top \mathbf{W}_2^\bullet$ *rather than merely* $\mathbf{R}_{21}^\bullet \left(\mathbf{Q}_1^\bullet\right)^\top$*, with* $\mathbf{W}_1^\bullet$ *and* $\mathbf{W}_2^\bullet$ *denoting weighting matrices of appropriate dimensions. The choice of these weighting matrices depends on the algorithm chosen to perform the SVD (see (Overschee & Moor 1996) for further details).*

Remember that by construction of the block matrices $\mathbf{X}_f^h$ and $\mathbf{X}_f^v$, their common part is restricted to $(r, s) \in \{i, \ldots, i+j-1\}^2$, which implies that the state variables can only be estimated inside this domain. By defining

$$\begin{aligned} \mathbf{f}_y &= \begin{pmatrix} \mathbf{y}_{i,i:i+j-2} & \cdots & \mathbf{y}_{i+j-2,i:i+j-2} \end{pmatrix}, \\ \mathbf{f}_{x^+}^h &= \begin{pmatrix} \mathbf{x}_{i+1,i:i+j-2}^h & \cdots & \mathbf{x}_{i+j-1,i:i+j-2}^h \end{pmatrix}, \\ \mathbf{f}_{x^+}^v &= \begin{pmatrix} \mathbf{x}_{i,i+1:i+j-1}^v & \cdots & \mathbf{x}_{i+j-2,i+1:i+j-1}^v \end{pmatrix}, \\ \mathbf{f}_x^h &= \begin{pmatrix} \mathbf{x}_{i,i:i+j-2}^h & \cdots & \mathbf{x}_{i+j-2,i:i+j-2}^h \end{pmatrix}, \\ \mathbf{f}_x^v &= \begin{pmatrix} \mathbf{x}_{i,i:i+j-2}^v & \cdots & \mathbf{x}_{i+j-2,i:i+j-2}^v \end{pmatrix}, \\ \mathbf{f}_e &= \begin{pmatrix} \mathbf{e}_{i,i:i+j-2} & \cdots & \mathbf{e}_{i+j-2,i:i+j-2} \end{pmatrix}, \end{aligned} \tag{1.56}$$

where

$$\mathbf{p}_{i,j:k} = \begin{pmatrix} \mathbf{p}_{i,j} & \cdots & \mathbf{p}_{i,j+1} & \cdots & \mathbf{p}_{i,k} \end{pmatrix}, \tag{1.57}$$

the basic equations of the Roesser model given by Eq. (1.2) can be rewritten as the following least-squares regression problem

$$\underbrace{\begin{pmatrix} \mathbf{f}_{x^+}^h \\ \mathbf{f}_{x^+}^v \\ \mathbf{f}_y \end{pmatrix}}_{\mathbf{Y}} = \underbrace{\begin{pmatrix} \mathbf{A}_1 & \mathbf{A}_2 \\ \mathbf{A}_3 & \mathbf{A}_4 \\ \mathbf{C}_1 & \mathbf{C}_2 \end{pmatrix}}_{\mathbf{A}} \underbrace{\begin{pmatrix} \mathbf{f}_x^h \\ \mathbf{f}_x^v \end{pmatrix}}_{\mathbf{X}} + \underbrace{\begin{pmatrix} \mathbf{K}_1 \\ \mathbf{K}_2 \\ \mathbf{I}_{n_y} \end{pmatrix}}_{\mathbf{E}} \mathbf{f}_e, \tag{1.58}$$

where $\mathbf{I}_{n_y}$ denotes the identity matrix of size $n_y \times n_y$. Consistent estimates of $\mathbf{A}_1$, $\mathbf{A}_2$, $\mathbf{A}_3$, $\mathbf{A}_4$, $\mathbf{C}_1$, $\mathbf{C}_2$ can then be computed by using ordinary linear least-squares algorithms (Ramos & Mercère 2018). Finally, the innovation sequence and its covariance matrix are computed as

$$\begin{cases} \mathbf{E} & = \mathbf{Y} - \mathbf{A}\mathbf{X}, \\ \begin{pmatrix} \mathbf{Q} & \mathbf{S} \\ \mathbf{S}^\top & \mathbf{R} \end{pmatrix} & = \mathbf{E}\mathbf{E}^\top / j, \end{cases} \tag{1.59}$$

with

$$\begin{aligned} \mathbf{Q} &= \begin{pmatrix} \mathbf{K}_1\mathbf{R}\mathbf{K}_1^\top & \mathbf{K}_1\mathbf{R}\mathbf{K}_2^\top \\ \mathbf{K}_2\mathbf{R}\mathbf{K}_1^\top & \mathbf{K}_2\mathbf{R}\mathbf{K}_2^\top \end{pmatrix}, \\ \mathbf{S} &= \begin{pmatrix} \mathbf{K}_1\mathbf{R} \\ \mathbf{K}_2\mathbf{R} \end{pmatrix}, \end{aligned} \tag{1.60}$$

from which $\mathbf{K}_1$ and $\mathbf{K}_2$ can be estimated by solving standard Riccati equations (see (Ramos & Mercère 2018, Overschee & Moor 1996) for details). This concludes the estimation algorithm.

1.3.5 Importance of the innovation sequence

Though not focused on image processing, (Kailath et al. 2000) highlights the importance of the innovation sequence and the fact that it cannot be fully characterized by second order statistics. This section aims at illustrating this statement with real textures. Indeed, Figure 1.6 shows that, after estimating the model through the algorithm described in the previous sections, some information remain in the innovation sequence, even if the horizontal and vertical orders n_h and n_v are raised beyond 5. In order to highlight the crucial information contained in the innovation sequence, a random i.i.d. Gaussian sequence $\mathbf{e}'$ of size $M \times N$ is generated, with each of the terms being zero-mean and of covariance matrix $\mathbf{R}$. This sequence $\mathbf{e}'$ is then used as an input in the Roesser model to generate a new image with the same parameters and state variables as the original texture. As shown in Figure 1.7, though the color content and global dynamic are preserved thanks to the reliable parameter estimations provided by the algorithm, the image looks smoothed and a great amount of its local variations are lost. If the error estimated from the sand texture is used as an input to generate the grass texture, then some of the edges of the sand texture appear in the grass texture, as is shown in Figure 1.8. When the Roesser model is applied to texture completion in Section 1.5, the choice of the innovation sequence constitutes one of the most crucial steps, as it is the part of the image that is not captured by the model. Before that, a colorimetric study of the estimation algorithm is performed in Section 1.4.1 to highlight its ability to extract the color structure of the processed image.

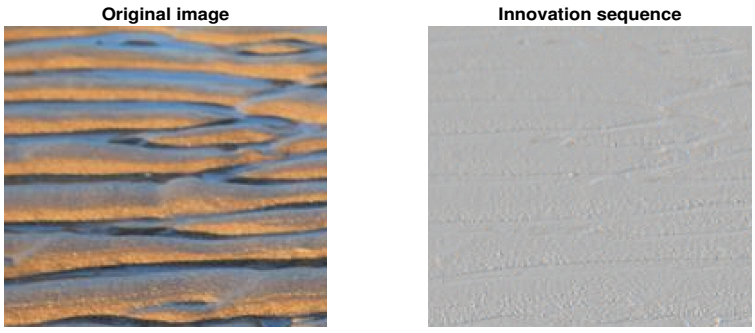

Figure 1.6: A sand texture and its estimated innovation sequence.

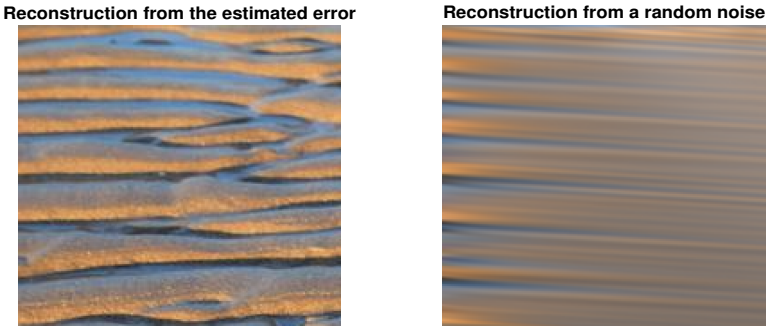

Figure 1.7: Comparison between the sand texture reconstructed from the estimated error (left) and the image reconstructed from a random Gaussian noise (right).

Figure 1.8: Comparison between the grass texture reconstructed from the grass error (left) and the image reconstructed from the sand error (right).

1.4 Color covariances

1.4.1 Link between the projection and the color covariances

As recalled in the introduction, treating the color components of $\mathbf{y}$ marginally requires that the three color channels vary independently, while in practice they are usually correlated (Xu et al. 2015). This implies that treating them as three independent scalar series may cause a partial loss of the color information contained inside the image (Hosono et al. 2019). One of the main advantages of the algorithm presented in Section 1.3 is that the color covariances are directly implied in the estimation process, hence its non-marginal nature. This can be highlighted by rewriting the projection of the future on the past performed in Eq. (1.50) as autocovariance matrix products. If k and m are positive integers, let $\mathbf{\Lambda}_{k,m}$ denote the autocovariance matrix of $(\mathbf{y}_{r,s})_{r,s}$ defined for all $(r,s) \in \mathbb{N}^2$ by

$$\mathbf{\Lambda}_{k,m} = \mathbb{E}\left[\mathbf{y}_{r+k,s+m}\mathbf{y}_{r,s}^\top\right], \tag{1.61}$$

where $\mathbb{E}[\cdot]$ denotes the mean operator (Papoulis & Pillai 2002). Using Eq. (1.13) to explicitly express the orthogonal projection $\mathbf{\Pi}_{\mathbf{Y}_p^\bullet}$ leads to

$$\mathbf{Y}_f^\bullet \mathbf{Y}_p^{\bullet\top}\left(\mathbf{Y}_p^\bullet \mathbf{Y}_p^{\bullet\top}\right)^{-1}\mathbf{Y}_p^\bullet = \mathbf{\Gamma}_f^\bullet \mathbf{X}_f^\bullet. \tag{1.62}$$

These matrix products can then be expressed with the color covariance matrices $\mathbf{\Lambda}_{k,m}$. Indeed, if $(k,m) \in \{1,\dots i\}^2$, the block (k,m) of the matrices $\mathbf{Y}_p^\bullet \mathbf{Y}_p^{\bullet\top}$, $\bullet \in \{h,v\}$, is given by

$$\begin{aligned}
\left(\mathbf{Y}_p^h \mathbf{Y}_p^{h\top}\right)_{k,m} &= \sum_{\ell=0}^{N-1}\sum_{\iota=0}^{j-1} \mathbf{y}_{k+\iota-1,\ell}\mathbf{y}_{m+\iota-1,\ell}^\top, \\
\left(\mathbf{Y}_p^v \mathbf{Y}_p^{v\top}\right)_{k,m} &= \sum_{\ell=0}^{M-1}\sum_{\iota=0}^{j-1} \mathbf{y}_{\ell,k+\iota-1}\mathbf{y}_{\ell,m+\iota-1}^\top.
\end{aligned} \tag{1.63}$$

If M, N and j are sufficiently large, these sample covariances provide reliable approximations of the corresponding autocovariance matrices (Johnson & Wichern 2002), hence

$$\begin{aligned}
\left(\mathbf{Y}_p^h \mathbf{Y}_p^{h\top}\right)_{k,m} &= jN\mathbf{\Lambda}_{|k-m|,0}, \\
\left(\mathbf{Y}_p^v \mathbf{Y}_p^{v\top}\right)_{k,m} &= jM\mathbf{\Lambda}_{0,|k-m|}.
\end{aligned} \tag{1.64}$$

Similarly, if $(k,m) \in \{1,\dots i\}^2$,

$$\begin{aligned}
\left(\mathbf{Y}_f^h \mathbf{Y}_p^{h\top}\right)_{k,m} &= jN\mathbf{\Lambda}_{i+k-m,0}, \\
\left(\mathbf{Y}_f^v \mathbf{Y}_p^{v\top}\right)_{k,m} &= jM\mathbf{\Lambda}_{0,i+k-m}.
\end{aligned} \tag{1.65}$$

Eq. (1.62) can hence be rewritten for $\bullet \in \{h,v\}$ as

$$\mathbf{\Lambda}_f^\bullet \left(\mathbf{\Lambda}_p^\bullet\right)^{-1}\mathbf{Y}_p^\bullet = \mathbf{\Gamma}_f^\bullet \mathbf{X}_f^\bullet, \tag{1.66}$$

where

$$
\begin{aligned}
\boldsymbol{\Lambda}_p^h &= \begin{pmatrix} \boldsymbol{\Lambda}_{0,0} & \boldsymbol{\Lambda}_{1,0} & \dots & \boldsymbol{\Lambda}_{i-1,0} \\ \boldsymbol{\Lambda}_{1,0} & \boldsymbol{\Lambda}_{0,0} & \dots & \boldsymbol{\Lambda}_{i-2,0} \\ \vdots & \vdots & \ddots & \vdots \\ \boldsymbol{\Lambda}_{i-1,0} & \boldsymbol{\Lambda}_{i-2,0} & \dots & \boldsymbol{\Lambda}_{0,0} \end{pmatrix}, \\
\boldsymbol{\Lambda}_f^h &= \begin{pmatrix} \boldsymbol{\Lambda}_{i,0} & \boldsymbol{\Lambda}_{p-1,0} & \dots & \boldsymbol{\Lambda}_{1,0} \\ \boldsymbol{\Lambda}_{i+1,0} & \boldsymbol{\Lambda}_{p,0} & \dots & \boldsymbol{\Lambda}_{2,0} \\ \vdots & \vdots & \ddots & \vdots \\ \boldsymbol{\Lambda}_{2i-1,0} & \boldsymbol{\Lambda}_{2i-2,0} & \dots & \boldsymbol{\Lambda}_{i,0} \end{pmatrix}, \\
\boldsymbol{\Lambda}_p^v &= \begin{pmatrix} \boldsymbol{\Lambda}_{0,0} & \boldsymbol{\Lambda}_{0,1} & \dots & \boldsymbol{\Lambda}_{0,i-1} \\ \boldsymbol{\Lambda}_{0,1} & \boldsymbol{\Lambda}_{0,0} & \dots & \boldsymbol{\Lambda}_{0,i-2} \\ \vdots & \vdots & \ddots & \vdots \\ \boldsymbol{\Lambda}_{0,i-1} & \boldsymbol{\Lambda}_{0,i-2} & \dots & \boldsymbol{\Lambda}_{0,0} \end{pmatrix}, \\
\boldsymbol{\Lambda}_f^v &= \begin{pmatrix} \boldsymbol{\Lambda}_{0,i} & \boldsymbol{\Lambda}_{0,i-1} & \dots & \boldsymbol{\Lambda}_{0,1} \\ \boldsymbol{\Lambda}_{0,i+1} & \boldsymbol{\Lambda}_{0,i} & \dots & \boldsymbol{\Lambda}_{0,2} \\ \vdots & \vdots & \ddots & \vdots \\ \boldsymbol{\Lambda}_{0,2i-1} & \boldsymbol{\Lambda}_{0,2i-2} & \dots & \boldsymbol{\Lambda}_{0,i} \end{pmatrix}.
\end{aligned}
\tag{1.67}
$$

Eq. (1.66) hence provides a rewriting of the projection of the future on the past performed in Eq. (1.50) in terms of color channel interdependency. This highlights the explicit involvement of the color covariances of the original image $\mathbf{Y}$ in the estimation process and, as a result, the non-marginal nature of the model learning algorithm.

1.4.2 Formal expressions of the color covariances

As shown in (Ramos & Mercère 2016), the matrices $\boldsymbol{\Lambda}_{k,m}$ can be formally expressed with the parameters of the model under the condition given by Eq. (1.5), *i.e.*, if the state variables are assumed to be uncorrelated. Focusing on the matrices involved in Eq. (1.66) only, $\boldsymbol{\Lambda}_{k,0}$ and $\boldsymbol{\Lambda}_{0,m}$ can be expressed for all $(k,m) \in (\mathbb{N}^*)^2$ as

$$
\begin{cases}
\boldsymbol{\Lambda}_{0,0} &= \mathbf{C}_1 \boldsymbol{\Pi}_h \mathbf{C}_1^\top + \mathbf{C}_2 \boldsymbol{\Pi}_v \mathbf{C}_2^\top + \mathbf{R}, \\
\boldsymbol{\Lambda}_{k,0} &= \mathbf{C}_1 \mathbf{A}_1^{k-1} \left(\mathbf{A}_1 \boldsymbol{\Pi}_h \mathbf{C}_1^\top + \mathbf{A}_2 \boldsymbol{\Pi}_v \mathbf{C}_2^\top + \mathbf{K}_1 \mathbf{R} \right), \\
\boldsymbol{\Lambda}_{0,m} &= \mathbf{C}_2 \mathbf{A}_4^{m-1} \left(\mathbf{A}_3 \boldsymbol{\Pi}_h \mathbf{C}_1^\top + \mathbf{A}_4 \boldsymbol{\Pi}_v \mathbf{C}_2^\top + \mathbf{K}_2 \mathbf{R} \right).
\end{cases}
\tag{1.68}
$$

Though these formal expressions are taken from (Ramos & Mercère 2016, Ramos & Mercère 2018), no interpretation in terms of color content is given therein. Yet, in the specific case of $n_y = 3$, the coefficients of these matrices can be understood as color and spatial covariances. Focusing on the color correlations only, the expression of $\boldsymbol{\Lambda}_{0,0}$ illustrates the impact of the parameters of the model on the color content of the image. The matrices $\mathbf{C}_1$ and $\mathbf{C}_2$ color the horizontal and vertical structures characterized by $\boldsymbol{\Pi}_h$ and $\boldsymbol{\Pi}_v$, respectively, while $\mathbf{R}$ corresponds to the color structure of the innovation as seen in Section 1.1.3. Notice that the color information brought by the model is combined with the original color information contained in the innovation sequence through an addition. Therefore, besides being explicitly involved in the estimation algorithm, the color covariances can be directly linked with the parameters of the model, which further shows how the interdependency between the color channels is fully taken into account. The involvement of the matrix $\mathbf{R}$ in Eq. (1.68) also highlights the importance of the innovation process in the color structure of the image, as already mentioned in Sections 1.1.4 and 1.3.5, respectively. Section 1.5

shows how this purely vectorial treatment of the color components of $\mathbf{Y}$ is crucial in reliably reconstructing the color structure of a damaged image in the context of texture completion.

1.5 Application to texture completion

Many inpainting techniques are developed to handle greyscale images, thus yielding color distortions when they are used with colored images (Hosono et al. 2019). As explained, *e.g.*, in (Xu et al. 2015), this important issue can be bypassed by developing techniques which take into account the correlations between the RGB channels explicitly instead of using a simple concatenation of the 3 channels composing the image or processing the luminance component only. As shown hereafter, one of the main advantages of the subspace-based technique introduced in this chapter is its ability to deal with multivalued data within the formulation of the parametric 2-D Roesser model. More precisely, the correlation constraint pointed out in (Xu et al. 2015) is satisfied with the subspace-based algorithm introduced in the previous sections, thanks to the use of Hankel data matrices, or more specifically, thanks to the projections involving these Hankel matrices.

1.5.1 General assumptions and issues

Texture completion, or inpainting, consists in reliably reconstructing damaged or missing parts of an image by inferring from a user-defined learning area. More precisely, it aims at generating a piece of texture that looks as similar as possible to the available part of the original image in order to yield a reliable substitute for the missing part. Furthermore, this substitute must not look identical to another part of the image, *i.e.*, copy/paste effects must be limited. Notice that though efficient texture similarity measures exist for greyscale images, extending them to color textures is still a challenge (Zujovic, Pappas & Neuhoff 2013). The purpose of texture completion is illustrated in Figure 1.9.

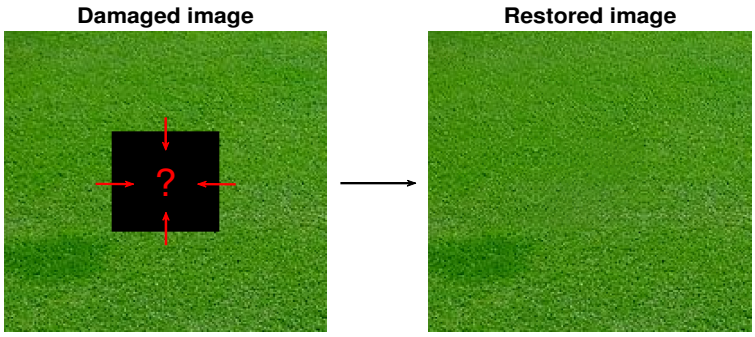

Figure 1.9: Example of a damaged image restored through an inpainting technique.

In this section, $\mathbf{Y}$ denotes a color image of size $M \times N$, where each pixel $\mathbf{y}_{r,s}$, $(r,s) \in \{0,\ldots,M-1\} \times \{0,\ldots,N-1\}$, is a vector of $\mathbb{R}^3$. The missing part of $\mathbf{Y}$ is modeled as a subset of pixels $(r,s) \in I \subset \{0,\ldots,M-1\} \times \{0,\ldots,N-1\}$ where $\mathbf{y}_{r,s} = 0$, while the learning area is the remaining part. Because inpainting heavily relies on inference from available data, it can only create patterns that already exist in the learning area. The solution described in this work hence requires the texture to fulfill two main conditions, which are

- stationarity in the learning area,

- structural coherency between the available and masked areas.

The first step of the inpainting process consists in defining a reliable training area. Similarly to what is done for 2D AR models (Köppel et al. 2015), both causal and anticausal neighborhood structures are used in this work. Remember that, as stated in Section 1.3.2, the horizontal space variable is assumed to evolve from left to right, while the vertical space variable is assumed to evolve from top to bottom. As illustrated in Figure 1.10, a causal neighborhood is hence defined as the region located on the left and at the top of the masked area, while an anticausal neighborhood is defined as the region located on the right and at the bottom of the masked area.

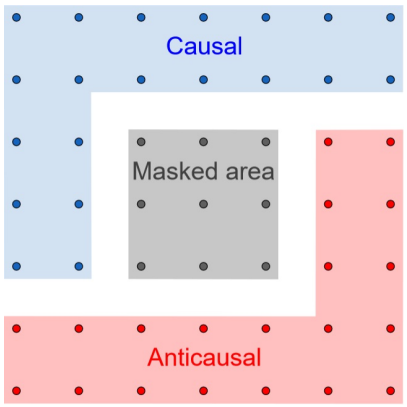

Figure 1.10: Causal (in blue) and anticausal (in red) training neighborhood.

In order to avoid border effects and copy/paste effects as much as possible, one possible approach is to combine both causal and anticausal structures. Section 1.5.2 details the application of the subspace-based algorithm presented in Section 1.3 to texture completion, as well as the strategy used to combine causal and anticausal learning.

1.5.2 Subspace-based texture completion

Though parametric techniques usually handle matrices, damaged areas may have irregular shapes in practice. In this case, the border is reshaped as the smallest rectangle that contains the whole damaged area. In subsequent developments, the masked area is hence assumed to be a rectangular domain I defined by

$$I = \{m_1, \ldots, m_2\} \times \{n_1, \ldots, n_2\}, \tag{1.69}$$

with $0 < m_1 < m_2 < M-1$ and $0 < n_1 < n_2 < N-1$. The causal and anticausal learning areas are respectively defined as

$$C_{\mathbf{Y}} = \begin{pmatrix} \mathbf{y}_{0,0} & \cdots & \cdots & \cdots & \mathbf{y}_{0,N-1} \\ \vdots & \cdots & \cdots & \cdots & \vdots \\ \mathbf{y}_{m_1-1,0} & \cdots & \cdots & \cdots & \mathbf{y}_{m_1-1,N-1} \\ \mathbf{y}_{m_1,0} & \cdots & \mathbf{y}_{m_1,n_1-1} & \blacksquare & \blacksquare \\ \vdots & \cdots & \cdots & \blacksquare & \blacksquare \\ \mathbf{y}_{m_2,0} & \cdots & \mathbf{y}_{m_2,n_1-1} & \blacksquare & \blacksquare \end{pmatrix}, \quad A_{\mathbf{Y}} = \begin{pmatrix} \mathbf{y}_{M-1,N-1} & \cdots & \cdots & \cdots & \mathbf{y}_{M-1,0} \\ \vdots & \cdots & \cdots & \cdots & \vdots \\ \mathbf{y}_{m_2+1,N-1} & \cdots & \cdots & \cdots & \mathbf{y}_{m_2+1,0} \\ \mathbf{y}_{m_2,N-1} & \cdots & \mathbf{y}_{m_2,n_2+1} & \blacksquare & \blacksquare \\ \vdots & \cdots & \cdots & \blacksquare & \blacksquare \\ \mathbf{y}_{m_1,N-1} & \cdots & \mathbf{y}_{m_1,n_2+1} & \blacksquare & \blacksquare \end{pmatrix}. \tag{1.70}$$

Because the Roesser model requires at least rectangular matrices, the black squares are filled with available data from the areas left and right of the masked zone. The subspace-based estimation algorithm described in Section 1.3 is then applied to both $C_{\mathbf{Y}}$ and $A_{\mathbf{Y}}$. Once the Hankel parameter i is fixed, the algorithm can be automatically executed, except from the choice of the horizontal and vertical orders, *i.e.*, the dimensions of the state variables $\mathbf{x}^h_{r,s}$ and $\mathbf{x}^v_{r,s}$, denoted by n_h and n_v, respectively. As with any parametric model, a good selection of the model orders is essential to guarantee a good trade-off between complexity and accuracy (Katayama 2005). In this particular approach, these two parameters correspond to the number of non-zero singular values of the matrices $\mathbf{\Gamma}^h_f \mathbf{X}^h_f$ and $\mathbf{\Gamma}^v_f \mathbf{X}^v_f$, respectively (see Section 1.3.4). More precisely, after the SVD is performed, $n_\bullet$ ($\bullet \in \{h, v\}$) is chosen by the user as the order of the lowest singular value before the expected quick drop. Figures 1.11 and 1.12 show examples of horizontal and vertical singular values sorted in descending order, respectively. In both cases, a drop is observed after the third singular value, from which it can be deduced that $n_h = n_v = 3$.

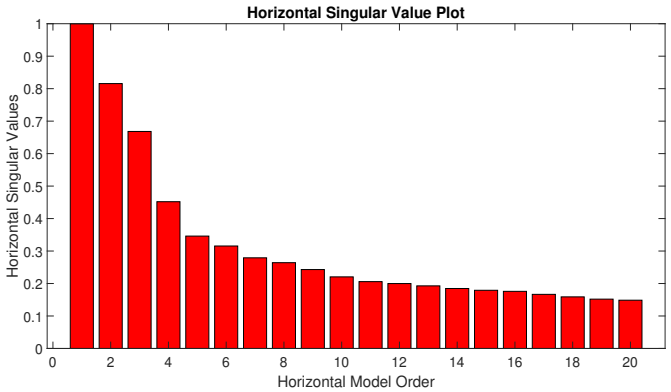

Figure 1.11: Horizontal singular values.

Once the causal and anticausal models are estimated from the learning neighborhoods $C_{\mathbf{Y}}$ and $A_{\mathbf{Y}}$, two distinct sets of parameters, state variables and innovation sequence are available, respectively. These are given in Table 1.1.
Notice that for all $\mathbf{u} \in \{\mathbf{x}^h, \mathbf{x}^v, \mathbf{e}\}$, $\mathbf{u}^c \in \mathbb{R}^{(m_2+1)\times N}$ and $\mathbf{u}^a \in \mathbb{R}^{(M-m_1)\times N}$. In order to fill the missing part of the original image, two output sequences, denoted by $\mathbf{Y}^c$ and $\mathbf{Y}^a$, respectively, are generated. Let $\mathbf{y}^c_{r,s}$ and $\mathbf{y}^a_{r,s}$ denote the values of the causal and anticausal

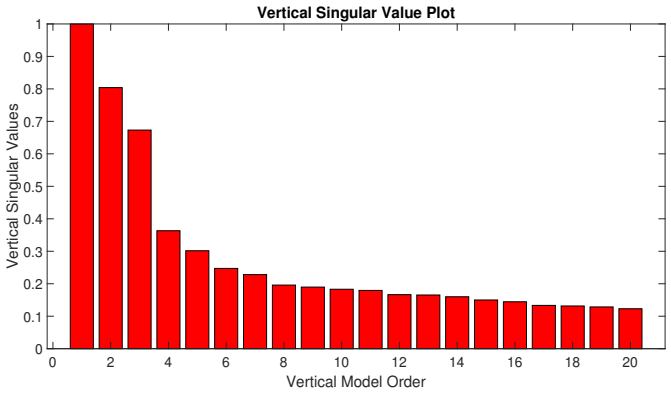

Figure 1.12: Vertical singular values.

	Causal	Anticausal
$\mathbf{A}$ parameters	$\mathbf{A}_1^c$, $\mathbf{A}_2^c$, $\mathbf{A}_3^c$, $\mathbf{A}_4^c$	$\mathbf{A}_1^a$, $\mathbf{A}_2^a$, $\mathbf{A}_3^a$, $\mathbf{A}_4^a$
$\mathbf{K}$ parameters	$\mathbf{K}_1^c$, $\mathbf{K}_2^c$	$\mathbf{K}_1^a$, $\mathbf{K}_2^a$
$\mathbf{C}$ parameters	$\mathbf{C}_1^c$, $\mathbf{C}_2^c$	$\mathbf{C}_1^a$, $\mathbf{C}_2^a$
state variables	$\mathbf{x}^{hc}$, $\mathbf{x}^{vc}$	$\mathbf{x}^{ha}$, $\mathbf{x}^{va}$
innovation sequence	$\mathbf{e}^c$	$\mathbf{e}^a$

Table 1.1: Parameters estimated from the causal and anticausal learning areas.

outputs at the pixel $(r,s) \in I$, respectively, with I denoting the set of indices of the masked area defined in Eq. (1.69). The main issue in generating these output sequences is that they require knowing the innovation sequence and the initial values of the state variables inside the masked area, which is impossible. In order to bypass this difficulty, parts of the sequences extracted from the causal and anticausal model learning are used. More precisely, the innovation sequences $\mathbf{e}_{r,s}^c$, $(r,s) \in \{m_1,\dots,m_2\} \times \{n_1,\dots,n_2\}$, and $\mathbf{e}^a$, $(r,s) \in \{M-1-m_2,\dots,M-1-m_1\} \times \{N-1-n_2,\dots,N-1-n_1\}$, estimated from the rectangular causal and anticausal training areas, respectively, are re-used to generate the new piece of texture. Therefore, for all $(r,s) \in \{m_1,\dots,m_2\} \times \{n_1,\dots,n_2\}$, $\mathbf{y}_{r,s}^c$ is constructed as

$$\begin{cases} \widetilde{\mathbf{x}}_{r+1,s}^{hc} &= \mathbf{A}_1^c \widetilde{\mathbf{x}}_{r,s}^{hc} + \mathbf{A}_2^c \widetilde{\mathbf{x}}_{r,s}^{vc} + \mathbf{K}_1^c \mathbf{e}_{r,s}^c, \\ \widetilde{\mathbf{x}}_{r,s+1}^{vc} &= \mathbf{A}_3^c \widetilde{\mathbf{x}}_{r,s}^{hc} + \mathbf{A}_4^c \widetilde{\mathbf{x}}_{r,s}^{vc} + \mathbf{K}_2^c \mathbf{e}_{r,s}^c, \\ \mathbf{y}_{r,s}^c &= \mathbf{C}_1^c \widetilde{\mathbf{x}}_{r,s}^{hc} + \mathbf{C}_2^c \widetilde{\mathbf{x}}_{r,s}^{vc} + \mathbf{e}_{r,s}^c, \end{cases} \tag{1.71}$$

where $\widetilde{\mathbf{x}}^{hc}$ and $\widetilde{\mathbf{x}}^{vc}$ denote the horizontal and vertical reconstructed state variables, respectively, with their initial values taken from $\mathbf{x}^{hc}$ and $\mathbf{x}^{vc}$, respectively. Notice that the choice of the innovation could be further discussed and opens interesting perspectives for future works. A possible solution to improve the results is the addition of a random perturbation to the extracted innovation sequence, which could reduce the copy-paste effect. Further tests would be necessary to study the potential benefits of this technique.

The state variables are reconstructed at the same time as the image itself by using the recursive equations that define the Roesser model. Similarly, for all $(r,s) \in \{m_1,\dots,m_2\} \times \{n_1,\dots,n_2\}$, $\mathbf{y}_{r,s}^a$ is constructed as

$$\begin{cases} \widetilde{\mathbf{x}}^{ha}_{r-1,s} &= \mathbf{A}^a_1 \widetilde{\mathbf{x}}^{ha}_{r,s} + \mathbf{A}^a_2 \widetilde{\mathbf{x}}^{va}_{r,s} + \mathbf{K}^a_1 \mathbf{e}^a_{r,s}, \\ \widetilde{\mathbf{x}}^{va}_{r,s-1} &= \mathbf{A}^a_3 \widetilde{\mathbf{x}}^{ha}_{r,s} + \mathbf{A}^a_4 \widetilde{\mathbf{x}}^{va}_{r,s} + \mathbf{K}^a_2 \mathbf{e}^a_{r,s}, \\ \mathbf{y}^a_{r,s} &= \mathbf{C}^a_1 \widetilde{\mathbf{x}}^{ha}_{r,s} + \mathbf{C}^a_2 \widetilde{\mathbf{x}}^{va}_{r,s} + \mathbf{e}^a_{r,s}. \end{cases} \tag{1.72}$$

These estimated causal and anticausal values are then merged into a single output sequence $\mathbf{Y}_f = \left(\mathbf{y}^f_{r,s}\right)_{(r,s)\in I}$ defined for all $(r,s) \in I$ as

$$\mathbf{y}^f_{r,s} = (1 - v_{r,s})\, \mathbf{y}^c_{r,s} + v_{r,s} \mathbf{y}^a_{r,s}, \tag{1.73}$$

where $v = (v_{r,s})_{(r,s)\in I}$ is a weighting function that fulfills the following conditions :

- $v_{m_1,n} = v_{m,n_1} = 0$ for all $(m,n) \in I$,
- $v_{m_2,n_2} = 1$,
- if $(m_3,n_3) \in I$, then $v_{m_3,n_3} \geq v_{m,n}$ for all $m_1 \leq m \leq m_3$ and $n_1 \leq n \leq n_3$.

These conditions ensure that the closer a pixel is from the causal (resp. anticausal) area, the greater the influence of $\mathbf{Y}_c$ (resp. $\mathbf{Y}_a$) on the final value of the pixel is. In the synthetic tests presented in Section 1.5.4, the chosen weighting function v is defined for $(r,s) \in I$ as

$$v_{r,s} = \sin\left[\frac{(r-m_1)\,\pi}{2\,(m_2-m_1)}\right] \sin\left[\frac{(s-n_1)\,\pi}{2\,(n_2-n_1)}\right]. \tag{1.74}$$

Figure 1.13 shows an example of such a weighting function with $I = \{61,\dots,120\}^2$.

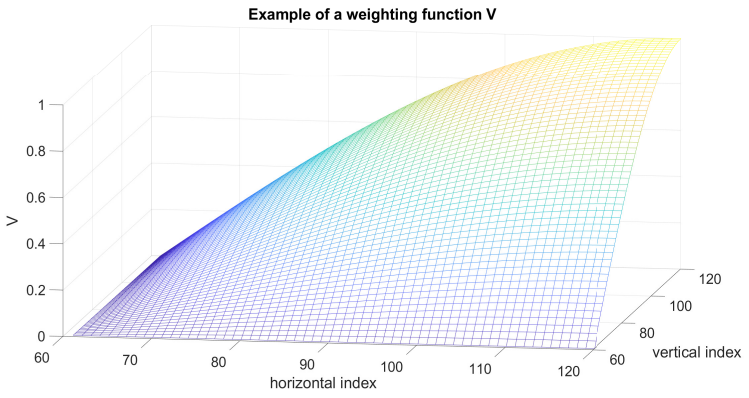

Figure 1.13: Example of a weighting function v with $I = \{61,\dots,120\}^2$.

Be careful that although the innovation sequences $\mathbf{e}^c$ and $\mathbf{e}^a$ are copied from non-masked areas, the output sequences $\mathbf{y}^c$ and $\mathbf{y}^a$, as well as the resulting inpainted piece of texture $\mathbf{y}^f$, are not mere recombinations of available data, but rather generated data through the Roesser recursive model. Notice furthermore that unlike many parametric methods applied on color images, no artificial post-treatment is needed to reconstruct the color structure, *i.e.*, the correlations between the color channels. Indeed, as shown in Section 1.4, the link between the color channels is directly involved in the identification process. The synthetic tests performed in Section 1.5.4 show how the color structure is preserved in the reconstructed areas without the need of any post-treatment, and how this represents a huge advantage over the marginal approaches described in Section 1.5.3.

1.5.3 Comparison with marginal approaches

In order to illustrate the benefits of a vectorial treatment of the color content, the approach presented in the previous sections is compared with marginal approaches, *i.e.*, the treatment of the color channels as three independent scalar signals rather than one single vectorial signal with correlated components. This section briefly explains the marginal techniques to which the vectorial Roesser model is compared with in Section 1.5.4. Although the colorimetric interpretation of the autocovariance matrices $\mathbf{\Lambda}_{k,m}$ defined by Eq. (1.61) only holds if $n_y = 3$, the algorithm presented in Section 1.3 can be applied for any $n_y \in \mathbb{N}^*$, including the special case of a greyscale image, *i.e*, $n_y = 1$. Three separate Roesser models can hence be estimated from the available values of the three color components of $(\mathbf{y}_{r,s})_{r,s}$, respectively, yielding three reconstructed signals, one for each color component. Another possible approach is to apply a Principal Component Analysis (PCA) on the image to decorrelate its components before applying the marginal Roesser procedure. The treatment of the vectorial information is still marginal, but it can be expected that the loss of the color structure is not as important as in the case of a direct marginal approach. However, the synthetic tests performed in Section 1.5.4 show that such marginal approaches, even when reinforced by a PCA, fail to properly reconstruct the color structure of the original image, which highlights the benefits of the vectorial treatment presented in this work.

1.5.4 Synthetic tests

The subspace-based texture completion technique is now applied to real images. In all the tests, the images are of size 180×180, *i.e.*, $M = N = 180$, while the masked area is the square $\{61, \dots, 120\}^2$, *i.e.*, $m_1 = n_1 = 61$ and $m_2 = n_2 = 120$. As stated in Section 1.3.2, the Hankel parameter i has to be sufficiently large compared to the horizontal and vertical orders n_h and n_v, respectively, to fulfill the rank conditions given by Eq. (1.45). In the tested images, the drop of singular values usually occurs between the third and the fifth order, similarly to what is observed in Figures 1.11 and 1.12. The parameter i must hence be chosen sufficiently larger than 5. Furthermore, remember that by definition of the Hankel matrices (see Section 1.3.2), i and j are linked by the constraint $2i + j - 2 = \min\{M - 1, N - 1\}$, which implies that if i increases, then j decreases. The parameter j must however stay large enough so that the empirical estimations of the color covariances evoked in Section 1.4.1 remain reliable. Choosing $i = 20$, and consequently $j = 141$, ensures that both conditions are fulfilled. Table 1.2 shows the results obtained on a set of color textures. In each case, after the masked area is removed from the image, three subspace-based reconstruction algorithms are applied :

- a vectorial algorithm that involves the color covariances, *i.e.*, $n_y = 3$,
- a marginal algorithm applied on each color component, *i.e.*, $n_y = 1$,
- a marginal algorithm preceded by a PCA to decorrelate the color components.

In the case of the grass texture, the color remains stable in the whole image, which explains why no difference is observed between the three approaches. However, when more complex color structures come into play, the vectorial approach manages to produce pixels that always lie in the right color space, which is not the case for the two marginal approaches, especially for the sand and wall textures. Even when preceded by a PCA, the marginal treatment of the color channels fails to restore the original color content of the image, and

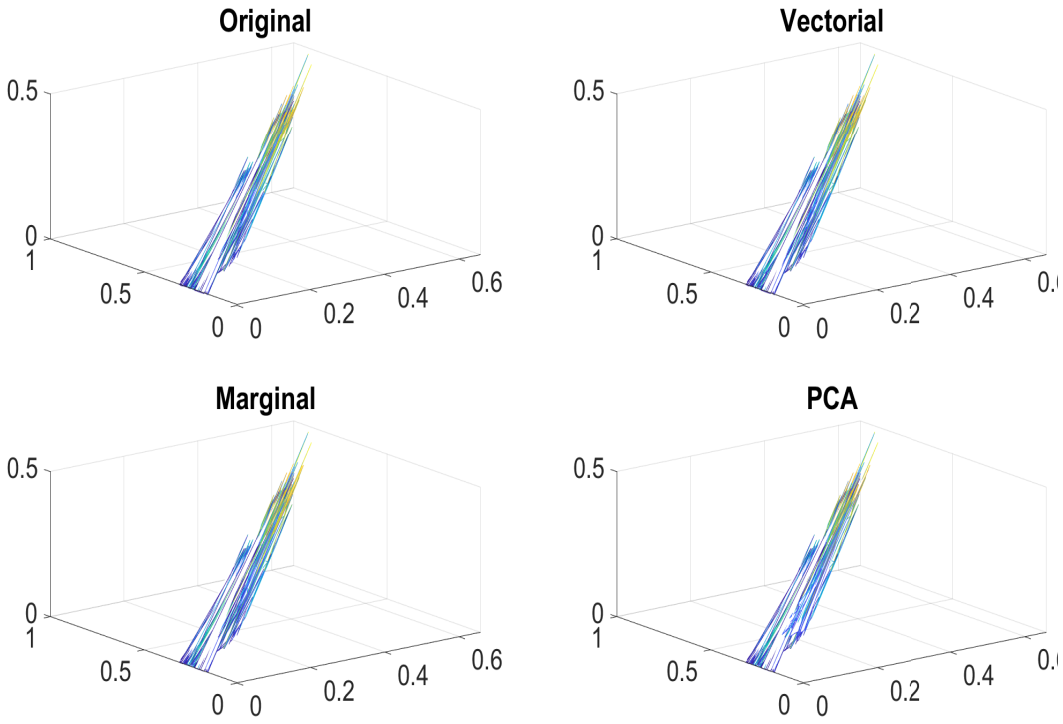

Figure 1.14: Area occupied by the original (top left) and inpainted grass textures inside the RGB cube in the case of vectorial (top right), marginal (bottom left) and PCA-based (bottom right) inpainting.

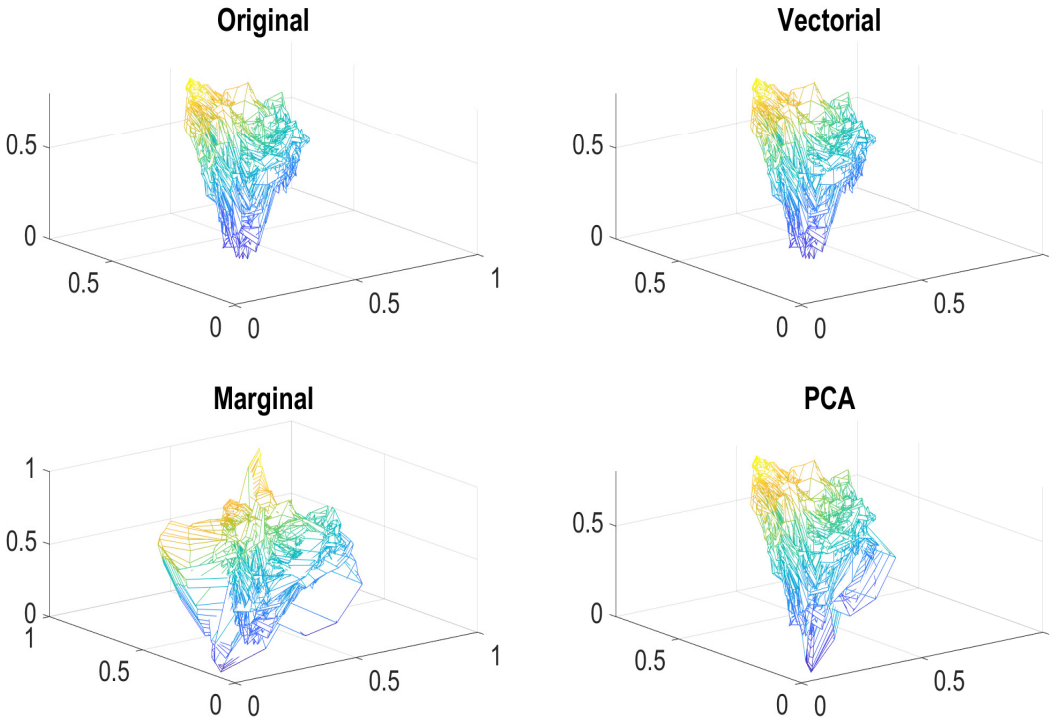

Figure 1.15: Area occupied by the original (top left) and inpainted sand textures inside the RGB cube in the case of vectorial (top right), marginal (bottom left) and PCA-based (bottom right) inpainting.

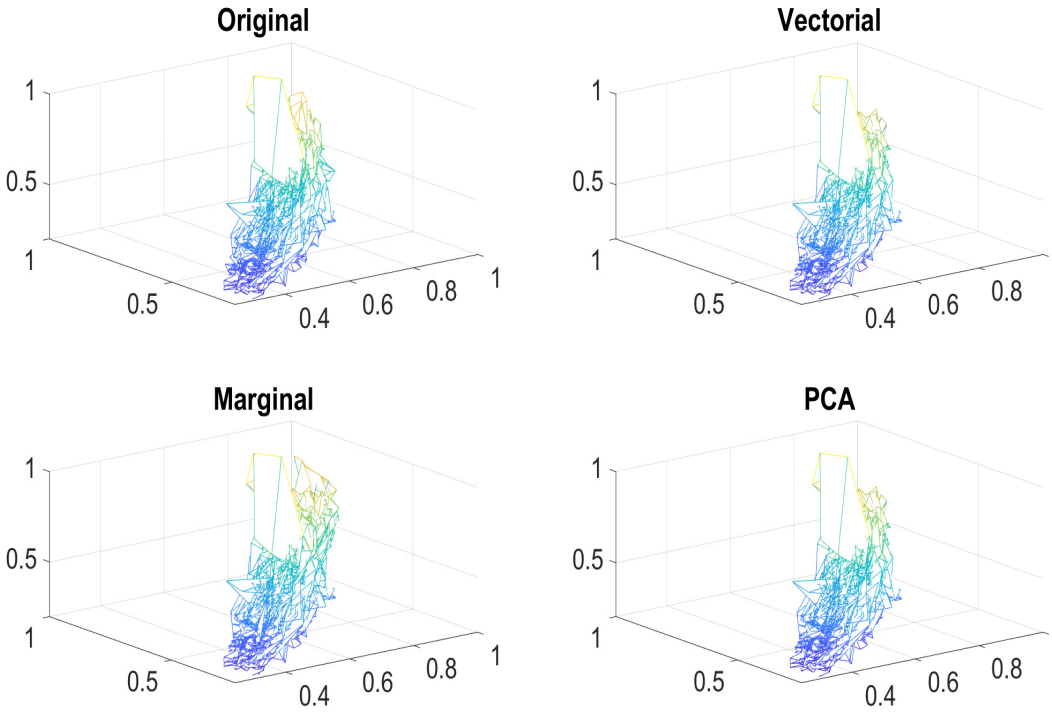

Figure 1.16: Area occupied by the original (top left) and inpainted marble textures inside the RGB cube in the case of vectorial (top right), marginal (bottom left) and PCA-based (bottom right) inpainting.

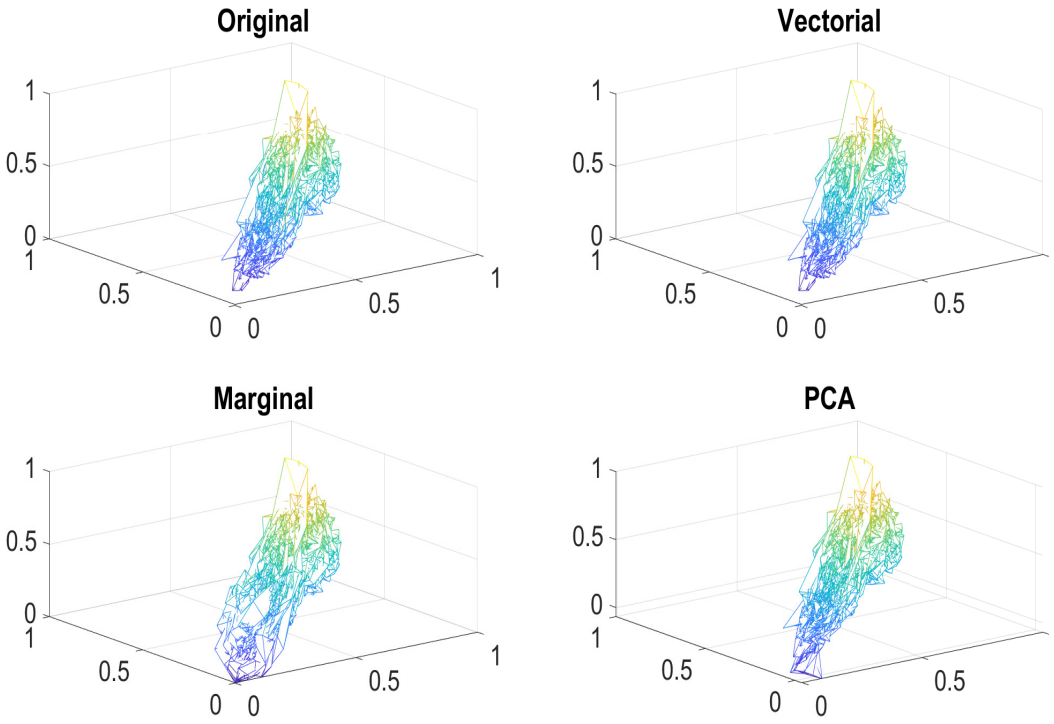

Figure 1.17: Area occupied by the original (top left) and inpainted wall textures inside the RGB cube in the case of vectorial (top right), marginal (bottom left) and PCA-based (bottom right) inpainting.

produces pixels with a clearly different tint. This is reflected in Figures 1.14, 1.15, 1.16 and 1.17 which compare the areas occupied by the original and inpainted textures inside the RGB cube. Though the four techniques give similar results in the cases of the grass and marble textures, the Roesser-based vectorial inpainted texture appears to be the closest to the original image in terms of color content in the cases of the sand and wall textures. This illustrates the benefits of involving the color covariances in the estimation algorithm, as highlighted in Section 1.4.1.

1.6 Conclusion

The main objective of this chapter was to study the application of the parametric representation of multivariate systems provided by the Roesser model to color textures. The results given in Section 1.5.4 confirm the main assertion of the introduction, *i.e.*, that a color texture has to be treated as a dynamic 3D vector rather than three marginal signals. The direct implication of the color covariances in the estimation algorithm is what enables the vectorial Roesser model to reliably extract the color structure of the original image, which is a clear advantage over marginal solutions. Though the relevance of the Roesser model in the field of image restoration had already been highlighted in previous works (Ramos & Mercère 2016), the crucial impact of this non-marginal treatment on its performances is rarely put forward.

The developments performed in this chapter also highlight the importance of the innovation sequence. Though usually described as a white noise (Köppel et al. 2015), this sequence contains some crucial features of the texture that cannot be extracted by the Roesser parameters. Consequently, as highlighted in Section 1.3.5, the choice of the innovation terms strongly impacts the reconstruction of the image, and only knowing its second order statistics is not enough to fully characterize it. While many works dealing with 2D ARMA models (Kokaram 2004, Köppel et al. 2015) or the Roesser model (Ramos & Mercère 2016, Ramos & Mercère 2018) focus mostly on the estimation of the parameters and the statistical behavior of the involved variables, this suggests paying more attention on the innovation sequence in future studies.

One of the main difficulties in the Roesser model is that the parameters of the model are difficult to interpret in terms of characterization of the texture. Firstly, the matrices $\mathbf{A}_i$, $\mathbf{C}_j$ and $\mathbf{K}_j$, with $(i,j) \in \{1,\dots,4\} \times \{1,2\}$, are only known up to a similarity transformation (Ramos & Mercère 2018), which makes it hard to compare them to the parameters extracted from another texture. Additionally, as shown in Figure 1.7, these parameters only describe the global dynamic of the texture, not its local structure at each pixel which is contained in the innovation sequence. Recent works such as (Leclaire & Moisan 2015) suggest that this is due to the inner characteristics of the ARMA and Roesser parameters, respectively. More precisely, (Leclaire & Moisan 2015) use Fourier analysis to show how the parameters of such models capture the information contained in the Fourier amplitude, but fail to extract what lies in the Fourier phase. Because the structure of an image is encoded in its Fourier phase function (Oppenheim & Lim 1981), this urges the need to introduce tools that are able to characterize this information. Before focusing on color textures, the next two chapters define these tools in the greyscale case to highlight their ability to extract local features.

Texture	Grass	Sand	Marble	Wall
Original				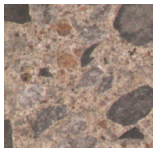
Damaged	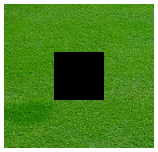			
Vectorial				
Marginal			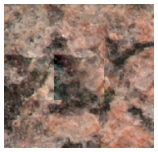	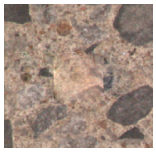
PCA				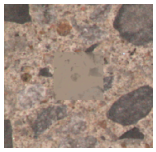

Table 1.2: Comparison between reconstructions performed by the vectorial Roesser model and two marginal approaches, direct and combined with an PCA

CHAPTER 2

The Riesz transform and the monogenic signal

As seen in the previous chapter, the Roesser model focuses on the global dynamics of the texture, but fails to extract its local features, which are left in the innovation term $\mathbf{e}$. Consequently, this chapter aims at introducing tools to extract these features, from which an accurate description of the local behavior of the texture can be deduced. These tools are first introduced and studied for greyscale images in Chapters 2 and 3 before being generalized to color images in Chapters 4 and 5.

A first approach consists in considering the 2D Fourier spectrum of the texture, more precisely the amplitude and phase information it provides. Indeed, it is well known that the structure of an image is contained in its Fourier phase, *i.e.*, the argument of its Fourier transform (Oppenheim & Lim 1981). This is illustrated in Figure 2.1, which shows pebble and sand textures before and after their respective Fourier phase signals have been switched. While the Fourier amplitude carries the intensity information, the structure of the texture, including the edges, are contained in the Fourier phase. Other works highlight the importance of the Fourier phase in the perception of the image, such as (Field, Hayes & Hess 2000, Hansen & Hess 2006). However, the fact that the Fourier phase lies in the frequency domain rather than the spatial domain makes it difficult to handle (Felsberg 2002). Some works like, *e.g.*, (Kovesi 2000, Leclaire & Moisan 2015), managed to define reliable tools to characterize phase coherence and link them some visual aspects, but the local behavior of the image is still left unmodeled in such approaches. Figure 2.2 highlights the chaotic visual aspect of the phase signals, which are hence difficult to directly connect with the local structure of the original texture, hence the need of a localized definition of phase.

In the field of 1D signal processing, the Hilbert transform and the analytic representation (Hilbert 1912, Ville 1948, Oswald 1956) have proved their relevance in extracting the local properties of a signal (Milkereit & Spencer 1990, Picinbono 2008, Langley & Anderson 2010). These tools were originally developed as a way to generalize the embedding of cosine waves into complex exponentials (Picinbono 2008). By extending any real-valued signal to the complex domain, the analytic representation enables the definition of an instantaneous modulus (or amplitude) and an instantaneous argument (or phase), which are to be interpreted as a measure of local energy and local structure of the signal, respectively (Felsberg 2002). There have been many attempts to generalize the Hilbert transform to 2D real-valued signals in the 80s and 90s (see (Langley & Anderson 2010) for a good survey of these works), but it was not until the early 2000s with the works of (Larkin et al. 2001) and (Felsberg & Sommer 2001) that this goal was fully reached. These works use the Riesz-transform, first introduced in (Riesz 1928), as a 2D analog of

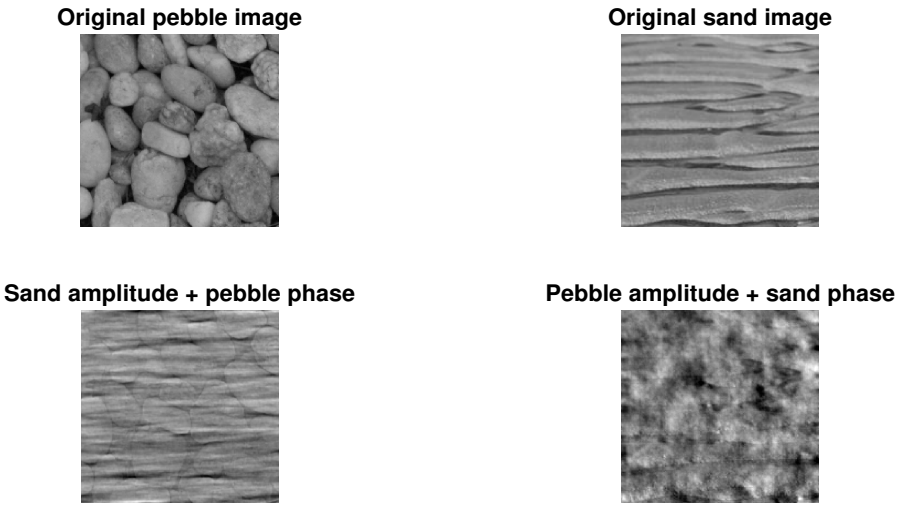

Figure 2.1: Phase switch between pebble and sand textures.

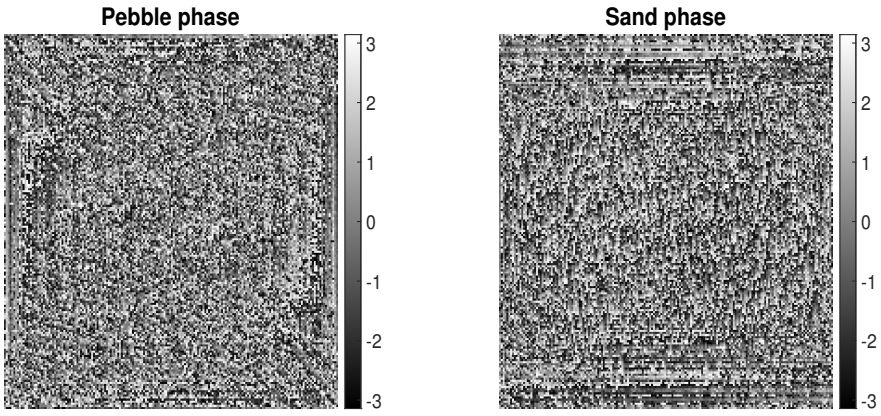

Figure 2.2: Fourier phase signals of the pebble (left) and sand (right) textures.

the Hilbert transform, and enable the extension of a 2D real-valued signal to an $\mathbb{R}^3$-valued signal called the monogenic signal (Felsberg 2002). The spherical coordinates of this monogenic signal then give a measure of local energy, structure and orientation of the original image. The characterization of an image by these three quantities has been applied to various domains, including hologram demodulation (Seelamantula et al. 2012), spatial vision (Langley & Anderson 2010), interferometry (Kaseb et al. 2019) and medical imaging (Alessandrini et al. 2013). The particular impact of the phase function on the local texture of the image has also been illustrated in the field of computer graphics (Tricard et al. 2019). However, the link between the measures given by the monogenic tool and their physical interpretation is not obvious (Kaseb et al. 2019). Indeed, because the monogenic signal was originally designed for purely monochromatic waves (Felsberg & Sommer 2001), the measures of phase and orientation it provides are theoretically optimal only for such images (Seelamantula et al. 2012).

One of the main goals of this chapter is hence to study the reliability of the monogenic-based extraction of the local features of an image when more complex oscillating patterns come into play. While some regularity conditions were given in (Larkin et al. 2001, Seelamantula et al. 2012) to ensure the quality of the monogenic phase extraction, this chapter goes further by formally studying how the Riesz transform deals with patterns displaying more curves than purely monochromatic waves. These mathematical developments are used to establish the asymptotic convergence of the monogenic estimation of both phase and orientation. The monogenic tool is then applied to interferometric fringes to confirm the theoretical results. While the relevance of the monogenic signal to extract the oscillating features of fringe patterns was already highlighted in (Larkin et al. 2001, Seelamantula et al. 2012, Kaseb et al. 2019), this chapter gives stronger theoretical guarantees to ensure the reliability of this extraction.

The rest of the chapter is organized as follows. Before dealing with 2D images, some of the key results of the 1D case are recalled in Section 2.1, which are then illustrated by synthetic tests in Section 2.2. After recalling the main properties of the 2D Fourier transform in Section 2.3, the 1D results are generalized to the 2D case by use of the Riesz transform in Section 2.4. 2D synthetic tests are then performed in Section 2.5 with a special focus on the discretization process. The Riesz-based monogenic extraction of phase is finally applied to real interferometric fringes in Section 2.6, in which the benefits of this approach are highlighted.

2.1 Case of 1D signals: the Hilbert transform and the analytic signal

2.1.1 Definition and first properties

In the 1D case, a wave signal can be modeled as a function $s : \mathbb{R} \to \mathbb{R}$ defined for all $t \in \mathbb{R}$ by

$$s(t) = a(t) \cos\left[\varphi(t)\right], \tag{2.1}$$

where $a(t)$ denotes the amplitude of s and $\varphi(t)$ its phase at each instant (or position) $t \in \mathbb{R}$ (Picinbono 2008). These functions are sometimes called instantaneous amplitude and instantaneous phase, respectively, to distinguish them from the frequency-depending Fourier amplitude and phase functions (Picinbono 2008). In practice, s is the only known

function, while a and φ have to be estimated from it. Notice however that there exist an infinity of functions $\widetilde{a}$ and $\widetilde{\varphi}$ such that for all $t \in \mathbb{R}$,

$$s(t) = \widetilde{a}(t) \cos\left[\widetilde{\varphi}(t)\right], \tag{2.2}$$

which complicates the extraction of a and φ from s only (see Chapter 2 of (Picinbono 2008) for details). In order to bypass this difficulty, the signal s is extended to the complex domain by using the Hilbert transform, first introduced in Chapter 10 of (Hilbert 1912), and extended in (Riesz 1928). Let h denote the Hilbert kernel defined for $t \in \mathbb{R}^*$ by

$$h(t) = \frac{1}{\pi t}. \tag{2.3}$$

Then, the Hilbert transform of s, denoted by $\mathcal{H}s$, is defined for all $t \in \mathbb{R}$ as the convolution product between s and h, *i.e.*,

$$\begin{aligned} \mathcal{H}s(t) &= s * h(t), \\ &= \frac{1}{\pi} \text{p.v.} \left(\int_{\mathbb{R}} \frac{s(\tau)}{t-\tau} d\tau \right), \end{aligned} \tag{2.4}$$

where p.v. denotes the Cauchy principal value (Hilbert 1912). Though the convolution product involving an improper integral makes this definition difficult to handle, a much more convenient definition can be formulated in the Fourier domain (Bracewell 1965). Indeed, if $\mathcal{F}$ denotes the Fourier transform, the Hilbert transform of s can be defined for all $\xi \in \mathbb{R}^*$ as

$$\mathcal{F}\left[\mathcal{H}s\right](\xi) = H(\xi)\mathcal{F}s(\xi), \tag{2.5}$$

where H denotes the Fourier transform of the Hilbert kernel h, given by

$$H(\xi) = -\mathbf{i}\frac{\xi}{|\xi|}. \tag{2.6}$$

The complex analytic extension of s is then defined for all $t \in \mathbb{R}^*$ as

$$A_s(t) = s(t) + \mathbf{i}\mathcal{H}s(t), \tag{2.7}$$

and is called the analytic signal of f (Ville 1948). The modulus and argument of A_s, denoted by $A(t)$ and $\phi(t)$ respectively, give instantaneous measures of amplitude and phase, respectively (Picinbono 2008).

2.1.2 Case of a pure cosine wave

The most canonical class of signals first considered in works dealing with the Hilbert transform is the class of the pure cosine waves (Ville 1948, Oswald 1956). A 1D signal is a pure cosine wave if it has a constant amplitude and a linear phase, *i.e.*, for all $t \in \mathbb{R}$,

$$s(t) = a_0 \cos(\omega t), \tag{2.8}$$

where $a_0 \in \mathbb{R}^*$ and $\omega \in \mathbb{R}^*$ denote the amplitude and frequency of the signal, respectively. As shown in (Ville 1948), the Hilbert transform of such a signal is given for all $t \in \mathbb{R}$ by

$$\mathcal{H}s(t) = a_0 \sin(\omega t). \tag{2.9}$$

This is due to the Hilbert transform having been purposely designed as a quadrature filter (Ville 1948, Oswald 1956). Consequently, the analytic signal is given for all $t \in \mathbb{R}$ by

$$\begin{aligned} A_s(t) &= a_0 \left[\cos(\omega t) + \mathbf{i}\sin(\omega t)\right], \\ &= a_0 e^{\mathbf{i}\omega t}. \end{aligned} \tag{2.10}$$

From an estimation point of view, this also implies that, in the case of an unknown cosine wave signal, the amplitude and phase functions A and ϕ extracted by the Hilbert transform and the analytic signal coincide with their respective physical counterparts, *i.e.*, for all $t \in \mathbb{R}$,

$$\left\{ \begin{array}{ll} A(t) & = a_0, \\ \phi(t) & = \varphi(t) = \omega t \ \ [2\pi]. \end{array} \right. \tag{2.11}$$

2.1.3 Case of a parabolic chirp

As stated in (Picinbono 1997, Seelamantula et al. 2012), the equality between the physical phase φ and the analytic phase ϕ is only true for cosine waves. Outside this ideal case, the analytic measures of amplitude $A(t)$ and phase and $\phi(t)$ at each time $t \in \mathbb{R}$ do not match their expected physical values $a(t)$ and $\varphi(t)$, respectively. However, if the amplitude and phase functions are slowly and smoothly varying, it can be shown that the analytic signal still provides reliable estimations of these functions (Seelamantula et al. 2012). Other conditions on the phase function are given in (Edwards & Parrent 1959, Picinbono 1997). Chapter 2 of (Picinbono 2008) goes further by formally studying the case of a parabolic chirp, defined for all $t \in \mathbb{R}$ by

$$s(t) = a_0 \cos(a^2 t^2), \tag{2.12}$$

with $a_0 \in \mathbb{R}_+^*$ and $a \in \mathbb{R}_+^*$. The further developments of this chapter show how the 2D generalization of these results are particularly relevant in the field of fringe pattern analysis, which explains why they are recalled here. As stated in (Picinbono 2008), the Hilbert transform of a 1D parabolic chirp is given for all $t \in \mathbb{R}$ by

$$\mathcal{H}s(t) = a_0 \sqrt{\frac{2}{\pi}} \left\{ \left[C(at) + S(at)\right] \sin(a^2 t^2) + \left[C(at) - S(at)\right] \cos(a^2 t^2) \right\}, \tag{2.13}$$

where C and S denote the Fresnel integrals defined for all $\theta \in \mathbb{R}$ by

$$\left\{ \begin{array}{ll} C(\theta) & = \int_0^\theta \cos\left(u^2\right) du, \\ S(\theta) & = \int_0^\theta \sin\left(u^2\right) du. \end{array} \right. \tag{2.14}$$

In this case, it is obvious that the argument of the analytic signal $A_s(t) = s(t) + \mathbf{i}\mathcal{H}s(t)$ is not equal to $a^2 t^2$, which illustrates the fact that the analytic phase does not match its physical counterpart. However, this observation does not imply that the analytic phase fails to extract the local structure of the signal. Indeed, as stated in (Picinbono 2008), the Fresnel integrals satisfy

$$\lim_{\theta \to +\infty} C(\theta) = \lim_{\theta \to +\infty} S(\theta) = \sqrt{\frac{\pi}{8}}, \tag{2.15}$$

which implies that

$$\begin{aligned}\mathcal{H}s(t) &= a_0\sqrt{\frac{2}{\pi}}\left\{[C(at)+S(at)]\sin(a^2t^2)+[C(at)-S(at)]\cos(a^2t^2)\right\},\\ &=_{t\to+\infty} a_0\sqrt{\frac{2}{\pi}}\left[2\sqrt{\frac{\pi}{8}}\sin(a^2t^2)\right]+\mathrm{o}(1),\\ &=_{t\to+\infty} a_0\sin(a^2t^2)+\mathrm{o}(1).\end{aligned} \tag{2.16}$$

This implies that the analytic signal is asymptotically equal to $a_0 e^{\mathbf{i}a^2t^2}$. In this case, the analytic phase, which is defined as the argument of the analytic signal, is asymptotically equal (modulo 2π) to the physical phase $\varphi(t) = a^2t^2$. Furthermore, notice that $C(at)$ and $S(at)$ also tend towards $\sqrt{\frac{\pi}{8}}$ when a tends towards $+\infty$. Thus, for any fixed $t \in \mathbb{R}$,

$$\mathcal{H}s(t) =_{a\to+\infty} a_0\sin(a^2t^2)+\mathrm{o}(1). \tag{2.17}$$

Consequently, the analytic and physical phases also coincide for large values of a. These results illustrate the ability of the analytic signal to extract the phase function outside the case of pure cosine waves. This stands in line with the conclusion of (Seelamantula et al. 2012) in the case of 1D holograms. Before generalizing to 2D images, synthetic tests are performed in Section 2.2 to give numerical confirmations of these theoretical results.

2.2 1D synthetic tests

Though the previous section deals with infinite and continuous signals, the signals handled in practice are usually finite and discrete. The main goal of this section is hence to determine whether the discretization affects the theoretical results presented in Section 2.1 or not. In other words, whether the analytic measure of phase remains close to the expected physical phase function as stated in the continuous case. Additionally, comparing estimated and expected values can be eased by the use of numerical criteria of similarity. Before performing synthetic tests, this section details the discretization process and introduces similarity criteria to evaluate the quality of the analytic estimation of phase.

2.2.1 Discretization

Let $(t^j)_j$ be a discrete time sequence, with $j \in \{0,\dots,N-1\}$ and $N \in \mathbb{N}^*$, such that

$$t^j = jT, \tag{2.18}$$

where $T > 0$ denotes the sampling period. The corresponding discrete frequency sequence, denotes by $(\xi^j)_j$, is defined for all $j \in \{0,\dots,N-1\}$ by

$$\xi^j = \frac{j}{NT}. \tag{2.19}$$

In the general case, $s = (s^j)_{j\in\{0,\dots,N-1\}}$ denotes a discrete signal defined for all $j \in \{0,\dots,N-1\}$ by

$$s^j = a^j\cos\left(\varphi^j\right), \tag{2.20}$$

where a^j and φ^j denote the physical amplitude and phase of s^j, respectively. If S denotes the discrete Fourier transform of s, the discrete Fourier transform of the Hilbert transform of s, denoted by H_s, is defined for all $j \in \{1\dots N-1\}$ as

$$H_s^j = -\mathbf{i}\frac{\xi^j}{|\xi^j|}S^j. \tag{2.21}$$

Notice that the Hilbert transform is not defined for $j = 0$, *i.e.*, for the null frequency. In practice, a high-pass filter has to be applied to s to eliminate the low frequencies. The discrete Hilbert transform of s, denoted by h_s, is obtained from H_s by using the inverse Fourier transform. The discrete analytic signal A_s can then be defined for all $j \in \{0, \dots, N-1\}$ as

$$A_s^j = s^j + \mathbf{i}h_s^j, \tag{2.22}$$

whose modulus A^j and argument ϕ^j provide a measure of analytic amplitude and phase, respectively. The analytic phase signal $(\phi^j)_j$ is then compared to the expected physical phase $(\varphi^j)_j$ to determine if the Hilbert transform manages to reliably extract local phase. The synthetic tests focus on two cases:

- the pure cosine wave, defined for all $j \in \{0, \dots, N-1\}$ as

$$s^j = a_0 \cos(\omega t^j), \tag{2.23}$$

  where $a_0 \in \mathbb{R}^*$ and $\omega \in \mathbb{R}^*$ denote the amplitude and frequency of the signal, respectively,

- the parabolic chirp, defined for all $j \in \{0, \dots, N-1\}$ as

$$s^j = a_0 \cos[a^2 \left(t^j\right)^2], \tag{2.24}$$

  with $a_0 \in \mathbb{R}_+^*$ and $a \in \mathbb{R}_+^*$.

In the first case, the analytic and physical phase signals are expected to coincide perfectly (see Section 2.1.2), while, in the second, they only coincide asymptotically, or if a is large enough (see Section 2.1.3). This would show how the theoretical results of the continuous domain are preserved in the discrete domain. However, because the phase signals consist of angular values, comparing them can be difficult due to the 2π-periodicity. In order to bypass this problem, numerical criteria of similarity between two angular signals are introduced in Section 2.2.2.

2.2.2 Numerical measure of similarity

This section aims at defining numerical criteria that measure the similarity between the analytic and physical phase signals, denoted by $(\phi^j)_j$ and $(\varphi^j)_j$, $j \in \{0, \dots, N-1\}$, respectively. Because these two signals contain angles defined modulo 2π, the quality of the estimation cannot be evaluated by simply calculating the difference between the extracted and expected values. Indeed, values like $-\pi+\epsilon$ and $\pi-\epsilon$ (ϵ being a small positive real number) would be deemed as highly different while they hold the same angular information. A good way to bypass this difficulty is to compare their respective cosines, which yields a measure of similarity at each time. A more global comparison between the estimated and expected values of phase is then performed by using the two numerical criteria of similarity defined, *e.g.*, in (Tóth 2007), the Best Fit Rate (BFR) and the Variance Accounted For (VAF). If $g = \left(g^j\right)_{j\in\{0,\dots,N-1\}}$ denotes a real-valued signal, and $\left(\widehat{g}^j\right)_{j\in\{0,\dots,N-1\}}$ the estimates of g at each point, then the BFR and VAF criteria are calculated as

$$\begin{cases} \mathrm{BFR}(\widehat{g},g) = \max\{100(1-\frac{\|\widehat{g}-g\|_2}{\|g-\overline{g}\|_2}),0\}, \\ \mathrm{VAF}(\widehat{g},g) = \max\{(100(1-\frac{V(\widehat{g}-g)}{V(g)}),0\}, \end{cases} \tag{2.25}$$

where for all signal $h = \left(h^j\right)_{j\in\{0,\dots,N-1\}}$,

$$\left\{ \ \|h\|_2^2 = \sum_{j=0}^{N-1}\left(h^j\right)^2, \overline{h} = \frac{1}{N}\sum_{j=0}^{N-1} h^j, V(h) = \frac{1}{N}\|h\|_2^2 - \overline{h}^2. \right. \tag{2.26}$$

The BFR and VAF criteria are to be interpreted as a bias and variance information, respectively, which is very instructive when testing an estimation technique. Note that both BFR and VAF are not defined for constant signals, but the phase functions studied in this work should not be constant. In the subsequent tests, these criteria are applied to $g = \cos(\varphi)$ and $\widehat{g} = \cos(\phi)$. The closer to 100% these criteria are, the better the analytic extraction of the phase is.

2.2.3 Phase extraction of a cosine wave

Figure 2.3 shows an analytic phase function ϕ extracted through the Hilbert transform from a discrete cosine wave generated with $N = 1000$, $T = 0.002$, $a_0 = 0.5$ and $\omega = 10\pi$. The expected physical phase function φ is also represented. As predicted by Eq. (2.11) in the continuous case, both phase functions coincide perfectly, which is confirmed by the BFR and VAF criteria, which are both equal to 100%.

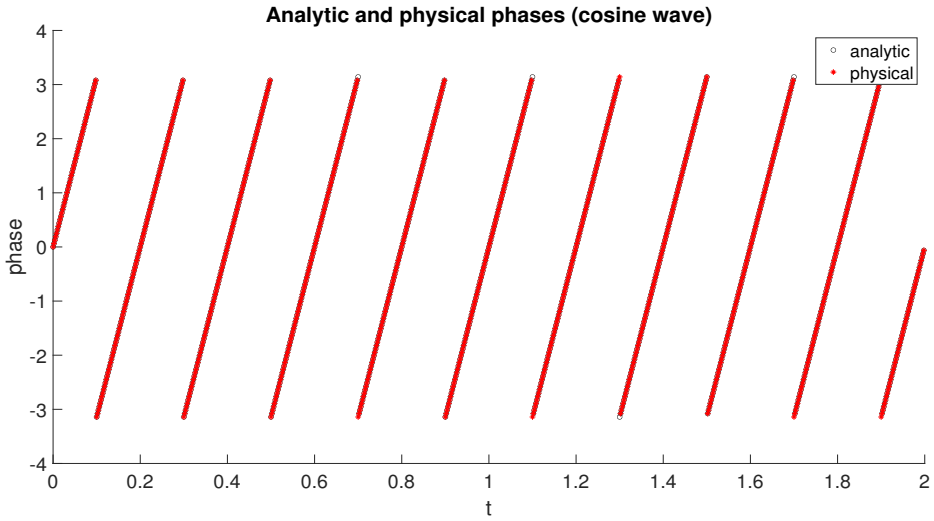

Figure 2.3: Comparison between the analytic (black circles) and physical (red line) measures of amplitude and phase in the case of a cosine wave, $N = 1000$, $T = 0.002$, $a_0 = 0.5$, $\omega = 10\pi$, BFR = VAF = 100%.

Applying the same process to cosine waves of different frequencies $\omega \in \{\pi(1+\ell), \ell = 0,\dots,9\}$ yields exactly the same results, *i.e.*, the BFR and VAF criteria remain exactly equal to 100%. This confirms the theoretical results of Section 2.1.2.

2.2.4 Phase extraction of a parabolic chirp

Figure 2.4 shows the analytic and physical phase functions of a discrete parabolic chirp generated with $N = 1000$, $T = 0.002$, $a_0 = 0.5$ and $a = 3$. This time, the phase extrac-

tion does not work perfectly, but the two functions remain close to each other, which is confirmed by the high values of BFR and VAF (BFR = 90.07%, VAF = 99.02%). As predicted by Eq. (2.16), the quality of the estimation increases with t, which explains why the initial phase values ($t < 0.2$) are badly estimated.

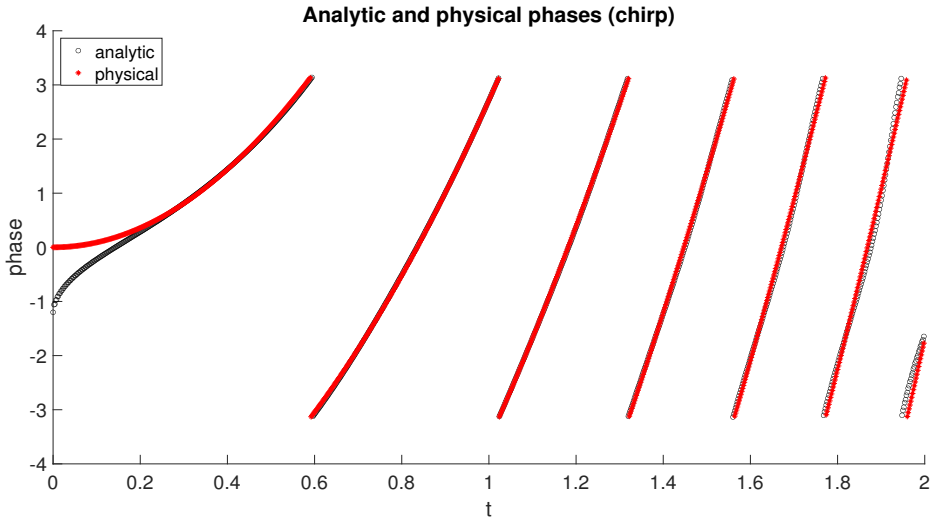

Figure 2.4: Comparison between the analytic (black circles) and physical (red line) measures of amplitude and phase in the case of a parabolic chirp, $N = 1000$, $T = 0.002$, $a_0 = 0.5$, $a = 3$, BFR = 90.07%, VAF = 99.02%.

Figure 2.5 illustrates the influence of the parameter a on the quality of the analytic extraction of phase. As predicted by Eq. (2.17) in the continuous case, increasing a improves the phase extraction, which is reflected by the BFR and VAF criteria becoming close to 100% for higher values of a.

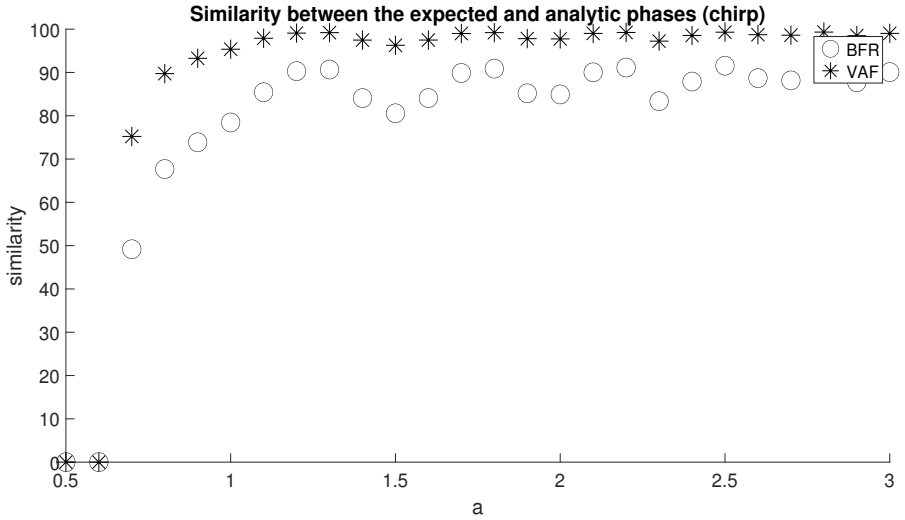

Figure 2.5: Comparison between the physical and analytic phase functions through the BFR and VAF criteria in the case of a parabolic chirp.

The previously performed synthetic tests show how the results established in the continuous case remain true when discrete signals come into play. Of course, the relevance of the Hilbert transform in the field of signal processing is not to be proved anymore (Seelamantula et al. 2012), but focusing on 1D signals enables the introduction of some of the main issues encountered in the case of 2D structure extraction. Though focusing on parabolic chirps may seem restrictive at first, generalizing the results presented in this section to 2D images is of particular interest in the field of interferometry, as highlighted in Sections 2.4 2.5 and 2.6. Before handling 2D images, Section 2.3 properly introduces the 2D Fourier transform and its main properties.

2.3 The 2D Fourier transform

In the 1D case, the Fourier transform is crucial in defining and computing the Hilbert transform, from which a reliable measure of phase is obtained. Generalizing this procedure to 2D images hence requires a proper definition of a 2D Fourier transform. Though it is a commonly used tool in image processing, the available literature generally focuses on computing aspects (as in (Smith 1995)) and lacks the theoretical results of the continuous domain that can be found in the 1D case, according to the authors' knowledge. Consequently, this section aims at introducing the 2D Fourier transform and some of its useful properties properly, a crucial step before dealing with 2D phase extraction.

2.3.1 Definition

Let $s : \mathbb{R}^2 \to \mathbb{R}$ be an integrable function. The 2D Fourier transform of s, denoted by $\mathcal{F}_2 s$, is defined for all $\xi \in \mathbb{R}^2$ as

$$\mathcal{F}_2 s(\xi) = \int_{\mathbb{R}^2} s(\mathbf{x}) e^{-\mathbf{i}\mathbf{x}^\top \xi} d\mathbf{x}. \tag{2.27}$$

In the subsequent developments, the more concise notation $\widehat{s}$ is also used for the Fourier transform of s.

2.3.2 Basic properties

Linearity

If $s_1, s_2 : \mathbb{R}^2 \to \mathbb{R}$ are integrable functions and $\lambda \in \mathbb{R}$, then,

$$\mathcal{F}_2 \left[\lambda s_1 + s_2\right] = \lambda \mathcal{F}_2 s_1 + \mathcal{F}_2 s_2. \tag{2.28}$$

This is directly deduced from the linearity of the integral.

Dilation

If $\mathbf{A}$ is an 2×2 invertible dilation matrix, $s : \mathbb{R}^2 \to \mathbb{R}$ an integrable function and $s_{\mathbf{A}} : \mathbf{x} \mapsto s(\mathbf{A}\mathbf{x})$, then for all $\xi \in \mathbb{R}^2$,

$$\mathcal{F}_2 s_{\mathbf{A}}(\xi) = \frac{1}{|\det(\mathbf{A}^{-1})|} \mathcal{F}_2 s(\mathbf{A}^{-1}\xi). \tag{2.29}$$

Because $\mathbf{A}$ is assumed to be invertible, this property is proved by using the substitutions $\mathbf{x} = \mathbf{A}\mathbf{x}$.

Convolution theorem

If $s_1, s_2 : \mathbb{R}^2 \to \mathbb{R}$ are integrable functions, then

$$\mathcal{F}_2 \left[s_1 * s_2 \right] (\xi) = \mathcal{F}_2 s_1(\xi) \times \mathcal{F}_2 s_2(\xi), \tag{2.30}$$

where $s_1 * s_2$ denotes the 2D convolution product of s_1 and s_2 defined for all $\mathbf{x} \in \mathbb{R}^2$ by

$$s_1 * s_2(\mathbf{x}) = \int_{\mathbb{R}^2} s_1(\mathbf{y}) s_2(\mathbf{x} - \mathbf{y}) d\mathbf{y}. \tag{2.31}$$

This is proved by using Fubini's theorem (Fubini 1907) and a substitution.

Space domain derivation

Let $s : \mathbb{R}^2 \to \mathbb{R}$ be an integrable and differentiable function. For $j \in \{1, 2\}$, if $\frac{\partial s}{\partial x_j}$ is integrable, its Fourier transform satisfies for all $\xi \in \mathbb{R}^2$,

$$\mathcal{F}_2 \frac{\partial s}{\partial x_j}(\xi) = \mathbf{i} \xi_j \mathcal{F}_2 s(\xi). \tag{2.32}$$

The proof relies on an integration by parts.

Frequency domain derivation

Let $s : \mathbb{R}^2 \to \mathbb{R}$ be an integrable function, and let s_j denote the function defined for all $\mathbf{x} = (x_1, x_2) \in \mathbb{R}^2$ as

$$s_j(\mathbf{x}) = x_j s(\mathbf{x}), \tag{2.33}$$

with $j \in \{1, 2\}$. Assuming that s_1 and s_2 are integrable, then, for all $j \in \{1, 2\}$ and $\xi \in \mathbb{R}^2$,

$$\mathcal{F}_2 s_j(\xi) = \mathbf{i} \frac{\partial \mathcal{F}_2 s}{\partial \xi_j}(\xi). \tag{2.34}$$

The proof relies on a derivation under the integral sign.

2.3.3 2D Gaussian function

2D Gaussian functions are widely used as window functions in the field of texture synthesis (Lagae, Lefebvre, Drettakis & Dutré 2009), similarly to their use in 1D signal processing (Picinbono 2008). As a result, they frequently appear in the subsequent developments. In this section, the Fourier transform of a 2D Gaussian function is formally calculated, a result that, according to the authors' knowledge, is rarely explicitly given in the current literature dealing with signal and image processing. However, it is much more frequently found in the random fields literature (see, *e.g.*, Theorem 3.2.3 in (Tong 1989)).

Theorem 1. *Let $g : \mathbb{R}^2 \to \mathbb{R}$ be a 2D Gaussian function defined for all $\mathbf{x} = (x_1, x_2) \in \mathbb{R}^2$ by*

$$g(\mathbf{x}) = e^{-(a_1^2 x_1^2 + a_2^2 x_2^2)}, \tag{2.35}$$

where $(a_1, a_2) \in (\mathbb{R}_+^*)^2$. The Fourier transform of g is given for all $\xi = (\xi_1, \xi_2) \in \mathbb{R}^2$ by

$$\mathcal{F}_2 g(\xi) = \frac{\pi}{a_1 a_2} e^{-\frac{1}{4}\left(\frac{\xi_1^2}{a_1^2} + \frac{\xi_2^2}{a_2^2} \right)}. \tag{2.36}$$

The proof is given in Appendix A.1. Let $(\mathbf{e}_1, \mathbf{e}_2)$ denote the canonical basis of $\mathbb{R}^2$. The 2D Gaussian function g defined in Eq. (2.35) is called anisotropic because its variance is not the same along the two directions $\mathbf{e}_1$ and $\mathbf{e}_2$ of $\mathbb{R}^2$. The more different a_1 and a_2 are, the more anisotropic the Gaussian is. In the special case of $a_1 = a_2$, the Gaussian function is isotropic, *i.e.*, the variance does not change with the direction. Because isotropic Gaussian functions frequently appear in the subsequent developments, the 2D Fourier transform of such functions is given in Corollary 1.

Corollary 1. *Let $g : \mathbb{R}^2 \to \mathbb{R}$ be a 2D isotropic Gaussian function defined for all $\mathbf{x} \in \mathbb{R}^2$ by*

$$g(\mathbf{x}) = e^{-a^2 \|\mathbf{x}\|^2}, \tag{2.37}$$

where $a \in \mathbb{R}^*$ and $\|.\|$ denotes the Euclidian norm of $\mathbb{R}^2$. The Fourier transform of g is given for all $\xi = (\xi_1, \xi_2) \in \mathbb{R}^2$ by

$$\mathcal{F}_2 g(\xi) = \frac{\pi}{a^2} e^{-\frac{1}{4a^2}\|\xi\|^2}. \tag{2.38}$$

This is obviously a particular case of Theorem 1 with $a_1 = a_2 = a$. Now that some fundamental properties of the 2D Fourier transform are formally expressed, the 1D results about phase estimation given in Section 2.1 can be generalized to 2D images.

2.4 Case of 2D images: the Riesz transform and the monogenic signal

2.4.1 Definition and first properties

In this section, s denotes a 2D greyscale image modeled as a function $s : \mathbb{R}^2 \to \mathbb{R}$ defined for all $\mathbf{x} \in \mathbb{R}^2$ by (Seelamantula et al. 2012)

$$s(\mathbf{x}) = a(\mathbf{x}) \cos\left[\varphi(\mathbf{x})\right], \tag{2.39}$$

where $a(\mathbf{x})$ denotes the amplitude of s and $\varphi(\mathbf{x})$ its phase at each pixel $\mathbf{x} \in \mathbb{R}^2$. Similarly to the 1D case, these functions give measures of local amplitude and local phase, respectively. In order to extract a and φ from s as done for 1D signals, the Hilbert transform is generalized to the 2D case by using the Riesz transforms $\mathcal{R}_k$, $k \in \{1, 2\}$, introduced in (Felsberg 2002). For $k \in \{1, 2\}$, let r_k denote the 2D Riesz kernel defined for all $\mathbf{x} = (x_1, x_2) \in (\mathbb{R}^*)^2$ as

$$r_k(\mathbf{x}) = \frac{x_k}{2\pi \|\mathbf{x}\|_2^3}. \tag{2.40}$$

Then, the Riesz transforms of s, denoted by $\mathcal{R}_k s$, are defined for all $\mathbf{x} = (x_1, x_2) \in \mathbb{R}^2$ as the 2D improper convolution product between s and r_k, *i.e.*,

$$\begin{aligned} \mathcal{R}_k s(\mathbf{x}) &= s * r_k(\mathbf{x}), \\ &= \frac{1}{2\pi} \lim_{\epsilon \to 0} \left(\int_{\mathbb{R}^2 \setminus \mathcal{B}_\epsilon(\mathbf{x})} \frac{(x_k - y_k)\, s(\mathbf{x})}{\|\mathbf{x} - \mathbf{y}\|_2^3} d\mathbf{y} \right), \end{aligned} \tag{2.41}$$

where $\mathcal{B}_\epsilon(\mathbf{x})$ denotes the open disk of center $\mathbf{x}$ and radius ϵ. As in the 1D case, a much more convenient definition can be formulated in the Fourier domain, *i.e.*, for all $\xi = (\xi_1, \xi_2) \in (\mathbb{R}^*)^2$ and $k \in \{1, 2\}$

$$\mathcal{F}_2\left[\mathcal{R}_k s\right](\xi) = R_k(\xi)\mathcal{F}_2 s(\xi), \tag{2.42}$$

where R_k denotes the 2D Fourier transform of the Riesz kernel r_k, defined by

$$R_k(\xi) = -\mathbf{i}\frac{\xi_k}{\|\xi\|_2}. \tag{2.43}$$

The 3D signal whose components are s, $\mathcal{R}_1 s$ and $\mathcal{R}_2 s$, respectively, is called the monogenic signal of s (Felsberg & Sommer 2001). The spherical coordinates of this 3D signal yield the definition of the monogenic amplitude $A(\mathbf{x})$ and two angular values at each point $\mathbf{x}$, the monogenic phase $\phi(\mathbf{x})$ and the orientation $\theta(\mathbf{x})$, respectively, *i.e.*,

$$\begin{pmatrix} s(\mathbf{x}) \\ \mathcal{R}_1 s(\mathbf{x}) \\ \mathcal{R}_2 s(\mathbf{x}) \end{pmatrix} = A(\mathbf{x}) \begin{pmatrix} \cos\left[\phi(\mathbf{x})\right] \\ \cos\left[\theta(\mathbf{x})\right]\sin\left[\phi(\mathbf{x})\right] \\ \sin\left[\theta(\mathbf{x})\right]\sin\left[\phi(\mathbf{x})\right] \end{pmatrix}. \tag{2.44}$$

The amplitude, phase and orientation of the monogenic signal can be interpreted as a measure of local energy, geometrical structure and main direction of oscillation of the original image, respectively (Felsberg 2002). Of course, as in the 1D case, the functions A and ϕ do not necessarily coincide with their physical counterparts a and φ, respectively. However, the next sections show how the monogenic measures given in Eq. (2.44) provide a relevant description of the local behavior of the texture under certain conditions.

2.4.2 Case of a pure cosine wave

As in the 1D case, the first class of signals to which the Riesz transform is applied is the class of 2D pure cosine waves (Larkin et al. 2001, Seelamantula et al. 2012). Pure cosine waves are generalized to the 2D case as functions s defined for all $\mathbf{x} = (x_1, x_2) \in \mathbb{R}^2$ as

$$s(\mathbf{x}) = a_0 \cos(\omega \mathbf{u}^\top \mathbf{x}), \tag{2.45}$$

where $\omega \in \mathbb{R}_+^*$, $\mathbf{u} = (\cos\alpha, \sin\alpha)^\top$ and $\alpha \in \left]-\frac{\pi}{2}; \frac{\pi}{2}\right]$. Visually, such signals correspond to parallel fringes oscillating with a constant frequency. The parameter ω corresponds to the frequency of the fringes, while α denotes their orientation and $\mathbf{u}$ their wave vector (Kaseb et al. 2019). Figure 2.6 shows an example of such an image.

As stated in (Seelamantula et al. 2012, Polisano 2017), the Riesz transforms of a pure cosine wave are given for all $\mathbf{x} \in \mathbb{R}^2$ by

$$\begin{cases} \mathcal{R}_1 s(\mathbf{x}) = a_0 \sin(\omega \mathbf{u}^\top \mathbf{x}) \cos\alpha, \\ \mathcal{R}_2 s(\mathbf{x}) = a_0 \sin(\omega \mathbf{u}^\top \mathbf{x}) \sin\alpha. \end{cases} \tag{2.46}$$

The monogenic signal of s has thus two spherical representations, which are $(a_0, \omega\mathbf{u}^\top\mathbf{x}, \alpha)$ and the monogenic measures of amplitude, phase and orientation $(A(\mathbf{x}), \phi(\mathbf{x}), \theta(\mathbf{x}))$ defined in Eq. (2.44), respectively. By identification of the spherical coordinates term by term, the monogenic and physical functions coincide perfectly, *i.e.*, for all $\mathbf{x} \in \mathbb{R}^2$,

$$\begin{cases} A(\mathbf{x}) = a_0, \\ \phi(\mathbf{x}) = \varphi(\mathbf{x}) = \omega\mathbf{u}^\top\mathbf{x}\ [2\pi], \\ \theta(\mathbf{x}) = \alpha\ [2\pi]. \end{cases} \tag{2.47}$$

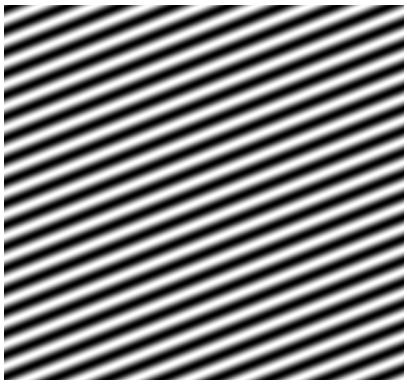

Figure 2.6: Example of a 2D cosine wave with $\omega = 20\pi$ and $\alpha = \frac{\pi}{6}$.

Notice furthermore that, by shifting the cosine to a sine, the Riesz transform operates as a 2D quadrature filter, which is exactly what it was designed for (Larkin et al. 2001, Felsberg & Sommer 2001). This illustrates how the Riesz transform generalizes the Hilbert transform to 2D signals. While cosine waves are a limited class of images, more complex patterns are studied in Section 2.4.3.

2.4.3 Case of a parabolic chirp

Though the monogenic signal is suitable for any oscillating texture (Felsberg & Sommer 2001), it is often used within an interferometry framework (Larkin et al. 2001, Seelamantula et al. 2012, Kaseb et al. 2019). Consequently, the theoretical developments introduced here can find their motivation in the field of interferometry, where extracting the phase function is a crucial issue (Robin, Valle & Brémand 2005).

As in the 1D case, the monogenic measures of amplitude, phase and orientation provided by Eq. (2.44) match their expected physical counterparts only in the case of pure cosine waves. However, assuming that the amplitude and phase functions a and φ are slowly and smoothly varying, the monogenic signal manages to reliably estimate these quantity, as shown in works dealing with interferometric fringe patterns such as (Larkin et al. 2001, Seelamantula et al. 2012). Because real interferometric fringes often exhibit circular fringes, as can be seen in Figure 2.7, this section aims at further studying how the Riesz transform deals with such patterns, with a special focus on the estimation of the phase and the orientation, respectively.

To do so, one possible approach is to model circular fringes as 2D parabolic chirps. While Sections 2.1 and 2.2 show how the analytic phase function of a 1D parabolic chirp is asymptotically equal to its physical counterpart, no analogous result has been established in the 2D case yet. The parabolic chirp can be generalized to the 2D case as a function s defined for all $\mathbf{x} = (x_1, x_2) \in \mathbb{R}^2$ as

$$s(\mathbf{x}) = a_0 \cos(a^2 \|\mathbf{x}\|^2), \tag{2.48}$$

where $a_0 \in \mathbb{R}_+^*$ and $a \in \mathbb{R}_+^*$. As can be seen in Figure 2.8, parabolic chirps visually correspond to circular patterns, which makes them relevant to model interferometric fringes.

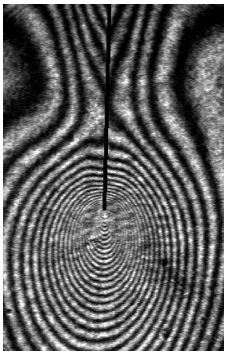

Figure 2.7: Example of a real 2D fringe pattern.

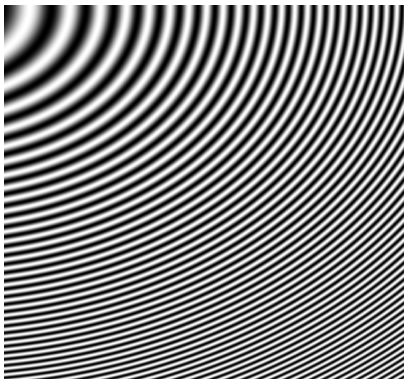

Figure 2.8: Example of a 2D parabolic chirp with $a = 7$.

In order to generalize the asymptotic result of the 1D case, the Riesz transform of a parabolic chirp is first properly calculated.

Theorem 2 (Riesz transform of a 2D parabolic chirp)**.** *If $\mathbf{x} = (x_1, x_2) \in \mathbb{R}^2$, let $\theta_{\mathbf{x}}$ denote the argument of the complex number $x_1 + \mathbf{i}x_2$. The Riesz transforms of a parabolic chirp s as defined in Eq.* (2.48) *are given for all $\mathbf{x} \in \mathbb{R}^2$ by*

$$\begin{aligned}\mathcal{R}_1 s(\mathbf{x}) = a_0 a\sqrt{\pi}\frac{\|\mathbf{x}\|}{2}\cos\theta_{\mathbf{x}} \times \Bigg[& J_0\left(\frac{a^2\|\mathbf{x}\|^2}{2}\right)\cos\left(\frac{\pi}{4} - \frac{a^2\|\mathbf{x}\|^2}{2}\right) \\ & + J_1\left(\frac{a^2\|\mathbf{x}\|^2}{2}\right)\sin\left(\frac{\pi}{4} - \frac{a^2\|\mathbf{x}\|^2}{2}\right)\Bigg],\end{aligned} \tag{2.49}$$

and

$$\begin{aligned}\mathcal{R}_2 s(\mathbf{x}) = a_0 a\sqrt{\pi}\frac{\|\mathbf{x}\|}{2}\sin\theta_{\mathbf{x}} \times \Bigg[& J_0\left(\frac{a^2\|\mathbf{x}\|^2}{2}\right)\cos\left(\frac{\pi}{4} - \frac{a^2\|\mathbf{x}\|^2}{2}\right) \\ & + J_1\left(\frac{a^2\|\mathbf{x}\|^2}{2}\right)\sin\left(\frac{\pi}{4} - \frac{a^2\|\mathbf{x}\|^2}{2}\right)\Bigg],\end{aligned} \tag{2.50}$$

where J_n denotes the Bessel functions defined for all $n \in \mathbb{Z}$ and $z \in \mathbb{C}$ by (Abramowitz & Segun 1964)

$$J_n(z) = \frac{1}{\pi}\int_0^{\pi}\cos(n\tau - z\sin\tau)\,d\tau. \tag{2.51}$$

The proof is given in Appendix A.2. As in the 1D case, the physical and monogenic amplitudes and phases do not match, *i.e.*,

$$A(\mathbf{x}) \neq a_0 \text{ and } \phi(\mathbf{x}) \neq a^2\|\mathbf{x}\|^2. \tag{2.52}$$

However, by using the asymptotic expressions of the Bessel functions given in (Abramowitz & Segun 1964), it is possible to show that the monogenic measure of amplitude and phase are asymptotically close to their physical counterparts. If $n \in \mathbb{N}$ and $u \in \mathbb{R}$, the Bessel functions can be asymptotically expanded for $u \to +\infty$ as

$$J_n(u) = \sqrt{\frac{2}{\pi u}}\left[\cos\left(u - \frac{n\pi}{2} - \frac{\pi}{4}\right) + \mathrm{O}\left(\frac{1}{u}\right)\right]. \tag{2.53}$$

In Eq. (2.49) and (2.50), the argument of the Bessel functions J_0 and J_1 is $u = \frac{a^2\|\mathbf{x}\|^2}{2}$. This expression tends towards infinity when $\|\mathbf{x}\|$ does, *i.e.*, when the signal moves away from its initial point $(0,0)$. Therefore, it is possible to apply Eq. (2.53) to $u = \frac{a^2\|\mathbf{x}\|^2}{2}$ and $n \in \{0,1\}$, which gives

$$J_0\left(\frac{a^2\|\mathbf{x}\|^2}{2}\right) = \frac{2}{a\|\mathbf{x}\|\sqrt{\pi}}\left[\cos\left(\frac{a^2\|\mathbf{x}\|^2}{2} - \frac{\pi}{4}\right) + \mathrm{O}\left(\frac{1}{a^2\|\mathbf{x}\|^2}\right)\right], \tag{2.54}$$

$$J_1\left(\frac{a^2\|\mathbf{x}\|^2}{2}\right) = \frac{2}{a\|\mathbf{x}\|\sqrt{\pi}}\left[\sin\left(\frac{a^2\|\mathbf{x}\|^2}{2} - \frac{\pi}{4}\right) + \mathrm{O}\left(\frac{1}{a^2\|\mathbf{x}\|^2}\right)\right]. \tag{2.55}$$

These expressions can then be injected in Eq. (2.49), hence

$$\begin{aligned}\mathcal{R}_1 s(\mathbf{x}) = a_0 \cos\theta_{\mathbf{x}} \left[\cos^2\left(\frac{\pi}{4} - \frac{a^2\left\|\mathbf{x}\right\|^2}{2}\right) - \sin^2\left(\frac{\pi}{4} - \frac{a^2\left\|\mathbf{x}\right\|^2}{2}\right)\right] \\ + \mathrm{O}\left(\frac{1}{a^2\left\|\mathbf{x}\right\|^2}\right).\end{aligned} \tag{2.56}$$

Using the equalities $\cos^2(\theta) - \sin^2(\theta) = \cos(2\theta)$ and $\cos\left(\frac{\pi}{2} - \theta\right) = \sin(\theta)$ finally gives the following asymptotic expansion of $\mathcal{R}_1 s(\mathbf{x})$,

$$\mathcal{R}_1 s(\mathbf{x}) = a_0 \cos\theta_{\mathbf{x}} \sin(a^2\left\|\mathbf{x}\right\|^2) + \mathrm{O}\left(\frac{1}{a^2\left\|\mathbf{x}\right\|^2}\right), \tag{2.57}$$

when $\|\mathbf{x}\| \to +\infty$. Similarly,

$$\mathcal{R}_2 s(\mathbf{x}) = a_0 \sin\theta_{\mathbf{x}} \sin(a^2\left\|\mathbf{x}\right\|^2) + \mathrm{O}\left(\frac{1}{a^2\left\|\mathbf{x}\right\|^2}\right), \tag{2.58}$$

when $\|\mathbf{x}\| \to +\infty$. Notice that the O term tends towards 0 when $\|\mathbf{x}\|$ tends towards infinity, which yields an asymptotic expression of the monogenic signal associated with s for high values of $\|\mathbf{x}\|$, *i.e.*,

$$\begin{pmatrix} s(\mathbf{x}) \\ \mathcal{R}_1 s(\mathbf{x}) \\ \mathcal{R}_2 s(\mathbf{x}) \end{pmatrix} \approx a_0 \begin{pmatrix} \cos(a^2\left\|\mathbf{x}\right\|^2) \\ \cos\theta_{\mathbf{x}} \sin(a^2\left\|\mathbf{x}\right\|^2) \\ \sin\theta_{\mathbf{x}} \sin(a^2\left\|\mathbf{x}\right\|^2) \end{pmatrix}. \tag{2.59}$$

Because the spherical coordinates are unique (modulo 2π in the case of angular values), the asymptotic expressions of the local amplitude, phase and orientation of the parabolic chip can be deduced from Eq. (2.44) and (2.59), *i.e.*,

$$\begin{cases} A(\mathbf{x}) \approx a_0, \\ \phi(\mathbf{x}) \approx \varphi(\mathbf{x}) = a^2\left\|\mathbf{x}\right\|^2 \ [2\pi], \\ \theta(\mathbf{x}) \approx \theta_{\mathbf{x}} = \arg(\mathbf{x}) \ [2\pi], \end{cases} \tag{2.60}$$

when $\|\mathbf{x}\| \to +\infty$. This shows that the amplitude and phase values calculated by the monogenic tool are asymptotically equal to their expected physical values. Furthermore, Eq. (2.60) shows that the monogenic orientation is exactly the argument of $\mathbf{x}$.

It was in fact possible to predict this latter result by using the notion of wave vector presented in (T. D. Carozzi & Gough 2004). Indeed, the wave vector of (T. D. Carozzi & Gough 2004) is defined as the gradient of the phase, which in the case of a parabolic chirp is given for all $\mathbf{x} \in \mathbb{R}^2$ by

$$\nabla\varphi(\mathbf{x}) = 2a^2\mathbf{x}. \tag{2.61}$$

Because the wave vector gives the local direction of propagation of the wave, the orientation can be calculated as the argument of this vector, which here is exactly equal to $\theta_{\mathbf{x}}$ because $\nabla\varphi(\mathbf{x})$ and $\mathbf{x}$ share the same direction.

Remark (Influence of the a parameter)**.** *The O terms in Eq.* (2.57) *and* (2.58) *not only tend towards* 0 *when* $\|\mathbf{x}\|$ *tends towards infinity, but also when the* a *parameter does. This implies that, for high values of* a*, the monogenic amplitude, phase and orientation converge*

faster towards their respective asymptotic expressions. This parallels the influence of a highlighted in Section 2.1.3 in the 1D case. From a physical point of view, this means that the faster the chirp oscillates, the better the monogenic estimation of its local features is.

In the next section, numerical illustrations of these properties are given, with a special attention on the phase and the orientation, respectively. An adaptation of the Shannon-Nyquist theorem to 2D parabolic chirps is also proposed in order to avoid the classical phenomenon of aliasing (Marks 1991).

2.5 2D synthetic tests

2.5.1 Discretization

Let (t^j, t^k) be a 2D discrete grid, with $(j,k) \in \{0,\dots,M-1\} \times \{0,\dots,N-1\}$ and $(M,N) \in \mathbb{N}^2$ such that

$$\left\{ \begin{array}{l} t^j = jT_x, \\ t^k = kT_y, \end{array} \right. \tag{2.62}$$

where $T_x > 0$ and $T_y > 0$ denote the horizontal and vertical sampling periods, respectively. Similarly to the 1D case, $s = (s^{j,k})_{(j,k)\in\{0,\dots,M-1\}\times\{0,\dots,N-1\}}$ denotes a discrete signal defined for all $(j,k) \in \{0,\dots,M-1\} \times \{0,\dots,N-1\}$ by

$$s^{j,k} = a^{j,k} \cos\left(\varphi^{j,k}\right), \tag{2.63}$$

where $a^{j,k}$ and $\varphi^{j,k}$ denote the physical amplitude and phase of $s^{j,k}$, respectively. Using the 2D discrete Fourier transform (see, *e.g.*, (Ballard & Brown 1982, Burger & Burge 2008) for details), the Fourier transform of s, denoted by $S = (S^{j,k})_{(j,k)\in\{0,\dots,M-1\}\times\{0,\dots,N-1\}}$, can be computed. The Riesz kernel is then applied to S (see (Soulard & Carré 2017) for more details about the way the Riesz kernel is computed), and the discrete Riesz transform of s, a complex-valued signal denoted by $\mathcal{R}s$, is obtained by reversing the 2D discrete Fourier transform (Burger & Burge 2008). The three components of the discrete monogenic signal of s are then s itself, the real part of $\mathcal{R}s$ and its imaginary part, respectively. The discrete monogenic amplitude, phase and orientation are finally computed from these three components by using the spherical coordinates. In the subsequent developments, the discrete monogenic measures of phase and orientation at each pixel $(j,k) \in \{0,\dots,M-1\} \times \{0,\dots,N-1\}$ are denoted by $\phi^{j,k}$ and $\theta^{j,k}$, respectively. These monogenic measures of phase and orientation are then compared with their respective physical counterparts. As done in Section 2.2 in the 1D case, the synthetic tests focus on two cases:

- the 2D pure cosine wave, defined for all $(j,k) \in \{0,\dots,M-1\} \times \{0,\dots,N-1\}$ as

$$s^{j,k} = a_0 \cos\left[\omega\left(t^j \cos\alpha + t^k \sin\alpha\right)\right], \tag{2.64}$$

  where $a_0 \in \mathbb{R}^*$, $\omega \in \mathbb{R}^*$ and $\alpha \in \left]-\frac{\pi}{2}, \frac{\pi}{2}\right]$ denote the amplitude, frequency and orientation of the signal, respectively,

- the 2D parabolic chirp, defined for all $(j,k) \in \{0,\dots,M-1\} \times \{0,\dots,N-1\}$ as

$$s^{j,k} = a_0 \cos\left\{a^2\left[\left(t^j\right)^2 + \left(t^k\right)^2\right]\right\}, \tag{2.65}$$

  with $a_0 \in \mathbb{R}_+^*$ and $a \in \mathbb{R}_+^*$.

Again, the monogenic and physical phase and orientation signals are expected to coincide perfectly in the first case (see Section 2.4.2), while in the second, they only coincide asymptotically, or if a is large enough (see Section 2.4.3). In order to compare these angular signals, the similarity criteria introduced in Section 2.2.2 in the 1D case are used. Notice however that, contrary to cosine waves, parabolic chirps display accelerating oscillations. More precisely, at each pixel (jT_x, kT_y), $(j,k) \in \{0,\dots,M-1\} \times \{0,\dots,N-1\}$, the local horizontal and vertical frequencies are respectively equal to $\frac{a^2 jT_x}{2\pi}$ and $\frac{a^2 kT_y}{2\pi}$. In order to satisfy the Shannon-Nyquist condition (Oppenheim 1996), the horizontal and vertical sampling frequencies must be at least twice as high as the maximal horizontal and vertical frequencies of the image, respectively. In both horizontal and vertical cases, the maximal frequency is reached at the last pixel $[(M-1)T_x, (N-1)T_y]$, which leads to the following conditions,

$$\begin{cases} \frac{a^2(M-1)T_x^2}{\pi} < 1, \\ \frac{a^2(N-1)T_y^2}{\pi} < 1. \end{cases} \tag{2.66}$$

In all the subsequent tests involving parabolic chirps, after the size of the image $(M \times N)$ is fixed, the sampling periods T_x and T_y are systematically chosen small enough to satisfy these two conditions and hence avoid aliasing.

2.5.2 Phase extraction of a cosine wave

The discrete transform is first applied to a 2D cosine wave generated with $M = N = 1000$, $T_x = T_y = 0.002$, $a_0 = 0.5$, $\omega = 20\pi$, $\alpha = \frac{\pi}{6}$, respectively. Notice that T_x and T_y are chosen small enough to fit the Shannon-Nyquist bound. The estimated monogenic phase and its expected physical counterpart are represented in the top part of Figure 2.9, as well as their cosine difference $\cos(\phi - \varphi)$ (bottom left). As predicted by the theoretical results of Section 2.4.2, the two phase functions look very close to each other, which is confirmed by their high values of BFR and VAF, 99, 96% and 100%, respectively. Additionally, 97.41% of the cosine difference values $\cos(\phi - \varphi)$ are higher than 0.999, and 98.56% are higher than 0.99, with the problematic pixels being located exclusively along the top and bottom borders, which further confirms how ϕ and φ are close to each other. Notice furthermore that the orientation, expected to be constantly equal to α, is also well extracted by the monogenic signal. Though the BFR and VAF criteria cannot be applied to constant signals (see Section 2.2.2), the cosine difference between the monogenic orientation θ and α remains close to 1, as shown in Figure 2.9 (bottom right). This gives a good numerical illustration of the theoretical results found in (Larkin et al. 2001, Seelamantula et al. 2012) and recalled in Section 2.4.2.

Because the Riesz kernel has a singularity at the null frequency $(0,0)$ (see Eq. (2.43)), it can be expected that the frequency parameter ω impacts the quality of the phase extraction. In order to confirm this assumption, the Riesz transform is applied to cosine waves of different frequencies $\omega \in \{2\pi(1+\ell), \ell = 0,\dots,9\}$, from which the monogenic phase function can be extracted and compared to the physical phase through the BFR and VAF criteria. Figure 2.10 confirms that the monogenic estimation of phase loses quality for low values of ω. Given the fact that the Riesz transform requires clear oscillating patterns to work well, it is not surprising that it cannot extract the local structure of an image whose frequency is too low to complete a full period.

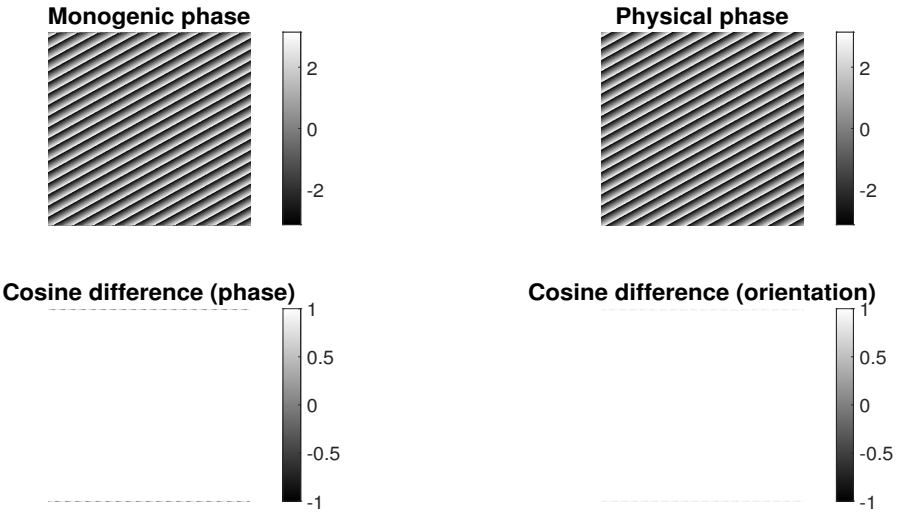

Figure 2.9: Monogenic (top left) and physical (top right) measures of phase, cosine differences between the monogenic and physical values of phase (bottom left) and orientation (bottom right) in the case of a cosine wave, $M = N = 1000$, $T_x = T_y = 0.002$, $a_0 = 0.5$, $\omega = 20\pi$, $\alpha = \frac{\pi}{6}$, BFR $= 99.96\%$, VAF $= 100\%$.

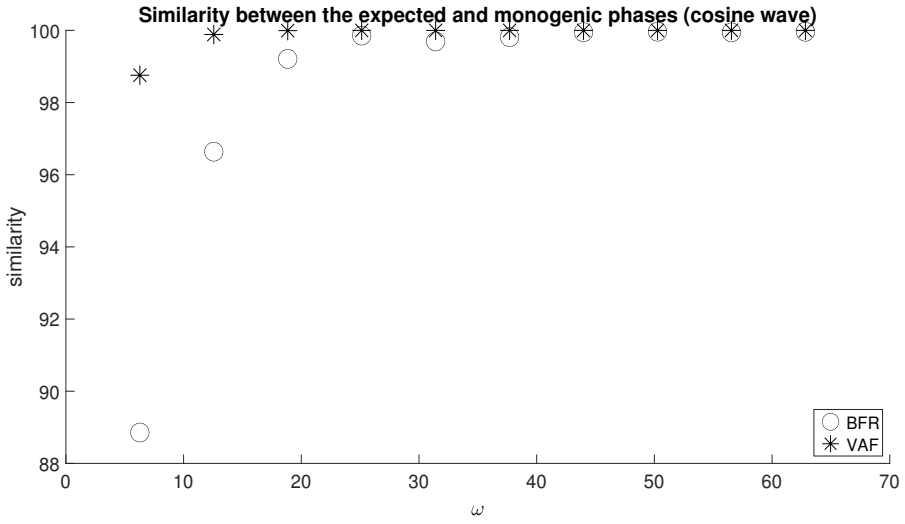

Figure 2.10: BFR and VAF criteria between the monogenic and physical phase functions for cosine waves of different frequencies $\omega \in \{2\pi(1+\ell), \ell = 0, \ldots, 9\}$.

2.5.3 Phase and orientation extraction of a parabolic chirp

The Riesz transform is now applied to a discrete parabolic chirp as defined in Eq. (2.5.3), with $M = N = 1000$, $T_x = T_y = 0.002$, $a_0 = 0.5$ and $a = 7$. According to Eq. (2.60), the monogenic and physical measures of phase and orientation are expected to get closer and closer to each others as the indices $j \in \{0, \dots, M-1\}$ and $k \in \{0, \dots, N-1\}$ increase. As shown in Figure 2.11, both the monogenic phase and orientation become close to their respective physical counterparts in zones located far enough from the top-left corner. Moreover, the convergence seems fast, as it is not necessary to move very far from the initial pixel $(0, 0)$ to notice the similarity. These observations are confirmed by the cosine difference signals displayed in the bottom part of Figure 2.11, whose values are close to 1 outside the top and left borders for both phase and orientation. Calculating the BFR and VAF criteria in the area $\{30, \dots, 970\} \times \{30, \dots, 1000\}$ yields BFR = 93.71% and VAF = 99.6% for the phase, BFR = 95.99% and VAF = 99.84% for the orientation, which further confirms the similarity between the monogenic and physical values outside the initial zone. Notice that the sampling conditions given in Eq. 2.66 are satisfied with this choice of parameters.

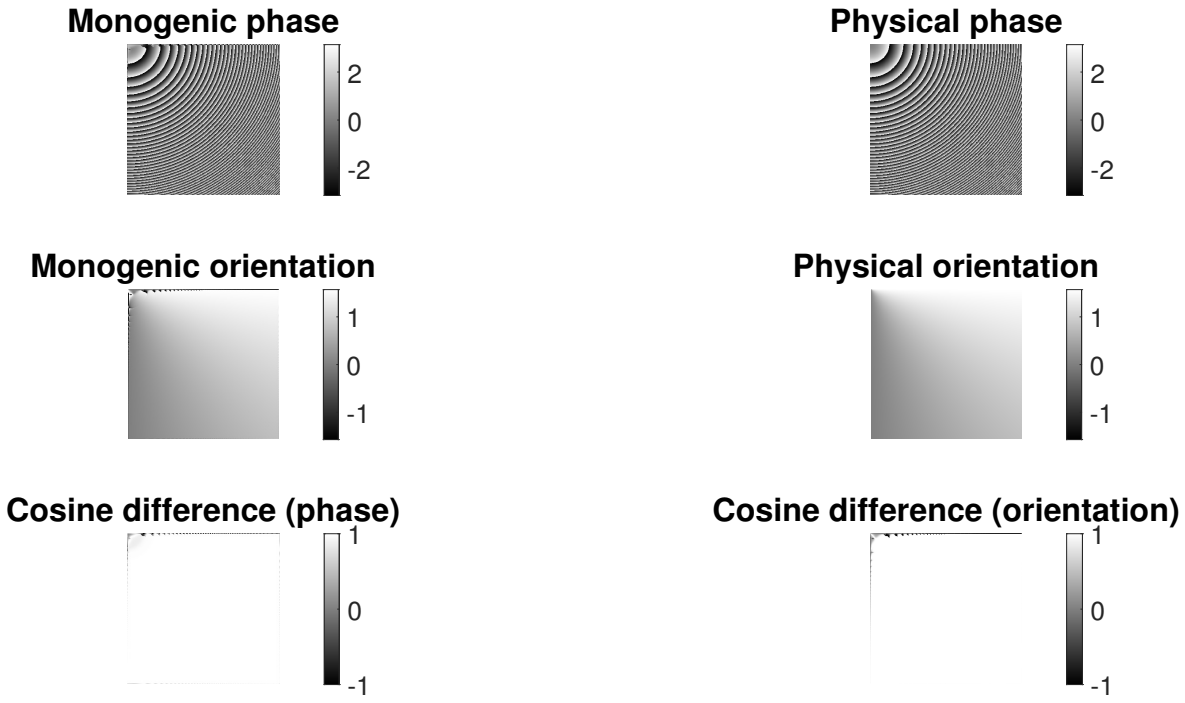

Figure 2.11: Monogenic phase (top left), physical phase (top right), monogenic orientation (center left), physical orientation (center right), cosine difference between the monogenic and physical values of phase (bottom left) and orientation (bottom right) of a parabolic chirp, $M = N = 1000$, $T_x = T_y = 0.002$, $a_0 = 0.5$, $a = 7$, BFR = 93.71%, VAF = 99.6% (phase), BFR = 95.99%, VAF = 99.84% (orientation).

As stated in Remark 2.4.3, the quality of the monogenic extraction of phase and orientation not only increases with $\|\mathbf{x}\|$, but also with a. This statement can be confirmed numerically by applying the Riesz transform to parabolic chirps of different parameters $a \in \{1 + 0.2\ell, \ell = 0, \dots, 35\}$, from which estimated values of phase and ori-

entation can be extracted. The BFR and VAF criteria are then calculated in the area $\{30, \dots, 970\} \times \{30, \dots, 1000\}$. Figure 2.12 shows how both criteria increase with a, which highlights the impact of a predicted in the continuous case.

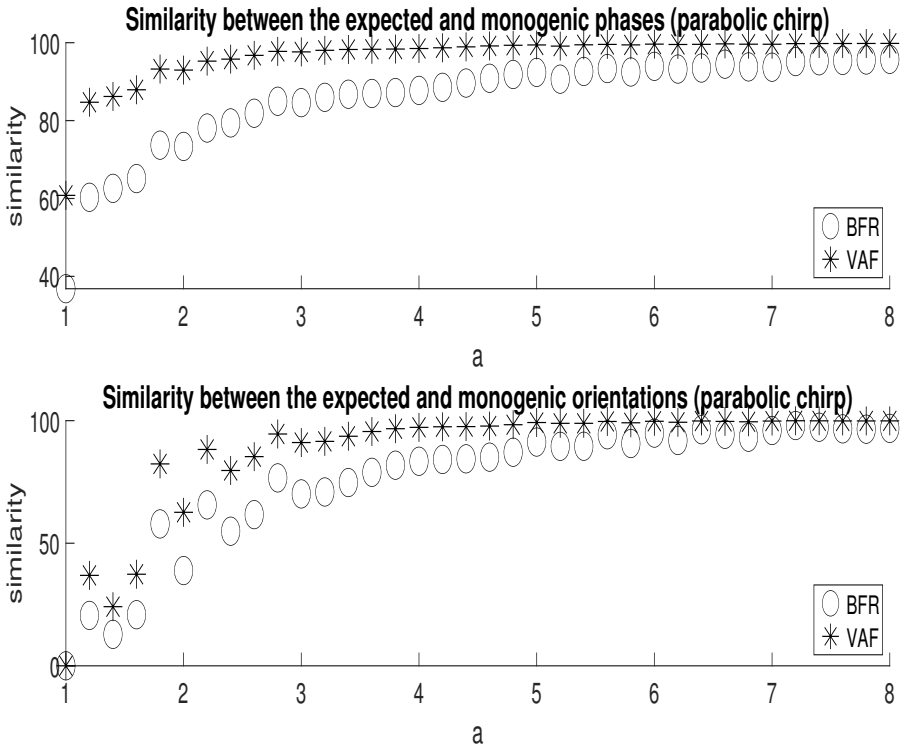

Figure 2.12: BFR and VAF criteria between the monogenic and physical phase (top) and orientation (bottom) functions for parabolic chirps of different parameters $a \in \{1+0.2\ell, \ell = 0, \dots, 35\}$.

2.5.4 Phase and orientation extraction of an anisotropic parabolic chirp

In Section 2.4.3, the parabolic chirp is generalized to the 2D case by using the Euclidian norm. The resulting images are isotropic, *i.e.*, they are invariant under rotations around the initial pixel $(0, 0)$. However, such a property is very specific, and in practice most images do not satisfy it (Polisano 2017). This is the case of the interferometric fringes displayed in Figure 2.7, whose patterns are not perfectly circular and thus display some degree of anisotropy. By using a weighted square norm instead of the classical Euclidian norm, it is possible to make the parabolic chirp anisotropic, *i.e.*, affected by rotations around the origin, which for all $\mathbf{x} = (x_1, x_2) \in \mathbb{R}^2$ leads to the following expression,

$$s(\mathbf{x}) = a_0 \cos\left(a_1^2 x_1^2 + a_2^2 x_2^2\right), \tag{2.67}$$

with $a_0 \in \mathbb{R}_+^*$ and $(a_1, a_2) \in (\mathbb{R}_+^*)^2$. Contrary to the previous case, the phase inside the cosine function now depends on the direction of $\mathbf{x}$. In this case, no analytical expression of the Riesz-transform has been calculated yet, hence no proper asymptotic consideration can be made. If the monogenic tool is well-suited for this type of image, the estimated phase should get close to the expression inside the cosine function in Eq. (2.67) when $\|\mathbf{x}\|$

tends towards infinity. Furthermore, as in the end of Section 2.4.3, the expected physical orientation can be expressed as the argument of the gradient of the phase, *i.e.*, for all $\mathbf{x} = (x_1, x_2) \in \mathbb{R}^2$,

$$\theta_{\mathbf{x}} = \arg\left(a_1^2 x_1 + \mathbf{i} a_2^2 x_2\right). \tag{2.68}$$

Though these conjectures are not formally proved yet, they can be confirmed with synthetic tests. Figure 2.13 shows the monogenic and physical measures of phase and orientation of an anisotropic parabolic chirp generated with $M = N = 1000$, $T_x = T_y = 0.002$, $a_0 = 0.5$, $a_1 = 8$ and $a_2 = 5$. Similarly to what happens in the isotropic case, both the monogenic phase and orientation become close to their respective physical counterparts when moving away from the top-left corner, with the same convergence speed. This is again confirmed by the cosine difference signals displayed in the bottom part of Figure 2.13 and the BFR and VAF criteria calculated in the area $\{30, \ldots, 970\} \times \{30, \ldots, 1000\}$, which are BFR = 94.14% and VAF = 99.66% for the phase, BFR = 92.99% and VAF = 99.51% for the orientation. This supports the conjecture made in the beginning of this section.

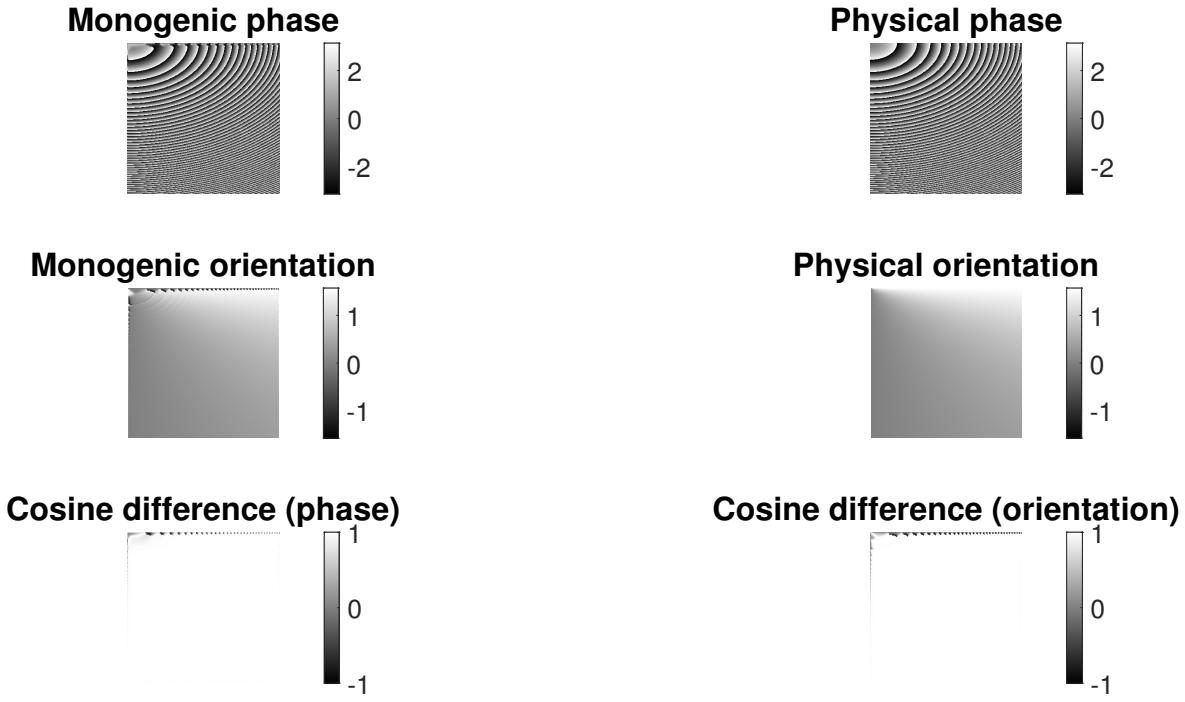

Figure 2.13: Monogenic phase (top left), physical phase (top right), monogenic orientation (center left), physical orientation (center right), cosine difference between the monogenic and physical values of phase (bottom left) and orientation (bottom right) of an anisotropic parabolic chirp, $M = N = 1000$, $T_x = T_y = 0.002$, $a_0 = 0.5$, $a_1 = 8$, $a_2 = 5$, BFR = 94.14%, VAF = 99.66% (phase), BFR = 92.99%, VAF = 99.51% (orientation).

Figure 2.14 shows how making a_1 increase (while a_2 stays equal to 6) makes the BFR and VAF criteria get close to 100%. The same observation can be made when a_2 varies while a_1 does not. This further shows that the monogenic estimation of phase and orientation performs well even when dealing with anisotropic images, *i.e.*, images that are not

rotation-invariant.

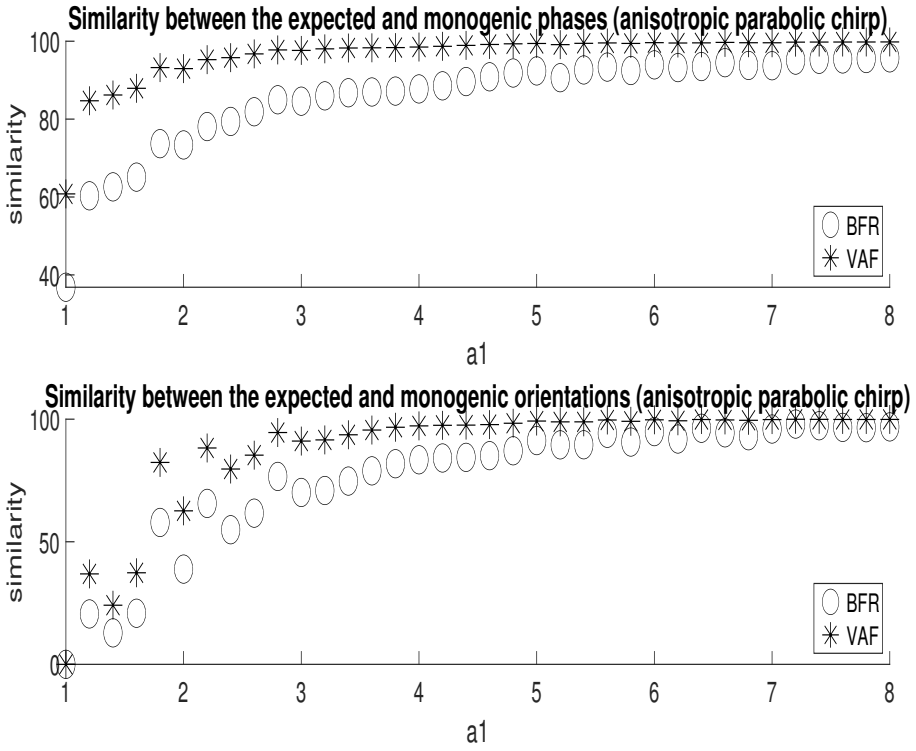

Figure 2.14: BFR and VAF criteria between the monogenic and physical phase (top) and orientation (bottom) functions for anisotropic parabolic chirps of different parameters $a_1 \in \{1 + 0.2\ell, \ell = 0, \ldots, 35\}$, with $a_2 = 6$.

2.6 Application to interferometry

2.6.1 Framework

Interference is the name of the phenomenon in which the superimposition of two waves results in the formation of a new wave (Steel 1986). The term interferometry in turn refers to the various techniques in which interference fringes are used to extract information (Steel 1986). Such techniques are of great interest for measuring various dynamical processes like structure deformation because they are purely optical and thus do not require any physical perturbation of the analyzed material (Robinson & Reid 1993, Robin et al. 2005). Because the geometrical structure of the fringe network is contained in its phase function and can be directly linked with physical quantities of the studied image (like relief and deformation), its estimation is of great importance (Robin et al. 2005).

Before the introduction of the monogenic signal in (Larkin et al. 2001, Felsberg & Sommer 2001), the most widely used techniques to estimate the phase involved the generation of several fringe patterns by moving one of the two networks (Bruning, Herriott, Gallagher, Rosenfeld, White & Bragaccio 1974). The phase values were then extracted point by point using these shifted images (see, *e.g.*, (Bruning et al. 1974) for further details about phase

shifting techniques). The main problem of these techniques is their lack of practical use when dynamic processes come into play, because it would require several phase shifting processes at each time, which is complicated to perform in practice. The application of signal processing tools like the Fourier and Hilbert transforms was originally performed to solve this problem, but these 1D techniques show their limits when dealing with complex 2D patterns (Morimoto, Seguchi & Higashi 1989). More recently, a technique requiring only one image, the polynomial Modulated Phase Correlation (pMPC), has been developed in (Robin et al. 2005) and is more suitable to 2D signals than 1D techniques. This method consists in dividing the image into patches, then fitting the parameters of a fixed model on each patch. Such a procedure can be very time consuming especially when the number of patches is high (Robin et al. 2005), while a smaller number of patches gives a far less reliable phase estimation. Furthermore, local singularities may appear because of the segmentation, hence the need of a better approach.

As a proper 2D generalization of the Hilbert transform, the Riesz transform, as well as the consistent extraction of phase it provides, opened the door for new solutions when it was introduced (Larkin et al. 2001). Since then, its relevance in the field of interferometry has been illustrated in numerous works dealing with fringe demodulation (Larkin et al. 2001), hologram demodulation (Seelamantula et al. 2012) and phase estimation (Kaseb et al. 2019). The quality of the phase and orientation extraction from oscillating textures provided by the Riesz-based monogenic signal has also been highlighted in Sections 2.4 and 2.5, with brand new theoretical and numerical results. In order to further study the benefits of the monogenic approach in the field of interferometry, a collaboration has been led with the Institut Pprime, which is a research laboratory specialized in the fields of physics and engineering sciences based in Poitiers. The institute has provided a data basis of real interferometric fringes (see Figure 2.15), from which the phase functions can be extracted by use of the monogenic signal. A numerical comparison with the pMPC technique has also been performed to illustrate the relevance of the monogenic tool in the interferometry framework. This section details the results of this collaboration, which has led to the publication of (Kaseb et al. 2019).

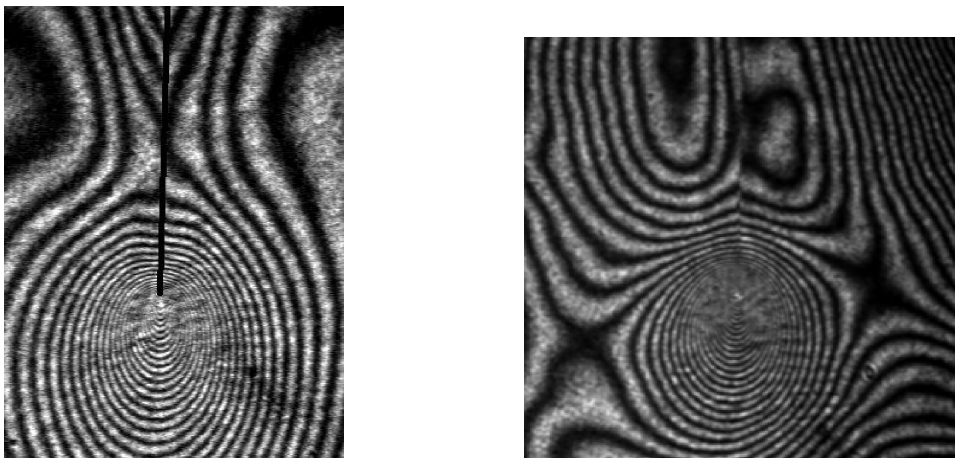

Figure 2.15: Examples of real interferometric fringes provided by the data basis of the Institut Pprime.

2.6.2 Synthesized concentric fringes

In this section, a numerical comparison is performed between the phase computed through the monogenic signal and the one computed through the pMPC technique developed in (Robin et al. 2005). In the pMPC procedure, the image is first divided into patches of equal size and an *a priori* model is chosen for the amplitude and phase of the fringes located inside the patches. At each patch, several fringe patterns are generated (with different parametrizations depending on the chosen model) and the closest to the original fringes according to statistical correlation is selected. The most canonical example treated in (Robin et al. 2005) is the case of concentric circular fringes. These fringes are modelled by a constant amplitude and a phase function defined for all $\mathbf{x} = (x_1, x_2) \in \mathbb{R}^2$ by

$$\varphi(\mathbf{x}) = \frac{2\pi}{p}\sqrt{(x_1 - x_1^c)^2 + (x_2 - x_2^c)^2}, \tag{2.69}$$

where $p \in \mathbb{R}_+^*$ denotes the interfringe and $(x_1^c, x_2^c) \in \mathbb{R}^2$ are the coordinates of the central pixel of the image. In practice, such fringes may correspond to level sets on a spherical dome (Robin et al. 2005). Notice that such concentric fringes are not strictly equivalent to the parabolic chirps studied in Section 2.5 despite their similar appearance. As in the case of anisotropic parabolic chirps, no theoretical result about the quality of the monogenic phase extraction has been proved yet. After generating a discrete sample of concentric circular fringes on the discrete grid defined in Section 2.5.1 with $M = N = 200$, $T_s = 1$, $\frac{2\pi}{p} = \sqrt{0.05}$ and $(x_1^c, x_2^c) = (100, 100)$, the monogenic tool is applied, from which an estimation of local phase can be computed at each point, and then compared with the phase obtained by the pMPC in (Robin et al. 2005). The choice of parameters is the same as in the synthetic tests performed in (Robin et al. 2005) to enable the comparison with the pMPC technique. The results are given in Figure 2.16. Both techniques perform well, but the monogenic approaches give better results at the center of the image, which is confirmed by the BFR and VAF criteria, *i.e.*, BFR = 80.56%, VAF = 96.23% for the pMPC, BFR = 90.82%, VAF = 99.16% for the monogenic tool.

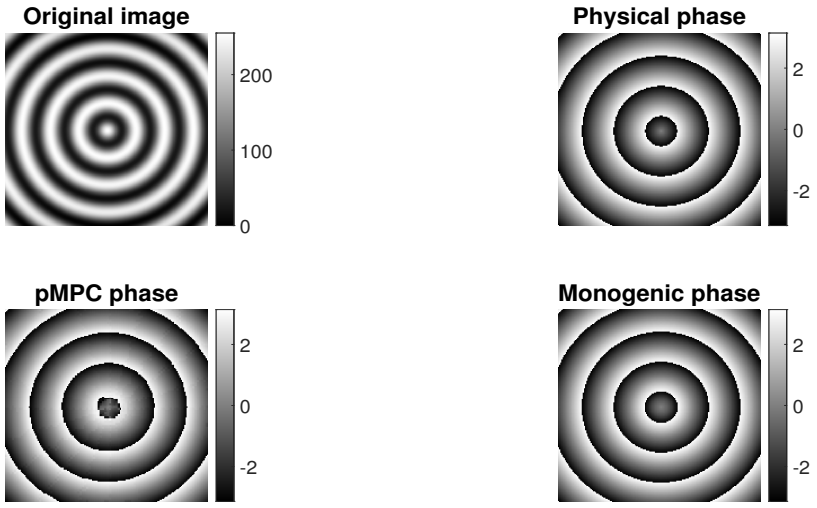

Figure 2.16: Original image (top left), expected phase (top right), pMPC phase (bottom left) and monogenic phase (bottom right) of concentric fringes, BFR = 80.56%, VAF = 96.23% (pMPC), BFR = 90.82%, VAF = 99.16% (monogenic).

These results are further reinforced by the cosine differences given in Figure 2.17, as well as their respective histograms given in Figure 2.18. The values are substantially closer to 1 in the case of the monogenic estimation than in the case of the pMPC.

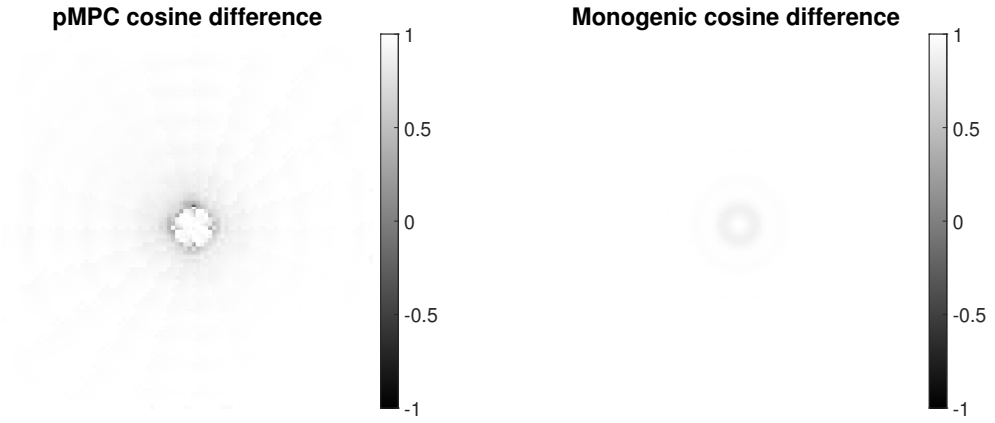

Figure 2.17: Cosine difference between the expected phase and the pMPC (left) and monogenic (right) phase functions.

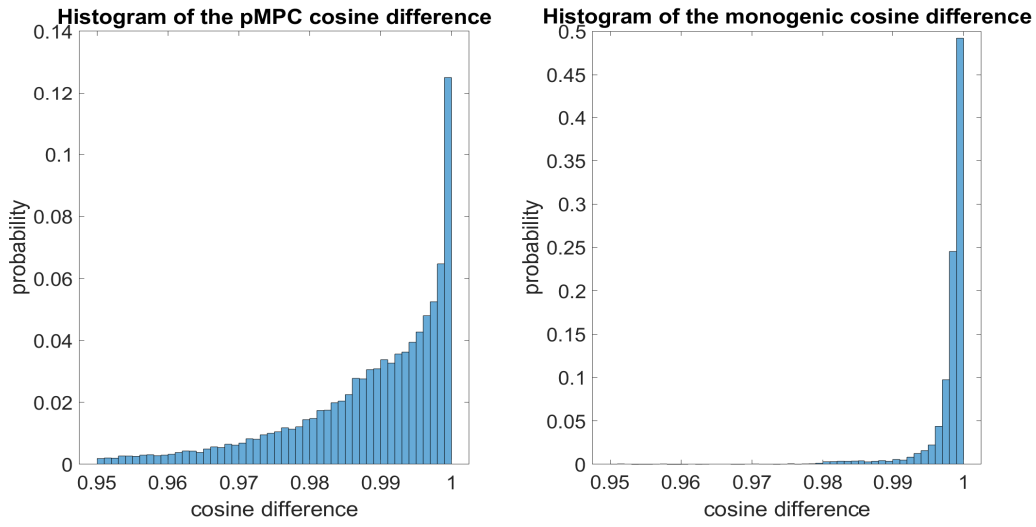

Figure 2.18: Histograms of the pMPC (left) and monogenic (right) cosine differences.

2.6.3 Application to real 2D fringe patterns

The synthetic tests performed in the previous sections highlight the reliability of the monogenic extraction of phase, even in cases where no theoretical support of its reliability can be provided, apart from the condition of slow and smooth variations given in (Larkin et al. 2001, Seelamantula et al. 2012). The monogenic tool is now applied to a real fringe pattern, and its phase estimation is then compared to the one given by the pMPC in (Robin et al. 2005). This time, the comparison can only be qualitative since the expected physical phase is unknown. As can be seen in Figure 2.19, the lower part of the image is well estimated by the monogenic tool while, in the upper part, it struggles with lower

frequencies. The pMPC however works the same way in every part of the image. As seen in Section 2.4.1, the Riesz kernel has a singularity at the null frequency $(0, 0)$, which explains the numerical difficulties in dealing with the low frequency fringes on the upper half of the image. However, Figure 2.20 shows that the monogenic-base phase estimation extracts the finer details of the circular fringes better than the pMPC. This confirms that the monogenic tool can provide a precise estimation of the phase, which is totally in line with the conclusions found in (Larkin et al. 2001, Seelamantula et al. 2012).

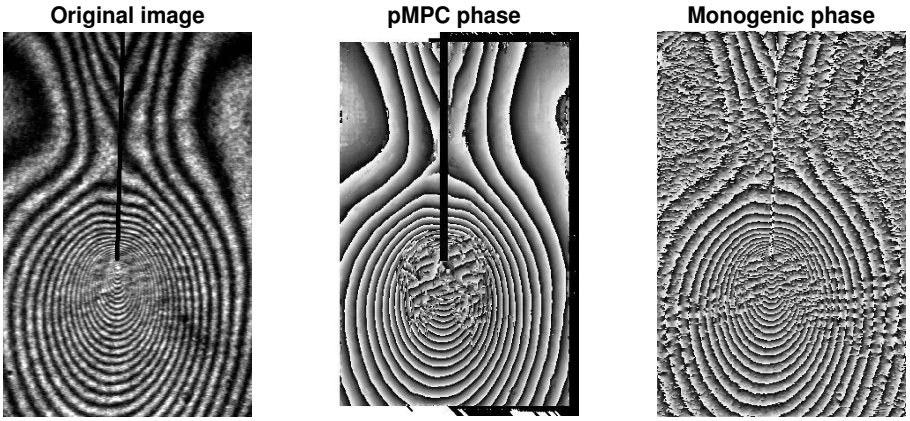

Figure 2.19: Original image (left), pMPC phase (middle) and monogenic phase (right) of a real fringe pattern.

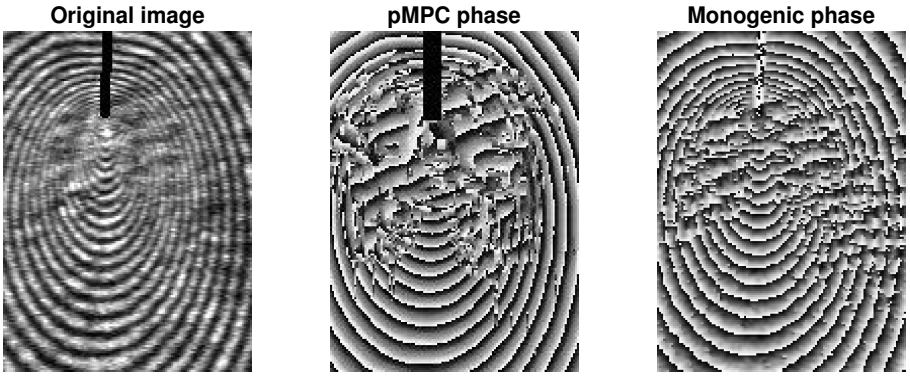

Figure 2.20: Original image (left), pMPC phase (middle) and monogenic phase (right) of a specific area of the fringe pattern.

Figure 2.21 shows the results obtained from another example of real fringe pattern, this time only involving the monogenic tool. Again, the monogenic phase manages to extract the local structure of the fringes, including the finer details at the center of the circle,

though it still struggles in low frequency areas. Given the fact that such circular fringes could be modeled by parabolic chirps, the asymptotic equivalence between the monogenic and physical phase functions proved in Section 2.4.3 provides a theoretical background to the observed quality of the phase extraction of such patterns.

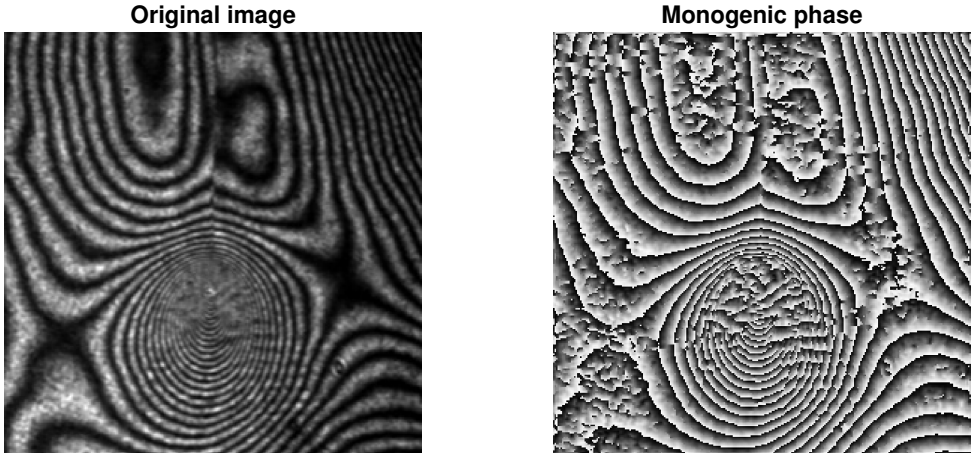

Figure 2.21: Original image (left) and monogenic phase (right) of a real fringe pattern.

Though it is out of the scope of this work, a further step of the phase extraction process consists in unwrapping the values from $[-\pi, \pi]$ to $\mathbb{R}$ (Brémand 1994). Indeed, the phase function measured by the monogenic signal is only known up to a multiple of 2π, while the physical phase of the interferometric fringes has to be fully known to be linked with other physical quantities (Robin et al. 2005). While the unwrapping of 2D angular signals is still an open question, interesting solutions exist in the literature such as (Arevallilo-Herráez, Burton, Lalor & Gdeisat 2002, Zhao, Zhang, Xiao, Du, Zhuang, Fan & Zhao 2018). Now that the reliability of the monogenic-based phase estimation has been established, future works could complete the process by focusing on the unwrapping step.

2.7 Conclusion

As said in the introduction, the main purpose of this chapter is the introduction of relevant tools to characterize the local behavior of textures displaying oscillating patterns, though at this stage no color image is considered. This goal is reached by using the monogenic signal introduced in (Felsberg & Sommer 2001, Larkin et al. 2001). Indeed, even though perfectly identifying the monogenic measures of amplitude, phase and orientation with their physical counterparts is only possible for pure cosine wave, the monogenic tool still manages to extract the local structure of 2D oscillating images, *i.e.*, phase and orientation, outside this ideal case. Though this was already highlighted in (Larkin et al. 2001, Seelamantula et al. 2012, Kaseb et al. 2019), this chapter goes further by providing a formal proof of the asymptotic convergence of the monogenic estimators in the case of a parabolic chirp, hence generalizing the analogous result of the 1D case. Synthetic tests then show how the monogenic phase and orientation get rapidly close to their expected values, which makes the monogenic tool work almost as perfectly as in the case of pure cosine waves outside the areas near the initial pixel. The same numerical results are also observed for the more general anisotropic parabolic chirps, though no theoretical proof has been provided yet.

Though focusing on parabolic chirps may seem limited at first, such circular patterns are frequently encountered in the field of interferometry, as highlighted in Section 2.6 where the monogenic phase estimation is applied to interference fringes. The results obtained by the monogenic tool are substantially better than those obtained with the patch-based pMPC technique, which can be theoretically supported by the asymptotic equivalence between the monogenic and physical phase functions in the case of a parabolic chirp.

Notice that Section 2.5.4 adds anisotropy in the model to cover a wider range of images. In practice, images not only display anisotropy but may also contain stochastic features. 2D signals consisting of a deterministic part (either a cosine wave or a parabolic chirp) and a stochastic variable (a Gaussian noise) were numerically studied in (Kaseb et al. 2019), and it was observed that the variance of the stochastic variable greatly affects the phase estimation. After dealing with purely deterministic oscillating images in this chapter, the next chapter focuses on how the monogenic tool manages to extract the local structure of images containing noise components.

APPENDIX A

Appendices

A.1 Proof of Theorem 1

The proof relies heavily on the analogous result of the 1D case, which is recalled before being generalized to the 2D case. Let $f : \mathbb{R} \to \mathbb{R}$ be a 1D Gaussian function defined for all $t \in \mathbb{R}$ by

$$f(t) = e^{-a^2 t^2}, \tag{A.1}$$

where $a \in \mathbb{R}^*$. The 1D Fourier transform of f is given for all $\xi \in \mathbb{R}$ by

$$\mathcal{F}f(\xi) = \frac{\sqrt{\pi}}{a} e^{-\frac{\xi^2}{4a^2}}. \tag{A.2}$$

This result is now generalized to the case of a 2D Gaussian function g as defined in Eq. (2.35). Let f_1 and f_2 denote the 1D Gaussian functions defined for all $\in \mathbb{R}$ by

$$f_1(t) = e^{-a_1^2 t^2} \quad f_2(t) = e^{-a_2^2 t^2}, \tag{A.3}$$

respectively. Then, using the separability of the function g leads for all $\xi = (\xi_1, \xi_2) \in \mathbb{R}^2$ to

$$\begin{aligned}
\mathcal{F}_2 g(\xi) &= \int_{\mathbb{R}^2} g(\xi) e^{-\mathbf{i}\mathbf{x}^\top \xi} d\mathbf{x}, \\
&= \int_{\mathbb{R}^2} e^{-a_1^2 x_1^2} e^{-a_2^2 x_2^2} e^{-\mathbf{i}x_1\xi_1} e^{-\mathbf{i}x_2\xi_2} dx_1 dx_2, \\
&= \int_{\mathbb{R}} e^{-a_1^2 x_1^2} e^{-\mathbf{i}x_1\xi_1} dx_1 \times \int_{\mathbb{R}} e^{-a_2^2 x_2^2} e^{-\mathbf{i}x_2\xi_2} dx_2, \\
&= \mathcal{F}f_1(\xi_1) \times \mathcal{F}f_2(\xi_2).
\end{aligned} \tag{A.4}$$

Applying the 1D formula to both f_1 and f_2 finally yields for all $\xi = (\xi_1, \xi_2) \in \mathbb{R}^2$,

$$\begin{aligned}
\mathcal{F}_2 g(\xi) &= \frac{\sqrt{\pi}}{a_1} e^{-\frac{\xi^2}{4a_1^2}} \times \frac{\sqrt{\pi}}{a_2} e^{-\frac{\xi^2}{4a_2^2}}, \\
&= \frac{\pi}{a_1 a_2} e^{-\frac{1}{4}\left(\frac{\xi_1^2}{a_1^2} + \frac{\xi_2^2}{a_2^2}\right)}.
\end{aligned} \tag{A.5}$$

A.2 Proof of Theorem 2

Let ϵ be a strictly positive real number and $s_\epsilon : \mathbb{R}^2 \to \mathbb{C}$ the function defined for $\mathbf{x} \in \mathbb{R}^2$ by

$$s_\epsilon(\mathbf{x}) = e^{-(\epsilon + \mathbf{i}a^2)\|\mathbf{x}\|^2}. \tag{A.6}$$

s_ϵ is thus a complex function whose real part is given by

$$\Re s_\epsilon(\mathbf{x}) = e^{-\epsilon\|\mathbf{x}\|^2} \cos\left(a^2 \|\mathbf{x}\|^2\right). \tag{A.7}$$

Hence, for all $\mathbf{x} \in \mathbb{R}^2$,

$$\lim_{\epsilon \to 0} s_\epsilon(\mathbf{x}) = s(\mathbf{x}), \tag{A.8}$$

where s is a parabolic chirp as defined in Eq. (2.48). The Riesz-transform of s can then be calculated as the limit of the real part of the Riesz transform of s_ϵ when ϵ tends to 0, *i.e.*, for $k \in \{1, 2\}$,

$$\mathcal{R}_k s = \lim_{\epsilon \to 0} \Re(\mathcal{R}_k s_\epsilon). \tag{A.9}$$

To apply the Riesz operator to s_ϵ, a switch to the frequency domain must first be performed. Since s_ϵ is a Gaussian function, its 2D Fourier transform can be expressed by using Theorem 1, hence for all $\xi \in \mathbb{R}^2$

$$\mathcal{F}_2 s_\epsilon(\xi) = \frac{\pi}{\alpha_\epsilon} e^{-\frac{||\xi||^2}{4\alpha_\epsilon}}, \tag{A.10}$$

where $\alpha_\epsilon = \epsilon + \mathbf{i}a^2$. Applying the Riesz kernel to the Fourier transform of s_ϵ then leads for all $\xi = (\xi_1, \xi_2) \in \mathbb{R}^2$ to

$$\mathcal{F}_2(\mathcal{R}_k s_\epsilon)(\xi) = -\mathbf{i} \frac{\pi \xi_k}{\alpha_\epsilon ||\xi||} e^{-\frac{||\xi||^2}{4\alpha_\epsilon}}. \tag{A.11}$$

The Riesz transforms of s_ϵ, $\mathcal{R}_k s_\epsilon$ ($k \in \{1, 2\}$), can then be obtained in the space domain by using the inverse Fourier transform, *i.e.*,

$$\begin{aligned} \mathcal{R}_k s_\epsilon(\mathbf{x}) &= \frac{1}{(2\pi)^2} \int_{\mathbb{R}^2} \mathcal{F}_2(\mathcal{R}_k s_\epsilon)(\xi) e^{\mathbf{i}\mathbf{x}^\top \xi} d\xi \\ &= -\frac{1}{(2\pi)^2} \int_{\mathbb{R}^2} \mathbf{i} \frac{\pi \xi_k}{\alpha_\epsilon ||\xi||} e^{-\frac{||\xi||^2}{4\alpha_\epsilon}} e^{\mathbf{i}\mathbf{x}^\top \xi} d\xi \\ &= -\frac{\mathbf{i}}{4\pi\alpha_\epsilon} \int_{\mathbb{R}^2} \frac{\xi_k}{||\xi||} e^{-\frac{||\xi||^2}{4\alpha_\epsilon}} e^{\mathbf{i}\mathbf{x}^\top \xi} d\xi. \end{aligned} \tag{A.12}$$

By switching to the polar coordinates $\xi = r\Theta$, with $r \in]-\infty, +\infty[$ and $\Theta = (\Theta_1, \Theta_2) \in \mathbb{S}^1_+$, the Riesz transforms become

$$\begin{aligned} \mathcal{R}_k s_\epsilon(\mathbf{x}) &= -\frac{\mathbf{i}}{4\pi\alpha_\epsilon} \int_{\mathbb{S}^1_+} \int_{-\infty}^{+\infty} \Theta_k r e^{-\frac{r^2}{4\alpha_\epsilon}} e^{\mathbf{i}r\mathbf{x}^\top \Theta} dr d\Theta \\ &= -\frac{\mathbf{i}}{4\pi\alpha_\epsilon} \int_{\mathbb{S}^1_+} \Theta_k \left[\int_{-\infty}^{+\infty} r e^{-\frac{r^2}{4\alpha_\epsilon}} e^{\mathbf{i}r\mathbf{x}^\top \Theta} dr \right] d\Theta. \end{aligned} \tag{A.13}$$

By integrating by parts, the expression inside the square brackets becomes

$$\int_{-\infty}^{+\infty} re^{-\frac{r^2}{4\alpha_\epsilon}} e^{\mathbf{i}r\mathbf{x}^\top\Theta} dr = \left[-2\alpha_\epsilon e^{-\frac{r^2}{4\alpha_\epsilon}} e^{\mathbf{i}r\mathbf{x}^\top\Theta}\right]_{-\infty}^{+\infty} + 2\alpha_\epsilon \mathbf{i}\mathbf{x}^\top\Theta \int_{-\infty}^{+\infty} e^{-\frac{r^2}{4\alpha_\epsilon}} e^{\mathbf{i}r\mathbf{x}^\top\Theta} dr. \quad \text{(A.14)}$$

Because

$$\lim_{|r|\to+\infty} |-2\alpha_\epsilon e^{-\frac{r^2}{4\alpha_\epsilon}} e^{\mathbf{i}r\mathbf{x}^\top\Theta}| = \lim_{|r|\to+\infty} 2|\alpha_\epsilon| e^{-\frac{r^2}{4\alpha_\epsilon}} = 0, \quad \text{(A.15)}$$

the term $[-2\alpha_\epsilon e^{-\frac{r^2}{4\alpha_\epsilon}} e^{\mathbf{i}r\mathbf{x}^\top\Theta}]_{-\infty}^{+\infty}$ is equal to 0, hence

$$\int_{-\infty}^{+\infty} re^{-\frac{r^2}{4\alpha_\epsilon}} e^{\mathbf{i}r\mathbf{x}^\top\Theta} dr = 2\alpha_\epsilon \mathbf{i}\mathbf{x}^\top\Theta \int_{-\infty}^{+\infty} e^{-\frac{r^2}{4\alpha_\epsilon}} e^{\mathbf{i}r\mathbf{x}^\top\Theta} dr. \quad \text{(A.16)}$$

This integral can then be calculated by using the characteristic function of a Gaussian random variable X with mean $\mu = 0$ and variance $\sigma^2 = 2\alpha_\epsilon$. If M_R denotes this function, then for all $t \in \mathbb{R}$,

$$\begin{aligned} M_X(t) &= \mathbb{E}[e^{\mathbf{i}tX}] \\ &= \frac{1}{\sqrt{2\pi\sigma^2}} \int_{-\infty}^{+\infty} e^{-\frac{(x-\mu)^2}{2\sigma^2}} e^{\mathbf{i}tx} dx \\ &= e^{\mu\mathbf{i}t - \frac{\sigma^2 t^2}{2}}, \end{aligned} \quad \text{(A.17)}$$

by using the expression of the 1D Fourier transform of a Gaussian function recalled in Eq. A.2. In particular, if $\mu = 0$, $\sigma^2 = 2\alpha_\epsilon$ and $t = \mathbf{x}^\top\Theta$, Eq. (A.17) becomes

$$\frac{1}{\sqrt{4\pi\alpha_\epsilon}} \int_{-\infty}^{+\infty} e^{-\frac{r^2}{4\alpha_\epsilon}} e^{\mathbf{i}\mathbf{x}^\top\Theta r} dr = e^{-\alpha_\epsilon(\mathbf{x}^\top\Theta)^2}. \quad \text{(A.18)}$$

Injecting this expression to Eq. (A.16) then leads to

$$\int_{-\infty}^{+\infty} re^{-\frac{r^2}{4\alpha_\epsilon}} e^{\mathbf{i}r\mathbf{x}^\top\Theta} dr = 4(\alpha_\epsilon)^{\frac{3}{2}} \sqrt{\pi} \mathbf{i}\mathbf{x}^\top\Theta e^{-\alpha_\epsilon(\mathbf{x}^\top\Theta)^2}. \quad \text{(A.19)}$$

Finally, combining Eq. (A.13) and (A.19) gives

$$\begin{aligned} \mathcal{R}_k s_\epsilon(\mathbf{x}) &= -\frac{\mathbf{i}}{4\pi\alpha_\epsilon} \int_{\mathbb{S}^1_+} \Theta_k \left[4(\alpha_\epsilon)^{\frac{3}{2}} \sqrt{\pi} \mathbf{i}\mathbf{x}^\top\Theta e^{-\alpha_\epsilon(\mathbf{x}^\top\Theta)^2}\right] d\Theta \\ &= \sqrt{\frac{\alpha_\epsilon}{\pi}} \int_{\mathbb{S}^1_+} \Theta_k \mathbf{x}^\top\Theta e^{-\alpha_\epsilon(\mathbf{x}^\top\Theta)^2} d\Theta. \end{aligned} \quad \text{(A.20)}$$

If θ and $\theta_{\mathbf{x}}$ denote the arguments of Θ and $\mathbf{x}$, respectively, then $\mathbf{x}^\top\Theta$ can be expressed with θ and $\theta_{\mathbf{x}}$, *i.e.*,

$$\begin{aligned} \mathbf{x}^\top\Theta &= \|\mathbf{x}\| (\cos\theta \cos\theta_{\mathbf{x}} + \sin\theta \sin\theta_{\mathbf{x}}) \\ &= \|\mathbf{x}\| \cos(\theta - \theta_{\mathbf{x}}) \end{aligned}. \quad \text{(A.21)}$$

Eq. (A.20) then becomes

$$\left\{\begin{array}{ll}\mathcal{R}_1 s_\epsilon(\mathbf{x}) & = \sqrt{\frac{\alpha_\epsilon}{\pi}}\,\|\mathbf{x}\| \int_0^\pi \cos\theta\cos(\theta-\theta_{\mathbf{x}}) e^{-\alpha_\epsilon\|\mathbf{x}\|^2\cos^2(\theta-\theta_{\mathbf{x}})}d\theta,\\ \mathcal{R}_2 s_\epsilon(\mathbf{x}) & = \sqrt{\frac{\alpha_\epsilon}{\pi}}\,\|\mathbf{x}\| \int_0^\pi \sin\theta\cos(\theta-\theta_{\mathbf{x}}) e^{-\alpha_\epsilon\|\mathbf{x}\|^2\cos^2(\theta-\theta_{\mathbf{x}})}d\theta.\end{array}\right. \tag{A.22}$$

The calculation of $\mathcal{R}_1 s_\epsilon(\mathbf{x})$ and $\mathcal{R}_2 s_\epsilon(\mathbf{x})$ are based on the same ideas. In the following lines, only the calculation of $\mathcal{R}_1 s_\epsilon(\mathbf{x})$ is detailed. Using the substitution $u = \theta - \theta_{\mathbf{x}}$ leads to

$$\mathcal{R}_1 s_\epsilon(\mathbf{x}) = \sqrt{\frac{\alpha_\epsilon}{\pi}}\,\|\mathbf{x}\| \int_{-\theta_{\mathbf{x}}}^{\pi+\theta_{\mathbf{x}}} \cos(\theta+\theta_{\mathbf{x}})\cos\theta e^{-\alpha_\epsilon\|\mathbf{x}\|^2\cos^2\theta}d\theta. \tag{A.23}$$

Notice that the integrated function is π-periodic, which implies that the bounds can be brought back to $[0,\pi]$, hence

$$\mathcal{R}_1 s_\epsilon(\mathbf{x}) = \sqrt{\frac{\alpha_\epsilon}{\pi}}\,\|\mathbf{x}\| \int_{0}^{\pi} \cos(\theta+\theta_{\mathbf{x}})\cos\theta e^{-\alpha_\epsilon\|\mathbf{x}\|^2\cos^2\theta}d\theta. \tag{A.24}$$

Using the π-periodicity again then gives

$$\mathcal{R}_1 s_\epsilon(\mathbf{x}) = \sqrt{\frac{\alpha_\epsilon}{\pi}}\frac{\|\mathbf{x}\|}{2} \int_{-\pi}^{\pi} \cos(\theta+\theta_{\mathbf{x}})\cos\theta e^{-\alpha_\epsilon\|\mathbf{x}\|^2\cos^2\theta}d\theta. \tag{A.25}$$

$\cos(\theta+\theta_{\mathbf{x}})$ can then be developed, hence

$$\mathcal{R}_1 s_\epsilon(\mathbf{x}) = \sqrt{\frac{\alpha_\epsilon}{\pi}}\frac{\|\mathbf{x}\|}{2} \int_{-\pi}^{\pi} (\cos\theta\cos\theta_{\mathbf{x}} - \sin\theta\sin\theta_{\mathbf{x}})\cos\theta e^{-\alpha_\epsilon\|\mathbf{x}\|^2\cos^2\theta}d\theta. \tag{A.26}$$

Because $\theta \mapsto \sin\theta\cos\theta$ is an odd function, Eq. (A.26) becomes

$$\mathcal{R}_1 s_\epsilon(\mathbf{x}) = \sqrt{\frac{\alpha_\epsilon}{\pi}}\frac{\|\mathbf{x}\|}{2}\cos\theta_{\mathbf{x}} \int_{-\pi}^{\pi} \cos^2\theta e^{-\alpha_\epsilon\|\mathbf{x}\|^2\cos^2\theta}d\theta. \tag{A.27}$$

This time the integrated functions are even, which leads to

$$\mathcal{R}_1 s_\epsilon(\mathbf{x}) = \sqrt{\frac{\alpha_\epsilon}{\pi}}\,\|\mathbf{x}\|\cos\theta_{\mathbf{x}} \int_{0}^{\pi} \cos^2\theta e^{-\alpha_\epsilon\|\mathbf{x}\|^2\cos^2\theta}d\theta. \tag{A.28}$$

The square cosine $\cos^2\theta$ can be linearised as $\frac{1+\cos 2\theta}{2}$, hence (after a substitution $u = 2\theta$)

$$\mathcal{R}_1 s_\epsilon(\mathbf{x}) = \sqrt{\frac{\alpha_\epsilon}{\pi}}\frac{\|\mathbf{x}\|}{4}\cos\theta_{\mathbf{x}} e^{-\frac{\alpha_\epsilon\|\mathbf{x}\|^2}{2}} \int_{0}^{2\pi} (1+\cos\theta) e^{-\frac{\alpha_\epsilon\|\mathbf{x}\|^2}{2}\cos\theta}d\theta. \tag{A.29}$$

$e^{-\frac{\alpha_\epsilon\|\mathbf{x}\|^2}{2}\cos\theta}$ can then be developed by using the Jacobi-Anger expansion, *i.e.*, for all $z \in \mathbb{C}$ and $\theta \in \mathbb{R}$

$$e^{\mathbf{i}z\cos\theta} = \sum_{n\in\mathbb{Z}} \mathbf{i}^n J_n(z) e^{\mathbf{i}n\theta}, \tag{A.30}$$

where J_n denotes the Bessel functions defined in Eq. (2.51). Applying Eq. (A.30) with $z = \mathbf{i}\frac{\alpha_\epsilon\|\mathbf{x}\|^2}{2}$ and injecting it in Eq. (A.29) leads to

$$\mathcal{R}_1 s_\epsilon(\mathbf{x}) = \sqrt{\frac{\alpha_\epsilon}{\pi}}\frac{\|\mathbf{x}\|}{4}\cos\theta_{\mathbf{x}} e^{-\frac{\alpha_\epsilon\|\mathbf{x}\|^2}{2}} \times \sum_{n\in\mathbb{Z}} \mathbf{i}^n J_n\left(\mathbf{i}\frac{\alpha_\epsilon\,\|\mathbf{x}\|^2}{2}\right) \int_{0}^{2\pi} (1+\cos\theta) e^{-\mathbf{i}n\theta}d\theta. \tag{A.31}$$

After using the substitution $u = -\theta$ and then the 2π-periodicity to switch the interval from $[-2\pi, 0]$ to $[0, 2\pi]$, Eq. (A.31) becomes

$$\mathcal{R}_1 s_\epsilon(\mathbf{x}) = \sqrt{\frac{\alpha_\epsilon}{\pi}} \frac{\|\mathbf{x}\|}{4} \cos\theta_{\mathbf{x}} e^{-\frac{\alpha_\epsilon \|\mathbf{x}\|^2}{2}} \sum_{n\in\mathbb{Z}} \mathbf{i}^n J_n\left(\mathbf{i}\frac{\alpha_\epsilon \|\mathbf{x}\|^2}{2}\right) \int_0^{2\pi} (1+\cos\theta) e^{\mathbf{i}n\theta} d\theta. \quad \text{(A.32)}$$

By using Euler's formula, the integral can be expressed as

$$\begin{aligned} \int_0^{2\pi} (1+\cos\theta) e^{\mathbf{i}n\theta} d\theta &= \int_0^{2\pi} \left(1 + \frac{e^{\mathbf{i}\theta} + e^{-\mathbf{i}\theta}}{2}\right) e^{\mathbf{i}n\theta} d\theta \\ &= \int_0^{2\pi} e^{\mathbf{i}n\theta} d\theta + \frac{1}{2}\left[\int_0^{2\pi} e^{\mathbf{i}(n+1)\theta} d\theta + \int_0^{2\pi} e^{\mathbf{i}(n-1)\theta} d\theta\right] \\ &= 2\pi(\delta_{0,n} + \frac{1}{2}\delta_{1,n} + \frac{1}{2}\delta_{-1,n}), \end{aligned} \quad \text{(A.33)}$$

with $\delta_{k,n} = 0$ if $n \neq k$ and $\delta_{k,n} = 1$ if $n = k$, $k \in \{-1, 0, 1\}$. Therefore, all the terms of the sum in Eq. (A.32) are zero except for $n = 0$, $n = 1$ and $n = -1$. Using the equality $J_{-1} = -J_1$ finally leads to

$$\mathcal{R}_1 s_\epsilon(\mathbf{x}) = \sqrt{\alpha_\epsilon \pi} \frac{\|\mathbf{x}\|}{2} \cos\theta_{\mathbf{x}} e^{-\frac{\alpha_\epsilon \|\mathbf{x}\|^2}{2}} \left[J_0\left(\mathbf{i}\frac{\alpha_\epsilon \|\mathbf{x}\|^2}{2}\right) + \mathbf{i} J_1\left(\mathbf{i}\frac{\alpha_\epsilon \|\mathbf{x}\|^2}{2}\right)\right]. \quad \text{(A.34)}$$

If $\epsilon \to 0$, then $\alpha_\epsilon \to \mathbf{i}a^2$ and $\sqrt{\alpha_\epsilon} \to e^{\mathbf{i}\frac{\pi}{4}} a$, hence

$$\mathcal{R}_1 s(\mathbf{x}) = \Re\left\{ a\sqrt{\pi} \frac{\|\mathbf{x}\|}{2} \cos\theta_{\mathbf{x}} e^{\mathbf{i}\left(\frac{\pi}{4} - \frac{a^2\|\mathbf{x}\|^2}{2}\right)} \left[J_0\left(-\frac{a^2 \|\mathbf{x}\|^2}{2}\right) + \mathbf{i} J_1\left(-\frac{a^2 \|\mathbf{x}\|^2}{2}\right)\right]\right\}. \quad \text{(A.35)}$$

Using the equality $J_n(-x) = (-1)^n J_n(x)$ leads to

$$\mathcal{R}_1 s(\mathbf{x}) = \Re\left\{ a\sqrt{\pi} \frac{\|\mathbf{x}\|}{2} \cos\theta_{\mathbf{x}} e^{\mathbf{i}\left(\frac{\pi}{4} - \frac{a^2\|\mathbf{x}\|^2}{2}\right)} \left[J_0\left(\frac{a^2 \|\mathbf{x}\|^2}{2}\right) - \mathbf{i} J_1\left(\frac{a^2 \|\mathbf{x}\|^2}{2}\right)\right]\right\}. \quad \text{(A.36)}$$

Taking the real part of the expression inside the braces finally gives

$$\begin{aligned} \mathcal{R}_1 s(\mathbf{x}) = a\sqrt{\pi} \frac{\|\mathbf{x}\|}{2} \cos\theta_{\mathbf{x}} \Bigg[& J_0\left(\frac{a^2 \|\mathbf{x}\|^2}{2}\right) \cos\left(\frac{\pi}{4} - \frac{a^2 \|\mathbf{x}\|^2}{2}\right) \\ & + J_1\left(\frac{a^2 \|\mathbf{x}\|^2}{2}\right) \sin\left(\frac{\pi}{4} - \frac{a^2 \|\mathbf{x}\|^2}{2}\right)\Bigg]. \end{aligned} \quad \text{(A.37)}$$

Applying the same operations to $\mathcal{R}_2 s_\epsilon(\mathbf{x})$ also leads to

$$\begin{aligned} \mathcal{R}_2 s(\mathbf{x}) = a\sqrt{\pi} \frac{\|\mathbf{x}\|}{2} \sin\theta_{\mathbf{x}} \Bigg[& J_0\left(\frac{a^2 \|\mathbf{x}\|^2}{2}\right) \cos\left(\frac{\pi}{4} - \frac{a^2 \|\mathbf{x}\|^2}{2}\right) \\ & + J_1\left(\frac{a^2 \|\mathbf{x}\|^2}{2}\right) \sin\left(\frac{\pi}{4} - \frac{a^2 \|\mathbf{x}\|^2}{2}\right)\Bigg]. \end{aligned} \quad \text{(A.38)}$$

CHAPTER 3

Monogenic-based structure extraction of a Gabor noise

Chapter 2 shows how the monogenic tool manages to extract the local phase, *i.e.*, the local structure of oscillating textures, with theoretical guarantees in the case of regular textures. It is worth noting that when applied to real fringe patterns displaying noise, the monogenic tool still works well, though no formal study of how it handles stochastic textures is performed in Chapter 2. This is precisely the subject of this chapter.

According to the authors' knowledge, few works focus on the application of the Riesz operator to stochastic textures in the literature. In (Olhede, Ramirez & Schreier 2014), the covariance matrix of the Riesz transform is used as a structure tensor, and yields a measure of global anisotropy, *i.e.*, the existence of a preferred direction of variation. In (Polisano 2017), the Riesz transform also provides a measure of local anisotropy for Gaussian random fields. However, these works do not tackle the phase estimation issue and focus mainly on orientation. This chapter aims at going further by studying the monogenic extraction of both phase and orientation within a stochastic texture framework. This is motivated by the fact that, in practice, real textures usually display stochastic features, unlike the purely deterministic waves studied in Chapter 2. This step is crucial before tackling color textures in Chapter 4.

Before dealing with real images, the monogenic signal is first applied to random fields to determine the robustness of its measures. Because the monogenic representation of images aims at describing local oscillating behaviors (Felsberg & Sommer 2001), this requires the use of a proper random texture model that is well-suited to design realistic oscillating images. Introduced in (Lewis 1989), sparse convolution noises enable the generation of random textures with prescribed frequency content, which makes them particularly suitable for the monogenic framework. This parallels the sparse representations mentioned in Chapter 1, as sparsity enables the generation of precise texture properties with a limited number of parameters (Lagae et al. 2009). The subclass of Gabor noises, introduced in (Lagae et al. 2009), provides an even more accurate control on the frequency content of the synthesized image (Gilet et al. 2014), and is hence widely used in the field of texture synthesis (Galerne et al. 2012). Another notable work in the field of oscillating stochastic texture synthesis is the recent introduction of the phasor noise in (Tricard et al. 2019), which improves the Gabor noise by removing its local losses of contrast without impacting the control over its frequency content. The proper definition of amplitude and phase provided by (Tricard et al. 2019) is also of great interest when studying how the monogenic signal estimates such functions. Consequently, this chapter aims at showing how the monogenic signal is still able to extract the structure and the orientation in the case of such

procedural noises. By doing so, theoretical guarantees can be established before applying the monogenic signal to real textures.

After some crucial properties of sparse convolution noises are recalled in Section 3.1, the Gabor noise and its statistical features are studied in Section 3.2. Section 3.3 then focuses on the estimation of the local phase of a Gabor noise provided by the monogenic signal, while Section 3.4 uses the monogenic-based stochastic structure tensor introduced in (Olhede et al. 2014) to measure the directionality of the noise. Section 3.5 finally applies these tools to real textures displaying both oscillating and noisy features.

3.1 Sparse convolution noise

3.1.1 Poisson point process and sparse convolution noise with general kernel

Before focusing on the Gabor noise specifically, this section gives some basic results about general sparse convolution noises. These results are useful for the further developments involving the monogenic signal and Gabor noises. The key idea of sparse convolution noises is to combine a kernel function that contains the frequency information and overall aspect of the texture with a random process that adds stochastic variation (Lagae et al. 2009). Following the works of (Lagae et al. 2009, Lagae & Drettakis 2011, Galerne et al. 2012, Gilet et al. 2014, Tricard et al. 2019) on procedural noises, this study focuses on homogenous Poisson point processes, whose definition is recalled here. Let $(\mathbf{x}_i)_i$ be a realization of a homogeneous Poisson point process with intensity $\mu \in \mathbb{R}_+^*$ (Chiu, Stoyan, Kendall & Mecke 2013), *i.e.*,

- $\forall A \subset \mathbb{R}^2$, if $N(A)$ denotes the number of points contained in A, *i.e.*, $N(A) = \#\{i|\mathbf{x}_i \in A\}$, then $N(A) \sim \mathcal{P}(\mu|A|)$, where $\mathcal{P}$ denotes the Poisson distribution and $|.|$ denotes the Lebesgue measure in $\mathbb{R}^2$,
- if $A \cap B = \emptyset$, then $N(A)$ and $N(B)$ are independent random variables.

The first condition implies that increasing the size of the area A increases the probability of meeting points of the process inside A, while the second condition ensures that the occurrence of points in two disjunct areas is independent. For any $\mathbf{y} \in \mathbb{R}^2$, let $\delta_{\mathbf{y}}$ denote the function defined for all $\mathbf{x} \in \mathbb{R}^2$ as

$$\begin{cases} \delta_{\mathbf{y}}(\mathbf{x}) = 0 & \text{if } \mathbf{x} \neq \mathbf{y}, \\ \delta_{\mathbf{y}}(\mathbf{x}) = 1 & \text{if } \mathbf{x} = \mathbf{y}. \end{cases} \tag{3.1}$$

Then, for all kernel function $g \in L^1(\mathbb{R}^2)$, the sparse convolution noise s is defined for all $\mathbf{x} \in \mathbb{R}^2$ by

$$s(\mathbf{x}) = \sum_i g(\mathbf{x} - \mathbf{x}_i) = g * \Phi(\mathbf{x}), \tag{3.2}$$

where $\Phi = \sum_i \delta_{\mathbf{x}_i}$ (Lagae et al. 2009). In practice, the kernel g is usually chosen such that its support is compact (Lagae et al. 2009). Under this assumption, the points of the process located far from the considered pixel have a negligible contribution to its value, which ensures that the sum in Eq. (3.2) only contains a small amount of significant terms. This is exactly why this class of procedural noises are called sparse convolution noises (Lagae et al. 2009). Figure 3.1 illustrates the way these noises are generated. At each

pixel $\mathbf{x} \in \mathbb{R}^2$ (in blue), the contributions of the points of the Poisson process $\mathbf{x}_i$ (in red) are summed, the closest points having the most significant contribution as illustrated by the varying thickness of the red arrows. The sparseness of the convolution depends on the value of the intensity parameter μ, as well as the decreasing speed of g towards 0 when $\|\mathbf{x}\|$ tends towards $+\infty$.

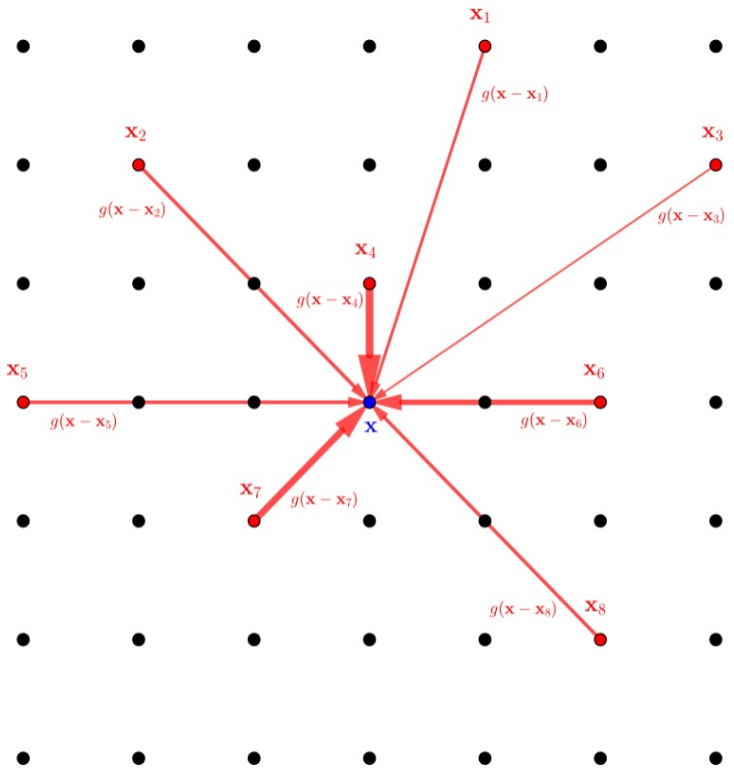

Figure 3.1: Illustration of the sparse convolution.

3.1.2 Second-order statistics

A first approach to study the behavior of the sparse convolution noise s is to express its mean and variance. As said in Section 3.1.1, the frequency content of the synthesized noise, and consequently its power spectrum (Lagae et al. 2009), is prescribed by the kernel g. Given the direct link between the power spectrum and the second order statistics (Jahne 2004), it is not surprising that the mean and variance of the noise s can be linked to g. The result given in Proposition 3.1 of (Galerne 2010) is recalled here with adjusted notations and, for the moment, a restriction to a standard Poisson process. The case of a marked Poisson process as studied in (Galerne 2010) is tackled in Section 3.1.3.

Theorem 3. *If s is a sparse convolution noise as defined in Eq. (3.2), then for all $\mathbf{x} \in \mathbb{R}^2$,*

- *s is stationary,*
- $\mathbb{E}\left[s(\mathbf{x})\right] = \mu \int_{\mathbb{R}^2} g(\mathbf{y}) d\mathbf{y}$,
- *if $g \in L^2(\mathbb{R}^2)$, then s is a second order process, and* $\mathrm{Var}\left[s(\mathbf{x})\right] = \mu \int_{\mathbb{R}^2} g(\mathbf{y})^2 d\mathbf{y}$.

The proof is given in Appendix B.1. As for the covariance function, the result found in (Galerne 2010) only focuses on the autocovariance of a single sparse convolution noise. The following theorem is a little more general as it expresses the covariance between two sparse convolution noises induced by the same Poisson point process.

Theorem 4. *Let $(\mathbf{x}_i)_i$ be a homogeneous Poisson point process with intensity $\mu > 0$ as defined in Section 3.1.1, g and h two kernel functions of $L^2(\mathbb{R}^2)$. If s^g and s^h denote the sparse convolution noises induced by g and h, respectively, then for all $\mathbf{x} \in \mathbb{R}^2$,*

$$\mathrm{Cov}\left[s^g(\mathbf{x}), s^h(\mathbf{x})\right] = \mu \int_{\mathbb{R}^2} g(\mathbf{y})h(\mathbf{y})d\mathbf{y} \tag{3.3}$$

The proof is given in Appendix B.2. This theorem can then be applied to express the covariance function of a sparse convolution noise.

Corollary 2. *If s is a sparse convolution noise as defined in Eq. (3.2), then the autocovariance function of s, denoted by σ, is given for all $(\mathbf{x}, \mathbf{z}) \in \left(\mathbb{R}^2\right)^2$,*

$$\begin{aligned} \sigma(\mathbf{z}) &= \mathrm{Cov}\left[s(\mathbf{x}), s(\mathbf{x}-\mathbf{z})\right], \\ &= \mathrm{Cov}\left[s(\mathbf{0}), s(\mathbf{z})\right], \\ &= \mu \int_{\mathbb{R}^2} g(\mathbf{y})g(\mathbf{y}-\mathbf{z})d\mathbf{y}. \end{aligned} \tag{3.4}$$

These results illustrate how the kernel function fully controls the second order statistics of the noise up to the intensity parameter μ. As highlighted in (Olhede et al. 2014), the covariance function of a random field not only determines its spectral behavior, but can also be linked to local directionality, *i.e.*, locally, the existence of a preferred direction of variation. Remember that these procedural noises are introduced to study how the monogenic signal extracts there local features. Fully controlling their directional properties is hence of great interest when studying the robustness of the monogenic extraction of orientation in the case of stochastic oscillating textures. This is further studied in Section 3.4.

3.1.3 Zero-mean sparse convolution noise

Because a lot of the fundamental results found in (Olhede et al. 2014) and investigated in the subsequent sections involve zero-mean noises, this section presents some of the techniques given in (Lagae et al. 2009, Lagae & Drettakis 2011, Galerne et al. 2012) to make sparse convolution noises zero-mean. A first approach detailed in (Lagae et al. 2009) is to assign random weights w_i to each point of the Poisson process $\mathbf{x}_i$ such that for all $\mathbf{x} \in \mathbb{R}^2$,

$$s(\mathbf{x}) = \sum_i w_i g(\mathbf{x} - \mathbf{x}_i), \tag{3.5}$$

with the w_i being i.i.d. realizations of a zero-mean random variable W. These weights are also independent from $\mathbf{x}_i$, which ensures that the mean of s is zero. Another approach detailed in (Lagae & Drettakis 2011, Galerne et al. 2012, Gilet et al. 2014) and widely used in the case of Gabor noises is the assignment of independent random phase shifts $(\psi_i)_i$ uniformly drawn in $]-\pi, \pi]$ and independently assigned to each point of the Poisson point process $\mathbf{x}_i$. Considering a kernel function $g : \mathbb{R}^2 \times]-\pi, \pi] \to \mathbb{R}$, the sparse convolution noise can then be defined for all $\mathbf{x} \in \mathbb{R}^2$ as

$$s(\mathbf{x}) = \sum_i g(\mathbf{x} - \mathbf{x}_i, \psi_i). \tag{3.6}$$

The process from which the pair of realizations $(\mathbf{x}_i, \psi_i)$ is drawn is called a marked Poisson process (Galerne 2010). This second approach is particularly well-suited for Gabor noises (Lagae & Drettakis 2011), which explains why it is used in the subsequent developments. The second order statistics given in Section 3.1.2 can then be expressed in this case. Assuming that the kernel g is in $L^2\left(\mathbb{R}^2 \times]-\pi, \pi]\right)$, then for all $(\mathbf{x}, \mathbf{z}) \in \left(\mathbb{R}^2\right)^2$, Proposition 3.1 in (Galerne 2010) states that

- s is stationary,
- $\mathbb{E}\left[s(\mathbf{x})\right] = \frac{\mu}{2\pi} \int_{-\pi}^{\pi} \int_{\mathbb{R}^2} g(\mathbf{y}, \psi) d\mathbf{y} d\psi$,
- $\mathrm{Var}\left[s(\mathbf{x})\right] = \frac{\mu}{2\pi} \int_{-\pi}^{\pi} \int_{\mathbb{R}^2} g(\mathbf{y}, \psi)^2 d\mathbf{y} d\psi$,
- $\mathrm{Cov}\left[s(\mathbf{0}), s(\mathbf{z})\right] = \frac{\mu}{2\pi} \int_{-\pi}^{\pi} \int_{\mathbb{R}^2} g(\mathbf{y}, \psi) g(\mathbf{y} - \mathbf{z}, \psi) d\mathbf{y} d\psi$.

Now that these general statistical results are given, Section 3.2 focuses on the special class of phase-augmented Gabor noises studied in (Lagae et al. 2009, Lagae & Drettakis 2011, Galerne et al. 2012). The motivation behind this choice is that the Gabor model generates noises with clear oscillating patterns, which makes it particularly relevant to formally study the ability of monogenic tool to extract the local features of oscillating stochastic textures. This would not only extend the mathematical background of the monogenic framework, but also provide theoretical guarantees when the monogenic signal is applied to real oscillating textures displaying stochastic features.

3.2 Phase-augmented Gabor noise

3.2.1 Gabor kernel

In (Lagae et al. 2009, Gilet et al. 2014, Tricard et al. 2019), the Gabor kernel, from which the Gabor noise is defined, is given for all $\mathbf{x} \in \mathbb{R}^2$ by

$$\widetilde{g}_{b,\omega,\alpha}(\mathbf{x}, \psi) = e^{-\pi b^2 \|\mathbf{x}\|^2} \cos\left(\omega \mathbf{u}^\top \mathbf{x} + \psi\right), \tag{3.7}$$

where $b \in \mathbb{R}_+^*$, $\omega \in \mathbb{R}_+^*$, $\mathbf{u} = (\cos\alpha, \sin\alpha)^\top$ and $\alpha \in \left]-\frac{\pi}{2}; \frac{\pi}{2}\right]$. However, in this thesis, the Gabor kernel is given for all $(\mathbf{x}, \psi) \in \mathbb{R}^2 \times]-\pi, \pi]$ by

$$g_{b,\omega,\alpha}(\mathbf{x}, \psi) = e^{-\pi b^2 \|\mathbf{x}\|^2} \cos\left(b\omega \mathbf{u}^\top \mathbf{x} + \psi\right), \tag{3.8}$$

In this model, the scale parameter b is explicitly included inside the cosine in order to clearly separate variations in scale and variations in frequency, similarly to how the kernel is parametrized in (Guehl, Allègre, Dischler, Benes & Galin 2020). In order to illustrate the advantages of this approach, let δ denote a strictly positive real number. If the parameter b is multiplied by δ, then for all $\mathbf{x} \in \mathbb{R}^2$,

$$\begin{aligned} &\widetilde{g}_{\delta b,\omega,\alpha}(\mathbf{x}, \psi) = e^{-\pi \delta^2 b^2 \|\mathbf{x}\|^2} \cos\left(\omega \mathbf{u}^\top \mathbf{x} + \psi\right), \\ \iff &\widetilde{g}_{\delta b,\omega,\alpha}(\frac{\mathbf{y}}{\delta}, \psi) = e^{-\pi b^2 \|\mathbf{y}\|^2} \cos\left(\frac{\omega}{\delta} \mathbf{u}^\top \mathbf{y} + \psi\right), \end{aligned} \tag{3.9}$$

where $\mathbf{y} = \delta\mathbf{x}$. This means that increasing b is equivalent to decreasing the frequency ω and the scale of the image, respectively. However, for all $\mathbf{x} \in \mathbb{R}^2$,

$$\begin{aligned} g_{\delta b,\omega,\alpha}(\mathbf{x},\psi) &= e^{-\pi\delta^2 b^2\|\mathbf{x}\|^2}\cos\left(\delta b\omega\mathbf{u}^\top\mathbf{x}+\psi\right), \\ \iff g_{\delta b,\omega,\alpha}(\frac{\mathbf{y}}{\delta},\psi) &= e^{-\pi b^2\|\mathbf{y}\|^2}\cos\left(\omega\mathbf{u}^\top\mathbf{y}+\psi\right). \end{aligned} \tag{3.10}$$

In this case, increasing b only affects the scale, while the frequency of the wave remains unaffected. As shown in Section 3.2.4, this separation between scale and frequency provides a clearer interpretation of the parameters and their respective effects on the visual aspect of the synthesized texture than in the case of the classic Gabor kernel. Notice that the kernel $g_{b,\omega,\alpha}$ here defined lies in $L^2\left(\mathbb{R}^2\right)$, which is a crucial property for the subsequent developments.

3.2.2 Gabor noise

The Gabor kernel $g_{b,\omega,\alpha}$ defined in Eq. (3.8) yields a phase-augmented Gabor noise $s : \mathbb{R}^2 \to \mathbb{R}^3$ defined for all $\mathbf{x} \in \mathbb{R}^2$ as

$$s(\mathbf{x}) = \sum_i a\left(\mathbf{x}-\mathbf{x}_i\right)\cos\left[b\omega\mathbf{u}^\top\left(\mathbf{x}-\mathbf{x}_i\right)+\psi_i\right], \tag{3.11}$$

where,

- $\{(\mathbf{x}_i,\psi_i)\}_i$ is a set of realizations of a marked Poisson point process on $\mathbb{R}^2\times]-\pi,\pi]$ such that,
  - the points $(\mathbf{x}_i)_i$ are generated through a homogeneous Poisson point process on $\mathbb{R}^2$ with intensity $\mu > 0$,
  - the marks $(\psi_i)_i$ are independent random phase-shifts uniformly drawn in $]-\pi,\pi]$ and independently assigned to each point of the Poisson point process $\mathbf{x}_i$,
- $a(\mathbf{x}) = e^{-\pi b^2\|\mathbf{x}\|^2}$, $b \in \mathbb{R}_+^*$, $\mathbf{x} \in \mathbb{R}^2$,
- $\omega \in \mathbb{R}_+^*$, $\mathbf{u} = (\cos\alpha, \sin\alpha)^\top$, $\alpha \in \left]-\frac{\pi}{2};\frac{\pi}{2}\right]$.

Visually, a Gabor noise looks like a set of linear parallel fringes with local perturbations (see the figures in Section 3.2.4). The parameter ω corresponds to the frequency of the fringes, while α corresponds to their orientation and b is a scale parameter. The fact that the three parameters ω, α and b can be directly linked with the visual aspect of the texture is what makes the Gabor noise model so valuable in the field of texture synthesis (Tricard et al. 2019). As said in Section 3.1.3, the random phase-shifts $(\psi_i)_i$ are included in the model to make the Gabor noise s zero-mean, similarly to what is done in (Lagae & Drettakis 2011, Galerne et al. 2012). Notice that, because the Gabor kernel $g_{b,\omega,\alpha}$ is a smooth function of $L^2\left(\mathbb{R}^2\right)$, *i.e.*, the integral of all its differentials are finite, the Gabor noise s is a smooth random field (see Theorem 3 in (Biermé & Desolneux 2020) for further details). This is the subject of Section 3.2.3, which focuses on the second order statistics of the Gabor noise.

3.2.3 Second order statistics of a Gabor noise and interpretation

Theorem 5. *The Gabor noise as defined in Eq.* (3.11) *is stationary, zero-mean, and its covariance function* $\sigma(\mathbf{z}) = \mathrm{Cov}\left[s(0), s(\mathbf{z})\right]$ *is given for all* $\mathbf{z} \in \mathbb{R}^2$ *by*

$$\sigma(\mathbf{z}) = \frac{\mu}{4b^2} \cos\left(b\omega \mathbf{u}^\top \mathbf{z}\right) e^{-\frac{1}{2}\pi b^2 \|z\|^2}. \tag{3.12}$$

The proof is given in Appendix B.3. It is worth noting that the covariance function of the Gabor noise given in Theorem 5 satisfies the following properties,

- $\sigma(\mathbf{0}) = \mathrm{Var}(s) = \frac{\mu}{4b^2}$,
- $\lim_{\|\mathbf{z}\| \to +\infty} \sigma(\mathbf{z}) = 0$.

The first property implies that increasing the parameter μ increases the variance of s. Because μ is the intensity of the Poisson point process, this means that increasing the number of random points occurring in the noise increases its variance. The second property implies that the more distant two points of the noise are, the least correlated they are, which is consistent with the intuition. Notice furthermore that if $\mathbf{x} \in \mathbb{R}^2$, $r \in \mathbb{R}_+^*$, and $\mathcal{C}(\mathbf{x}, r)$ denotes the circle of center $\mathbf{x}$ and radius r, then

$$\begin{aligned} & \mathbf{y}_M = \arg \max_{\mathbf{y} \in \mathcal{C}(\mathbf{x},r)} \sigma(\mathbf{y} - \mathbf{x}), \\ \iff & \mathbf{y}_M \in \left\{ \mathbf{y} \in \mathcal{C}(\mathbf{x}, r) | \mathbf{u}^\top (\mathbf{y} - \mathbf{x}) = 0 \right\}, \\ \iff & \mathbf{y}_M = \mathbf{x} \pm r\mathbf{u}^\perp, \end{aligned} \tag{3.13}$$

where $\mathbf{u}^\perp = \begin{pmatrix} -\sin\alpha & \cos\alpha \end{pmatrix}^\top$. This means that for delays located at the same distance from the pixel $\mathbf{x}$, the maximum of correlation between $s(\mathbf{x})$ and $s(\mathbf{x} + \mathbf{z})$ is reached along the direction orthogonal to $\mathbf{u}$, *i.e.*, along the fringes of the noise. This is consistent with the physical interpretation of α, which is to be understood as the main direction of oscillation of s.

3.2.4 Discretization and synthetic tests

Though the phase-augmented Gabor noise is introduced as a continuous object in the previous sections, it has to be discretized to perform synthetic tests. This section aims at properly presenting the techniques used to generate discrete Gabor noises. Let (t^j, t^k) be a discrete grid, with $(j,k) \in \{0 \dots M-1\} \times \{0 \dots N-1\}$ and $(M,N) \in \mathbb{N}^2$ such that

$$\begin{cases} t^j = \left(j - \frac{M}{2}\right) T_x, \\ t^k = \left(k - \frac{N}{2}\right) T_y, \end{cases} \tag{3.14}$$

where $T_x > 0$ and $T_y > 0$ denote the horizontal and vertical sampling periods, respectively. In order to simulate a Poisson process on this grid, an independent and identically distributed $M \times N$ sampling of a Bernoulli variable of parameter $p \in]0,1[$ is generated for each Gabor noise of the sum. For all $l \in \{1, \dots, n\}$, let $x^{j,k} \in \{0,1\}$ denote the Bernoulli number generated at the pixel (t^j, t^k) (with $(j,k) \in \{0 \dots M-1\} \times \{0 \dots N-1\}$). By doing so, the set of pixels (t^j, t^k) for which $x^{j,k} = 1$ form a sample of a Poisson point process with intensity $\mu = p \times S_d$, where S_d denotes the area of the domain on which the noise is generated. Then, an independent and identically distributed $M \times N$ sampling of a uniform

variable on $]-\pi,\pi]$ is generated at each pixel (t^j,t^k). These numbers correspond to the random phase-shifts ψ_i defined in Section 3.2.2 in the continuous model, and are denoted by $\psi^{j,k}$ for all $(j,k)\in\{0\dots M-1\}\times\{0\dots N-1\}$. Let h denote the complex-valued $M\times N$ discrete signal $(h^{j,k})_{j,k}$ such that for all $(j,k)\in\{0\dots M-1\}\times\{0\dots N-1\}$,

$$h^{j,k}=x^{j,k}e^{\mathbf{i}\left[-b\omega\left(t^j\cos\alpha+t^k\sin\alpha\right)+\psi^{j,k}\right]}, \tag{3.15}$$

where $b\in\mathbb{R}_+^*$, $\omega\in\mathbb{R}_+^*$ and $\alpha\in\left]-\frac{\pi}{2};\frac{\pi}{2}\right]$. The Gabor noise is finally computed as the real part of the complex random field $h*a$, where for all $(j,k)\in\{0\dots M-1\}\times\{0\dots N-1\}$,

$$a^{j,k}=e^{-\pi b^2\left[(t^j)^2+(t^k)^2\right]}. \tag{3.16}$$

This convolution product is performed in the frequency domain by using the 2D discrete Fourier transform. Tables 3.1, 3.2 and 3.3 shows examples of Gabor noises synthesized with this technique for different values of b, ω and α, respectively. The remaining parameters chosen to synthesize the texture are $M=N=1000$, $T_x=T_y=0.002$, $p=0.1$, respectively. Notice that the sampling periods T_x and T_y both satisfies Shannon's boundary, *i.e.*, $\frac{1}{T_x}>2b\omega$ and $\frac{1}{T_y}>2b\omega$.

b	2	3	4	5
Gabor noise	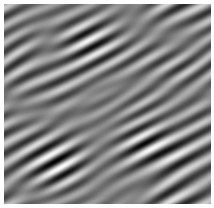	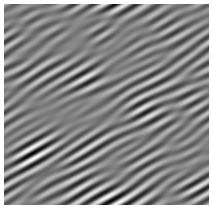	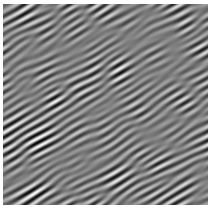	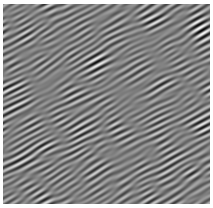

Table 3.1: Influence of the scale b on the visual aspect of the Gabor noise, with $M=N=1000$, $T_x=T_y=0.002$, $p=0.1$, $\omega=20$, $\alpha=\frac{\pi}{6}$.

ω	10	15	20	25
Gabor noise	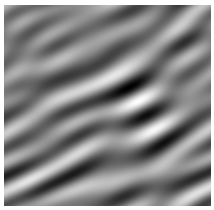	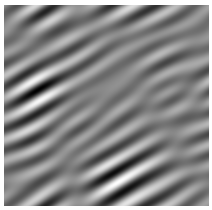	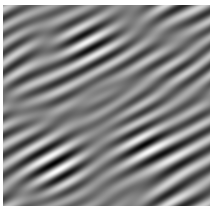	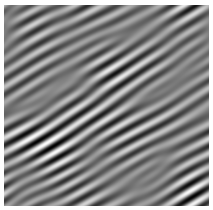

Table 3.2: Influence of the frequency ω on the visual aspect of the Gabor noise, with $M=N=1000$, $T_x=T_y=0.002$, $p=0.1$, $b=2$, $\alpha=\frac{\pi}{6}$.

Unlike what is observed, *e.g.*, in (Tricard et al. 2019), increasing the value of the parameter b only affects the scale, a direct consequence of the modification of the Gabor kernel detailed in Section 3.2.1. As expected, increasing the frequency parameter ω yields faster oscillations, while changing α affects the orientation of the fringes. This illustrates how the parameters of the Gabor kernel can be directly linked with the visual aspect of the noise, which is exactly the reason why it is chosen to generate random oscillating textures in this work. However, notice that slow fringes (small value of ω) at a lower resolution (high value

α	0	$\frac{\pi}{6}$	$\frac{\pi}{3}$	$\frac{\pi}{2}$
Gabor noise	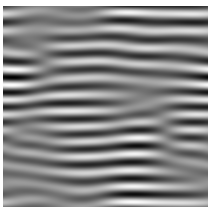	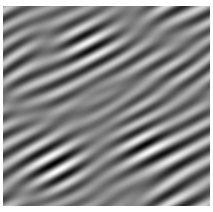	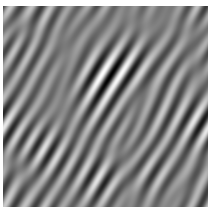	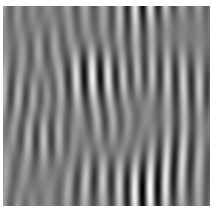

Table 3.3: Influence of the orientation α on the visual aspect of the Gabor noise, with $M = N = 1000$, $T_x = T_y = 0.002$, $p = 0.1$, $b = 2$, $\omega = 20$.

of b) have the same visual aspect as fast fringes (high value of ω) at a higher resolution (low value of b). This suggests that the overall behavior of the fringes is conditioned by the product $b\omega$. The question now is to study how the monogenic signal (introduced in Section 2.4 for deterministic oscillating images) manages to handle such stochastic textures in terms of phase and orientation estimation, which is the subject of the next sections. The theoretical and numerical results established in these sections highlight the key role of the product $b\omega$ already evoked in the previous tests.

3.3 Monogenic-based phase estimation of the Gabor noise

3.3.1 Unified expression of the Gabor noise

Sections 2.4 and 2.5 have highlighted the ability of the monogenic tool to extract the structural information of oscillating textures, modeled by the phase function, even in the case of real fringe patterns displaying noise. However, no formal study of how the Riesz transform deals with stochastic aspects has been performed yet. As said in Section 3.1.3, the Gabor noise provides an interesting point of entry into stochastic textures for the monogenic tool due to its mix of clear oscillating patterns and stochastic perturbations. Before involving the Riesz transform, the Gabor noise is first expressed as a single wave signal rather than a sparse convolution by using the phasor approach introduced in (Tricard et al. 2019). The main goal of doing so is to properly define physical amplitude and phase functions, respectively, and hence fitting the Gabor noise into the monogenic framework presented in Chapter 2. For all $\mathbf{x} \in \mathbb{R}^2$, (Tricard et al. 2019) states that s can be rewritten as

$$s(\mathbf{x}) = I(\mathbf{x}) \cos\left[\varphi(\mathbf{x})\right], \tag{3.17}$$

where

$$\begin{cases} I(\mathbf{x}) = \left| \sum_i a(\mathbf{x} - \mathbf{x}_i) e^{\mathbf{i}\left(-b\omega \mathbf{u}^\top \mathbf{x}_i + \psi_i\right)} \right|, \\ \varphi(\mathbf{x}) = b\omega \mathbf{u}^\top \mathbf{x} + \Psi(\mathbf{x}), \\ \Psi(\mathbf{x}) = \arg\left[\sum_i a(\mathbf{x} - \mathbf{x}_i) e^{\mathbf{i}\left(-b\omega \mathbf{u}^\top \mathbf{x}_i + \psi_i\right)} \right]. \end{cases} \tag{3.18}$$

The noise s can hence be seen as a cosine wave whose amplitude I and phase φ are random fields rather than deterministic functions unlike the deterministic signals studied in Chapter 2. These functions contain the energetic and structural information of the texture, respectively, similarly to the notion of physical amplitude and phase previously discussed.

3.3.2 Riesz transform and monogenic signal of a Gabor noise

Recall that s is centered, thanks to the inclusion of the phase-shift process $(\psi_i)_i$, which implies that each term of the sum is in $L^2(\mathbb{R}^2)$. The Riesz transform of s can then be defined as the sum of the Riesz transforms of each term (see (Kallenberg 2002) for further details). In the purely deterministic case, *i.e.*, $I(\mathbf{x}) = 1$ and $\Psi(\mathbf{x}) = 0$ for all $\mathbf{x} \in \mathbb{R}^2$, respectively, the Riesz transform shifts the cosine function into a sine (Felsberg & Sommer 2001). This result can be generalized to a Gabor noise as follows.

Theorem 6. *Let s be a phase-augmented Gabor noise defined for all $\mathbf{x} \in \Omega \subset \mathbb{R}^2$ as*

$$s(\mathbf{x}) = \sum_i a(\mathbf{x} - \mathbf{x}_i) \cos\left[b\omega \mathbf{u}^\top (\mathbf{x} - \mathbf{x}_i) + \psi_i\right], \tag{3.19}$$

where all the parameters are defined as in Section 3.2.2. If H_s denotes the noise defined for all $\mathbf{x} \in \mathbb{R}^2$ as

$$H_s(\mathbf{x}) = \sum_i a(\mathbf{x} - \mathbf{x}_i) \sin\left[b\omega \mathbf{u}^\top (\mathbf{x} - \mathbf{x}_i) + \psi_i\right], \tag{3.20}$$

there exists a constant $K \in \mathbb{R}_+^*$ such that for all $\mathbf{x} \in \mathbb{R}^2$,

$$\begin{cases} \mathbb{E}\left[|\mathcal{R}_1 s(\mathbf{x}) - \cos\alpha H_s(\mathbf{x})|^2\right] \leq \frac{K}{(b\omega)^2}, \\ \mathbb{E}\left[|\mathcal{R}_2 s(\mathbf{x}) - \sin\alpha H_s(\mathbf{x})|^2\right] \leq \frac{K}{(b\omega)^2}, \end{cases} \tag{3.21}$$

where $\mathbb{E}$ denotes the mean operator.

The proof is given in Appendix B.4. Theorem 6 implies that if the product $b\omega$ is big enough, the cosine is shifted to a sine as in the deterministic case. This condition is fulfilled if low frequency noises are generated with a low resolution (high value of b), or if noises generated with a high resolution (small value of b) have a high frequency. If both b and ω are small, the oscillations are too slow to be visible at a high resolution, which makes the Riesz transform diverge. In the subsequent developments, $b\omega$ is assumed to be big enough to apply Theorem 6. In the case of real textures, this condition implies that the oscillating patterns must be visible enough to be captured by the Riesz transform. Notice that the function H_s can be seen as the Hilbert transform of s directed towards the direction α, which is illustrated by the cosine shifted to a sine. This matches the notion of directional Riesz transform mentioned in (Soulard & Carré 2015). The Riesz transform of the Gabor noise s can then be approximated as

$$\mathcal{R}s(\mathbf{x}) \approx H_s(\mathbf{x}) \begin{pmatrix} \cos\alpha \\ \sin\alpha \end{pmatrix}. \tag{3.22}$$

This yields an approximation of the monogenic signal of s, denoted by M_s, which can be expressed for all $\mathbf{x} \in \mathbb{R}^2$ as

$$M_s(\mathbf{x}) \approx s(\mathbf{x})\mathbf{e}_1 + H_s(\mathbf{x})\mathbf{e}_\alpha, \tag{3.23}$$

with $\mathbf{e}_1 = \begin{pmatrix} 1 & 0 & 0 \end{pmatrix}^\top$ and $\mathbf{e}_\alpha = \begin{pmatrix} 0 & \cos\alpha & \sin\alpha \end{pmatrix}^\top$. Using the isomorphy between $\mathbb{C}$ and the 2D vector space spanned by $\mathbf{e}_1$ and $\mathbf{e}_\alpha$ leads to

$$\begin{aligned} M_s(\mathbf{x}) &\approx s(\mathbf{x}) + \mathbf{i}H_s(\mathbf{x}), \\ &\approx I(\mathbf{x}) e^{\mathbf{i}\left[b\omega \mathbf{u}^\top \mathbf{x} + \Psi(\mathbf{x})\right]}, \end{aligned} \tag{3.24}$$

where I and Ψ denote the unified amplitude and phase-shift functions defined in Eq. (4.39), respectively. It can hence be expected that the monogenic phase $\phi(\mathbf{x})$, defined in Section 2.4.1 as the argument of $M_s(\mathbf{x})$ at each pixel $\mathbf{x} \in \mathbb{R}^2$, is close to the phase function inside the complex exponential, *i.e.*, for all $\mathbf{x} \in \mathbb{R}^2$,

$$\phi(\mathbf{x}) \approx b\omega \mathbf{u}^\top \mathbf{x} + \Psi(\mathbf{x}) \quad [2\pi]. \tag{3.25}$$

3.3.3 Synthetic tests

This section aims at illustrating the previous result with synthetic tests. Let (t^j, t^k) denote the discrete grid introduced in Section 3.2.4, with $(j,k) \in \{0 \dots M-1\} \times \{0 \dots N-1\}$ and $(M,N) \in \mathbb{N}^2$. After the discrete Gabor noise $s = (s_{j,k})_{j,k}$ is generated through the technique described in Section 3.2.4, the Riesz transform is applied to the noise in order to extract its monogenic phase signal $\phi = (\phi_{j,k})_{j,k}$ as done in Section 2.5. Meanwhile, the physical phase signal $\varphi = (\varphi_{j,k})_{j,k}$, *i.e.*, the expected values of local phase, is computed for all $(j,k) \in \{0 \dots M-1\} \times \{0 \dots N-1\}$ as

$$\varphi_{j,k} = b\omega \left(t^j \cos\alpha + t^k \sin\alpha \right) + \Psi_{j,k} \ [2\pi], \tag{3.26}$$

where $\Psi_{j,k}$ denotes the argument of the complex signal $h * a$ defined in Section 3.2.4 at each pixel. Similarly to the deterministic case, both phase signals ϕ and φ are then compared by using the BFR and VAF criteria defined in Section 2.2.2. Figure 3.2 shows the monogenic and physical phases computed from a Gabor noise generated with $M = N = 1000$, $T_x = T_y = 0.002$, $b = 1$, $\omega = 50$, $\alpha = \frac{\pi}{6}$ and $p = 0.1$. Despite the addition of stochastic features in the texture, the results are similar those observed in the case of pure cosine waves in Section 2.5.2. The two phase signals look similar, which is reflected in the values of the similarity criteria, *i.e.*, BFR = 85.67%, VAF = 97.95%. The cosine difference displayed in Figure 3.3 confirms these observations, the values being close to 1 in most areas. Notice that the small black areas where the monogenic and physical phases differ from π correspond to abrupt jumps of phase in the original texture. Such jumps are called singularities in (Tricard et al. 2019) and are further studied in Chapter 5.

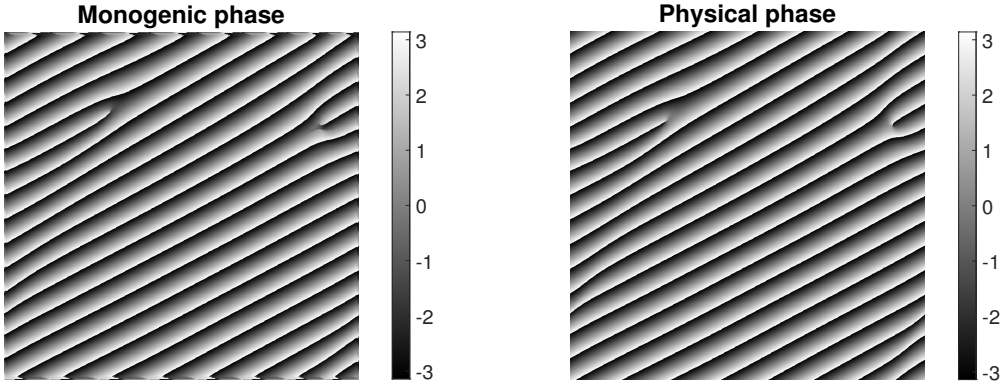

Figure 3.2: Comparison between the monogenic (left) and physical (right) measures of phase in the case of a Gabor noise, $M = N = 1000$, $T_x = T_y = 0.002$, $b = 1$, $\omega = 50$, $\alpha = \frac{\pi}{6}$, $p = 0.1$, BFR = 85.67%, VAF = 97.95%.

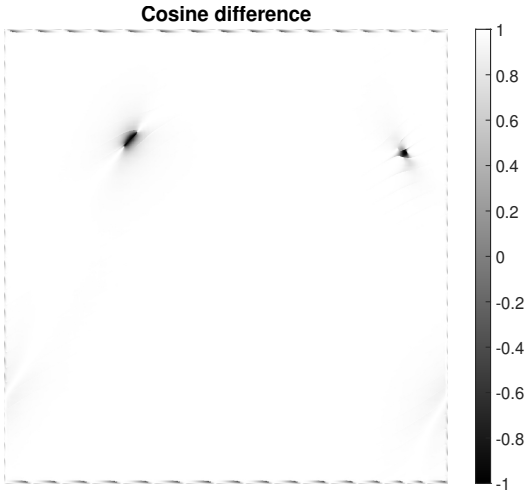

Figure 3.3: Cosine difference between the monogenic and physical measures of phase in the case of a Gabor noise, $M = N = 1000$, $T_x = T_y = 0.002$, $b = 1$, $\omega = 50$, $\alpha = \frac{\pi}{6}$.

As said in Section 3.3.2, the phase extraction provided by the monogenic signal is reliable only in the case where the product $b\omega$ is large enough, a consequence of Theorem 6. It can hence be expected that increasing these parameters increases the quality of the phase estimation, *i.e.*, the values of BFR and VAF between the cosines of the physical and monogenic phases, respectively. Figure 3.4 shows the boxplots of the BFR and VAF criteria calculated for $b \in \{1, \ldots, 5\}$, the other parameters being $M = N = 1000$, $T_x = T_y = 0.002$, $\omega = 30$, $\alpha = \frac{\pi}{6}$ and $p = 0.1$. For each value of b, $n = 50$ Gabor noises are generated. As expected, increasing the scale parameter b implies a reduction of the variances of the similarity criteria, but their respective means remain stable.

Applying the same procedures with $\omega = 10$ confirms that increasing b alone does not impact the means of the similarity criteria, as shown in Figure 3.5. Again, the variances are reduced when b increases, which implies that the phase estimation is more reliable, while the means stagnate at a lower value than in the case of $\omega = 30$.

Figure 3.6 now shows the boxplots of the BFR and VAF criteria calculated for $\omega \in \{10 + 5k, k = 0, \ldots, 4\}$, the other parameters being $M = N = 1000$, $T_x = T_y = 0.002$, $b = 5$, $\alpha = \frac{\pi}{6}$ and $p = 0.1$, with $n = 50$ Gabor noises generated for each value of ω. This time, increasing the frequency parameter ω implies a reduction of both the means and the variances of the similarity criteria. This can be explained by the fact that low frequency images damage both the computation of the Riesz transform and the subsequent monogenic phase extraction.

These tests illustrate how the monogenic extraction of phase remains reliable even when stochastic features come into play, which is consistent with what is observed in the case of real fringe patterns displaying noise in Section 2.6. While the robustness of the Riesz transform in the case of noisy textures is already highlighted by synthetic tests in (Kaseb et al. 2019), Theorem 6 goes further by giving an explicit theoretical argument to support these numerical observations. Additionally, unlike in (Kaseb et al. 2019), the noise signals studied in this section are not mere cosine waves with added random values, but proper

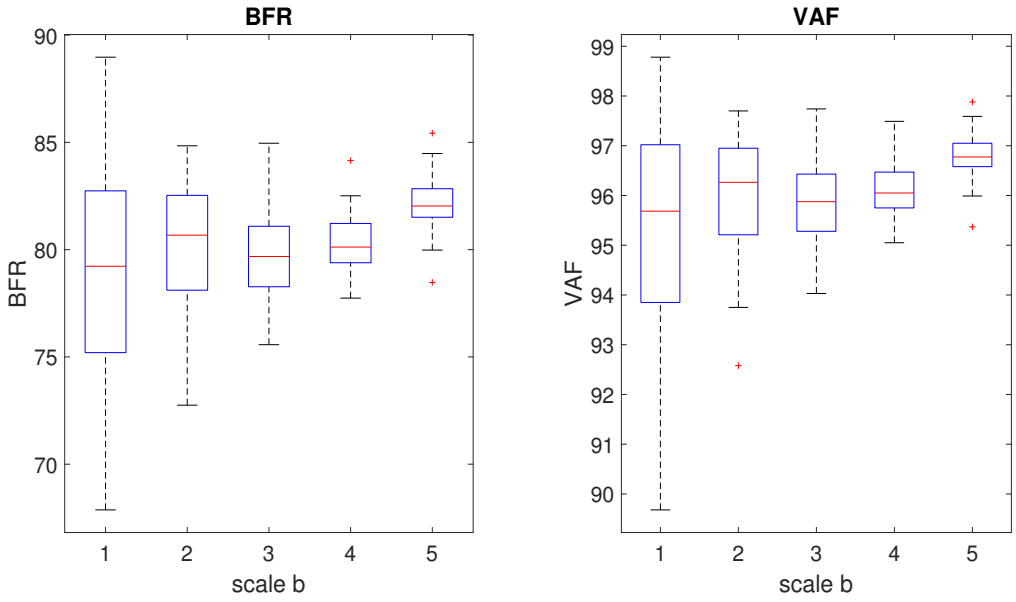

Figure 3.4: Boxplots of the BFR (left) and VAF (right) criteria measured from the cosines of the monogenic and physical phase functions for $n = 50$ Gabor noises, $b \in \{1, \ldots, 5\}$, $M = N = 1000$, $T_x = T_y = 0.002$, $\omega = 30$, $\alpha = \frac{\pi}{6}$, $p = 0.1$.

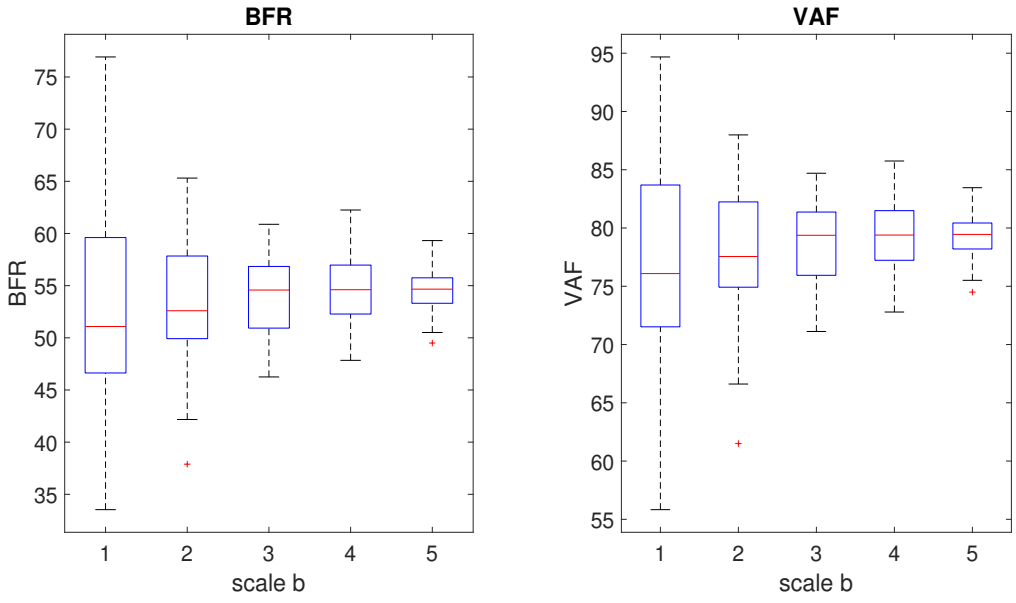

Figure 3.5: Boxplots of the BFR (left) and VAF (right) criteria measured from the cosines of the monogenic and physical phase functions for $n = 50$ Gabor noises, $b \in \{1, \ldots, 5\}$, $M = N = 1000$, $T_x = T_y = 0.002$, $\omega = 10$, $\alpha = \frac{\pi}{6}$, $p = 0.1$.

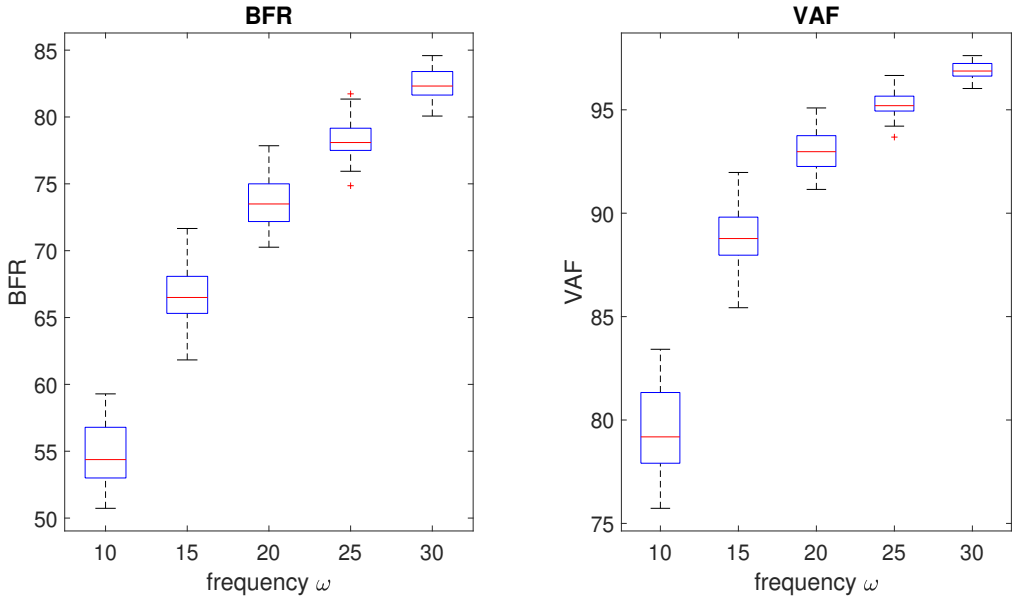

Figure 3.6: Boxplots of the BFR (left) and VAF (right) criteria measured from the cosines of the monogenic and physical phase functions for $n = 50$ Gabor noises, $\omega \in \{10 + 5k, k = 0, \dots, 4\}$, $M = N = 1000$, $T_x = T_y = 0.002$, $b = 5$, $\alpha = \frac{\pi}{6}$, $p = 0.1$.

procedural noises that are widely used in the field of texture synthesis for their ability to generate realistic oscillating textures (Galerne et al. 2012). It can hence be expected that the monogenic measure of phase remains reliable when applied to real textures displaying oscillating patterns. Further developments would then be necessary to characterize the structural information contained in the phase, similarly to what is done for the Fourier phase in (Leclaire & Moisan 2015). While not tackled in this study, this would be an interesting perspective.

As seen in Chapter 2 in the case of deterministic waves, the monogenic signal also provides a measure of orientation. Section 3.4 goes further by studying the monogenic extraction of orientation in the case of random fields.

3.4 Monogenic-based stochastic structure tensor

Detecting the directional structures of an image is of great importance in the field of texture analysis (Polisano 2017, Olhede et al. 2014). The gradient-based structure tensor, though well-suited for deterministic images, is much less reliable when stochastic elements are added to the image (Polisano 2017). Though Sections 2.4 and 2.5 show that the monogenic signal provides a reliable estimation of orientation at each pixel, the resulting orientation signal is of the same size as the original image, which makes it difficult to interpret in terms of global direction of oscillation, especially in the case of stochastic images. The synthetic tests performed in Section 3.2.4 show that Gabor noises display many local perturbations in their orientation, though the global direction of oscillation is still determined by the α parameter. Introduced in (Olhede et al. 2014), the monogenic-based measure of directionality provides an interesting extension of the monogenic estimation of orientation to stochastic stationary images. However, though the use of quaternion algebra offers convenient calculation rules, it obscures the more geometric aspects of the paper. In

this section, a geometrical study of this technique is performed to give it a more intuitive interpretation. The measure of directionality and the global orientation it provides are then applied to the Gabor noise to illustrate its relevance.

3.4.1 Measure of directionality

Because the measure of directionality introduced in (Olhede et al. 2014) is based on a quaternionic approach of the Riesz transform and the monogenic signal, this section makes use of the quaternionic formalism before linking it to more geometric spaces. Let $\mathbf{i}$, $\mathbf{j}$ and $\mathbf{k}$ denote the fundamental quaternion units (Via, Ramirez & Santamaría 2010). If $s : \mathbb{R}^2 \to \mathbb{R}$ is a 2D stochastic process in $L^2(\mathbb{R}^2)$, the quaternionic monogenic signal of s is defined for all $\mathbf{x} \in \mathbb{R}^2$ as

$$M_s(\mathbf{x}) = s(\mathbf{x}) + \mathcal{R}_1 s(\mathbf{x})\mathbf{i} + \mathcal{R}_2 s(\mathbf{x})\mathbf{j} + 0\mathbf{k}, \tag{3.27}$$

where $\mathcal{R}_1$ and $\mathcal{R}_2$ denote the Riesz operators. In the case of a phase-augmented Gabor noise, applying the approximation of the monogenic signal given in Section 3.3.2 leads for all $\mathbf{x} \in \mathbb{R}^2$ to

$$\begin{aligned} M_s(\mathbf{x}) &\approx \sum_i a(\mathbf{x}-\mathbf{x}_i)\cos\left[b\omega\mathbf{u}^\top(\mathbf{x}-\mathbf{x}_i)+\psi_i\right] \\ &\quad + [\cos(\alpha)\mathbf{i}+\sin(\alpha)\mathbf{j}]\sum_i a(\mathbf{x}-\mathbf{x}_i)\sin\left[b\omega\mathbf{u}^\top(\mathbf{x}-\mathbf{x}_i)+\psi_i\right], \\ &\approx s(\mathbf{x}) + \mathbf{u}_\alpha H_s(\mathbf{x}), \end{aligned} \tag{3.28}$$

where $\mathbf{u}_\alpha = \cos(\alpha)\mathbf{i} + \sin(\alpha)\mathbf{j}$ and $H_s(\mathbf{x}) = \sum_i a(\mathbf{x}-\mathbf{x}_i)\sin\left[\omega\mathbf{u}^\top(\mathbf{x}-\mathbf{x}_i)+\varphi_i\right]$. As said in Section 3.3.2, H_s can be interpreted as a Hilbert transform directed towards $\mathbf{u}_\alpha$. The quaternionic monogenic signal of a Gabor noise is hence to be interpreted as the analytic embedding of s in the 2D vector space spanned by the real number 1 and the quaternion $\mathbf{u}_\alpha$. The key idea of (Olhede et al. 2014) is to notice that the monogenic signal of such a directional signal is invariant with respect to the involution $T_\alpha : \mathbb{H} \to \mathbb{H}$ defined for all $\mathbf{q} \in \mathbb{H}$ by

$$T_\alpha(\mathbf{q}) = -\mathbf{u}_\alpha \mathbf{q} \mathbf{u}_\alpha. \tag{3.29}$$

Indeed, let $\mathbf{u}_\alpha^\perp$ denote the quaternion $-\sin(\alpha)\mathbf{i} + \cos(\alpha)\mathbf{j}$. Because $\mathbf{u}_\alpha$ and $\mathbf{u}_\alpha^\perp$ are linearly independent elements of the subspace spanned by $\mathbf{i}$ and $\mathbf{j}$, the elements $\left(1, \mathbf{u}_\alpha, \mathbf{u}_\alpha^\perp, \mathbf{k}\right)$ form a basis of the quaternion algebra. It can then be easily shown that the elements 1 and $\mathbf{u}_\alpha$ are invariant with respect to T_α, while $T_\alpha(\mathbf{u}_\alpha) = -\mathbf{u}_\alpha$ and $T_\alpha(\mathbf{k}) = -\mathbf{k}$. Consequently, if $\eta = a + b\mathbf{u}_\alpha + c\mathbf{u}_\alpha^\perp + d\mathbf{k}$ is a quaternion, with $(a, b, c, d) \in \mathbb{R}^4$, then,

$$T_\alpha(\eta) = a + b\mathbf{u}_\alpha - c\mathbf{u}_\alpha^\perp - d\mathbf{k}. \tag{3.30}$$

This shows that the invariants of T_α are exactly the quaternions $a + b\mathbf{u}_\alpha$, $(a, b) \in \mathbb{R}^2$. As seen in Eq. (3.28), the monogenic signal of a Gabor noise can be approached by such a quaternion, which implies that it is nearly invariant with respect to T_α. For more general noises s that do not have a constant orientation α, this is obviously not true anymore. The preferred direction can then be defined as the angle $\alpha \in \left[-\frac{\pi}{2}, \frac{\pi}{2}\right]$ that minimizes the mean distance between the monogenic signal M_s and its involuted form $T_\alpha(M_s)$, *i.e.*,

$$\begin{aligned} d_s &= \min_\theta \left\{ \mathbb{E}\left[\frac{1}{2} \left| M_s - T_\theta(M_s) \right|^2 \right] \right\}, \\ \alpha &= \arg\min_\theta \left\{ \mathbb{E}\left[\frac{1}{2} \left| M_s - T_\theta(M_s) \right|^2 \right] \right\}, \end{aligned} \tag{3.31}$$

where $|\cdot|$ denotes the modulus in the quaternion algebra. The minimal distance d_s itself provides a measure of directionality. The smallest d_s is, the more unidirectional the image is. In the case of a purely unidirectional image (*e.g.*, a Gabor noise), $d_s = 0$.

3.4.2 Geometric interpretation of the measure of directionality

Let $\mathbf{x} = x_0 + x_1\mathbf{i} + x_2\mathbf{j}$ be a quaternion of the hyperplane spanned by 1, $\mathbf{i}$ and $\mathbf{j}$. The element $\mathbf{x}$ could also be seen as a vector of $\mathbb{R}^3$. The aim of this section is to give a more geometric interpretation of the stochastic structure tensor introduced in (Olhede et al. 2014). As stated in (Via et al. 2010), the quaternonic operator T_θ used in (Olhede et al. 2014) can be expressed as a linear operator on $\mathbb{R}^3$, *i.e.*, for all $\mathbf{x} \in \mathbb{R}^3$,

$$T_\theta(\mathbf{x}) = \begin{pmatrix} 1 & 0 & 0 \\ 0 & \cos(2\theta) & -\sin(2\theta) \\ 0 & \sin(2\theta) & \cos(2\theta) \end{pmatrix} \begin{pmatrix} 1 & 0 & 0 \\ 0 & 1 & 0 \\ 0 & 0 & -1 \end{pmatrix} \begin{pmatrix} x_0 \\ x_1 \\ x_2 \end{pmatrix}. \tag{3.32}$$

Though this result was already given in (Via et al. 2010), the proof is recalled in Appendix B.5. If $(\mathbf{e}_1, \mathbf{e}_2, \mathbf{e}_3)$ denotes the canonical basis of $\mathbb{R}^3$, the operator T_θ hence corresponds to a symmetry with respect to the plane $\mathrm{vect}\{\mathbf{e}_1, \mathbf{e}_2\}$ followed by a rotation of angle 2θ around the axis $\mathbb{R}\mathbf{e}_1$. Since the operators T_θ leave the x-coordinate unchanged, they could be seen as plane operators. Remember that if s is a Gabor noise with orientation α, its monogenic signal M_s (seen as a vector of $\mathbb{R}^3$) is invariant with respect to the operator T_α, which implies that the estimated preferred direction of oscillation is exactly α. For more general noises s, the preferred direction is chosen as the angle θ_+ for which the 2D vector formed with the two Riesz components of s changes the least after undergoing a symmetry with respect to the x-axis followed by a rotation of angle $2\theta_+$. Section 3.4.3 gives a more stochastic interpretation of the angle θ_+ and the measure of directionality d_s thanks to the structure tensor framework.

3.4.3 Stochastic structure tensor

Let s be a stationary random process. By using the spectral representation of s (Loève 1978), it can be shown that if s is zero-mean, then its Riesz components $\mathcal{R}_1 s$ and $\mathcal{R}_2 s$ are zero-mean too, and their respective variances are linked by the following equation (Olhede et al. 2014),

$$\mathrm{Var}(s) = \mathrm{Var}(\mathcal{R}_1 s) + \mathrm{Var}(\mathcal{R}_2 s). \tag{3.33}$$

This equality yields following theorem, in which the measure of directionality of (Olhede et al. 2014) is reformulated as difference of variances.

Theorem 7. *Let s be a zero-mean random field, and let $\mathbf{u}_\theta$ denote the unit vector of $\mathbb{R}^2$ with argument $\theta \in \left]-\frac{\pi}{2}, \frac{\pi}{2}\right]$. Then, the distance d_s defined in Eq. (3.31) can be expressed as*

$$d_s = 2\,\mathrm{Var}(s) - 2 \max_\theta \mathrm{Var}\left(\mathbf{u}_\theta^\top \mathcal{R} s \right), \tag{3.34}$$

where $\mathcal{R}s$ denotes the Riesz transform of s.

Eq. (3.34) implies that preferred direction of s can be seen as the angle θ_+ for which the variance of the Riesz transform steered towards the direction θ_+ is maximal. This is analogous to the gradient-based oriented variation that can be found in (Soulard 2012) in the deterministic case. Here, the gradient is replaced by the Riesz transform, while the oriented variation is replaced by the variance operator. Eq. (3.34) can then be rewritten as

$$d_s = 2\,\mathrm{Var}(s) - 2\max_{\theta}\left(\mathbf{u}_\theta^\top T_s \mathbf{u}_\theta\right), \tag{3.35}$$

where

$$T_s = \begin{pmatrix} \mathrm{Var}(\mathcal{R}_1 s) & \mathrm{Cov}(\mathcal{R}_1 s, \mathcal{R}_2 s) \\ \mathrm{Cov}(\mathcal{R}_1 s, \mathcal{R}_2 s) & \mathrm{Var}(\mathcal{R}_2 s) \end{pmatrix}. \tag{3.36}$$

The matrix T_s is exactly the covariance matrix of the Riesz transform of s, and can be interpreted as a stochastic structure tensor formed with the Riesz components of s. A similar monogenic-based stochastic structure tensor can be found in (Polisano 2017) in the case of Gaussian fields. The more classical structure tensor found in (Jahne 2004, Soulard 2012) is formed with the components of the gradient instead (see (Köthe & Felsberg 2005) for more details about the link between the gradient and the Riesz transform). Notice that unlike these deterministic tensors, the components of T_s do not need to be convoluted with a smoothing function thanks to the variance operator.

The term $\mathbf{u}_\theta^\top T_s \mathbf{u}_\theta$ is maximized by using the the eigenvalues of the structure tensor T_s, which are given by

$$\begin{cases} \lambda_+ = \frac{1}{2}\left(\mathrm{Var}(s) + \sqrt{\left[\mathrm{Var}(\mathcal{R}_1 s) - \mathrm{Var}(\mathcal{R}_2 s)\right]^2 + 4\,\mathrm{Cov}(\mathcal{R}_1 s, \mathcal{R}_2 s)^2}\right), \\ \lambda_- = \frac{1}{2}\left(\mathrm{Var}(s) - \sqrt{\left[\mathrm{Var}(\mathcal{R}_1 s) - \mathrm{Var}(\mathcal{R}_2 s)\right]^2 + 4\,\mathrm{Cov}(\mathcal{R}_1 s, \mathcal{R}_2 s)^2}\right), \end{cases} \tag{3.37}$$

with $\lambda_- \leq \lambda_+$. Though the determination of the eigenvalues and eigenvectors of a gradient-based structure tensor can be found in, *e.g.*, (Soulard 2012), the proofs in the case of the stochastic structure tensor are given in Appendix B.5. Then, the term $\mathbf{u}_\theta^\top T_s \mathbf{u}_\theta$ is maximal when calculated along the eigenvector of T_s associated with its greatest eigenvalue, and minimal when calculated along the eigenvector of T_s associated with its smallest eigenvalue (see Appendix B.5). Applying this result to Eq. (3.35) implies that the measure of directionality d_s can be expressed as

$$d_s = 2\,\mathrm{Var}(s) - 2\lambda_+. \tag{3.38}$$

Notice that $\lambda_+ + \lambda_- = \mathrm{Var}(s)$, which yields a direct link between the measure of directionality d_s and λ_-, *i.e.*,

$$\begin{aligned} d_s &= 2\,\mathrm{Var}(s) - 2\lambda_+, \\ &= 2\left(\lambda_+ + \lambda_-\right) - 2\lambda_+, \\ &= 2\lambda_-. \end{aligned} \tag{3.39}$$

The directionality of the image is hence measured by calculating the lowest eigenvalue of the stochastic structure tensor. In the case of a purely unidirectional image, there is only one

preferred direction, which implies $\lambda_- = 0$. Otherwise, λ_- quantifies the importance of the second main direction of the image. The normalized measure of directionality, introduced in (Olhede et al. 2014) and denoted by $\mathcal{U}_s$, is then equivalent to the coherence index often used when dealing with structure tensors (*e.g.*, in (Soulard 2012, Polisano 2017)), *i.e.*,

$$\begin{aligned} \mathcal{U}_s &= \frac{2\max_\theta \left(\mathbf{u}_\theta^\top T_s \mathbf{u}_\theta\right)}{\mathrm{Var}(s)} - 1, \\ &= \frac{2\lambda_+}{\lambda_+ + \lambda_-} - 1, \\ &= \frac{\lambda_+ - \lambda_-}{\lambda_+ + \lambda_-}. \end{aligned} \tag{3.40}$$

Furthermore, the preferred direction of oscillation θ_+ is computed by using Eq. B.84 (see Appendix B.5), hence,

$$\theta_+ = \frac{1}{2}\arg\left[\mathrm{Var}(\mathcal{R}_1 s) - \mathrm{Var}(\mathcal{R}_2 s) + 2\mathbf{i}\,\mathrm{Cov}(\mathcal{R}_1 s, \mathcal{R}_2 s)\right] \ [2\pi]. \tag{3.41}$$

3.4.4 Case of a Gabor noise

This section aims at applying the stochastic structure tensor to the Gabor noise, which is the main focus of this chapter for its ability to model oscillating stochastic textures. Given that the stochastic structure tensor of (Olhede et al. 2014) is exactly the covariance matrix of the Riesz transform, the latter must be expressed in the case of a Gabor noise before applying the orientation estimation technique described in the previous sections. Let s be a phase-augmented Gabor noise as defined in Section 3.2.2. Assuming that the product $b\omega$ is small enough, Theorem 6 ensures that the Riesz transforms of s can be approached by using Eq. 3.22, *i.e.*, for all $\mathbf{x} \in \mathbb{R}^2$,

$$\mathcal{R}s(\mathbf{x}) \approx H_s(\mathbf{x}) \begin{pmatrix} \cos\alpha \\ \sin\alpha \end{pmatrix}, \tag{3.42}$$

where

$$H_s(\mathbf{x}) = \sum_i a(\mathbf{x} - \mathbf{x}_i) \sin\left[b\omega \mathbf{u}^\top (\mathbf{x} - \mathbf{x}_i) + \psi_i\right]. \tag{3.43}$$

The phase-shifted noise H_s can then be expressed as a sum of cosines, *i.e.*, for all $\mathbf{x} \in \mathbb{R}^2$,

$$H_s(\mathbf{x}) = \sum_i a(\mathbf{x} - \mathbf{x}_i) \cos\left[b\omega \mathbf{u}^\top (\mathbf{x} - \mathbf{x}_i) + \psi'_i\right], \tag{3.44}$$

where $\psi'_i = \psi_i - \frac{\pi}{2}\ [2\pi]$. Because the stochastic process $(\psi'_i)_i$ fulfills the same assumptions as $(\psi_i)_i$, H_s is a Gabor noise to which Theorem 5 can be applied, hence,

$$\mathrm{Var}\left(H_s\right) = \frac{\mu}{4b^2}, \tag{3.45}$$

which yields

$$\begin{cases} \mathrm{Var}\left(\mathcal{R}_1 s\right) = \frac{\mu}{4b^2}\cos^2\alpha, \\ \mathrm{Var}\left(\mathcal{R}_2 s\right) = \frac{\mu}{4b^2}\sin^2\alpha, \\ \mathrm{Cov}\left(\mathcal{R}_1 s, \mathcal{R}_2 s\right) = \frac{\mu}{4b^2}\cos\alpha\sin\alpha. \end{cases} \tag{3.46}$$

Therefore, in the case of a Gabor noise, the stochastic structure tensor T_s expressed in Eq. (3.36) becomes

$$T_s = \frac{\mu}{4b^2}\begin{pmatrix} \cos^2\alpha & \cos\alpha\sin\alpha \\ \cos\alpha\sin\alpha & \sin^2\alpha \end{pmatrix}, \tag{3.47}$$

The eigenvalues of T_s can then be calculated by applying Eq. (B.79) to the case of a Gabor noise, *i.e.*,

$$\begin{aligned}
\lambda_+ &= \frac{\mu}{4b^2} \times \frac{1}{2}\left(1 + \sqrt{\left(\cos^2\alpha - \sin^2\alpha\right)^2 + 4\cos^2\alpha\sin\alpha^2}\right), \\
&= \frac{\mu}{4b^2} \times \frac{1}{2}\left(1 + \sqrt{\left(\cos^2\alpha + \sin^2\alpha\right)^2}\right), \\
&= \frac{\mu}{4b^2}. \\
\lambda_- &= \frac{\mu}{4b^2} \times \frac{1}{2}\left(1 - \sqrt{\left(\cos^2\alpha - \sin^2\alpha\right)^2 + 4\cos^2\alpha\sin\alpha^2}\right), \\
&= \frac{\mu}{4b^2} \times \frac{1}{2}\left(1 - \sqrt{\left(\cos^2\alpha + \sin^2\alpha\right)^2}\right), \\
&= 0.
\end{aligned} \tag{3.48}$$

This leads to $d_s = 0$ and $\mathcal{U}_s = 1$, which is consistent with the unidirectional nature of s. As can be expected, the preferred direction of oscillation θ_+ is exactly α, *i.e.*, by using Eq. (B.84),

$$\begin{aligned}
\theta_+ &= \frac{1}{2}\arg\left[\mathrm{Var}(\mathcal{R}_1 s) - \mathrm{Var}(\mathcal{R}_2 s) + 2\mathbf{i}\,\mathrm{Cov}(\mathcal{R}_1 s), \mathcal{R}_2 s)\right] \ [2\pi], \\
&= \frac{1}{2}\arg\left[\frac{\mu}{4b^2}\left(\cos^2\alpha - \sin^2\alpha + 2\mathbf{i}\cos\alpha\sin\alpha\right)\right] \ [2\pi], \\
&= \frac{1}{2}\arg\left[\cos^2\alpha - \sin^2\alpha + 2\mathbf{i}\cos\alpha\sin\alpha\right] \ [2\pi], \\
&= \frac{1}{2}\arg\left[\cos\left(2\alpha\right) + \mathbf{i}\sin\left(2\alpha\right)\right] \ [2\pi], \\
&= \alpha \ [2\pi].
\end{aligned} \tag{3.49}$$

Synthetic tests are now performed to illustrate the reliability of this orientation extraction technique.

3.4.5 Synthetic tests

The Gabor noises are again synthesized on the discrete grid (t^j, t^k), $(j,k) \in \{0 \dots M-1\} \times \{0 \dots N-1\}$, $(M,N) \in \mathbb{N}^2$, similarly to what is done in Sections 3.2.4 and 3.3.3, respectively. After the discrete Gabor noise $s = (s_{j,k})_{j,k}$ is generated, the Riesz transforms $\mathcal{R}_1 s$ and $\mathcal{R}_2 s$ are computed, from which the discrete stochastic structure tensor T_s, *i.e.*, the empirical covariance matrix of the Riesz transforms, can be deduced. Once the matrix T_s is available, its eigenvalues and eigenvectors can be calculated. The argument of the affix of the eigenvector associated with the largest eigenvalue then yields a measure of orientation, which is compared with the expected orientation α. Given the fact that the developments performed in this section rely on Theorem 6, it can be expected that increasing the parameters b and ω increase the reliability of the orientation extraction, similarly to what

is observed in Section 3.3.3 when focusing on the phase extraction. Figure 3.7 shows the boxplots of the estimated orientations calculated for $b \in \{1, \dots, 5\}$, the other parameters being $M = N = 1000$, $T_x = T_y = 0.002$, $\omega = 30$, $\alpha = \frac{\pi}{6}$ and $p = 0.1$. For each value of b, $n = 50$ Gabor noises are generated. As in the case of phase extraction, increasing the scale parameter b only reduces the variance of the estimated orientation, while the mean remains close to the expected value α, suggesting that the estimation is unbiased. From $b = 3$ onwards, the orientation becomes highly reliable.

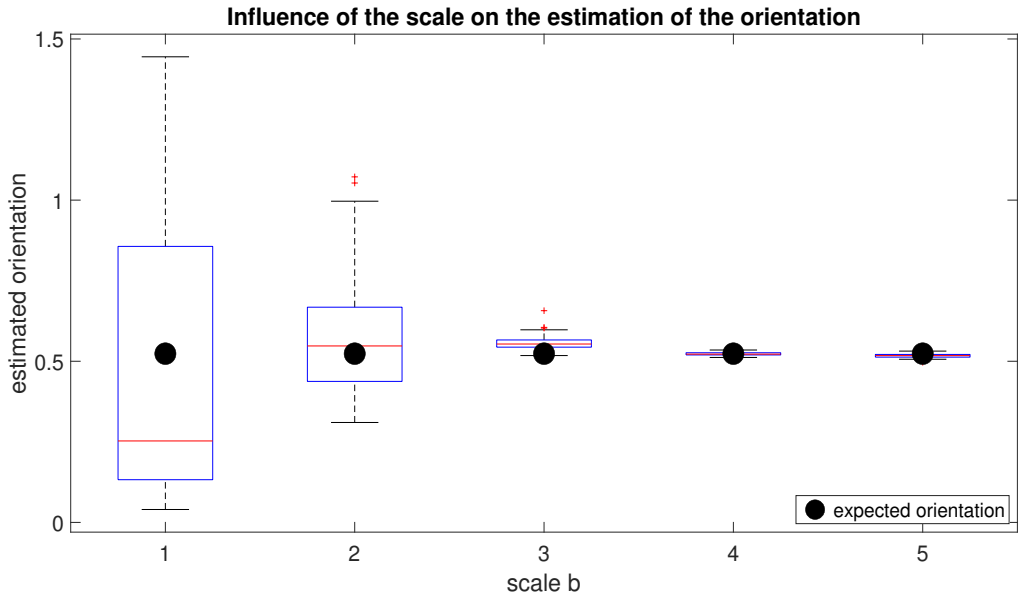

Figure 3.7: Boxplots of the estimated orientations measured from $n = 50$ Gabor noises, $b \in \{1, \dots, 5\}$, $M = N = 1000$, $T_x = T_y = 0.002$, $\omega = 30$, $\alpha = \frac{\pi}{6}$, $p = 0.1$.

Figure 3.8 now shows the boxplots of the estimated orientations calculated for $\omega \in \{10 + 5k, k = 0, \dots, 4\}$, the other parameters being $M = N = 1000$, $T_x = T_y = 0.002$, $b = 5$, $\alpha = \frac{\pi}{6}$, $p = 0.1$, with $n = 50$ Gabor noises generated for each value of ω. again, increasing the frequency parameter ω reduces both the mean and the variance of the estimator. For $\omega \geq 30$, the orientation estimation becomes highly reliable.

However, as shown in Figure3.9, the value of α does not seem to have any impact on the quality of the estimation. Generating $n = 50$ Gabor noises for each $\alpha \in \left\{\frac{\pi}{12}(1 + k)\right\}$, $k = 0, \dots, 5$, with $M = N = 1000$, $T_x = T_y = 0.002$, $b = 5$, $\omega = 30$ and $p = 0.1$, yields an unbiased estimation of orientation with a small variance in all cases. This highlights the ability of the monogenic-based stochastic structure tensor to extract the preferred direction of oscillation of a Gabor noise.

These results are consistent with what is observed on the normalized measure of unidirectionality $\mathcal{U}_s$. Figures 3.10 and 3.11 show that increasing the scale b and the frequency ω, respectively, yields more unidirectional textures, which is reflected by the values of the index $\mathcal{U}_s$ that tend towards 1, with a decreasing variance. Curiously, the orientation α has some impact on the mean and variance of the directionality $\mathcal{U}_s$, though the values remain close to 1 in all cases. A further statistical study could be performed to determine whether these variations are mere random fluctuations or not. Overall, these synthetic tests illus-

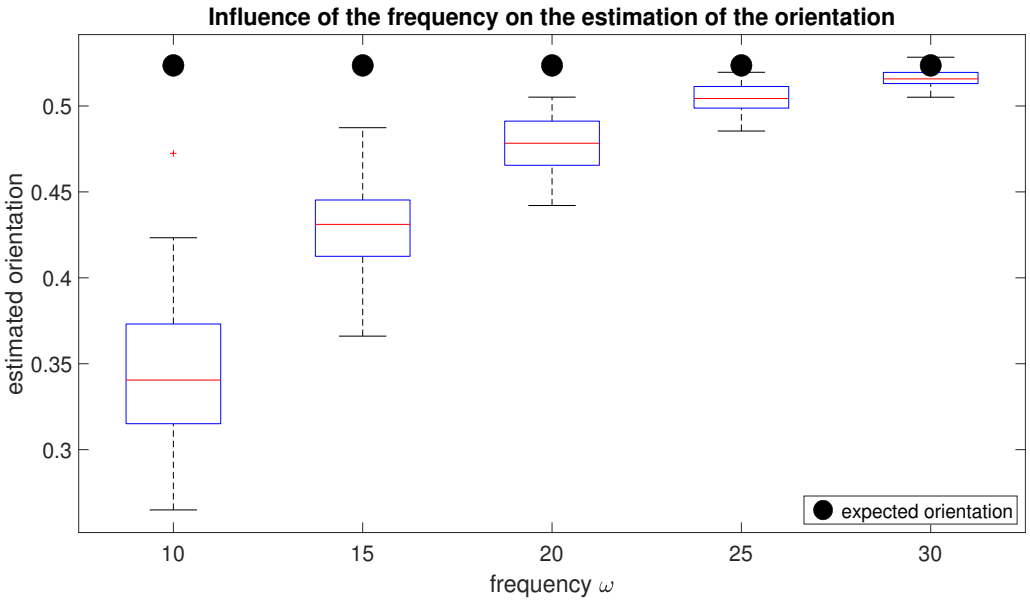

Figure 3.8: Boxplots of the estimated orientations measured from $n = 50$ Gabor noises, $\omega \in \{10 + 5k, k = 0, \ldots, 4\}$, $M = N = 1000$, $T_x = T_y = 0.002$, $b = 5$, $\alpha = \frac{\pi}{6}$, $p = 0.1$.

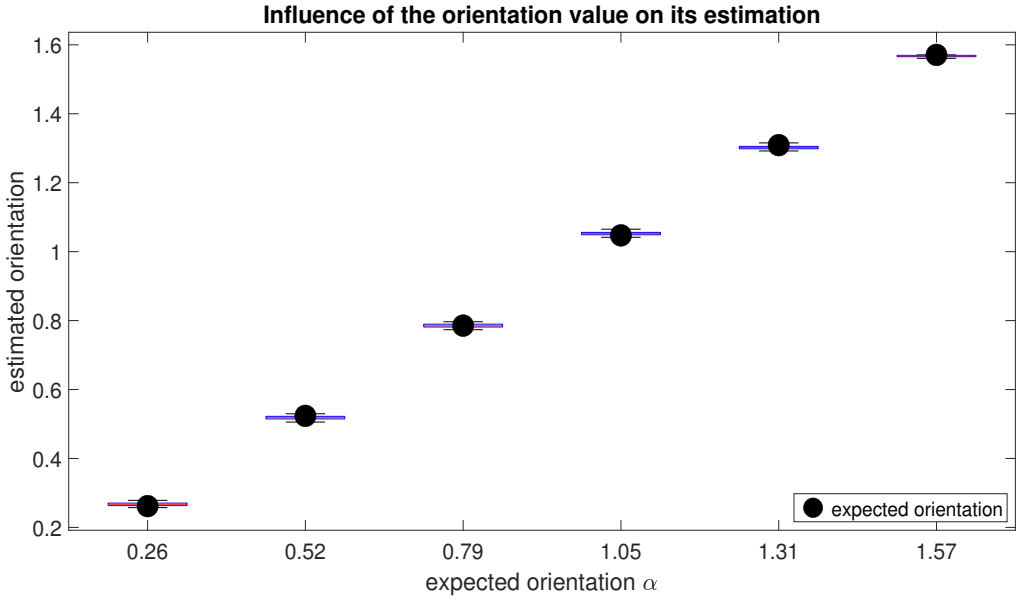

Figure 3.9: Boxplots of the estimated orientations measured from $n = 50$ Gabor noises, $\alpha \in \left\{\frac{\pi}{12}(1 + k), k = 0, \ldots, 5\right\}$, $M = N = 1000$, $T_x = T_y = 0.002$, $b = 5$, $\omega = 30$, $p = 0.1$.

trate how the measure of directionality introduced in (Olhede et al. 2014) generalizes the coherence index used for deterministic oscillating textures to random fields.

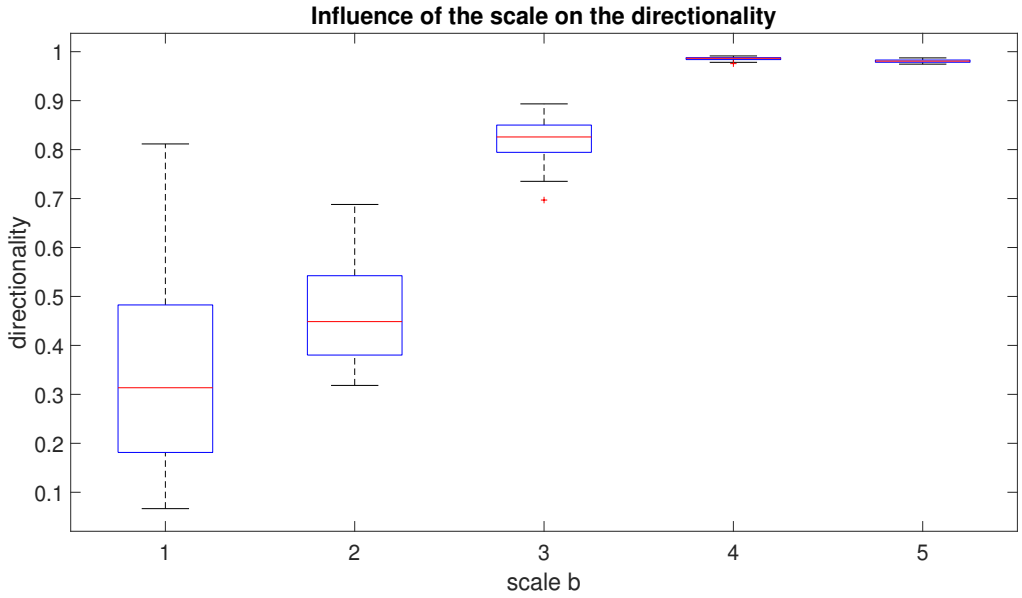

Figure 3.10: Boxplots of the normalized measures of directionality $\mathcal{U}_s$ calculated from $n = 50$ Gabor noises, $b \in \{1, \dots, 5\}$, $M = N = 1000$, $T_x = T_y = 0.002$, $\omega = 30$, $\alpha = \frac{\pi}{6}$, $p = 0.1$.

The relevance of the stochastic structure tensor and the index $\mathcal{U}_s$, respectively, can be further illustrated by considering a weighted sum of two Gabor noises with different orientations. Let s_1 and s_2 denote two independent discrete Gabor noises as defined in Section 3.2.4, generated with the same parameters except for the orientation. The orientations of s_1 and s_2 are denoted by α_1 and α_2, respectively. If $w \in [0, 1]$, let s be the weighted sum of s_1 and s_2 defined for all $\mathbf{x} \in \mathbb{R}^2$ by

$$s(\mathbf{x}) = (1 - w)s_1(\mathbf{x}) + ws_2(\mathbf{x}). \tag{3.50}$$

Figure 3.13 shows the boxplots of the estimated orientations calculated for $w \in \{0.1k, k = 0, \dots, 10\}$, the other parameters being $M = N = 1000$, $T_x = T_y = 0.002$, $b = 5$, $\omega = 30$, $\alpha_1 = \frac{\pi}{6}$, $\alpha_2 = \frac{\pi}{2}$ and $p = 0.1$. For each value of w, $n = 50$ Gabor noises are generated. As can be expected, the estimated orientation is close to α_1 when w is close to 0, and close to α_2 when w is close to 1. Notice that the shift between these two extremes is smooth, suggesting that in the case of two main directions of oscillation α_1 and α_2 ($w \approx 0.5$), the estimated orientation θ_+ corresponds to a mean between α_1 and α_2.

This shift is also reflected in the normalized measure of directionality $\mathcal{U}_s$. Indeed, as shown in Figure 3.14, this parameter is close to 1 when one Gabor noise significantly dominates the other ($w \approx 0$ or $w \approx 1$). When the two noises equally contribute in the texture ($w \approx 0.5$), the index $\mathcal{U}_s$ oscillates a little above 0.5. Again, this is similar to what is observed with the more classical coherence index in the case of deterministic images (Soulard 2012), except that the index $\mathcal{U}_s$ is designed for stochastic texture. Notice that an analogous coherence index is also used in (Polisano 2017) when dealing with Gaussian fields.

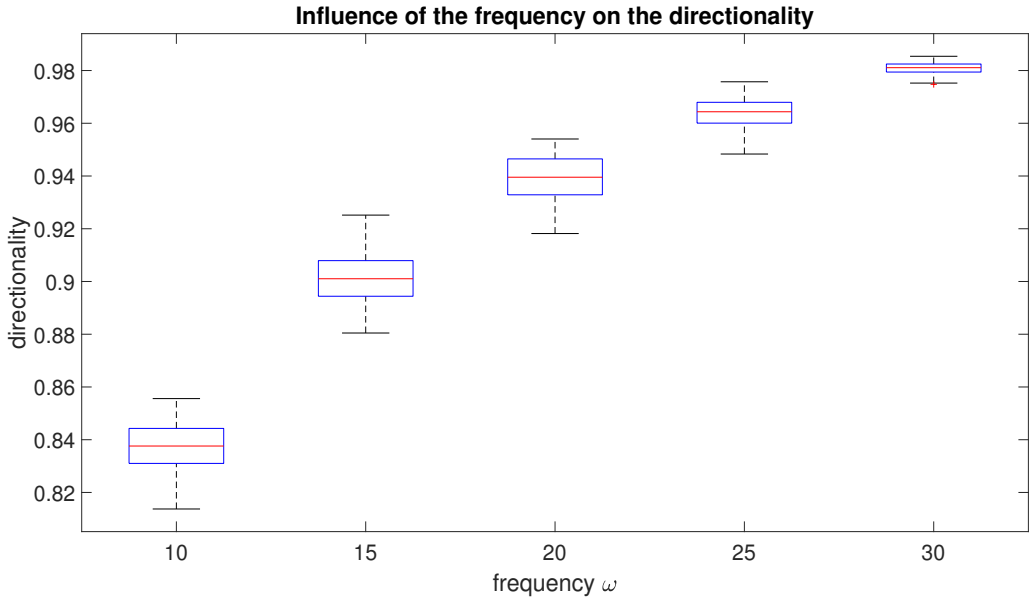

Figure 3.11: Boxplots of the normalized measures of directionality $\mathcal{U}_s$ calculated from $n = 50$ Gabor noises, $\omega \in \{10 + 5k, k = 0, \ldots, 4\}$, $M = N = 1000$, $T_x = T_y = 0.002$, $b = 5$, $\alpha = \frac{\pi}{6}$, $p = 0.1$.

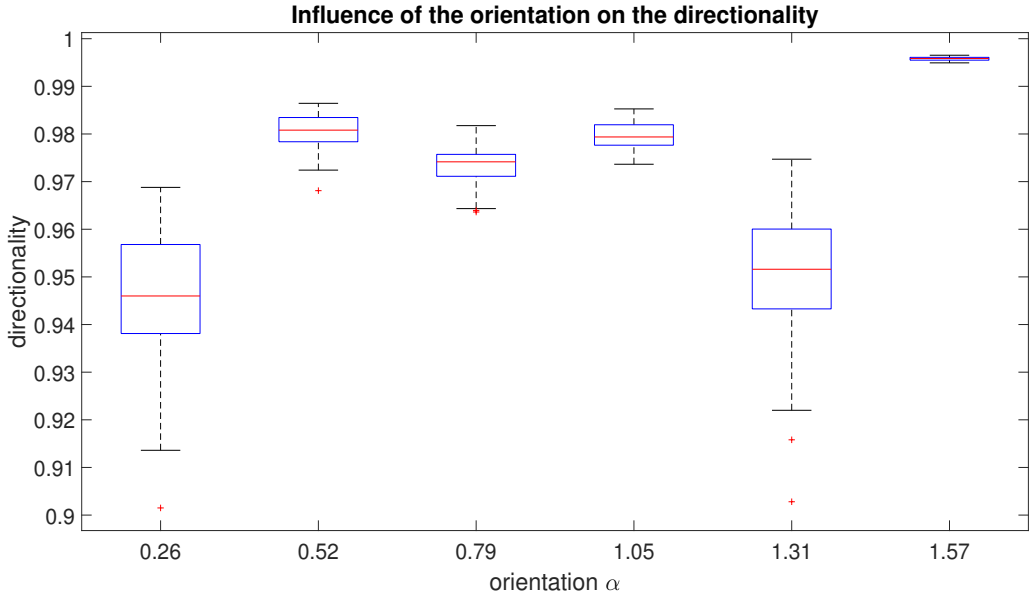

Figure 3.12: Boxplots of the normalized measures of directionality $\mathcal{U}_s$ calculated from $n = 50$ Gabor noises, $\alpha \in \left\{\frac{\pi}{12}(1 + k), k = 0, \ldots, 5\right\}$, $M = N = 1000$, $T_x = T_y = 0.002$, $b = 5$, $\omega = 30$, $p = 0.1$.

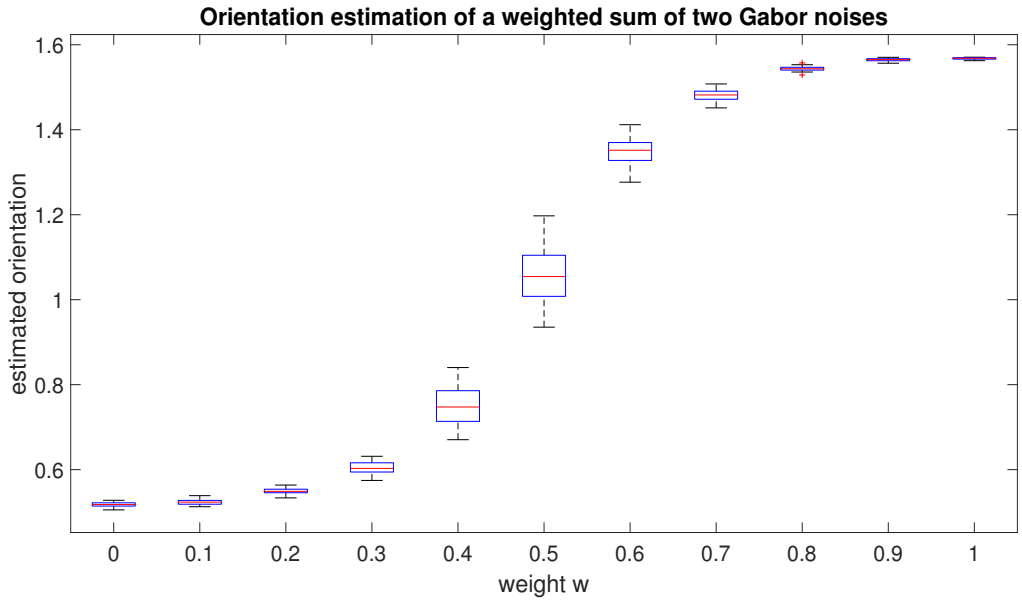

Figure 3.13: Boxplots of the estimated orientations measured from $n = 50$ sums of two Gabor noises, $w \in \{0.1k, k = 0, \ldots, 10\}$, $M = N = 1000$, $T_x = T_y = 0.002$, $b = 5$, $\omega = 30$, $\alpha_1 = \frac{\pi}{6}$, $\alpha_2 = \frac{\pi}{2}$, $p = 0.1$.

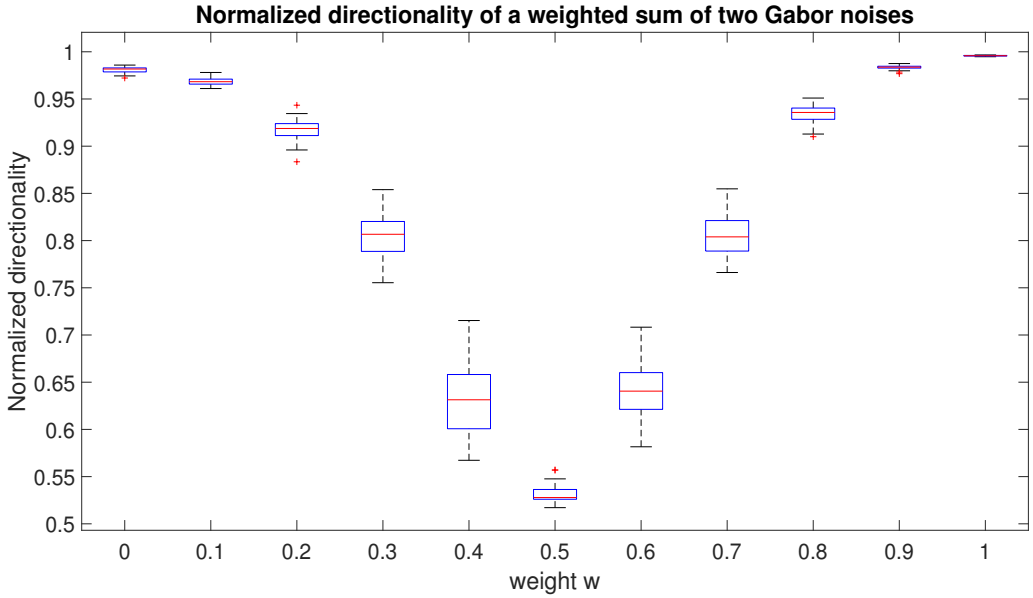

Figure 3.14: Boxplots of the normalized directionality indices measured from $n = 50$ sums of two Gabor noises, $w \in \{0.1k, k = 0, \ldots, 10\}$, $M = N = 1000$, $T_x = T_y = 0.002$, $b = 5$, $\omega = 30$, $\alpha_1 = \frac{\pi}{6}$, $\alpha_2 = \frac{\pi}{2}$, $p = 0.1$.

3.5 Application to real textures

Sections 3.3 and 3.4 provide relevant monogenic-based tools to extract phase and orientation, respectively, which is illustrated by the good results they give when applied to Gabor noises. Remember that the Gabor noise framework is originally chosen because it enables the synthesis of stochastic oscillating textures with prescribed frequency content. This section goes further by applying these tools to real textures displaying oscillating patterns. Table 3.4 shows the results obtained by applying the phase and orientation estimation processes described in the previous sections to grill, sand, metal and sheet textures. The directionality index $\mathcal{U}_s$ is also given. As was already observed in the case of interference fringes in Chapter 2, the monogenic phase manages to extract the oscillating structures of the images, though it struggles when the patterns are less obvious. This can be linked with Theorem 6, which states that the reliability of the monogenic extraction of phase decreases when $b\omega$ decreases, *i.e.*, when the oscillating patterns become less visible. Notice that, like in the case of fringe patterns, these tests only tackle the extraction of the phase. Now that the reliability of this extraction is established, further developments would be necessary to characterize the information contained in the phase function.

In all cases, the global orientation extracted from the monogenic structure tensor is consistent with the visual aspect of the texture, *i.e.*, the direction of the oscillating patterns is well extracted. This is also true for the directionality index, which increases as the texture displays more and more unidirectional oscillations. This shows how the monogenic-based tools developed in this chapter not only work for synthesized textures, but also real textures displaying oscillating patterns. Unlike the phase, the directionality information is encoded in a single parameter, which could then be used in texture classification in future works.

Texture	Grill	Sand	Metal	Sheet
Original	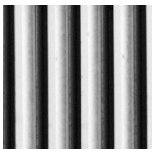	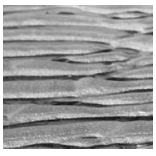	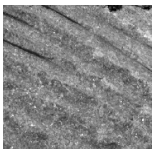	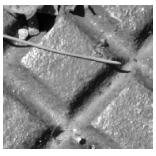
Phase	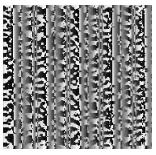	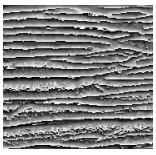	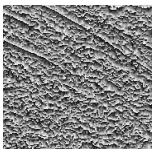	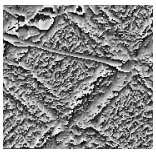
Orientation	$1.57 \approx \frac{\pi}{2}$	0.02	$-0.44 \approx -\frac{\pi}{7}$	$0.63 \approx \frac{\pi}{5}$
Directionality	0.99	0.94	0.3	0.12

Table 3.4: Monogenic extraction of local phase, global orientation and directionality of real textures

3.6 Conclusion

Highlighted in Chapter 2 in the case of deterministic waves, the quality of the monogenic extraction of phase generalizes well to random fields displaying oscillating patterns like Gabor noises, as shown in Section 3.3. This is supported by both theoretical results and synthetic tests. Furthermore, Section 3.4 shows how the monogenic-based stochastic structure tensor introduced in (Olhede et al. 2014) manages to extract the preferred direction of oscillation of a single Gabor noise, as well as evaluating the overall directionality when applied to a sum of Gabor noises. All these results rely on the approximation of the Riesz transform of a Gabor noise provided by Theorem 6, which is therefore one of the most important contributions of this chapter. Though dealing with synthesized images, these results give strong arguments for the robustness of the monogenic extraction of local features. Section 3.5 goes further by successfully extracting the phase and orientation of real oscillating textures by using the monogenic-based tools introduced in the two previous sections, which highlights the ability of these tools to capture the local behavior of such images.

Similarly to the case of deterministic waves tackled in Chapter 2, these results imply that the monogenic signal is still able to separate energetical, structural and directional information when stochastic features come into play, as long as the image displays clear oscillating patterns. Unlike the directional features, which can be summed up by the directionality index, the phase function still lacks a concise description. While the developments introduced in this study ensure the reliability of the phase extraction, further work could focus on how the information contained in this signal can be summed up in a small set of descriptors.

Notice that though the main topic of this work is the characterization of color textures, Chapter 2 and 3 only deal with greyscale textures. These steps were necessary to introduce the monogenic-based structure extraction techniques and illustrate their relevance for both deterministic and stochastic textures. The subsequent developments aim at extending these results to color textures. To do so, a suitable color model must be defined, which is the main topic of Chapter 4.

APPENDIX B

Appendices

B.1 Proof of Theorem 3

For $T > 0$, let A_T denote the square $[-T, T]^2 \subset \mathbb{R}^2$, and s_T the process defined for all $\mathbf{x} \in \mathbb{R}^2$ by

$$s_T(\mathbf{x}) = \sum_{i|\mathbf{x}_i \in A_T} g(\mathbf{x} - \mathbf{x}_i). \tag{B.1}$$

Because $(\mathbf{x}_i)_i$ is a Poisson process with intensity μ, $N(A_T)$ has a Poisson distribution with parameter $\mu|A_T| = \mu(2T)^2$. Moreover, given $N(A_T) = n$, with $n \in \mathbb{N}$, the points $\{\mathbf{y}_1, \ldots, \mathbf{y}_n\}$ inside A_T are independent and identically distributed according to a uniform distribution on A_T. $s_T(\mathbf{x})$ can hence be expressed as

$$s_T(\mathbf{x}) = \sum_{i=1}^{N(A_T)} g(\mathbf{x} - \mathbf{y}_i). \tag{B.2}$$

Mean :
The mean of s_T can then be calculated as a conditional mean,

$$\begin{aligned}
\mathbb{E}\left[s_T(\mathbf{x})\right] &= \mathbb{E}\left\{\mathbb{E}\left[s_T(\mathbf{x})|N(A_T)\right]\right\}, \\
&= \mathbb{E}\left\{\mathbb{E}\left[\sum_{i=1}^{N(A_T)} g(\mathbf{x} - \mathbf{y}_i)\middle| N(A_T)\right]\right\}, \\
&= \mathbb{E}\left\{N(A_T)\mathbb{E}\left[g(\mathbf{x} - \mathbf{y}_1)\right]\right\} \quad \text{because the } (\mathbf{y}_i)_i \text{ are i.i.d.}, \\
&= \mathbb{E}\left[N(A_T)\right] \times \mathbb{E}\left[g(\mathbf{x} - \mathbf{y}_1)\right] \quad \text{by linearity of the mean.}
\end{aligned} \tag{B.3}$$

Because the random variable $N(A_T)$ has a Poisson distribution with parameter $\mu(2T)^2$, its mean is exactly equal to its parameter. As for the mean of $g(\mathbf{x} - \mathbf{y}_1)$, it is calculated by using the uniform density on $A_T = [-T, T]^2$, which gives

$$\begin{aligned}
\mathbb{E}\left[s_T(\mathbf{x})\right] &= \mu(2T)^2 \int_{A_T} g(\mathbf{x} - \mathbf{u}) \frac{d\mathbf{u}}{(2T)^2}, \\
&= \mu \int_{A_T} g(\mathbf{x} - \mathbf{u}) d\mathbf{u}.
\end{aligned} \tag{B.4}$$

It is obvious that for all $\mathbf{x} \in \mathbb{R}^2$,

$$\lim_{T\to+\infty} s_T(\mathbf{x}) = s(\mathbf{x}). \tag{B.5}$$

By using Lebesgue's dominated convergence theorem (see, *e.g.*, Theorem 1.19 in (Evans & Gariepy 2015)), this implies that

$$\lim_{T\to+\infty} \mathbb{E}[s_T(\mathbf{x})] = \mathbb{E}[s(\mathbf{x})]. \tag{B.6}$$

Finally, making T tend towards $+\infty$ and applying the substitution $\mathbf{y} = \mathbf{x} - \mathbf{u}$ leads to

$$\mathbb{E}[s(\mathbf{x})] = \mu \int_{\mathbb{R}^2} g(\mathbf{y}) d\mathbf{y}. \tag{B.7}$$

Variance :
The same method can be used to calculate the second moment of $s_T(\mathbf{x})$, with $T > 0$ and $\mathbf{x} \in \mathbb{R}^2$.

$$\begin{aligned}
\mathbb{E}\left[s_T(\mathbf{x})^2\right] &= \mathbb{E}\left\{\mathbb{E}\left[s_T(\mathbf{x})^2 | N(A_T)\right]\right\}, \\
&= \mathbb{E}\left\{\mathbb{E}\left[\left(\sum_{i=1}^{N(A_T)} g(\mathbf{x}-\mathbf{y}_i)\right)^2 \middle| N(A_T)\right]\right\}, \\
&= \mathbb{E}\left\{\mathbb{E}\left[\sum_{i=1}^{N(A_T)} g(\mathbf{x}-\mathbf{y}_i)^2 + \sum_{i\neq j} g(\mathbf{x}-\mathbf{y}_i)g(\mathbf{x}-\mathbf{y}_j) \middle| N(A_T)\right]\right\}, \\
&= \mathbb{E}\left\{N(A_T)\mathbb{E}\left[g(\mathbf{x}-\mathbf{y}_1)^2\right] + N(A_T)(N(A_T)-1)\mathbb{E}\left[g(\mathbf{x}-\mathbf{y}_1)g(\mathbf{x}-\mathbf{y}_2)\right]\right\}, \\
&= \mathbb{E}\left[N(A_T)\right] \times \mathbb{E}\left[g(\mathbf{x}-\mathbf{y}_1)^2\right] + \mathbb{E}\left[N(A_T)(N(A_T)-1)\right] \times \mathbb{E}\left[g(\mathbf{x}-\mathbf{y}_1)\right]^2.
\end{aligned} \tag{B.8}$$

Because $N(A_T)$ has a Poisson distribution with parameter $\mu(2T)^2$, the mean of the random variable $N(A_T)(N(A_T)-1)$ can be expressed as follows,

$$\begin{aligned}
\mathbb{E}\left[N(A_T)(N(A_T)-1)\right] &= \mathbb{E}\left[N(A_T)^2\right] - \mathbb{E}\left[N(A_T)\right], \\
&= \mathrm{Var}(N(A_T)) + \mathbb{E}\left[N(A_T)\right]^2 - \mathbb{E}\left[N(A_T)\right], \\
&= \mu(2T)^2 + \mu^2(2T)^4 - \mu(2T)^2, \\
&= \mu^2(2T)^4.
\end{aligned} \tag{B.9}$$

Injecting this expression in the second moment of $s_T(\mathbf{x})$ leads to

$$\begin{aligned}
\mathbb{E}[s_T(\mathbf{x})^2] &= \mu(2T)^2 \int_{A_T} g(\mathbf{x}-\mathbf{u})^2 \frac{d\mathbf{u}}{(2T)^2} + \mu^2(2T)^4 \left(\int_{A_T} g(\mathbf{x}-\mathbf{u}) \frac{d\mathbf{u}}{(2T)^2}\right)^2, \\
&= \mu \int_{A_T} g(\mathbf{x}-\mathbf{u})^2 d\mathbf{u} + \mu^2 \left(\int_{A_T} g(\mathbf{x}-\mathbf{u}) d\mathbf{u}\right)^2.
\end{aligned} \tag{B.10}$$

Making T tend towards $+\infty$ gives

$$\mathbb{E}\left[s(\mathbf{x})^2\right] = \mu \int_{\mathbb{R}^2} g(\mathbf{y})^2 d\mathbf{y} + \mu^2 \left(\int_{\mathbb{R}^2} g(\mathbf{y}) d\mathbf{y}\right)^2. \tag{B.11}$$

Finally, the variance is obtained as the difference between the second moment and the square of the previously calculated mean, *i.e.*,

$$\begin{aligned}\mathrm{Var}\left[s(\mathbf{x})\right] &= \mathbb{E}\left[s(\mathbf{x})^2\right] - \mathbb{E}\left[s(\mathbf{x})\right]^2, \\ &= \mu \int_{\mathbb{R}^2} g(\mathbf{y})^2 d\mathbf{y} + \mu^2 \left(\int_{\mathbb{R}^2} g(\mathbf{y}) d\mathbf{y}\right)^2 - \mu^2 \left(\int_{\mathbb{R}^2} g(\mathbf{y}) d\mathbf{y}\right)^2, \\ &= \mu \int_{\mathbb{R}^2} g(\mathbf{y})^2 d\mathbf{y}.\end{aligned} \tag{B.12}$$

B.2 Proof of Theorem 3

As in the calculation of the variance, the covariance is first expressed in a square $A_T = [-T,T]^2 \subset \mathbb{R}^2$, $T>0$. Let s_T^g and s_T^h denote the processes defined for all $\mathbf{x} \in \mathbb{R}^2$ by

$$\begin{aligned} s_T^g(\mathbf{x}) &= \sum_{i=1}^{N(A_T)} g(\mathbf{x}-\mathbf{y}_i), \\ s_T^h(\mathbf{x}) &= \sum_{i=1}^{N(A_T)} h(\mathbf{x}-\mathbf{y}_i). \end{aligned} \tag{B.13}$$

The mean of the product $s_T^g(\mathbf{x})s_T^h(\mathbf{x})$ is first calculated

$$\begin{aligned} &\mathbb{E}[s_T^g(\mathbf{x})s_T^h(\mathbf{x})] = \mathbb{E}\{\mathbb{E}[s_T^g(\mathbf{x})s_T^h(\mathbf{x})|N(A_T)]\}, \\ &= \mathbb{E}\left\{\mathbb{E}\left[\left(\sum_{i=1}^{N(A_T)} g(\mathbf{x}-\mathbf{y}_i)\right)\left(\sum_{j=1}^{N(A_T)} h(\mathbf{x}-\mathbf{y}_j)\right)\middle| N(A_T)\right]\right\}, \\ &= \mathbb{E}\left\{\mathbb{E}\left[\sum_{i=1}^{N(A_T)} g(\mathbf{x}-\mathbf{y}_i)h(\mathbf{x}-\mathbf{y}_i) + \sum_{i\neq j} g(\mathbf{x}-\mathbf{y}_i)h(\mathbf{x}-\mathbf{y}_j)\middle| N(A_T)\right]\right\}, \\ &= \mathbb{E}\left\{N(A_T)\mathbb{E}\left[g(\mathbf{x}-\mathbf{y}_1)h(\mathbf{x}-\mathbf{y}_1)\right] + N(A_T)(N(A_T)-1)\mathbb{E}\left[g(\mathbf{x}-\mathbf{y}_1)h(\mathbf{x}-\mathbf{y}_2)\right]\right\}, \\ &= \mathbb{E}\left[N(A_T)\right] \times \mathbb{E}\left[g(\mathbf{x}-\mathbf{y}_1)h(\mathbf{x}-\mathbf{y}_1)\right], \\ &\quad + \mathbb{E}\left[N(A_T)(N(A_T)-1)\right] \times \mathbb{E}\left[g(\mathbf{x}-\mathbf{y}_1)\right] \times \mathbb{E}\left[h(\mathbf{x}-\mathbf{y}_1)\right], \\ &= \mu(2T)^2 \int_{A_T} g(\mathbf{x}-\mathbf{u})h(\mathbf{x}-\mathbf{u})\frac{d\mathbf{u}}{(2T)^2}, \\ &\quad + \mu^2(2T)^4 \left(\int_{A_T} g(\mathbf{x}-\mathbf{u})\frac{d\mathbf{u}}{(2T)^2}\right) \times \left(\int_{A_T} h(\mathbf{x}-\mathbf{u})\frac{d\mathbf{u}}{(2T)^2}\right), \\ &= \mu \int_{A_T} g(\mathbf{x}-\mathbf{u})h(\mathbf{x}-\mathbf{u})d\mathbf{u} + \mu^2 \left(\int_{A_T} g(\mathbf{x}-\mathbf{u})d\mathbf{u}\right)\left(\int_{A_T} h(\mathbf{x}-\mathbf{u})d\mathbf{u}\right). \end{aligned} \tag{B.14}$$

Making T tend towards $+\infty$ gives

$$\mathbb{E}\left[s^g(\mathbf{x})s^h(\mathbf{x})\right] = \mu \int_{\mathbb{R}^2} g(\mathbf{y})h(\mathbf{y})d\mathbf{y} + \mu^2 \left(\int_{\mathbb{R}^2} g(\mathbf{y})d\mathbf{y}\right)\left(\int_{\mathbb{R}^2} h(\mathbf{y})d\mathbf{y}\right). \tag{B.15}$$

Finally, the covariance is obtained as the difference between the mean of the product and the product of the means,

$$\begin{aligned} &Cov\left[s^g(\mathbf{x})s^h(\mathbf{x})\right] = \mathbb{E}\left[s^g(\mathbf{x})s^h(\mathbf{x})\right] - \mathbb{E}\left[s^g(\mathbf{x})\right]\mathbb{E}\left[s^h(\mathbf{x})\right], \\ &= \mu \int_{\mathbb{R}^2} g(\mathbf{y})h(\mathbf{y})d\mathbf{y} + \mu^2 \left(\int_{\mathbb{R}^2} g(\mathbf{y})d\mathbf{y}\right)\left(\int_{\mathbb{R}^2} h(\mathbf{y})d\mathbf{y}\right) - \mu^2 \left(\int_{\mathbb{R}^2} g(\mathbf{y})d\mathbf{y}\right)\left(\int_{\mathbb{R}^2} h(\mathbf{y})d\mathbf{y}\right), \\ &= \mu \int_{\mathbb{R}^2} g(\mathbf{y})h(\mathbf{y})d\mathbf{y}. \end{aligned} \tag{B.16}$$

B.3 Proof of Theorem 5

The proof basically consists in applying Proposition 3.1 of (Galerne 2010) (recalled in Section 3.1.3) to the gabor kernel g defined in Eq. (3.8).
Mean :

$$\begin{aligned}
\mathbb{E}\left[s(\mathbf{x})\right] &= \frac{\mu}{2\pi}\int_{-\pi}^{\pi}\int_{\mathbb{R}^2} g(\mathbf{y},\psi)d\mathbf{y}d\psi,\\
&= \frac{\mu}{2\pi}\int_{-\pi}^{\pi}\int_{\mathbb{R}^2} e^{-\pi b^2\|\mathbf{y}\|^2}\cos\left(b\omega\mathbf{u}^\top\mathbf{y}+\psi\right)d\mathbf{y}d\psi,\\
&= \frac{\mu}{2\pi}\Re\left[\int_{-\pi}^{\pi}\int_{\mathbb{R}^2} e^{-\pi b^2\|\mathbf{y}\|^2}e^{\mathbf{i}\left(b\omega\mathbf{u}^\top\mathbf{y}+\psi\right)}d\mathbf{y}d\psi\right],\\
&= \frac{\mu}{2\pi}\Re\left[\int_{-\pi}^{\pi} e^{\mathbf{i}\psi}\int_{\mathbb{R}^2} e^{-\pi b^2\|\mathbf{y}\|^2}e^{\mathbf{i}\left(b\omega\mathbf{u}^\top\mathbf{y}\right)}d\mathbf{y}d\psi\right],\\
&= \frac{\mu}{2\pi}\Re\left[\underbrace{\int_{-\pi}^{\pi} e^{\mathbf{i}\psi}d\psi}_{=0}\int_{\mathbb{R}^2} e^{-\pi b^2\|\mathbf{y}\|^2}e^{\mathbf{i}\left(b\omega\mathbf{u}^\top\mathbf{y}\right)}d\mathbf{y}\right], \quad \text{by using Fubini's theorem}\\
&= 0.
\end{aligned} \tag{B.17}$$

Covariance function :

Let $\mathbf{z}\in\mathbf{R}^2$ be a 2D spatial delay. Using the expression of the covariance given at the end of Section 3.1.3 leads to

$$\begin{aligned}
\mathrm{Cov}\left[s(\mathbf{0}),s(\mathbf{z})\right] &= \frac{\mu}{2\pi}\int_{-\pi}^{\pi}\int_{\mathbb{R}^2} g(\mathbf{y},\psi)g(\mathbf{y}-\mathbf{z},\psi)d\mathbf{y}d\psi,\\
&= \frac{\mu}{2\pi}\int_{-\pi}^{\pi}\int_{\mathbb{R}^2} a(\mathbf{y})a(\mathbf{y}-\mathbf{z})\\
&\quad\times\cos\left(b\omega\mathbf{u}^\top\mathbf{y}+\psi\right)\cos\left[b\omega\mathbf{u}^\top(\mathbf{y}-\mathbf{z})+\psi\right]d\mathbf{y}d\psi,\\
&= \frac{\mu}{2\pi}\int_{-\pi}^{\pi}\int_{\mathbb{R}^2} e^{-\pi b^2\|\mathbf{y}\|^2}e^{-\pi b^2\|\mathbf{y}-\mathbf{z}\|^2}\\
&\quad\times\cos\left(b\omega\mathbf{u}^\top\mathbf{y}+\psi\right)\cos\left[b\omega\mathbf{u}^\top(\mathbf{y}-\mathbf{z})+\psi\right]d\mathbf{y}d\psi,\\
&= \frac{\mu}{4\pi}\int_{-\pi}^{\pi}\int_{\mathbb{R}^2} e^{-\pi b^2\|\mathbf{y}\|^2}e^{-\pi b^2\|\mathbf{y}-\mathbf{z}\|^2}\\
&\quad\times\left\{\cos\left[b\omega\mathbf{u}^\top(2\mathbf{y}-\mathbf{z})+2\psi\right]+\cos\left(b\omega\mathbf{u}^\top\mathbf{z}\right)\right\}d\mathbf{y}d\psi.
\end{aligned} \tag{B.18}$$

The two terms of the integral are now calculated seperately. The first term, denoted by I_1 can be expressed in the complex domain, hence

$$\begin{aligned}
I_1 &= \frac{\mu}{4\pi}\int_{-\pi}^{\pi}\int_{\mathbb{R}^2} e^{-\pi b^2\|\mathbf{y}\|^2}e^{-\pi b^2\|\mathbf{y}-\mathbf{z}\|^2}\cos\left[b\omega\mathbf{u}^\top(2\mathbf{y}-\mathbf{z})+2\psi\right]d\mathbf{y}d\psi,\\
&= \frac{\mu}{4\pi}\Re\left[\int_{-\pi}^{\pi}\int_{\mathbb{R}^2} e^{-\pi b^2\|\mathbf{y}\|^2}e^{-\pi b^2\|\mathbf{y}-\mathbf{z}\|^2}e^{\mathbf{i}\left[b\omega\mathbf{u}^\top(2\mathbf{y}-\mathbf{z})+2\psi\right]}d\mathbf{y}d\psi\right].
\end{aligned} \tag{B.19}$$

The integration variables can be separated as is done for the mean, leading to

$$\begin{aligned} I_1 &= \frac{\mu}{4\pi}\Re\left[\int_{\mathbb{R}^2} e^{-\pi b^2\|\mathbf{y}\|^2} e^{-\pi b^2\|\mathbf{y}-\mathbf{z}\|^2} e^{\mathbf{i}\omega\mathbf{u}^\top(2\mathbf{y}-\mathbf{z})} d\mathbf{y} \times \underbrace{\int_{-\pi}^{\pi} e^{2\mathbf{i}\psi} d\psi}_{=0}\right], \\ &= 0. \end{aligned} \tag{B.20}$$

The second term of Eq. (B.18), denoted by I_2, can be expressed as the convolution product between the Gaussian function a defined in Section 3.2.2 and itself, *i.e.*,

$$\begin{aligned} I_2 &= \frac{\mu}{4\pi}\int_{-\pi}^{\pi}\int_{\mathbb{R}^2} e^{-\pi b^2\|\mathbf{y}\|^2} e^{-\pi b^2\|\mathbf{y}-\mathbf{z}\|^2} \cos\left(b\omega\mathbf{u}^\top\mathbf{z}\right) d\mathbf{y} d\psi, \\ &= \frac{\mu}{2}\cos\left(b\omega\mathbf{u}^\top\mathbf{z}\right)\int_{\mathbb{R}^2} e^{-\pi b^2\|\mathbf{y}\|^2} e^{-\pi b^2\|\mathbf{y}-\mathbf{z}\|^2} d\mathbf{y}, \\ &= \frac{\mu}{2}\cos\left(b\omega\mathbf{u}^\top\mathbf{z}\right) a * a(\mathbf{z}). \end{aligned} \tag{B.21}$$

This convolution product is first calculated in the Fourier domain. Let $\mathcal{F}_2$ denote the 2D Fourier transform defined in Section 2.3. Applying the expression of the 2D Fourier transform of a Gaussian function given in Theorem 1 to the convolution product $a*a$, with $a_1 = a_2 = b\sqrt{\pi}$, leads for all $\xi \in \mathbb{R}^2$ to

$$\begin{aligned} \mathcal{F}_2(a*a)(\xi) &= \left[\mathcal{F}(a)(\xi)\right]^2, \\ &= \left[\frac{1}{b^2} e^{-\frac{1}{4\pi b^2}\|\xi\|^2}\right]^2, \\ &= \frac{1}{b^4} e^{-\frac{1}{2\pi b^2}\|\xi\|^2}. \end{aligned} \tag{B.22}$$

This is exactly the Fourier transform of a Gaussian function with $a_1 = a_2 = b\sqrt{\frac{\pi}{2}}$, hence, for $\mathbf{z} \in \mathbb{R}^2$,

$$\begin{aligned} a * a(\mathbf{z}) &= \frac{b^2\pi}{2\pi b^4} e^{-\frac{1}{2}\pi b^2\|\mathbf{z}\|^2}, \\ &= \frac{1}{2b^2} e^{-\frac{1}{2}\pi b^2\|\mathbf{z}\|^2}. \end{aligned} \tag{B.23}$$

Injecting this expression in Eq. (B.21) finally leads to

$$\mathrm{Cov}\left[s(\mathbf{0}), s(\mathbf{z})\right] = \frac{\mu}{4b^2}\cos\left(b\omega\mathbf{u}^\top\mathbf{z}\right) e^{-\frac{1}{2}\pi b^2\|z\|^2}. \tag{B.24}$$

B.4 Proof of Theorem 6

Let h denote the complex Gabor kernel defined for all $\mathbf{x} \in \mathbb{R}^2$,

$$h(\mathbf{x}) = e^{-\pi||\mathbf{x}||^2} e^{\mathbf{i}\omega \mathbf{u}^\top \mathbf{x}}, \tag{B.25}$$

where $\omega \in \mathbb{R}_+^*$, $\mathbf{u} = (\cos\alpha, \sin\alpha)^\top$ and $\alpha \in \left]-\frac{\pi}{2}; \frac{\pi}{2}\right]$. Because the Riesz transform is defined in the Fourier domain in Section 2.4.1, a preliminary step consists in calculating the 2D Fourier transform of h, denoted by $\widehat{h}$. Hence, for all $\xi \in \mathbb{R}^2$,

$$\begin{aligned} \widehat{h}(\xi) &= \int_{\mathbb{R}^2} e^{-\pi||\mathbf{x}||^2} e^{\mathbf{i}\omega \mathbf{u}^\top \mathbf{x}} e^{-\mathbf{i}\xi^\top \mathbf{x}} d\mathbf{x}, \\ &= \int_{\mathbb{R}^2} e^{-\pi||\mathbf{x}||^2} e^{-\mathbf{i}(\xi - \omega\mathbf{u})^\top \mathbf{x}} d\mathbf{x}. \end{aligned} \tag{B.26}$$

This is exactly the 2D Fourier transform of a Gaussian function evaluated at $\xi - \omega\mathbf{u}$. Appliyng the formula given in Theorem 1 with $a_1 = a_2 = \sqrt{\pi}$ leads to

$$\widehat{h}(\xi) = e^{-\frac{1}{4\pi}||\xi - \omega\mathbf{u}||^2}. \tag{B.27}$$

Let S denote the complex Gabor noise defined from the complex Gabor kernel h, *i.e.*, for all $\mathbf{x} \in \mathbb{R}^2$,

$$S(\mathbf{x}) = \sum_i e^{\mathbf{i}\psi_i} h\left(\mathbf{x} - \mathbf{x}_i\right), \tag{B.28}$$

where the random points $\mathbf{x}_i$ and phase-shifts ψ_i are defined as in Section 3.2.2. If the Riesz transform acts as a phase-shift operator, it can be expected that

$$\begin{cases} \mathcal{R}_1 h \approx -\mathbf{i}\cos(\alpha)\, h, \\ \mathcal{R}_2 h \approx -\mathbf{i}\sin(\alpha)\, h, \end{cases} \tag{B.29}$$

The proof now focuses only on $\mathcal{R}_1$, but similar developments can be done for $\mathcal{R}_2$. The goal is to compare the first Riesz transform of S, *i.e.*, $\mathcal{R}_1 S$, and the noise defined from the approximated Riesz transform of the Gabor kernel $-\mathbf{i}\cos(\alpha)\, h$ in terms of quadratic error. This noise, denoted by $\widetilde{S}$, can be expressed for all $\mathbf{x} \in \mathbb{R}^2$ as

$$\widetilde{S}(\mathbf{x}) = -\mathbf{i}\cos(\alpha) \sum_i e^{\mathbf{i}\psi_i} h\left(\mathbf{x} - \mathbf{x}_i\right). \tag{B.30}$$

To do so, the quadratic error is expressed by applying Proposition 3.1 of (Galerne 2010) recalled in Section 3, *i.e.*, for all $\mathbf{x} \in \mathbb{R}^2$,

$$\mathbb{E}\left[\left|\mathcal{R}_1 S(\mathbf{x}) - \widetilde{S}(\mathbf{x})\right|^2\right] = \mu \int_{\mathbb{R}^2} \left|\mathcal{R}_1 h(\mathbf{y}) + \mathbf{i}\cos(\alpha)\, h(\mathbf{y})\right|^2 d\mathbf{y}, \tag{B.31}$$

where μ denotes the intensity of the Poisson process from which the points $\mathbf{x}_i$ are generated. This is enabled by the stationarity of the noise (Galerne 2010). According to the Plancherel theorem, the Fourier transform is an isometry, meaning that it preserves the Euclidian norm of $L^2(\mathbb{R}^2)$. This implies that the quadratic error of Eq. (B.31), now denoted by D_S, can be calculated in the Fourier domain, *i.e.*,

$$D_S(\mathbf{x}) = \frac{\mu}{(2\pi)^2} \int_{\mathbb{R}^2} \left|\widehat{\mathcal{R}_1 h}(\xi) + \mathbf{i}\cos(\alpha)\, \widehat{h}(\xi)\right|^2 d\xi. \tag{B.32}$$

For all $\xi = (\xi_1, \xi_2) \in \mathbb{R}^2$, let θ_ξ denote an argument of the complex number $\xi_1 + \mathbf{i}\xi_2$. Then the Riesz transforms of h can be rewritten for all $\xi \in \mathbb{R}^2$ as

$$\begin{cases} \widehat{\mathcal{R}_1 h}(\xi) = -\mathbf{i}\cos(\theta_\xi)\,\widehat{h}(\xi), \\ \widehat{\mathcal{R}_2 h}(\xi) = -\mathbf{i}\sin(\theta_\xi)\,\widehat{h}(\xi), \end{cases} \tag{B.33}$$

The quadratic error $D_S(\mathbf{x})$ can hence be expressed for all $\mathbf{x} \in \mathbb{R}^2$ as

$$\begin{aligned} D_S(\mathbf{x}) &= \frac{\mu}{(2\pi)^2}\int_{\mathbb{R}^2} \left[\cos(\theta_\xi) - \cos(\alpha)\right]^2 \left|\widehat{h}(\xi)\right|^2 d\xi, \\ &= \frac{\mu}{(2\pi)^2}\int_{\mathbb{R}^2} \left[\cos(\theta_\xi) - \cos(\alpha)\right]^2 e^{-\frac{1}{2\pi}\|\xi - \omega\mathbf{u}\|^2} d\xi \end{aligned} \tag{B.34}$$

Using the substitution $\xi' = \xi - \omega\mathbf{u}$ then leads to

$$D_S(\mathbf{x}) = \frac{\mu}{(2\pi)^2}\int_{\mathbb{R}^2} \left[\cos(\theta_{\xi+\omega\mathbf{u}}) - \cos(\alpha)\right]^2 e^{-\frac{1}{2\pi}\|\xi\|^2} d\xi. \tag{B.35}$$

Let $\mathbf{u}^\perp$ denote the vector of $\mathbb{R}^2$ given by $\mathbf{u}^\perp = \begin{pmatrix} -\sin\alpha & \cos\alpha \end{pmatrix}^\top$. Because $\mathbf{u}$ and $\mathbf{u}^\perp$ form an orthonormal basis of $\mathbb{R}^2$ equipped with the scalar product, any 2D frequency ξ of $\mathbb{R}^2$ can be expressed as a linear combination of $\mathbf{u}$ and $\mathbf{u}^\perp$. Thus, for all $\mathbf{x} \in \mathbb{R}^2$, $D_S(\mathbf{x})$ can be expressed as

$$\begin{aligned} D_S(\mathbf{x}) &= \frac{\mu}{(2\pi)^2}\int_{\mathbb{R}^2} \left[\cos\left(\theta_{(\xi_1+\omega)\mathbf{u}+\xi_2\mathbf{u}^\perp}\right) - \cos(\alpha)\right]^2 e^{-\frac{1}{2\pi}(\xi_1^2+\xi_2^2)} d\xi_1 d\xi_2, \\ &= \frac{\mu}{(2\pi)^2}\int_{\mathbb{R}^2} \left[\left(\frac{(\xi_1+\omega)\,\mathbf{u} + \xi_2\mathbf{u}^\perp}{||\,(\xi_1+\omega)\,\mathbf{u} + \xi_2\mathbf{u}^\perp||} - \mathbf{u}\right)^\top \mathbf{e}_1\right]^2 e^{-\frac{1}{2\pi}(\xi_1^2+\xi_2^2)} d\xi_1 d\xi_2, \end{aligned} \tag{B.36}$$

where $\mathbf{e}_1 = \begin{pmatrix} 1 & 0 \end{pmatrix}^\top$. For all $(\xi_1, \xi_2) \in \mathbb{R}^2$, let $\Delta_\omega(\xi_1, \xi_2)$ denote the vector of $\mathbb{R}^2$ defined as

$$\Delta_\omega(\xi_1, \xi_2) = \frac{(\xi_1+\omega)\,\mathbf{u} + \xi_2\mathbf{u}^\perp}{||\,(\xi_1+\omega)\,\mathbf{u} + \xi_2\mathbf{u}^\perp||} - \mathbf{u}. \tag{B.37}$$

The Pythagorean theorem implies that the square of any of the coordinates of $\Delta_\omega(\xi_1, \xi_2)$ is necessarily lower than its Euclidian norm, hence,

$$\begin{aligned} \left[\Delta_\omega(\xi_1, \xi_2)^\top \mathbf{e}_1\right]^2 &\leq ||\Delta_\omega(\xi_1, \xi_2)||^2, \\ &= \left|\left|\frac{(\xi_1+\omega)\,\mathbf{u} + \xi_2\mathbf{u}^\perp}{\sqrt{(\xi_1+\omega)^2 + \xi_2^2}} - \mathbf{u}\right|\right|^2, \\ &= \left(\frac{\xi_1+\omega}{\sqrt{(\xi_1+\omega)^2 + \xi_2^2}} - 1\right)^2 + \frac{\xi_2^2}{(\xi_1+\omega)^2 + \xi_2^2}, \\ &= \frac{(\xi_1+\omega)^2}{(\xi_1+\omega)^2 + \xi_2^2} - 2\frac{\xi_1+\omega}{\sqrt{(\xi_1+\omega)^2 + \xi_2^2}} + 1 + \frac{\xi_2^2}{(\xi_1+\omega)^2 + \xi_2^2}, \\ &= 2\left(1 - \frac{\xi_1+\omega}{\sqrt{(\xi_1+\omega)^2 + \xi_2^2}}\right). \end{aligned} \tag{B.38}$$

Notice that for all $(\xi_1, \xi_2) \in \mathbb{R}^2$,

$$\left| \frac{\xi_1 + \omega}{\sqrt{(\xi_1 + \omega)^2 + \xi_2^2}} \right| \leq 1, \tag{B.39}$$

which implies that

$$\left[\Delta_\omega \left(\xi_1, \xi_2\right)^\top \mathbf{e}_1 \right]^2 \leq 4. \tag{B.40}$$

Moreover, if $\xi_1 + \omega \neq 0$, then,

$$\frac{\xi_1 + \omega}{\sqrt{(\xi_1 + \omega)^2 + \xi_2^2}} = \frac{1}{\sqrt{1 + \frac{\xi_2^2}{(\xi_1+\omega)^2}}}. \tag{B.41}$$

Let r be a real function defined for all $t \in \mathbb{R}_+$ by

$$r(t) = \frac{1}{2}t + \frac{1}{\sqrt{1+t}} - 1. \tag{B.42}$$

For all $t \in \mathbb{R}_+$, the derivative of r is well-defined and given by

$$r'(t) = \frac{1}{2} - \frac{1}{2\sqrt{(1+t)^3}}. \tag{B.43}$$

This quantity is positive for all $t \in \mathbb{R}_+$, which implies that r is an increasing function on $\mathbb{R}_+$. In particular, for all $t \in \mathbb{R}_+$,

$$\begin{aligned} r(t) \geq r(0) &\iff \frac{1}{2}t + \frac{1}{\sqrt{1+t}} - 1 \geq 0, \\ &\iff 1 - \frac{1}{\sqrt{1+t}} \leq \frac{1}{2}t. \end{aligned} \tag{B.44}$$

Applying this inequality to $t = \frac{\xi_2^2}{(\xi_1+\omega)^2}$ and injecting it in Eq. (B.38) finally leads to

$$\left[\Delta_\omega \left(\xi_1, \xi_2\right)^\top \mathbf{e}_1 \right]^2 \leq \frac{\xi_2^2}{(\xi_1 + \omega)^2}. \tag{B.45}$$

The inequalities (B.40) and (B.45) are now used to bound the expression of $D_S(\mathbf{x})$ given in Eq. (B.36). Hence, for all $\mathbf{x} \in \mathbb{R}^2$,

$$D_S(\mathbf{x}) \leq \underbrace{\frac{\mu}{(2\pi)^2} \int_{\mathbb{R}^2} \min\left(4, \frac{\xi_2^2}{(\xi_1 + \omega)^2}\right) e^{-\frac{1}{2\pi}(\xi_1^2+\xi_2^2)} d\xi_1 d\xi_2}_{I}. \tag{B.46}$$

The integral, denoted by I, is now split in two terms that will be bounded independently. Let I_1 and I_2 denote the integrals respectively defined as

$$\begin{cases} I_1 = \frac{\mu}{(2\pi)^2} \int_{\mathbb{R}} \int_{-\frac{\omega}{2}}^{\frac{\omega}{2}} \min\left(4, \frac{\xi_2^2}{(\xi_1+\omega)^2}\right) e^{-\frac{1}{2\pi}(\xi_1^2+\xi_2^2)} d\xi_1 d\xi_2, \\ I_2 = I - I_1. \end{cases} \tag{B.47}$$

After noticing that for all $\xi_1 \in \left[-\frac{\omega}{2}, \frac{\omega}{2}\right]$,

$$\frac{1}{(\xi_1+\omega)^2} \leq \frac{4}{\omega^2}, \tag{B.48}$$

I_1 can be bounded as follows,

$$\begin{aligned} I_1 &\leq \frac{\mu}{(2\pi)^2} \int_{\mathbb{R}} \int_{-\frac{\omega}{2}}^{\frac{\omega}{2}} \frac{4\xi_2^2}{\omega^2} e^{-\frac{1}{2\pi}(\xi_1^2+\xi_2^2)} d\xi_1 d\xi_2, \\ &\leq \frac{\mu}{(2\pi)^2} \int_{\mathbb{R}^2} \frac{4\xi_2^2}{\omega^2} e^{-\frac{1}{2\pi}(\xi_1^2+\xi_2^2)} d\xi_1 d\xi_2, \\ &= \frac{K_1}{\omega^2}, \end{aligned} \tag{B.49}$$

where

$$K_1 = \frac{\mu}{\pi^2} \int_{\mathbb{R}^2} \xi_2^2 e^{-\frac{1}{2\pi}(\xi_1^2+\xi_2^2)} d\xi_1 d\xi_2. \tag{B.50}$$

Notice that K_1 does not depend on ω. In the case of I_2, the inequality given in Eq. (B.48) does not hold anymore. Instead, the bound 4 given in Eq. (B.40) is used in Eq. (B.46), such that

$$\begin{aligned} I_2 &\leq \frac{\mu}{\pi^2} \int_{\mathbb{R}} \int_{\mathbb{R}\setminus\left[-\frac{\omega}{2},\frac{\omega}{2}\right]} e^{-\frac{1}{2\pi}(\xi_1^2+\xi_2^2)} d\xi_1 d\xi_2, \\ &= \frac{2\mu}{\pi^2} \int_{\mathbb{R}} \int_{\frac{\omega}{2}}^{+\infty} e^{-\frac{1}{2\pi}(\xi_1^2+\xi_2^2)} d\xi_1 d\xi_2, \end{aligned} \tag{B.51}$$

by using the symmetry of the integrated Gaussian function. This integral can be bounded by using the Lemma 2 sound in (Feller 1968), which states that for all $t \in \mathbb{R}_+^*$,

$$\int_t^{+\infty} e^{-\frac{y^2}{2}} dy \leq \frac{1}{t} e^{-\frac{t^2}{2}}, \tag{B.52}$$

which can be generalized as

$$\int_{\sigma t}^{+\infty} e^{-\frac{y^2}{2\sigma^2}} dy \leq \sigma \frac{1}{t} e^{-\frac{t^2}{2}}, \tag{B.53}$$

with $\sigma \in \mathbb{R}_+^*$. This implies in particular that for all $t \in \mathbb{R}_+^*$,

$$\int_{\sigma t}^{+\infty} e^{-\frac{y^2}{2\sigma^2}} dy \leq \frac{\sigma}{t^2}, \tag{B.54}$$

by using the fact that, for all $t \in \mathbb{R}_+^*$,

$$e^{-\frac{t^2}{2}} \leq \frac{1}{t}. \tag{B.55}$$

Applying this inequality with $t = \frac{\omega}{2\sigma}$ and $\sigma = \sqrt{\pi}$ leads to

$$\begin{aligned} I_2 &\leq \frac{8\mu}{\omega^2\sqrt{\pi}} \int_{\mathbb{R}} e^{-\frac{\xi_2^2}{2\pi}} d\xi_2, \\ &= \frac{K_2}{\omega^2}, \end{aligned} \tag{B.56}$$

where

$$K_2 = \frac{8\mu}{\sqrt{\pi}} \int_{\mathbb{R}} e^{-\frac{\xi_2^2}{2\pi}} d\xi_2. \tag{B.57}$$

Finally, combining Eq. (B.49) and (B.56) yields a uniform bound for the norm of the quadratic error between $\mathcal{R}_1 S$ and its expected approximation, *i.e.*, for all $\mathbf{x} \in \mathbb{R}^2$,

$$\mathbb{E}\left[\left|\mathcal{R}_1 S(\mathbf{x}) - \widetilde{S}(\mathbf{x})\right|^2\right] \leq \frac{K}{\omega^2}, \tag{B.58}$$

where $K = K_1 + K_2$. A similar bound can be obtained for $\mathcal{R}_2 S$. The scale parameter b is now included in the model. If $b \in \mathbb{R}_+^*$, let h_b denote the complex Gabor kernel defined for all $\mathbf{x} \in \mathbb{R}^2$,

$$\begin{aligned} h_b(\mathbf{x}) &= h(b\mathbf{x}), \\ &= e^{-\pi b^2 ||\mathbf{x}||^2} e^{\mathbf{i} b \omega \mathbf{u}^\top \mathbf{x}}. \end{aligned} \tag{B.59}$$

The complex Gabor noise with scale $b \in \mathbb{R}_+^*$ is similarly defined for all $\mathbf{x} \in \mathbb{R}^2$ as

$$S_b(\mathbf{x}) = \sum_i e^{\mathbf{i}\psi_i} h_b\left(\mathbf{x} - \mathbf{x}_i\right). \tag{B.60}$$

The goal now is to bound the error between $\mathcal{R}_1 S_b$ and the noise $\widetilde{S}_b$ defined for all $\mathbf{x} \in \mathbb{R}^2$ as

$$\widetilde{S}_b(\mathbf{x}) = -\mathbf{i}\cos\left(\alpha\right) \sum_i e^{\mathbf{i}\psi_i} h_b\left(\mathbf{x} - \mathbf{x}_i\right). \tag{B.61}$$

It can be easily verified that the Riesz transform commutes with changes of scale. Thus, for all $\mathbf{x} \in \mathbb{R}^2$, applying Proposition 3.1 in (Galerne 2010) again leads to

$$\begin{aligned} \mathbb{E}\left[\left|\mathcal{R}_1 S_b(\mathbf{x}) - \widetilde{S}_b(\mathbf{x})\right|^2\right] &= \mu \int_{\mathbb{R}^2} \left|\mathcal{R}_1 h_b(\mathbf{x}) + \mathbf{i}\cos\left(\alpha\right) h_b(\mathbf{x})\right|^2 d\mathbf{x}, \\ &= \mu \int_{\mathbb{R}^2} \left|\mathcal{R}_1 h(b\mathbf{x}) + \mathbf{i}\cos\left(\alpha\right) h(b\mathbf{x})\right|^2 d\mathbf{x}, \\ &= \frac{\mu}{b^2} \int_{\mathbb{R}^2} \left|\mathcal{R}_1 h(\mathbf{x}) + \mathbf{i}\cos\left(\alpha\right) h(\mathbf{x})\right|^2 d\mathbf{x}, \\ &= \frac{1}{b^2} \mathbb{E}\left[\left|\mathcal{R}_1 S(\mathbf{x}) - \widetilde{S}(\mathbf{x})\right|^2\right]. \end{aligned} \tag{B.62}$$

Applying the inequality given in Eq. (B.58) to bound the integral finally leads to

$$\mathbb{E}\left[\left|\mathcal{R}_1 S_b(\mathbf{x}) - \widetilde{S}_b(\mathbf{x})\right|^2\right] \leq \frac{K}{(b\omega)^2}. \tag{B.63}$$

Let s and H_s denote the real and imaginary parts of S_b, respectively. The complex noise $\widetilde{S}_b$ can then be expressed by using s and H_s, *i.e.*, for all $\mathbf{x} \in \mathbb{R}^2$,

$$
\begin{aligned}
\widetilde{S}_b(\mathbf{x}) &= -\mathbf{i}\cos(\alpha)\sum_i e^{\mathbf{i}\psi_i} h_b(\mathbf{x}-\mathbf{x}_i), \\
&= -\mathbf{i}\cos(\alpha)\sum_i e^{\mathbf{i}\psi_i} e^{-\pi b^2||\mathbf{x}-\mathbf{x}_i||^2} e^{\mathbf{i}b\omega\mathbf{u}^\top(\mathbf{x}-\mathbf{x}_i)}, \\
&= \cos(\alpha)\sum_i e^{\mathbf{i}\psi_i} e^{-\pi b^2||\mathbf{x}-\mathbf{x}_i||^2} e^{\mathbf{i}\left[b\omega\mathbf{u}^\top(\mathbf{x}-\mathbf{x}_i)-\frac{\pi}{2}\right]}, \\
&= \cos(\alpha)\sum_i e^{-\pi b^2||\mathbf{x}-\mathbf{x}_i||^2}\left\{\cos\left[b\omega\mathbf{u}^\top(\mathbf{x}-\mathbf{x}_i)+\psi_i-\frac{\pi}{2}\right]\right. \\
&\quad \left.+\mathbf{i}\sin\left[b\omega\mathbf{u}^\top(\mathbf{x}-\mathbf{x}_i)+\psi_i-\frac{\pi}{2}\right]\right\}, \\
&= \cos(\alpha)\sum_i e^{-\pi b^2||\mathbf{x}-\mathbf{x}_i||^2}\left\{\sin\left[b\omega\mathbf{u}^\top(\mathbf{x}-\mathbf{x}_i)+\psi_i\right]\right. \\
&\quad \left.-\mathbf{i}\cos\left[b\omega\mathbf{u}^\top(\mathbf{x}-\mathbf{x}_i)+\psi_i\right]\right\}, \\
&= \cos(\alpha)\left[H_s(\mathbf{x})-\mathbf{i}s(\mathbf{x})\right].
\end{aligned}
\tag{B.64}
$$

Therefore, for all $\mathbf{x}\in\mathbb{R}^2$,

$$
\begin{aligned}
\mathbb{E}\left[\left|\mathcal{R}_1 s(\mathbf{x})-\cos(\alpha)H_s(\mathbf{x})\right|^2\right] &= \mathbb{E}\left[\left|\Re\left\{\mathcal{R}_1 S(\mathbf{x})-\widetilde{S}(\mathbf{x})\right\}\right|^2\right], \\
&\leq \mathbb{E}\left[\left|\mathcal{R}_1 S(\mathbf{x})-\widetilde{S}(\mathbf{x})\right|^2\right], \\
&\leq \frac{K}{(b\omega)^2}.
\end{aligned}
\tag{B.65}
$$

Similarly, for all $\mathbf{x}\in\mathbb{R}^2$,

$$
\mathbb{E}\left[\left|\mathcal{R}_2 s(\mathbf{x})-\sin(\alpha)H_s(\mathbf{x})\right|^2\right] \leq \frac{K}{(b\omega)^2}.
\tag{B.66}
$$

B.5 Proofs of the results given Section 3.4

Rewriting of the quaterionic involution of Section 3.4.2 as a linear operator

$$\begin{aligned}
T_\theta(\mathbf{x}) &= -\mathbf{u}_\theta \mathbf{x} \mathbf{u}_\theta \\
&= -\left[\cos(\theta)\,\mathbf{i} + \sin(\theta)\,\mathbf{j}\right](x_0 + x_1\mathbf{i} + x_2\mathbf{j})\left[\cos(\theta)\,\mathbf{i} + \sin(\theta)\,\mathbf{j}\right], \\
&= x_0\cos^2(\theta) + x_0\cos(\theta)\sin(\theta)\,\mathbf{k} + x_1\cos^2(\theta)\,\mathbf{i} + x_1\cos(\theta)\sin(\theta)\,\mathbf{j} \\
&\quad - x_2\cos^2(\theta)\,\mathbf{j} + x_2\cos(\theta)\sin(\theta)\,\mathbf{i} - x_0\cos(\theta)\sin(\theta)\,\mathbf{k} + x_0\sin^2(\theta) \\
&\quad + x_1\cos(\theta)\sin(\theta)\,\mathbf{j} - x_1\sin^2(\theta)\,\mathbf{i} + x_2\cos(\theta)\sin(\theta)\,\mathbf{i} + x_2\sin^2(\theta)\,\mathbf{j}, \\
&= x_0 + \left[x_1\cos^2(\theta) - x_1\sin^2(\theta) + 2x_2\cos(\theta)\sin(\theta)\right]\mathbf{i} \\
&\quad + \left[-x_2\cos^2(\theta) + x_2\sin^2(\theta) + 2x_1\cos(\theta)\sin(\theta)\right]\mathbf{j}, \\
&= x_0 + \left[x_1\cos(2\theta) + x_2\sin(2\theta)\right]\mathbf{i} + \left[x_1\sin(2\theta) - x_2\cos(2\theta)\right]\mathbf{j}.
\end{aligned} \tag{B.67}$$

This can be expressed in $\mathbb{R}^3$ as

$$\begin{aligned}
T_\theta(\mathbf{x}) &= \begin{pmatrix} 1 & 0 & 0 \\ 0 & \cos(2\theta) & \sin(2\theta) \\ 0 & \sin(2\theta) & -\cos(2\theta) \end{pmatrix} \begin{pmatrix} x_0 \\ x_1 \\ x_2 \end{pmatrix}, \\
&= \begin{pmatrix} 1 & 0 & 0 \\ 0 & \cos(2\theta) & -\sin(2\theta) \\ 0 & \sin(2\theta) & \cos(2\theta) \end{pmatrix} \begin{pmatrix} 1 & 0 & 0 \\ 0 & 1 & 0 \\ 0 & 0 & -1 \end{pmatrix} \begin{pmatrix} x_0 \\ x_1 \\ x_2 \end{pmatrix}.
\end{aligned} \tag{B.68}$$

Proof of Theorem 7

If the monogenic signal of s, denoted by M_s, is seen as a vector of $\mathbb{R}^3$, the distance d_s defined in Eq. (3.31) can be expressed as

$$d_s = \min_\theta \left\{ \mathbb{E}\left[\frac{1}{2}\left\|M_s - T_\theta(M_s)\right\|^2\right]\right\}, \tag{B.69}$$

where $\|.\|$ denotes the Euclidian norm of $\mathbb{R}^3$. Because T_θ is an isometry (Via et al. 2010), the vectors M_s and $T_\theta(M_s)$ both have the same norm. This yields a different expression of the Euclidian distance between M_s and $T_\theta(M_s)$, *i.e.*,

$$\begin{aligned}
\|M_s - T_\theta(M_s)\|^2 &= \|M_s\|^2 + \|T_\theta(M_s)\|^2 - 2M_s^\top T_\theta(M_s), \\
&= 2\|M_s\|^2 - 2M_s^\top T_\theta(M_s).
\end{aligned} \tag{B.70}$$

The measure of directionality d_s can hence be expressed as

$$d_s = \mathbb{E}\left[\|M_s\|^2\right] - \max_\theta \mathbb{E}\left[M_s^\top T_\theta(M_s)\right]. \tag{B.71}$$

The term $\mathbb{E}\left[\|M_s\|^2\right]$ can be expressed with the variances of s and its two Riesz transforms, *i.e.*,

$$\begin{aligned}\mathbb{E}\left[\|M_s\|^2\right] &= \mathbb{E}\left[s^2 + (\mathcal{R}_1 s)^2 + (\mathcal{R}_2 s)^2\right], \\ &= \mathbb{E}\left[s^2\right] + \mathbb{E}\left[(\mathcal{R}_1 s)^2\right] + \mathbb{E}\left[(\mathcal{R}_2 s)^2\right], \\ &= \mathrm{Var}(s) + \mathrm{Var}(\mathcal{R}_1 s) + \mathrm{Var}(\mathcal{R}_2 s), \\ &= 2\,\mathrm{Var}(s) \text{ (see Eq. (3.33))}.\end{aligned} \tag{B.72}$$

The scalar product $M_s^\top T_\theta(M_s)$ is now expressed as a quadratic form applied to a unit vector of $\mathbb{R}^2$, *i.e.*,

$$\begin{aligned}M_s^\top T_\theta(M_s) &= \begin{pmatrix} s & \mathcal{R}_1 s & \mathcal{R}_2 s \end{pmatrix} \begin{pmatrix} s \\ \mathcal{R}_1 s \cos(2\theta) + \mathcal{R}_2 s \sin(2\theta) \\ \mathcal{R}_1 s \sin(2\theta) - \mathcal{R}_2 s \cos(2\theta) \end{pmatrix}, \\ &= s^2 + \mathcal{R}_1 s^2 \cos(2\theta) + 2\mathcal{R}_1 s \mathcal{R}_2 s \sin(2\theta) - \mathcal{R}_2 s^2 \cos(2\theta), \\ &= s^2 - \mathcal{R}_1 s^2 - \mathcal{R}_2 s^2 + 2\mathcal{R}_1 s^2 \cos^2\theta + 2\mathcal{R}_2 s^2 \sin^2\theta \\ &\quad + 4\mathcal{R}_1 s \mathcal{R}_2 s \cos\theta \sin\theta, \\ &= \left(s^2 + \mathcal{R}_1 s^2 - \mathcal{R}_2 s^2\right)\cos^2\theta + \left(s^2 - \mathcal{R}_1 s^2 + \mathcal{R}_2 s^2\right)\sin^2\theta \\ &\quad + 4\mathcal{R}_1 s \mathcal{R}_2 s \cos\theta \sin\theta.\end{aligned} \tag{B.73}$$

The mean of $M_s^\top T_\theta(M_s)$ is obtained by applying the mean operator $\mathbb{E}$ to all its terms. Because these terms are all zero-mean, this leads to

$$\begin{aligned}\mathbb{E}\left[M_s^\top T_\theta(M_s)\right] &= \left[\mathrm{Var}(s) + \mathrm{Var}\left(\mathcal{R}_1 s\right) - \mathrm{Var}\left(\mathcal{R}_2 s\right)\right]\cos^2\theta \\ &\quad + \left[\mathrm{Var}(s) - \mathrm{Var}\left(\mathcal{R}_1 s\right) + \mathrm{Var}\left(\mathcal{R}_2 s\right)\right]\sin^2\theta \\ &\quad + 4\,\mathrm{Cov}\left(\mathcal{R}_1 s, \mathcal{R}_2 s\right)\cos\theta\sin\theta.\end{aligned} \tag{B.74}$$

Remember that the respective variances of s and its Riesz transforms are linked by Eq. (3.33), which yields

$$\begin{aligned}\mathbb{E}\left[M_s^\top T_\theta(M_s)\right] &= 2\,\mathrm{Var}\left(\mathcal{R}_1 s\right)\cos^2\theta + 2\,\mathrm{Var}\left(\mathcal{R}_2 s\right)\sin^2\theta \\ &\quad + 4\,\mathrm{Cov}\left(\mathcal{R}_1 s, \mathcal{R}_2 s\right)\cos\theta\sin\theta, \\ &= 2\,\mathrm{Var}\left(\mathcal{R}_1 s\cos\theta + \mathcal{R}_2 s\sin\theta\right), \\ &= 2\,\mathrm{Var}\left(\mathbf{u}_\theta^\top \mathcal{R} s\right).\end{aligned} \tag{B.75}$$

where $\mathbf{u}_\theta$ is the unit vector of $\mathbb{R}^2$ with argument θ. Injecting this expression in Eq. (B.71) then completes the proof.

Eigenvalues and eigenvectors of the stochastic structure tensor defined in Section 3.4.3

From now, the coefficients of the structure tensor T_s are denoted by

$$T_s = \begin{pmatrix} T_{11} & T_{12} \\ T_{12} & T_{22} \end{pmatrix}, \tag{B.76}$$

To express the eigenvalues of T_s, its characteristic polynomial, denoted by $P_T(X)$, is first calculated.

$$\begin{aligned} P_T(X) &= (T_{11} - X)(T_{22} - X) - T_{12}^2 \\ &= X^2 - (T_{11} + T_{22})X + T_{11}T_{22} - T_{12}^2 \end{aligned} \tag{B.77}$$

The eigenvalues of T_s, denoted by λ_+ and λ_-, respectively, with $0 \leq \lambda_- \leq \lambda_+$ are hence given by

$$\begin{cases} \lambda_+ = \frac{1}{2}\left(T_{11} + T_{22} + \sqrt{(T_{11} - T_{22})^2 + 4T_{12}^2}\right), \\ \lambda_- = \frac{1}{2}\left(T_{11} + T_{22} - \sqrt{(T_{11} - T_{22})^2 + 4T_{12}^2}\right). \end{cases} \tag{B.78}$$

Applying these formulas to the coefficients of T_s leads to

$$\begin{cases} \lambda_+ = \frac{1}{2}\left(\mathrm{Var}(s) + \sqrt{[\mathrm{Var}(\mathcal{R}_1 s) - \mathrm{Var}(\mathcal{R}_2 s)]^2 + 4\,\mathrm{Cov}(\mathcal{R}_1 s, \mathcal{R}_2 s)^2}\right), \\ \lambda_- = \frac{1}{2}\left(\mathrm{Var}(s) - \sqrt{[\mathrm{Var}(\mathcal{R}_1 s) - \mathrm{Var}(\mathcal{R}_2 s)]^2 + 4\,\mathrm{Cov}(\mathcal{R}_1 s, \mathcal{R}_2 s)^2}\right). \end{cases} \tag{B.79}$$

An eigenvector $\mathbf{x} \in \mathbb{R}^2$ of T_s associated with λ_+ must now be determined.

$$\begin{aligned} T\mathbf{x} = \lambda_+\mathbf{x} &\iff \begin{cases} T_{11}x_1 + T_{12}x_2 = \frac{1}{2}\left(T_{11} + T_{22} + \sqrt{(T_{11} - T_{22})^2 + 4T_{12}^2}\right)x_1 \\ T_{12}x_1 + T_{22}x_2 = \frac{1}{2}\left(T_{11} + T_{22} + \sqrt{(T_{11} - T_{22})^2 + 4T_{12}^2}\right)x_2 \end{cases}, \\ &\iff \begin{cases} \left(T_{22} - T_{11} + \sqrt{(T_{11} - T_{22})^2 + 4T_{12}^2}\right)x_1 - 2T_{12}x_2 = 0 \\ 2T_{12}x_1 + \left(T_{22} - T_{11} - \sqrt{(T_{11} - T_{22})^2 + 4T_{12}^2}\right)x_1 = 0 \end{cases}, \\ &\iff \begin{cases} \mathbf{x} \in \mathbb{R}\mathbf{u}_1 \\ \mathbf{x} \in \mathbb{R}\mathbf{u}_2 \end{cases}, \end{aligned} \tag{B.80}$$

with

$$\begin{cases} \mathbf{u}_1 = \begin{pmatrix} 2T_{12} \\ T_{22} - T_{11} + \sqrt{(T_{11} - T_{22})^2 + 4T_{12}^2} \end{pmatrix}, \\ \mathbf{u}_2 = \begin{pmatrix} T_{11} - T_{22} + \sqrt{(T_{11} - T_{22})^2 + 4T_{12}^2} \\ 2T_{12} \end{pmatrix}. \end{cases} \tag{B.81}$$

Notice that $\mathbf{u}_1$ and $\mathbf{u}_2$ are colinear, *i.e.*,

$$\mathbf{u}_2 = \frac{T_{11} - T_{22} + \sqrt{(T_{11} - T_{22})^2 + 4T_{12}^2}}{2T_{12}}\mathbf{u}_1, \tag{B.82}$$

which implies that $\mathbb{R}\mathbf{u}_1$ and $\mathbb{R}\mathbf{u}_2$ are the same vector space, *i.e.*, the eigenspace of T_s associated with λ_+, which is of dimension 1. From now, $\mathbf{u}_+$ denotes the eigenvector $\mathbf{u}_2$, and z_+ denotes its affix. Then,

$$
\begin{aligned}
z_+^2 &= \left(T_{11} - T_{22} + \sqrt{(T_{11} - T_{22})^2 + 4T_{12}^2} + 2\mathbf{i}T_{12}\right)^2 \\
&= (T_{11} - T_{22})^2 + (T_{11} - T_{22})^2 + 4T_{12}^2 - 4T_{12}^2 + 4\mathbf{i}\,(T_{11} - T_{22})\,T_{12} \\
&\quad + 2\,(T_{11} - T_{22})\sqrt{(T_{11} - T_{22})^2 + 4T_{12}^2} + 4\mathbf{i}T_{12}\sqrt{(T_{11} - T_{22})^2 + 4T_{12}^2} \\
&= 2\,(T_{11} - T_{22})^2 + 2\,(T_{11} - T_{22})\sqrt{(T_{11} - T_{22})^2 + 4T_{12}^2} \\
&\quad + 4\mathbf{i}T_{12}\left(T_{11} - T_{22} + \sqrt{(T_{11} - T_{22})^2 + 4T_{12}^2}\right) \\
&= 2\left(T_{11} - T_{22} + \sqrt{(T_{11} - T_{22})^2 + 4T_{12}^2}\right)(T_{11} - T_{22} + 2\mathbf{i}T_{12})
\end{aligned}
\tag{B.83}
$$

The argument of z_+, *i.e.*, the orientation of $\mathbf{u}_+$, denoted by θ_+, can then be expressed by using this equality. Assuming that $T_{12} \neq 0$ (which is the case for non degenerated images (Soulard 2012)), the factor $T_{11} - T_{22} + \sqrt{(T_{11} - T_{22})^2 + 4T_{12}^2}$ is strictly positive, hence,

$$
\begin{aligned}
&\arg\left(z_+^2\right) = \arg\left[2\left(T_{11} - T_{22} + \sqrt{(T_{11} - T_{22})^2 + 4T_{12}^2}\right)(T_{11} - T_{22} + 2\mathbf{i}T_{12})\right]\ [2\pi], \\
&\iff 2\arg\left(z_+\right) = \arg\left(T_{11} - T_{22} + 2\mathbf{i}T_{12}\right)\ [2\pi], \\
&\iff \theta_+ = \frac{1}{2}\arg\left(T_{11} - T_{22} + 2\mathbf{i}T_{12}\right)\ [2\pi].
\end{aligned}
\tag{B.84}
$$

Because T_s is symmetric and positive-definite, its eigenvectors are orthogonal, which implies that $\theta_- = \theta_+ \pm \frac{\pi}{2}$. The eigenvectors $\mathbf{u}_+ = (\cos\theta_+, \sin\theta_+)^\top$ and $\mathbf{u}_- = (\cos\theta_-, \sin\theta_-)^\top$ then yield a new expression for the term $\mathbf{u}_\theta^\top T_s \mathbf{u}_\theta$ of Eq. (3.35) by diagonalizing T_s in the orthonormal basis formed by $\mathbf{u}_+$ and $\mathbf{u}_-$, *i.e.*,

$$
\mathbf{u}_\theta^\top T_s \mathbf{u}_\theta = \begin{pmatrix}\cos\theta & \sin\theta\end{pmatrix} \underbrace{H \begin{pmatrix}\lambda_+ & 0 \\ 0 & \lambda_-\end{pmatrix} H^\top}_{T_s} \begin{pmatrix}\cos\theta \\ \sin\theta\end{pmatrix}, \tag{B.85}
$$

where

$$
H = \begin{pmatrix}\cos\theta_+ & \cos\theta_- \\ \sin\theta_+ & \sin\theta_-\end{pmatrix} \tag{B.86}
$$

is the transformation matrix between the canonical basis and the orthonormal basis $(\mathbf{u}_+, \mathbf{u}_-)$. This expression can be furthered simplified, *i.e.*,

$$
\begin{aligned}
\mathbf{u}_\theta^\top T_s \mathbf{u}_\theta &= \begin{pmatrix}\cos\theta & \sin\theta\end{pmatrix} H \begin{pmatrix}\lambda_+ & 0\\ 0 & \lambda_-\end{pmatrix} H^T \begin{pmatrix}\cos\theta\\ \sin\theta\end{pmatrix}, \\
&= \left[\lambda_+ \cos^2(\theta_+) + \lambda_- \cos^2(\theta_-)\right] \cos^2\theta \\
&\quad + 2\left[\lambda_+ \cos(\theta_+)\sin(\theta_+) + \lambda_- \cos(\theta_-)\sin(\theta_-)\right] \cos\theta\sin\theta \\
&\quad + \left[\lambda_+ \sin^2(\theta_+) + \lambda_- \sin^2(\theta_-)\right] \sin^2\theta, \\
&= \lambda_+ \left[\cos^2(\theta_+)\cos^2\theta + 2\cos(\theta_+)\sin\theta_+\cos\theta\sin\theta + \sin^2(\theta_+)\sin^2\theta\right] \\
&\quad + \lambda_- \left[\cos^2(\theta_-)\cos^2\theta + 2\cos(\theta_-)\sin\theta_-\cos\theta\sin\theta + \sin^2(\theta_-)\sin^2\theta\right], \\
&= \lambda_+ \left[\cos(\theta_+)\cos\theta + \sin(\theta_+)\sin\theta\right]^2 + \lambda_- \left[\cos(\theta_-)\cos\theta + \sin(\theta_-)\sin\theta\right]^2, \\
&= \lambda_+ \cos^2(\theta_+ - \theta) + \lambda_- \cos^2(\theta_- - \theta).
\end{aligned}
\tag{B.87}
$$

As said earlier, the eigenvectors $\mathbf{u}_+$ and $\mathbf{u}_-$ are orthogonal, which implies that θ_- is equal to $\theta_+ \pm \frac{\pi}{2}$ (depending on which eigenvector has been chosen). Choosing $\theta_- = \theta_+ + \frac{\pi}{2}$ or $\theta_- = \theta_+ - \frac{\pi}{2}$ is equivalent because Eq. (B.87) involves square cosines. Hence,

$$
\begin{aligned}
\mathbf{u}_\theta^\top T_s \mathbf{u}_\theta &= \lambda_+ \cos^2(\theta_+ - \theta) + \lambda_- \cos^2\left(\theta_+ + \frac{\pi}{2} - \theta\right), \\
&= \lambda_+ \cos^2(\theta_+ - \theta) + \lambda_- \sin^2(\theta_+ - \theta).
\end{aligned}
\tag{B.88}
$$

Remember that $\lambda_- \leq \lambda_+$, which implies that $\lambda_- \leq \mathbf{u}_\theta^\top T_s \mathbf{u}_\theta \leq \lambda_+$. Furthermore, the value λ_- is reached for $\theta = \theta_-$, while λ_+ is reached for $\theta = \theta_+$. This shows that the term $\mathbf{u}_\theta^\top T_s \mathbf{u}_\theta$ is maximal when calculated along the eigenvector of T_s associated with its greatest eigenvalue, and minimal when calculated along the eigenvector of T_s associated with its smallest eigenvalue.

CHAPTER 4

The elliptic color model and the color Gabor noise

While Chapters 2 and 3 have established reliable tools to extract the local features of greyscale textures by the use of the monogenic signal, the case of color images has not been tackled yet. Thus, this chapter aims at generalizing these tools to color textures. A special focus is put on the Gabor and phasor noise models discussed in Section 3, for which no formal color generalization has been introduced yet according to the author's knowledge. To do so, a color oscillating texture model must be introduced. In the case of 1D time signals, numerous works deal with the vectorial extension of the analytic signal and the instantaneous measures of energy, structure and frequency it provides (see, *e.g.*, (Lilly 2011, Olhede 2013)). A non-marginal treatment of bivariate time signals was introduced in (René, Fitter, Forsyth, Kim, Murray, Walters & Westerman 1986) and further studied in (Diallo, Kulesh, Holschneider, Scherbaum & Adler 2006) to handle seismic data, while a similar approach was used in (Lilly & Gascard 2006, Lilly & Olhede 2010) in the field of oceanography. The underlying idea in these works is the modeling of bivariate time signals as a dynamic 2D ellipse whose geometric parameters are directly linked to the instantaneous features of the signal. Later works such as (Lilly 2011, Olhede 2013) have extended this elliptic approach to trivariate time signals.

While these works do not mention any color aspect, their non-marginal treatment of trivariate signals makes them interesting in the perspective of a color extension of oscillating textures. Indeed, the notions of local energy, structure and orientation of a 2D oscillating image play a similar role as the instantaneous features of a 1D time signal (Felsberg & Sommer 2001). This observation suggests adapting the elliptic approach to 2D color textures. This is exactly the idea of (Soulard & Carré 2015), where a generalization of the elliptical model to color images $s : \mathbb{R}^2 \to \mathbb{R}^3$ is introduced. Similarly to the 1D case, one of the main advantages of this approach is its non-marginal treatment of multivariate oscillations. Indeed, the interdependency of the color channels is automatically taken into account by modeling the oscillations as a 3D geometrical trajectory inside the RGB cube rather than three separate univariate signals. The direct link between the color parameters of the image and the shape and position of the ellipse is also what makes this model of great interest in the field of both color texture analysis and synthesis.

The main contribution of this chapter is hence to extend the elliptic color model of (Soulard & Carré 2015) to stochastic textures, in order to define a proper color generalization of the Gabor noise that provides a full control over the color content of the synthesized image. Indeed, even though color textures are presented in works dealing with Gabor noises such as (Galerne et al. 2012, Tricard et al. 2019), no color model is formally introduced therein.

In many semi-procedural approaches, scalar Gabor noises are synthesized along the three color axes that maximize either uncorrelation (through a PCA) or independence in the exemplar texture (Galerne et al. 2012). With such techniques, the color texture is marginally synthesized in a decorrelated color space extracted from a real texture, which leaves the color covariances unmodeled. This is what motivates the choice of the elliptic approach to introduce a proper color Gabor noise, from which a color phasor noise can be derived. Following the works of (Tricard et al. 2019, Tricard, Tavernier, Zanni, Martinez, Hugron, Neyret & Lefebvre 2020) in the greyscale case, not only single Gabor noises are considered but also sums of Gabor noises of different wave vectors. Because only unidirectional deterministic color waves are considered in (Soulard & Carré 2015), this implies generalizing the elliptic color model to stochastic textures displaying richer frequency contents.

The rest of the chapter is organized as follows. The color wave model and the parametrization of the ellipse are first detailed in Section 4.1 in the case of deterministic color waves, with a strong emphasis on the direct control over the color content provided by its parameters. This model is then used to introduce the color phasor noise in Section 4.2, which yields a useful tool to generate color textures with prescribed frequency and color content. Section 4.3 further studies the color phasor noise by linking the color covariances to the elliptic parameters and the color information of the synthesized texture.

4.1 Color cosine wave and elliptical representation

4.1.1 Color cosine wave

A key step in (Soulard & Carré 2015) is to define a proper monochromatic color wave, from which notions of amplitude and phase can be derived. The 2D cosine wave of the greyscale case can hence be generalized to color images as a function $s = \begin{pmatrix} s^R & s^G & s^B \end{pmatrix}^\top : \mathbb{R}^2 \to \mathbb{R}^3$ where each color component s^C, $C \in \{R, G, B\}$, is a cosine wave with the same wave vector and channel-specific amplitudes and phase-shifts, denoted by A^C and φ^C, respectively (Soulard & Carré 2015). However, unlike (Soulard & Carré 2015), the version of the model presented here also includes an offset at each color channel, denoted by $s_0^C \in [0, 1]$. This ensures that the wave s is wholly contained in the RGB cube $[0, 1]^3$. If $\mathbf{x} \in \mathbb{R}^2$, this can be summed up as

$$s(\mathbf{x}) = \begin{pmatrix} s_0^R + A^R \cos\left(\omega \mathbf{u}^\top \mathbf{x} + \varphi^R\right) \\ s_0^G + A^G \cos\left(\omega \mathbf{u}^\top \mathbf{x} + \varphi^G\right) \\ s_0^B + A^B \cos\left(\omega \mathbf{u}^\top \mathbf{x} + \varphi^B\right) \end{pmatrix}, \tag{4.1}$$

where $\omega \in \mathbb{R}_+^*$, $\mathbf{u} = (\cos\alpha, \sin\alpha)^\top$, $\alpha \in \left]-\frac{\pi}{2}; \frac{\pi}{2}\right]$, and for all $C \in \{R, G, B\}$, $A^C \in \left[0, \frac{1}{2}\right]$ and $\varphi^C \in]-\pi, \pi]$. Again, in order to ensure that s takes its values in $[0, 1]^3$, *i.e.*, inside the RGB cube, the amplitudes A^C must lie between 0 and $\min\left\{s_0^C, 1 - s_0^C\right\}$. At this stage, it is not obvious at all that the set of points $\left\{s(\mathbf{x}), \mathbf{x} \in \mathbb{R}^2\right\}$ is an ellipse, hence the need of further developments. Indeed, using the trigonometric identity $\cos(a + b) = \cos(a)\cos(b) - \sin(a)\sin(b)$ leads to

$$s(\mathbf{x}) = \mathbf{s}_0 + \cos(\omega \mathbf{u}^\top \mathbf{x})\mathbf{v} + \sin(\omega \mathbf{u}^\top \mathbf{x})\mathbf{w}, \tag{4.2}$$

where

$$\begin{cases} \mathbf{s}_0 = \begin{pmatrix} s_0^R & s_0^G & s_0^B \end{pmatrix}^\top, \\ \mathbf{v} = \begin{pmatrix} A^R \cos\left(\varphi^R\right) & A^G \cos\left(\varphi^G\right) & A^B \cos\left(\varphi^B\right) \end{pmatrix}^\top, \\ \mathbf{w} = -\begin{pmatrix} A^R \sin\left(\varphi^R\right) & A^G \sin\left(\varphi^G\right) & A^B \sin\left(\varphi^B\right) \end{pmatrix}^\top. \end{cases} \tag{4.3}$$

This equation is exactly the parametric representation of an ellipse in $\mathbb{R}^3$, with $\mathbf{u}$ and $\mathbf{v}$ directing its two axes and $\mathbf{s}_0$ being its center. However, this representation does not provide any intuitive information about how the color wave oscillates inside the RGB cube, and is hence of little practical interest. Sections 4.1.2 and 4.1.3 detail the more useful parametrization of the ellipse given in (Soulard & Carré 2015).

4.1.2 Shape of the ellipse

As stated in (Soulard & Carré 2015), the color wave defined by Eq. (4.1) is intrinsically 1D, *i.e.*, it only depends on a 1D variable, which is $t = \omega \mathbf{u}^\top \mathbf{x}$ for all $\mathbf{x} \in \mathbb{R}^2$. Consequently, in (Soulard & Carré 2015), the parameters of the ellipse are expressed by using a 1D variable. Though this section only aims at recalling the main results of the elliptic model and does not introduce more complex textures yet, the proofs are performed with a 2D variable rather than a 1D variable. This enables a more straightforward generalization when color phasor noises are introduced in Section 4.2. Before localizing the ellipse inside the RGB cube, its shape is first determined by calculating the length of its axes. The semi-minor axis and semi-major axis values, denoted by r_- and r_+, respectively, can be expressed by optimizing the Euclidian distance between s and its offset $\mathbf{s}_0$ (Soulard & Carré 2015), *i.e.*,

$$\begin{cases} {r_-}^2 = \min_{\mathbf{x}} \|s(\mathbf{x}) - \mathbf{s}_0\|^2, \\ {r_+}^2 = \max_{\mathbf{x}} \|s(\mathbf{x}) - \mathbf{s}_0\|^2. \end{cases} \tag{4.4}$$

The quantity $\|s(\mathbf{x}) - \mathbf{s}_0\|^2$ is now calculated to get analytic expressions of r_- and r_+. For the sake of simplicity, the three color components are condensed into one via a sum indexed by the color channel. Thus,

$$\begin{aligned} \|s(\mathbf{x}) - \mathbf{s}_0\|^2 &= \sum_{C \in \{R,G,B\}} \left[\left(A^C\right)^2 \cos^2\left(\omega \mathbf{u}^\top \mathbf{x} + \varphi^C\right) \right], \\ &= \frac{1}{2} \sum_{C \in \{R,G,B\}} \left\{ \left(A^C\right)^2 \left[\cos\left(2\omega \mathbf{u}^\top \mathbf{x} + 2\varphi^C\right) + 1 \right] \right\}. \end{aligned} \tag{4.5}$$

Let A^2 denote the sum of the squares of the amplitudes, *i.e.*,

$$A^2 = \left(A^R\right)^2 + \left(A^G\right)^2 + \left(A^B\right)^2. \tag{4.6}$$

Then,

$$\begin{aligned}
\|s(\mathbf{x}) - \mathbf{s}_0\|^2 &= \frac{1}{2}A^2 + \frac{1}{2}\sum_{C\in\{R,G,B\}}\left[\left(A^C\right)^2\cos\left(2\omega\mathbf{u}^\top\mathbf{x} + 2\varphi^C\right)\right], \\
&= \frac{1}{2}A^2 + \frac{1}{2}\sum_{C\in\{R,G,B\}}\left\{\left(A^C\right)^2\left[\cos\left(2\omega\mathbf{u}^\top\mathbf{x}\right)\cos\left(2\varphi^C\right)\right.\right. \\
&\quad \left.\left. - \sin\left(2\omega\mathbf{u}^\top\mathbf{x}\right)\sin\left(2\varphi^C\right)\right]\right\}, \\
&= \frac{1}{2}A^2 + \frac{1}{2}\cos\left(2\omega\mathbf{u}^\top\mathbf{x}\right)\sum_{C\in\{R,G,B\}}\left[\left(A^C\right)^2\cos\left(2\varphi^C\right)\right] \\
&\quad - \frac{1}{2}\sin\left(2\omega\mathbf{u}^\top\mathbf{x}\right)\sum_{C\in\{R,G,B\}}\left[\left(A^C\right)^2\sin\left(2\varphi^C\right)\right].
\end{aligned} \tag{4.7}$$

Let Γ denote the color Fourier atom defined as the complex-valued vector

$$\Gamma = \begin{pmatrix} A^R e^{\mathbf{i}\varphi^R} \\ A^G e^{\mathbf{i}\varphi^G} \\ A^B e^{\mathbf{i}\varphi^B} \end{pmatrix}. \tag{4.8}$$

Then, it can be easily shown that

$$\Gamma^\top\Gamma = \sum_{C\in\{R,G,B\}}\left[\left(A^C\right)^2\cos\left(2\varphi^C\right)\right] + \mathbf{i}\sum_{C\in\{R,G,B\}}\left[\left(A^C\right)^2\sin\left(2\varphi^C\right)\right] \tag{4.9}$$

Combining Eq. (4.7) and Eq. (4.9) leads to

$$\begin{aligned}
\|s(\mathbf{x}) - \mathbf{s}_0\|^2 &= \frac{1}{2}A^2 + \frac{1}{2}\cos\left(2\omega\mathbf{u}^\top\mathbf{x}\right)\Re\left(\Gamma^\top\Gamma\right) - \frac{1}{2}\sin\left(2\omega\mathbf{u}^\top\mathbf{x}\right)\Im\left(\Gamma^\top\Gamma\right), \\
&= \frac{1}{2}A^2 + \frac{1}{2}\cos\left(2\omega\mathbf{u}^\top\mathbf{x}\right)|\Gamma^\top\Gamma|\cos\left[\arg\left(\Gamma^\top\Gamma\right)\right] \\
&\quad - \frac{1}{2}\sin\left(2\omega\mathbf{u}^\top\mathbf{x}\right)|\Gamma^\top\Gamma|\sin\left[\arg\left(\Gamma^\top\Gamma\right)\right], \\
&= \frac{1}{2}A^2 + \frac{1}{2}|\Gamma^\top\Gamma|\cos\left[2\omega\mathbf{u}^\top\mathbf{x} + \arg\left(\Gamma^\top\Gamma\right)\right], \\
&= \frac{1}{2}A^2 + |\Gamma^\top\Gamma|\cos^2\left[\omega\mathbf{u}^\top\mathbf{x} + \frac{1}{2}\arg\left(\Gamma^\top\Gamma\right)\right] - \frac{1}{2}|\Gamma^\top\Gamma|, \\
&= \frac{A^2 - |\Gamma^\top\Gamma|}{2} + |\Gamma^\top\Gamma|\cos^2\left[\omega\mathbf{u}^\top\mathbf{x} + \frac{1}{2}\arg\left(\Gamma^\top\Gamma\right)\right].
\end{aligned} \tag{4.10}$$

This quantity can then be bounded to get its extreme values. Because $0 \leq \cos\theta \leq 1$ for all $\theta \in \mathbb{R}$,

$$\frac{A^2 - |\Gamma^\top\Gamma|}{2} \leq \|s(\mathbf{x}) - \mathbf{s}_0\|^2 \leq \frac{A^2 + |\Gamma^\top\Gamma|}{2} \tag{4.11}$$

These extreme values are necessarily reached because the linear application $\mathbf{x} \mapsto \omega\mathbf{u}^\top\mathbf{x}$ is surjective. The parameters r_- and r_+ can finally be expressed as

$$\begin{aligned}
{r_-}^2 &= \tfrac{A^2 - |\Gamma^\top\Gamma|}{2}, \\
{r_+}^2 &= \tfrac{A^2 + |\Gamma^\top\Gamma|}{2}.
\end{aligned} \tag{4.12}$$

These are exactly the expressions given in (Soulard & Carré 2015), except that, in Eq. (4.10), the distance is expressed for a 2D spatial variable rather than a 1D time variable. Now that the link between the shape of the ellipse and its color parameters is established, its position inside the RGB cube must be determined.

4.1.3 RGB position of the ellipse

In order to localize the ellipse inside the RGB cube, the coordinates of its vertexes must be determined. This is performed by using the unified phase shift introduced in (Soulard & Carré 2015). This phase-shift, denoted by $\widehat{\varphi}$, is defined as the half of the argument of the complex number $\Gamma^\top\Gamma$, *i.e.*,

$$\widehat{\varphi} = \frac{1}{2}\arg\left(\Gamma^\top\Gamma\right) = \frac{1}{2}\arg\left[\left(A^R\right)^2 e^{2\mathbf{i}\varphi^R} + \left(A^G\right)^2 e^{2\mathbf{i}\varphi^G} + \left(A^B\right)^2 e^{2\mathbf{i}\varphi^B}\right]. \tag{4.13}$$

This unified phase can be interpreted as a weighted mean of the three color phases φ^R, φ^G and φ^B. Eq. (4.10) can hence be rewritten as

$$\|s(\mathbf{x}) - \mathbf{s}_0\|^2 = {r_-}^2 + \left({r_+}^2 - {r_-}^2\right)\cos^2\left(\omega\mathbf{u}^\top\mathbf{x} + \widehat{\varphi}\right). \tag{4.14}$$

The coordinates of the vertexes are now expressed. Notice that, in the degenerated case of $r_+ = r_-$, *i.e.*, if the ellipse is a circle, any point is a vertex, making their determination useless. Therefore, the subsequent developments are made under the assumption $r_+ > r_-$. Let $\mathbf{x}_+$ and $\mathbf{x}_-$ be two vectors of $\mathbb{R}^2$ such that the extreme values of $\|s(\mathbf{x}) - \mathbf{s}_0\|^2$ are reached, *i.e.*,

$$\begin{cases} \|s(\mathbf{x}_+) - \mathbf{s}_0\|^2 = {r_+}^2, \\ \|s(\mathbf{x}_-) - \mathbf{s}_0\|^2 = {r_-}^2. \end{cases} \tag{4.15}$$

Remember that the surjectivity of the function inside the square cosine ensures the existence of $\mathbf{x}_+$ and $\mathbf{x}_-$. Then, because $r_+ > r_-$,

$$\begin{aligned} \|s(\mathbf{x}_+) - \mathbf{s}_0\|^2 = {r_+}^2 &\iff {r_-}^2 + \left({r_+}^2 - {r_-}^2\right)\cos^2\left(\omega\mathbf{u}^\top\mathbf{x} + \widehat{\varphi}\right) = {r_+}^2 \\ &\iff \left({r_+}^2 - {r_-}^2\right)\cos^2\left(\omega\mathbf{u}^\top\mathbf{x} + \widehat{\varphi}\right) = {r_+}^2 - {r_-}^2 \\ &\iff \cos^2\left(\omega\mathbf{u}^\top\mathbf{x} + \widehat{\varphi}\right) = 1 \\ &\iff \omega\mathbf{u}^\top\mathbf{x} = -\widehat{\varphi}\ [\pi]. \end{aligned} \tag{4.16}$$

Similarly,

$$\|s(\mathbf{x}_-) - \mathbf{s}_0\|^2 = {r_-}^2 \iff \omega\mathbf{u}^\top\mathbf{x} = -\widehat{\varphi} - \frac{\pi}{2}\ [\pi]. \tag{4.17}$$

Of course $\mathbf{x}_+$ and $\mathbf{x}_-$ are not unique, but they can be used to localize the vertexes of the ellipse, *i.e.*, the closest and furthest points from the center. Let $\mathbf{s}_+$ denote one of the two vertexes of the ellipse, and $\mathbf{s}_-$ one of its two co-vertexes. Injecting Eq. (4.16) and Eq. (4.17) in Eq. (4.1) leads to

$$\mathbf{s}_+ = \mathbf{s}_0 + \begin{pmatrix} A^R\cos\left(\varphi^R - \widehat{\varphi}\right) \\ A^G\cos\left(\varphi^G - \widehat{\varphi}\right) \\ A^B\cos\left(\varphi^B - \widehat{\varphi}\right) \end{pmatrix}, \tag{4.18}$$

and

$$\mathbf{s}_- = \mathbf{s}_0 + \begin{pmatrix} A^R \sin\left(\varphi^R - \widehat{\varphi}\right) \\ A^G \sin\left(\varphi^G - \widehat{\varphi}\right) \\ A^B \sin\left(\varphi^B - \widehat{\varphi}\right) \end{pmatrix}. \tag{4.19}$$

Knowing these two points is enough to fully localize the ellipse inside the RGB cube. Trigonometric identities also yield an expression of s that only rely on the vertexes s_+ and s_-, as well as the unified phase-shift $\widehat{\varphi}$, *i.e.*,

$$s(\mathbf{x}) = \mathbf{s}_0 + \cos\left(\omega \mathbf{u}^\top \mathbf{x} + \widehat{\varphi}\right)(\mathbf{s}_+ - \mathbf{s}_0) - \sin\left(\omega \mathbf{u}^\top \mathbf{x} + \widehat{\varphi}\right)(\mathbf{s}_- - \mathbf{s}_0). \tag{4.20}$$

4.1.4 Linearity parameter and color content

The parametric representation of s given in Eq. (4.20) is equivalent to that of Eq. (4.2), but, unlike the latter, it clearly indicates the main axes of the ellipse. Notice that this equation still holds if $r_+ = r_-$. Furthermore, the shape of the ellipse is directly linked with the color content of the image. If the ellipse is very thin, almost linear, then the color wave oscillates along one color axis only. If the ellipse has a more circular shape, then the color wave oscillates in a much wider range of colors. This can be quantified by the linearity parameter λ defined as

$$\lambda = \frac{{r_+}^2 - {r_-}^2}{{r_+}^2 + {r_-}^2}. \tag{4.21}$$

This parameter was already used for trivariate time signals in (Lilly 2011) before being applied to color images in (Soulard & Carré 2015). Because no formal proof of the link between the linearity parameter and the color content of the texture is provided in (Soulard & Carré 2015), the following theorem aims at clarifying this link formally.

Theorem 8. *Let s be a color wave as defined in Eq. (4.1), and let λ denote its linearity parameter as defined in Eq. (4.21). Then, $\lambda = 1$ if and only if one of the three following assertions is true:*

- $A^{C_1} = A^{C_2} = 0$ *for at least two distinct color channels* $(C_1, C_2) \in \{R, G, B\}^2$,
- $A^{C_1} = 0$ *and* $\varphi^{C_2} = \varphi^{C_3}$ $[\pi]$, *with* C_1, C_2, C_3 *being three distinct color channels of* $\{R, G, B\}$,
- $\varphi^R = \varphi^G = \varphi^B$ $[\pi]$,

in which case the ellipse is flat. Furthermore,

$$\lambda = 0 \iff \begin{cases} \sum_{C \in \{R,G,B\}} \left(A^C\right)^2 \cos\left(2\varphi^C\right) = 0, \\ \sum_{C \in \{R,G,B\}} \left(A^C\right)^2 \sin\left(2\varphi^C\right) = 0, \end{cases} \tag{4.22}$$

in which case the ellipse is a circle.

The proof is given in Appendix C.1. In the case of $\lambda = 1$, if the first assertion is true, then the texture only oscillates along the color axis for which the color amplitude is not zero. If the second assertion is true, then $2\varphi^{C_2} = 2\varphi^{C_3}$ $[2\pi]$, which yields

$$\begin{aligned}\widehat{\varphi} &= \frac{1}{2}\arg\left[\left(A^R\right)^2 e^{2\mathbf{i}\varphi^R} + \left(A^G\right)^2 e^{2\mathbf{i}\varphi^G} + \left(A^B\right)^2 e^{2\mathbf{i}\varphi^B}\right], \\ &= \frac{1}{2}\arg\left[\left(A^{C_2}\right)^2 e^{2\mathbf{i}\varphi^{C_2}} + \left(A^{C_3}\right)^2 e^{2\mathbf{i}\varphi^{C_2}}\right], \\ &= \varphi^{C_2}\ [\pi].\end{aligned} \tag{4.23}$$

Assuming that, for example, $A^R = 0$ and $\varphi^G = \varphi^B\ [\pi]$, the vertexes of the ellipse given in Eq. (4.18) and Eq. (4.19) become

$$\mathbf{s}_+ = \mathbf{s}_0 + \begin{pmatrix} 0 \\ A^G \\ \pm A^B \end{pmatrix}, \quad \mathbf{s}_- = \mathbf{s}_0. \tag{4.24}$$

Consequently, the texture oscillates along a color axis directed by the vector

$$\begin{pmatrix} 0 \\ A^G \\ \pm A^B \end{pmatrix}, \tag{4.25}$$

with the sign of the third coordinate depending on whether $\varphi^G - \varphi^B = 0$ or $\varphi^G - \varphi^B = \pi\ [\pi]$. Assuming that $A^G = 0$ and $\varphi^R = \varphi^B\ [\pi]$ or $A^B = 0$ and $\varphi^R = \varphi^G\ [\pi]$ yields similar situations, respectively. Finally, if the third assertion is true, then, $2\varphi^R = 2\varphi^G = 2\varphi^B\ [2\pi]$, which yields

$$\begin{aligned}\widehat{\varphi} &= \frac{1}{2}\arg\left[\left(A^R\right)^2 e^{2\mathbf{i}\varphi^R} + \left(A^G\right)^2 e^{2\mathbf{i}\varphi^G} + \left(A^B\right)^2 e^{2\mathbf{i}\varphi^B}\right], \\ &= \frac{1}{2}\arg\left[\left(A^R\right)^2 e^{2\mathbf{i}\varphi^R} + \left(A^G\right)^2 e^{2\mathbf{i}\varphi^R} + \left(A^B\right)^2 e^{2\mathbf{i}\varphi^R}\right], \\ &= \varphi^R\ [\pi].\end{aligned} \tag{4.26}$$

This time, the vertexes of the ellipse become

$$\mathbf{s}_+ = \mathbf{s}_0 + \begin{pmatrix} \pm A^R \\ \pm A^G \\ \pm A^B \end{pmatrix}, \quad \mathbf{s}_- = \mathbf{s}_0. \tag{4.27}$$

Consequently, the texture oscillates along a color axis directed by the vector

$$\begin{pmatrix} \pm A^R \\ \pm A^G \\ \pm A^B \end{pmatrix}, \tag{4.28}$$

with the signs depending on whether $\varphi^{C_1} - \varphi^{C_2} = 0$ or $\varphi^{C_1} - \varphi^{C_2} = \pi\ [\pi]$. In all three cases, the texture oscillates along one single color axis, which is consistent with the flat shape of the ellipse.

The case $\lambda = 0$ allows more possibilities, but it can be noticed that, if all three color phase shifts φ^C belong to the same quadrant of the unit circle, then the sines of the angles $2\varphi^C$ are all of the same sign. The second condition in Eq. (4.22) then implies that all the terms of the sum are zero, *i.e.*, for all $C \in \{R, G, B\}$,

$$A^C = 0 \text{ or } \sin\left(2\varphi^C\right) = 0. \tag{4.29}$$

If all three amplitudes are non-zero, then $\sin\left(2\varphi^C\right) = 0$ for all $C \in \{R, G, B\}$, which necessarily implies that $\cos\left(2\varphi^C\right) = \pm 1$ for all $C \in \{R, G, B\}$. Because the color phase-shifts are assumed to lie inside the same quadrant of the unit circle, the two possibilities are $\cos\left(2\varphi^C\right) = 1$ for all $C \in \{R, G, B\}$ or $\cos\left(2\varphi^C\right) = -1$ for all $C \in \{R, G, B\}$, which automatically violates the first condition in Eq. (4.22). Consequently, if the ellipse associated with the texture is a circle, *i.e.*, if $\lambda = 0$, then the color phase-shifts cannot be located inside the same quadrant. This means that if the ellipse is a circle, then the color channels are significantly phase-shifted from one another, which implies a richer content.

This illustrates the link between the linearity parameter λ, the shape of the ellipse, the color parameters, and the color content of the texture. If λ is close to 1, the ellipse has a thin shape, and the color content of the texture is reduced to shades of a pair of colors. If λ is close to 0, the ellipse has a nearly circular shape, and the color content of the texture is richer. This is highlighted with synthetic tests in Section 4.1.5.

4.1.5 Interpretation of the parameters and synthetic tests

This section aims at illustrating how the elliptic color model provides a full control over the color content in the context of texture synthesis. Though a full parametrization of the ellipse associated with a color wave was already given in (Soulard & Carré 2015), here the link between the ellipse and the wave is further detailed. Synthetic tests are then performed to give a more physical meaning to the parameters. Let (t^j, t^k) be a discrete grid, with $(j, k) \in \{0 \dots M-1\} \times \{0 \dots N-1\}$ and $(M, N) \in \mathbb{N}^2$ such that

$$\begin{cases} t^j = \left(j - \frac{M}{2}\right) T_x, \\ t^k = \left(k - \frac{N}{2}\right) T_y, \end{cases} \tag{4.30}$$

where $T_x > 0$ and $T_y > 0$ denote the horizontal and vertical sampling periods, respectively. A discrete color wave s is generated for all $(j, k) \in \{0 \dots M-1\} \times \{0 \dots N-1\}$ as

$$s^{j,k} = \begin{pmatrix} s_0^R + A^R \cos\left[\omega(t^j \cos\alpha + t^k \sin\alpha) + \varphi^R\right] \\ s_0^G + A^G \cos\left(\omega(t^j \cos\alpha + t^k \sin\alpha) + \varphi^G\right) \\ s_0^B + A^B \cos\left(\omega(t^j \cos\alpha + t^k \sin\alpha) + \varphi^B\right) \end{pmatrix}, \tag{4.31}$$

where all the parameters are defined as in Section 4.1.1. Because s is generated inside the RGB cube $[0, 1]^3$, its coordinates directly give the intensity of each color channel at each pixel. The case where all three components of $s^{j,k}$ are equal to 0 corresponds to the black color, while the case where all three components of $s^{j,k}$ are equal to 1 corresponds to the white color.

The further developments involve some affine space formalism (for more details, see Chapter 2 in (Berger, Pansu, Berry & Saint-Raymond 1984)). In order to avoid confusion, the vectors are denoted by arrows to distinguish them from the points. In synthetic tests, the offset $\mathbf{s}_0$, *i.e.*, the color point around which s oscillates, is first fixed in the RGB cube $[0, 1]^3$. Then, each amplitude A^C is chosen between 0 and $\min\left\{s_0^C, 1 - s_0^C\right\}$, and finally each phase-shift φ^C is chosen between $-\pi$ and π. After the values of r_+ and r_- are calculated by using Eq. (4.12), the ellipse $\mathcal{E}$ is drawn in $\mathbb{R}^2$ as the set

$$\mathcal{E} = \left\{\left(r_+ \cos\theta \quad r_- \sin\theta\right), \theta \in]-\pi, \pi]\right\}. \tag{4.32}$$

This is exactly the parametric equation of $\mathcal{E}$ in the affine basis defined by the origin $\mathbf{s}_0$ and the two vectors that direct the main axes of the ellipse. In the affine space $\mathbb{R}^3 \times \mathbb{R}^3$, the

vertexes $\mathbf{s}_+$ and $\mathbf{s}_-$ can be decomposed as the sum of a point of $\mathbb{R}^3$ (here the center of the ellipse) and a vector of $\mathbb{R}^3$ (here the vectors directing the two main axes), *i.e.*,

$$\begin{cases} \mathbf{s}_+ = \mathbf{s}_0 + \vec{\mathbf{s}}_+, \\ \mathbf{s}_- = \mathbf{s}_0 + \vec{\mathbf{s}}_-, \end{cases} \tag{4.33}$$

Let $\vec{\mathbf{n}}$ denote the cross product of $\vec{\mathbf{s}}_+$ and $\vec{\mathbf{s}}_-$. Then $\mathcal{B}_s = \{\vec{\mathbf{s}}_+, \vec{\mathbf{s}}_-, \vec{\mathbf{n}}\}$ forms a basis of $\mathbb{R}^3$ for which the vectors of the ellipse have coordinates in the form of

$$\begin{pmatrix} r_+ \cos\theta \\ r_- \sin\theta \\ 0 \end{pmatrix}, \tag{4.34}$$

where $\theta \in]-\pi, \pi]$. The RGB triplet $\begin{pmatrix} x_\theta^R & x_\theta^G & x_\theta^B \end{pmatrix}^\top$ associated with the point of the ellipse parametrized by θ is determined by using the transfer matrix Π_s between the base $\mathcal{B}_s$ and the canonical base, *i.e.*,

$$\begin{pmatrix} x_\theta^R \\ x_\theta^G \\ x_\theta^B \end{pmatrix} = \mathbf{s}_0 + \Pi_s \begin{pmatrix} r_+ \cos\theta \\ r_- \sin\theta \\ 0 \end{pmatrix}. \tag{4.35}$$

This process enables the drawing of the ellipse for all images, and hence a better visualization of the color oscillation of the texture inside the RGB cube. Tables 4.1, 4.2 and 5.1 show examples of color waves and their corresponding ellipse synthesized with different color parameters, with $\omega = 30$ and $\alpha = \frac{\pi}{6}$ for all images. Table 4.1 gives three examples of textures with a flat ellipse, *i.e.*, $\lambda = 1$, each one corresponding to one of the three conditions given in Theorem 8. In order to generate an image that only contains shades of red, all the parameters are chosen equal to 0 except the parameters of the red channel, hence s_1. If the image is intended to oscillate between red and green, the red and green phase-shifts must be equal modulo π, while the blue amplitude must be 0, hence s_2. As stated in Theorem 8, if the color phase-shifts are all equal modulo π, then the image oscillates along one single color axis for any values of the color amplitudes, hence s_3. The choice of a high value for s_0^B is what gives the texture its blue color.

Table 4.2 gives examples of textures for which the ellipse is a circle, with the parameters being chosen to fulfill the condition given in Theorem 8. Image s_4 contains all of Newton's primary colors due to its equal amplitudes assigned to each channel and its maximally different phase-shifts. Images s_5 and s_6 show other configurations that lead to $\lambda = 0$. The respective circles of s_4, s_5 and s_6 illustrate how these textures cover a wide range of colors.

While the previous tables focus on degenerated cases, Table 4.2 gives examples of color textures with $\lambda \in]0, 1[$. In order to obtain a color wave that oscillates inside the RB plane, *i.e.*, the plane generated by the red and blue axes, the green parameters are all chosen equal to 0, hence image s_7. Notice that choosing equal amplitudes for the red and blue channels yields $\lambda = 0.5$. If the amplitudes are kept equal but the phase-shifts are chosen close to each other, the range of colors is not as complete as in image s_4, as can be seen in image s_8. This is reflected by the value of the linearity parameter, $\lambda = 0.33$. In order to make the image oscillate between shades of green and dark blue, the red parameters are all chosen equal to 0, while the green amplitude is chosen higher than the blue amplitude, hence image s_9. Unlike in image s_7, the two channels do not equally contribute, which yields a more linear ellipse reflected by $\lambda = 0.72$. Notice that if all color parameters are

equal (including the coordinates of the offset), then the generated image only contains shades of grey. The difference between these parameters is what creates a color content. Section 4.2 shows how this direct link between the parameters and the color content is a key feature when generalizing the Gabor noise framework to color spaces.

Name	s_1	s_2	s_3
s_0^R	0.5	0.5	0.3
s_0^G	0	0.5	0.6
s_0^B	0	0.5	0.7
A^R	0.3	0.5	0.1
A^G	0	0.5	0.2
A^B	0	0	0.3
φ^R	0	0	0
φ^G	0	π	π
φ^B	0	0	π
Image		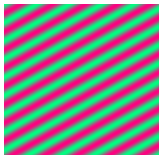	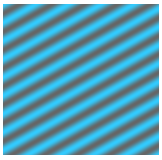
Ellipse			

Table 4.1: Examples of color waves with $\lambda = 1$, with $\omega = 30$ and $\alpha = \frac{\pi}{6}$.

4.2 Color extension of the Gabor and phasor noises

Now that the key features of the elliptic color model of (Soulard & Carré 2015) are recalled, this section aims at introducing a formal color extension of the phase-augmented Gabor noise defined in Section 3.2. As said in the introduction, the aim is to build a purely procedural color model that does not require exemplar textures (unlike, *e.g.*, (Galerne et al. 2012)), and enables the generation of textures with prescribed color content. The elliptic color model is hence chosen for the direct link between its parameters and the oscillations inside the RGB cube it provides, as highlighted in Section 4.1. From this color extension of the Gabor noise, a proper color phasor can then be introduced.

4.2.1 Set of destination of the Gabor and phasor noises

As shown in (Tricard et al. 2019) and recalled in Section 3.3.1, a greyscale Gabor noise s can be expressed for all $\mathbf{x} \in \mathbb{R}^2$ as

$$s(\mathbf{x}) = I(\mathbf{x}) \cos\left[\varphi(\mathbf{x})\right], \tag{4.36}$$

where I and φ denote the random amplitude and phase functions of s, respectively. While the cosine is necessarily bounded between -1 and 1, the amplitude function may take high values, which makes the Gabor noise s vary between $-\max(I)$ and $\max(I)$. Figure 4.1 shows how the maximal value of I highly fluctuates and depends on the generated noise.

Name	s_4	s_5	s_6
s_0^R	0.5	0.5	0.5
s_0^G	0.5	0.5	0.5
s_0^B	0.5	0.5	0.5
A^R	0.5	0.5	0.25
A^G	0.5	0	$\frac{1}{\sqrt{8}}$
A^B	0.5	0.5	0.25
φ^R	0	0	0
φ^G	$\frac{2\pi}{3}$	π	$\frac{\pi}{2}$
φ^B	$-\frac{2\pi}{3}$	$\frac{\pi}{2}$	π
Image	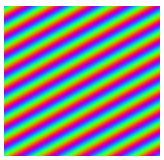	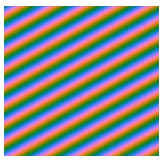	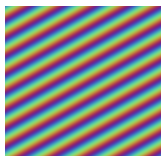
Ellipse			

Table 4.2: Examples of color waves with $\lambda = 0$, with $\omega = 30$ and $\alpha = \frac{\pi}{6}$.

By removing the amplitude function, the phasor noise not only suppresses the local losses of contrast (as highlighted in (Tricard et al. 2019)), but also ensures that the synthesized texture lies inside the cube $[-1;1]^3$. Similarly to what is done in Section 4.1.1 in the deterministic case, constraints are then imposed on the color parameters to ensure that the resulting texture lies inside the cube $[0;1]^3$. This makes the phasor more suitable for color image synthesis. As a result, the subsequent developments mainly focus on the color phasor noise after introducing a formal color extension of the Gabor noise.

4.2.2 Color Gabor noise

In this approach, the color Gabor noise is defined as a function $s : \mathbb{R}^2 \to \mathbb{R}^3$ such that for all $\mathbf{x} \in \mathbb{R}^2$,

$$s(\mathbf{x}) = \sum_i a\left(\mathbf{x} - \mathbf{x}_i\right) \begin{pmatrix} A^R \cos\left[b\omega \mathbf{u}^\top \left(\mathbf{x} - \mathbf{x}_i\right) + \psi_i + \varphi^R\right] \\ A^G \cos\left[b\omega \mathbf{u}^\top \left(\mathbf{x} - \mathbf{x}_i\right) + \psi_i + \varphi^G\right] \\ A^B \cos\left[b\omega \mathbf{u}^\top \left(\mathbf{x} - \mathbf{x}_i\right) + \psi_i + \varphi^B\right] \end{pmatrix}, \tag{4.37}$$

where

- $\{(\mathbf{x}_i, \psi_i)\}_i$ is a set of realizations of a marked Poisson point process on $\mathbb{R}^2 \times]-\pi, \pi]$ such that,
  - the points $(\mathbf{x}_i)_i$ are generated through a homogeneous Poisson point process on $\mathbb{R}^2$ with intensity $\mu > 0$,
  - the marks $(\psi_i)_i$ are independent random phase-shifts uniformly drawn in $]-\pi, \pi]$ and independently assigned to each point of the Poisson point process $\mathbf{x}_i$,
- $a(\mathbf{x}) = e^{-\pi b^2 \|\mathbf{x}\|^2}$, $b \in \mathbb{R}_+^*$, $\mathbf{x} \in \mathbb{R}^2$,

Name	s_7	s_8	s_9
s_0^R	0.5	0.5	0
s_0^G	0	0.5	0.5
s_0^B	0.5	0.5	0.25
A^R	0.5	0.5	0
A^G	0	0.5	0.5
A^B	0.5	0.5	0.25
φ^R	0	0	0
φ^G	0	$\frac{\pi}{3}$	$\frac{2\pi}{3}$
φ^B	$\frac{2\pi}{3}$	$\frac{\pi}{2}$	$-\frac{2\pi}{3}$
Image	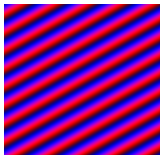	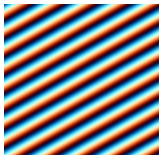	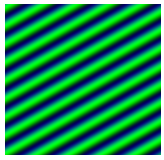
Ellipse			
λ	0.5	0.33	0.72

Table 4.3: Link between the color parameters, the color content of the texture and the shape of the corresponding ellipse, with $\omega = 30$ and $\alpha = \frac{\pi}{6}$.

- $\omega \in \mathbb{R}_+^*$, $\mathbf{u} = (\cos\alpha, \sin\alpha)^\top$, $\alpha \in \left]-\frac{\pi}{2}; \frac{\pi}{2}\right]$,
- for all $C \in \{R, G, B\}$, $A^C \in \left[0, \frac{1}{2}\right]$ and $\varphi^C \in]-\pi, \pi]$.

Similarly to what is done in Section 3.3.1 in the greyscale case, the noise s can then be written as a single color wave rather than a sparse convolution by applying the reformulation of the Gabor noise as a phasor field (as done in (Tricard et al. 2019)) to each color channel. The main reason for this is to define proper notions of amplitude and phase. Hence, for all $\mathbf{x} \in \mathbb{R}^2$,

$$s(\mathbf{x}) = I(\mathbf{x}) \begin{pmatrix} A^R \cos\left[b\omega \mathbf{u}^\top \mathbf{x} + \Psi(\mathbf{x}) + \varphi^R\right] \\ A^G \cos\left[b\omega \mathbf{u}^\top \mathbf{x} + \Psi(\mathbf{x}) + \varphi^G\right] \\ A^B \cos\left[b\omega \mathbf{u}^\top \mathbf{x} + \Psi(\mathbf{x}) + \varphi^B\right] \end{pmatrix} = \begin{pmatrix} s^R(\mathbf{x}) \\ s^G(\mathbf{x}) \\ s^B(\mathbf{x}) \end{pmatrix}. \tag{4.38}$$

where

$$\begin{cases} I(\mathbf{x}) = \left| \sum_i a(\mathbf{x} - \mathbf{x}_i) e^{\mathbf{i}\left(-b\omega \mathbf{u}^\top \mathbf{x}_i + \psi_i\right)} \right|, \\ \Psi(\mathbf{x}) = \arg\left[\sum_i a(\mathbf{x} - \mathbf{x}_i) e^{\mathbf{i}\left(-b\omega \mathbf{u}^\top \mathbf{x}_i + \psi_i\right)} \right]. \end{cases} \tag{4.39}$$

Each color component s^C of s, $C \in \{R, G, B\}$, can hence be seen as a cosine wave whose amplitude I and phase-shift Ψ are random fields rather than deterministic functions. These functions contain the underlying energical and structural information of the texture, respectively, but do not impact its color content. However, this does not imply that the color Gabor noise defined here is an intrinsically greyscale texture that varies along a color axis rather than a grey axis. The next developments show how the generated texture truly oscillates inside the RGB cube in a non-marginal way. This is first reflected in the

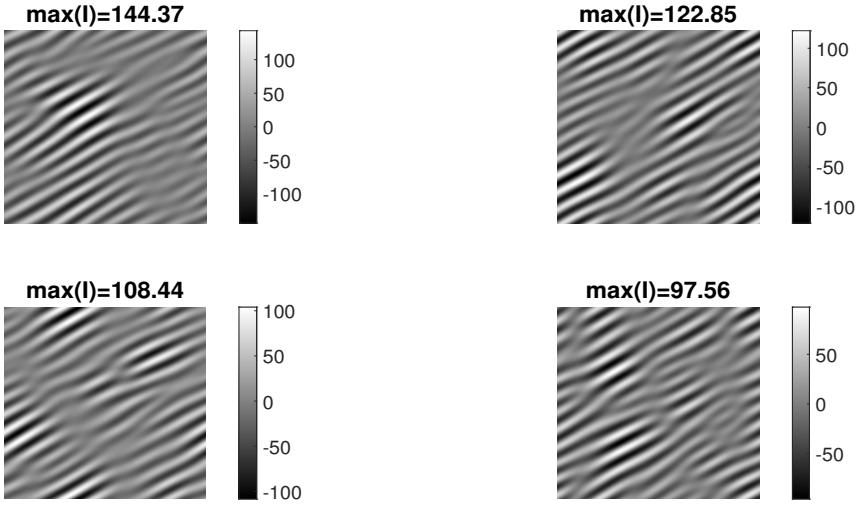

Figure 4.1: Four Gabor noises generated with $b = 2$, $\omega = 20$, $\alpha = \frac{\pi}{6}$, $p = 0.1$.

statistic behavior of the color channels, which is the subject of Section 4.3.1. Now that the basic color Gabor noise has been introduced, more general color procedural noises can be defined.

4.2.3 Sum of Gabor noises and phasor noise

The Gabor noise, as defined in the previous section, is unidirectional, *i.e.*, it only has one direction of oscillation, which is determined by the angle α. In order to generate richer patterns containing different directions of oscillation, Gabor noises of different wave vectors can be combined, as done in (Gilet et al. 2014, Tricard et al. 2019) in the greyscale case. Let $s_1, \ldots, s_n$ ($n \in \mathbb{N}^*$) be n independent Gabor noises that share the same parameter values except for their frequencies and orientations, which are denoted by ω_ℓ and α_ℓ for all $\ell \in \{1, \ldots, n\}$, with $\omega_\ell \in \mathbb{R}_+^*$ and $\alpha_\ell \in]-\frac{\pi}{2}, \frac{\pi}{2}]$. Their respective wave vectors are denoted by $\mathbf{u}_\ell = \begin{pmatrix} \cos\alpha_\ell & \sin\alpha_\ell \end{pmatrix}^\top$. Let s denote the sum of the n Gabor noises, *i.e.*, for all $\mathbf{x} \in \mathbb{R}^2$,

$$s(\mathbf{x}) = \sum_{\ell=1}^{n} s_\ell(\mathbf{x}). \tag{4.40}$$

The respective Poisson and phase shifts processes, through which the n Gabor noises s_ℓ ($\ell \in \{1, \ldots, n\}$) are generated, are assumed to be independent. Each color channel s_ℓ^C of each Gabor noise s_ℓ ($C \in \{R, G, B\}$ and $\ell \in \{1, \ldots, n\}$) is now rewritten as a single wave as done in the previous section, *i.e.*, for all $\mathbf{x} \in \mathbb{R}^2$ (Tricard et al. 2019),

$$s_\ell^C(\mathbf{x}) = A^C I_\ell(\mathbf{x}) \cos\left[b\omega_\ell \mathbf{u}_\ell^\top \mathbf{x} + \Psi_\ell(\mathbf{x}) + \varphi^C\right]. \tag{4.41}$$

Each color channel of the sum of the n Gabor noises s can hence be expressed for all $C \in \{R, G, B\}$ and $\mathbf{x} \in \mathbb{R}^2$ as

$$s^C(\mathbf{x}) = A^C e^{\mathbf{i}\varphi^C} \Re\left\{\sum_{\ell=1}^{n} I_\ell(\mathbf{x}) e^{\mathbf{i}\left[b\omega_\ell \mathbf{u}_\ell^\top \mathbf{x} + \Psi_\ell(\mathbf{x})\right]}\right\}. \tag{4.42}$$

Let $I(\mathbf{x})$ and $\varphi(\mathbf{x})$ denote the modulus and argument of the complex random field inside the square brackets for all $\mathbf{x} \in \mathbb{R}^2$. Then, a unified expression can be defined for s, *i.e.*, for all $\mathbf{x} \in \mathbb{R}^2$,

$$s(\mathbf{x}) = I(\mathbf{x}) \begin{pmatrix} A^R \cos\left[\varphi(\mathbf{x}) + \varphi^R\right] \\ A^G \cos\left[\varphi(\mathbf{x}) + \varphi^G\right] \\ A^B \cos\left[\varphi(\mathbf{x}) + \varphi^B\right] \end{pmatrix}. \tag{4.43}$$

The color phasor noise Φ is finally defined by removing the amplitude function I, similarly to what was done in (Tricard et al. 2019) in the greyscale case. However, the model introduced in this chapter also includes an offset $\Phi_0 \in [0,1]^3$ so that the phasor noise is wholly contained in the RGB cube $[0,1]^3$. Hence, for all $\mathbf{x} \in \mathbb{R}^2$,

$$\Phi(\mathbf{x}) = \Phi_0 + \begin{pmatrix} A^R \cos\left[\varphi(\mathbf{x}) + \varphi^R\right] \\ A^G \cos\left[\varphi(\mathbf{x}) + \varphi^G\right] \\ A^B \cos\left[\varphi(\mathbf{x}) + \varphi^B\right] \end{pmatrix} = \begin{pmatrix} \Phi_0^R + \Phi^R(\mathbf{x}) \\ \Phi_0^G + \Phi^G(\mathbf{x}) \\ \Phi_0^B + \Phi^B(\mathbf{x}) \end{pmatrix}. \tag{4.44}$$

The values of each color component range between $\Phi_0^C - A^C$ and $\Phi_0^C + A^C$ for all $C \in \{R, G, B\}$. The parameters Φ_0^C and A^C must hence satisfy the constraints $\Phi_0^C - A^C \geq 0$ and $\Phi_0^C + A^C \leq 1$ to ensure that Φ is an actual color image contained in $[0,1]^3$. Such constraints are impossible to define in the case of a Gabor noise as the values at each pixel vary in $\mathbb{R}^3$ rather than the cube $[-1;1]^3$, as highlighted in Section 4.2.1.

4.2.4 Discretization and synthetic tests

Though the color phasor noise is introduced as a continuous object in the previous sections, it has to be discretized to perform synthetic tests. This section aims at properly presenting the techniques used to generate discrete phasor noises. The impact of the Gabor parameters (scale, frequency, orientation) on the texture is then studied, while the impact of the color parameters is left for the next section.

Let (t^j, t^k) be a discrete grid, with $(j,k) \in \{0 \dots M-1\} \times \{0 \dots N-1\}$ and $(M,N) \in \mathbb{N}^2$ such that

$$\begin{cases} t^j = \left(j - \frac{M}{2}\right) T_x, \\ t^k = \left(k - \frac{N}{2}\right) T_y, \end{cases} \tag{4.45}$$

where $T_x > 0$ and $T_y > 0$ denote the horizontal and vertical sampling periods, respectively. Before generating a phasor noise, the sum of n Gabor noises s_ℓ ($\ell \in \{1, \dots, n\}$, $n \in \mathbb{N}^*$) defined in Eq. (4.40) and Eq. (4.41) must be properly discretized. In order to simulate a Poisson process on this grid, an independent and identically distributed $M \times N$ sampling of a Bernoulli variable of parameter $p \in]0,1[$ is generated for each Gabor noise of the sum. For all $\ell \in \{1, \dots, n\}$, let $x_\ell^{j,k} \in \{0,1\}$ denote the Bernoulli number generated at the pixel (t^j, t^k) (with $(j,k) \in \{0 \dots M-1\} \times \{0 \dots N-1\}$). Then, an independent and identically distributed $M \times N$ sampling of a uniform variable on $]-\pi, \pi]$ is generated at each pixel (t^j, t^k) and for Gabor noise of the sum. These numbers correspond to the random phase-shifts ψ_i of Eq. (4.37) in the continuous model, and are denoted by $\psi_\ell^{j,k}$ for all $(j,k) \in \{0 \dots M-1\} \times \{0 \dots N-1\}$, where ℓ denotes the index of the Gabor noise in the sum. Let h_ℓ denote the complex-valued $M \times N$ discrete signal $(h_\ell^{j,k})_{j,k}$ such that for all $(j,k) \in \{0 \dots M-1\} \times \{0 \dots N-1\}$,

$$h_\ell^{j,k} = x_\ell^{j,k} e^{\mathbf{i}\left[-b\omega_\ell\left(t^j \cos\alpha_\ell + t^k \sin\alpha_\ell\right) + \psi_\ell^{j,k}\right]}, \tag{4.46}$$

where $\omega_\ell \in \mathbb{R}_+^*$ and $\alpha_\ell \in \left]-\frac{\pi}{2};\frac{\pi}{2}\right]$ for all $\ell \in \{1,\dots,n\}$. The discrete amplitude and phase functions of each Gabor noise s_ℓ, denoted by $I_\ell = \left(I_\ell^{j,k}\right)_{j,k}$ and $\Psi_\ell = \left(\Psi_\ell^{j,k}\right)_{j,k}$, respectively, are then computed for all $(j,k) \in \{0\dots M-1\}\times\{0\dots N-1\}$ as the modulus and argument of the complex random field $h_\ell * a$, where $*$ denotes the discrete convolution product, and

$$a_{j,k} = e^{-\pi b^2\left[(t^j)^2+(t^k)^2\right]}, \tag{4.47}$$

with $b \in \mathbb{R}_+^*$. This convolution product is performed in the frequency domain by using the discrete Fourier transform. For all $(j,k) \in \{0\dots M-1\}\times\{0\dots N-1\}$, let $I_{j,k}$ and $\varphi_{j,k}$ denote the modulus and argument of the complex number

$$\sum_{\ell=1}^{n} I_\ell^{j,k} e^{\mathbf{i}\varphi_\ell^{j,k}}. \tag{4.48}$$

The sum of Gabor noises s is finally constructed for all $(j,k) \in \{0\dots M-1\}\times\{0\dots N-1\}$ as

$$s_{j,k} = I_{j,k}\begin{pmatrix} A^R\cos\left[\varphi_{j,k}+\varphi^R\right] \\ A^G\cos\left[\varphi_{j,k}+\varphi^G\right] \\ A^B\cos\left[\varphi_{j,k}+\varphi^B\right]\end{pmatrix}. \tag{4.49}$$

The resulting phasor noise Φ is then obtained by removing the amplitude signal I from the Gabor noise s and adding the remaining signal to a fixed offset $\Phi_0 \in [0,1]^3$, *i.e.*, for all $(j,k) \in \{0\dots M-1\}\times\{0\dots N-1\}$,

$$\Phi_{j,k} = \Phi_0 + \begin{pmatrix} A^R\cos\left[\varphi_{j,k}+\varphi^R\right] \\ A^G\cos\left[\varphi_{j,k}+\varphi^G\right] \\ A^B\cos\left[\varphi_{j,k}+\varphi^B\right]\end{pmatrix}. \tag{4.50}$$

This is exactly the discrete version of Eq. (4.44). Notice that Φ already lies inside the RGB cube $[0,1]^3$ by construction. This ensures that the images displayed in the subsequent synthetic tests exactly correspond to the model, and are not distorted by normalization. Figure 4.2 shows an example of a color phasor noise synthesized with this technique. The parameters chosen to synthesize the texture are $M = N = 1000$, $T_x = T_y = 0.002$, $b = 2$, $p = 0.1$, $\omega = 30$, $\alpha = \frac{\pi}{6}$, $n = 1$ (one single Gabor noise), $A^R = 0.2$, $A^G = 0.2$, $A^B = 0.1$, $\varphi^R = 0$, $\varphi^G = \frac{\pi}{3}$, $\varphi^B = \frac{\pi}{2}$ and $\Phi_0 = \begin{pmatrix}0.8 & 0.5 & 0.1\end{pmatrix}^\top$, respectively. Notice that the sampling periods T_x and T_y both satisfies Shannon's boundary, *i.e.*, $\frac{1}{T_x} > 2b\omega$ and $\frac{1}{T_y} > 2b\omega$.

Unlike what is observed in (Tricard et al. 2019), increasing the value of the parameter b only affects the scale, a direct consequence of the modification of the Gabor kernel detailed in Section 3.2.1. This is illustrated in Figure 4.3, which shows a phasor noise generated with $b = 5$, $A^R = 0.1$, $A^G = 0.2$, $A^B = 0.3$ and $\Phi_0 = \begin{pmatrix}0.3 & 0.6 & 0.5\end{pmatrix}^\top$, the other parameters being the same as in Figure 4.2. The image looks zoomed out compared to Figure 4.2, but its overall aspect is not impacted at all.

As expected, decreasing the frequency parameter ω while keeping b constant yields slower oscillations. This is illustrated in Figure 4.4, which shows a phasor noise generated with $\omega = 12$, $A^R = 0.2$, $A^G = 0.3$, $A^B = 0.4$ and $\Phi_0 = \begin{pmatrix}0.7 & 0.3 & 0.6\end{pmatrix}^\top$, the other parameters being the same as in Figure 4.2.

Similarly to what was done in (Tricard et al. 2019) in the greyscale case, more complex patterns are now introduced by summing two Gabor noises of different orientations α and

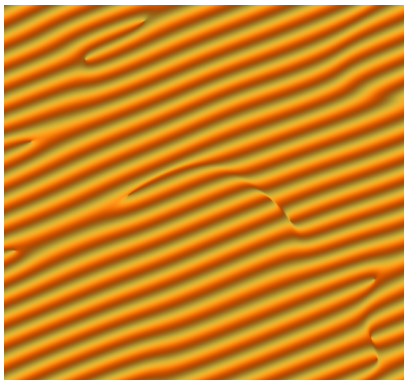

Figure 4.2: Example of a color phasor noise, $b = 2$, $\omega = 30$, $\alpha = \frac{\pi}{6}$, $n = 1$, $A^R = 0.2$, $A^G = 0.2$, $A^B = 0.1$, $\varphi^R = 0$, $\varphi^G = \frac{\pi}{3}$, $\varphi^B = \frac{\pi}{2}$ and $\Phi_0 = \begin{pmatrix} 0.8 & 0.5 & 0.1 \end{pmatrix}^\top$.

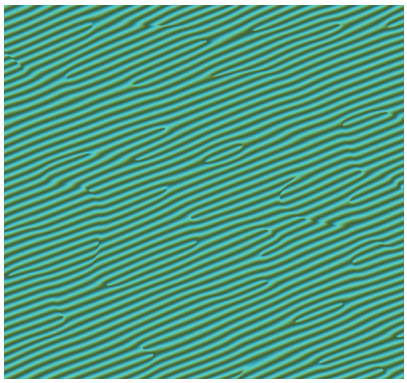

Figure 4.3: Example of a color phasor noise at a lower scale, $b = 5$, $\omega = 30$, $\alpha = \frac{\pi}{6}$, $n = 1$, $A^R = 0.1$, $A^G = 0.2$, $A^B = 0.3$, $\varphi^R = 0$, $\varphi^G = \frac{\pi}{3}$, $\varphi^B = \frac{\pi}{2}$ and $\Phi_0 = \begin{pmatrix} 0.3 & 0.6 & 0.5 \end{pmatrix}^\top$.

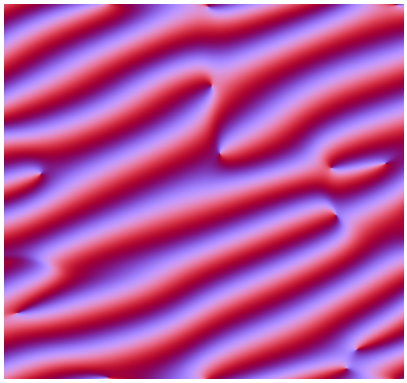

Figure 4.4: Example of a color phasor noise with a lower frequency, $b = 2$, $\omega = 12$, $\alpha = \frac{\pi}{6}$, $n = 1$, $A^R = 0.2$, $A^G = 0.3$, $A^B = 0.4$, $\varphi^R = 0$, $\varphi^G = \frac{\pi}{3}$, $\varphi^B = \frac{\pi}{2}$ and $\Phi_0 = \begin{pmatrix} 0.7 & 0.3 & 0.6 \end{pmatrix}^\top$.

$\alpha+\theta$, yielding a bidirectional phasor noise. Figure 4.5 shows an example of a color phasor noise synthesized with this technique. The parameters chosen to synthesize the texture are $M = N = 1000$, $T_x = T_y = 0.002$, $b = 1$, $p = 0.1$, $\omega = 30$, $\alpha = \frac{\pi}{6}$, $\theta = \frac{\pi}{12}$ $A^R = 0.3$, $A^G = 0.1$, $A^B = 0.3$, $\varphi^R = 0$, $\varphi^G = \frac{\pi}{4}$, $\varphi^B = \frac{3\pi}{4}$ and $\Phi_0 = \begin{pmatrix}0.7 & 0.1 & 0.5\end{pmatrix}^\top$, respectively.

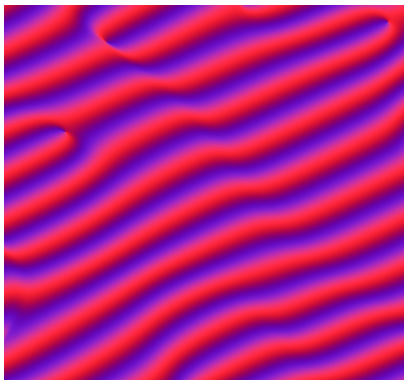

Figure 4.5: Example of a color bidirectional phasor noise, $b = 1$, $\omega = 30$, $\alpha = \frac{\pi}{6}$, $\theta = \frac{\pi}{12}$, $n = 2$, $A^R = 0.3$, $A^G = 0.1$, $A^B = 0.3$, $\varphi^R = 0$, $\varphi^G = \frac{\pi}{3}$, $\varphi^B = \frac{\pi}{2}$ and $\Phi_0 = \begin{pmatrix}0.7 & 0.1 & 0.5\end{pmatrix}^\top$.

Combining two waves with slightly different orientations makes the texture content richer. However, as stated in (Tricard et al. 2019), increasing the parameter θ yields a more discontinuous image. This is illustrated in Figure 4.6, which shows a bidirectional phasor noise generated with $b = 1$, $\theta = \frac{\pi}{3}$, $A^R = 0.1$, $A^G = 0.2$, $A^B = 0.3$ and $\Phi_0 = \begin{pmatrix}0.3 & 0.8 & 0.6\end{pmatrix}^\top$, the other parameter being the same as in Figure 4.5. The conflicts between the two waves become much more frequent, which is reflected in sudden changes of orientation.

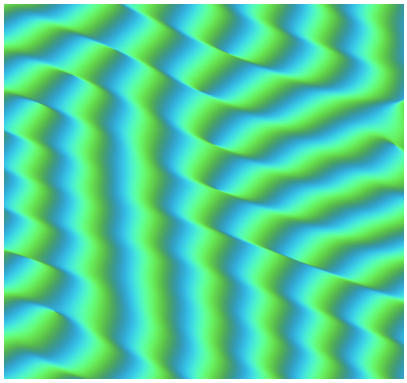

Figure 4.6: Example of a color bidirectional phasor noise with more distinct directions, $b = 1$, $\omega = 30$, $\alpha = \frac{\pi}{6}$, $\theta = \frac{\pi}{3}$, $n = 2$, $A^R = 0.1$, $A^G = 0.2$, $A^B = 0.3$, $\varphi^R = 0$, $\varphi^G = \frac{\pi}{3}$, $\varphi^B = \frac{\pi}{2}$ and $\Phi_0 = \begin{pmatrix}0.3 & 0.8 & 0.6\end{pmatrix}^\top$.

Just like in the greyscale case (Tricard et al. 2019), singularities occur in the synthesized textures, *i.e.*, abrupt jumps between two wave fronts, though the underlying oscillating structure is still clearly visible. Notice that these singularities and their links with the parameters are tackled in Chapter 5. While these synthetic tests focus only on the Gabor parameters, the color parameters A^C and φ^C ($C \in \{R, G, B\}$) and their impact on the color content of the texture are further studied in Section 4.3.

4.3 Interpretation of the elliptic color model

4.3.1 Color covariances and interpretation

While the direct link between the color parameters and the color content of the synthesized texture is already highlighted in Section 4.1.5 in the deterministic case, this section aims at studying how these color parameters provide a full control over the color covariances in the case of stochastic textures such as the Gabor noise. In many semi-procedural approaches, scalar Gabor noises are synthesized along the three color axes that maximize either uncorrelation (through a PCA) or independence (Galerne et al. 2012) in the exemplar texture. Rather than being eliminated, the covariances between the channels are fully modeled in the color extension introduced in this work. These covariances can be analytically expressed with the parameters of the model.

Theorem 9. *The color Gabor noise defined in Eq.* (4.37) *is stationary, zero-mean, and its covariance matrix* $\Sigma(\mathbf{z})$, $\mathbf{z} \in \mathbb{R}^2$, *is given by*

$$\begin{aligned}\Sigma(\mathbf{z}) &= \mathbb{E}\left[s(\mathbf{0})s(\mathbf{z})^\top\right], \\ &= \frac{\mu}{4b^2} e^{-\frac{1}{2}\pi b^2 \|\mathbf{z}\|^2} \left[\cos\left(b\omega \mathbf{u}^\top \mathbf{z}\right) C - \sin\left(b\omega \mathbf{u}^\top \mathbf{z}\right) S\right],\end{aligned} \tag{4.51}$$

where

$$C + \mathbf{i}S = \begin{pmatrix} \left(A^R\right)^2 & A^R A^G e^{\mathbf{i}\left(\varphi^R - \varphi^G\right)} & A^R A^B e^{\mathbf{i}\left(\varphi^R - \varphi^B\right)} \\ A^R A^G e^{\mathbf{i}\left(\varphi^G - \varphi^R\right)} & \left(A^G\right)^2 & A^G A^B e^{\mathbf{i}\left(\varphi^G - \varphi^B\right)} \\ A^R A^B e^{\mathbf{i}\left(\varphi^B - \varphi^R\right)} & A^G A^B e^{\mathbf{i}\left(\varphi^B - \varphi^G\right)} & \left(A^B\right)^2 \end{pmatrix}. \tag{4.52}$$

In the special case of $\mathbf{z} = 0$, *the covariance matrix becomes*

$$\begin{aligned}\Sigma(0) = \frac{\mu}{4b^2} \times \\ \begin{pmatrix} \left(A^R\right)^2 & A^R A^G \cos\left(\varphi^R - \varphi^G\right) & A^R A^B \cos\left(\varphi^R - \varphi^B\right) \\ A^R A^G \cos\left(\varphi^R - \varphi^G\right) & \left(A^G\right)^2 & A^G A^B \cos\left(\varphi^G - \varphi^B\right) \\ A^R A^B \cos\left(\varphi^R - \varphi^B\right) & A^G A^B \cos\left(\varphi^G - \varphi^B\right) & \left(A^B\right)^2 \end{pmatrix}.\end{aligned} \tag{4.53}$$

The proof is given in Appendix C.2. For the sake of simplicity, the matrix $\Sigma(0)$ is now denoted by Σ. This covariance matrix makes the link between the color channels explicit. Indeed, if C_1 and C_2 are two colors of $\{R, G, B\}$, then,

- s^{C_1} and s^{C_2} are positively correlated if $0 \leq |\varphi^{C_1} - \varphi^{C_2}| < \frac{\pi}{2}$ $[2\pi]$, with a maximal correlation reached when $\varphi^{C_1} = \varphi^{C_2}$ $[2\pi]$,
- s^{C_1} and s^{C_2} are negatively correlated if $\frac{\pi}{2} < |\varphi^{C_1} - \varphi^{C_2}| \leq \pi$ $[2\pi]$, with a maximal negative correlation when $\varphi^{C_1} = \varphi^{C_2} + \pi$ $[2\pi]$,
- s^{C_1} and s^{C_2} are uncorrelated if $\varphi^{C_1} = \varphi^{C_2} + \frac{\pi}{2}$ $[\pi]$.

The amplitude values A^R, A^G and A^B either amplify or attenuate these correlations. This explicit interpretation of the color parameters enables a complete control over the covariances between the color channels. In the case of an equal contribution of the red, green and blue channels, *i.e.*, if $A^R = A^G = A^B$ and $\varphi^R = \varphi^G = \varphi^B$, the color content of

the generated image only consists of shades of grey, which is consistent with what is said in Section 4.1.5 in the case of deterministic color waves. This implies that the more different the color parameters are from each other, the richer the color content of the texture is. The trajectory of the texture inside the color space can be characterized more precisely by applying the elliptic model developed in (Soulard & Carré 2015) to the Gabor noise.

4.3.2 Elliptical oscillation inside the RGB cube

As stated in (Soulard & Carré 2015) and recalled in Section 4.1, in the special case of a deterministic color cosine wave, *i.e.*, for all $\mathbf{x} \in \mathbb{R}^2$,

$$\Phi(\mathbf{x}) = \Phi_0 + \begin{pmatrix} A^R \cos\left[\omega \mathbf{u}^\top \mathbf{x} + \varphi^R\right] \\ A^G \cos\left[\omega \mathbf{u}^\top \mathbf{x} + \varphi^G\right] \\ A^B \cos\left[\omega \mathbf{u}^\top \mathbf{x} + \varphi^B\right] \end{pmatrix}, \tag{4.54}$$

then the trajectory of Φ inside the RGB cube $[0,1]^3$ is an ellipse whose parameters are given in Section 4.1.2 and 4.1.3. This result can be generalized to phasor noises as follows.

Theorem 10. *Let Φ be a phasor noise as defined in Eq. (4.44). Then the trajectory of Φ lies inside an ellipse $\mathcal{E}$ such that*

- *the center of $\mathcal{E}$ is Φ_0,*
- *the semi-major and semi-minor axes of $\mathcal{E}$, denoted by r_+ and r_-, respectively, are given by*

$$r_+^2 = \tfrac{A^2 + |\Gamma^\top \Gamma|}{2}, \quad r_-^2 = \tfrac{A^2 - |\Gamma^\top \Gamma|}{2}, \tag{4.55}$$

where A denotes the unified color amplitude defined by

$$A = \sqrt{(A^R)^2 + (A^G)^2 + (A^B)^2} \tag{4.56}$$

and Γ denotes the color Fourier atom defined by

$$\Gamma = \begin{pmatrix} A^R e^{\mathbf{i}\varphi^R} \\ A^G e^{\mathbf{i}\varphi^G} \\ A^B e^{\mathbf{i}\varphi^B} \end{pmatrix}, \tag{4.57}$$

- *the vertexes of $\mathcal{E}$, denoted by Φ_+ and Φ_-, respectively, are given by*

$$\Phi_+ = \Phi_0 + \begin{pmatrix} A^R \cos\big(\varphi^R - \widehat{\varphi}\big) \\ A^G \cos\big(\varphi^G - \widehat{\varphi}\big) \\ A^B \cos\big(\varphi^B - \widehat{\varphi}\big) \end{pmatrix}, \quad \Phi_- = \Phi_0 + \begin{pmatrix} A^R \sin\big(\varphi^R - \widehat{\varphi}\big) \\ A^G \sin\big(\varphi^G - \widehat{\varphi}\big) \\ A^B \sin\big(\varphi^B - \widehat{\varphi}\big) \end{pmatrix}, \tag{4.58}$$

where $\widehat{\varphi}$ denotes the unified color phase shift defined by

$$\widehat{\varphi} = \frac{1}{2} \arg\left(\Gamma^\top \Gamma\right). \tag{4.59}$$

This theorem is proved by applying the same procedures as in Sections 4.1.2 and 4.1.3, respectively. The main difference is that the phase function φ is not necessarily surjective, unlike the linear function $\mathbf{x} \mapsto \omega \mathbf{u}^\top \mathbf{x}$ in the case of a deterministic color wave. Consequently, all the points of the ellipse are not necessarily reached, *i.e.*, the trajectory of Φ inside the RGB cube may be strictly contained in $\mathcal{E}$ rather than being equal to $\mathcal{E}$. Despite that, the shape of the ellipse can still be directly linked with the color content of the image as in the deterministic case studied in (Soulard & Carré 2015) and Section 4.1. If the ellipse is very thin, almost linear, then the color wave oscillates along one color axis only. If the ellipse has a more circular shape, then the color wave oscillates in a much wider range of colors. This can be quantified by the linearity parameter λ defined in Eq. (4.21). Notice furthermore that the covariance matrix Σ defined in Eq. (4.53) can now be expressed as

$$\Sigma = \frac{\mu}{4b^2} \Re \{\Gamma \Gamma^*\}, \tag{4.60}$$

where Γ^* denotes the conjugate transpose of Γ, *i.e.*, $\overline{\Gamma}^\top$, with Γ given in Eq. (4.57). However, the underlying oscillating structure, characterized by the phase function φ defined in Section 4.2.3, cannot be extracted by such tools, and constitutes the main subject of Chapter 5.

4.3.3 Synthetic tests

In order to illustrate the elliptic model, five discrete bidirectional phasor noises $\Phi_1, \ldots, \Phi_5$ with different color parameters are synthesized with the same technique as in Section 4.2.4. The other parameter values are $M = N = 500$, $T_x = T_y = 0.002$, $b = 2$, $p = 0.1$, $\omega = 30$, $\alpha = \frac{\pi}{6}$, $\theta = \frac{\pi}{12}$ and $n = 2$ for all five noises. The results are given in Table 4.4.

Phasor	Φ_1	Φ_2	Φ_3	Φ_4	Φ_5
Φ_0^R	0.5	0.5	0.5	0.5	0
Φ_0^G	0	0	0.5	0.5	0.5
Φ_0^B	0	0.5	0.5	0.5	0.25
A^R	0.3	0.5	0.5	0.5	0
A^G	0	0	0.5	0.5	0.5
A^B	0	0.5	0.5	0.5	0.25
φ^R	0	0	0	0	0
φ^G	0	0	$\frac{2\pi}{3}$	$\frac{\pi}{2}$	$\frac{2\pi}{3}$
φ^B	0	$\frac{2\pi}{3}$	$-\frac{2\pi}{3}$	$\frac{\pi}{3}$	$-\frac{2\pi}{3}$
phasor		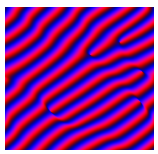	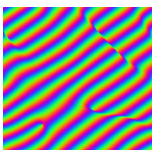	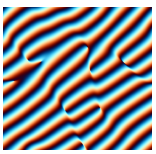	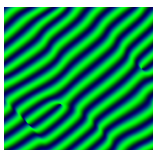
ellipse					
λ	1	0.5	0	0.33	0.72

Table 4.4: Link between the color parameters, the color content of the texture and the shape of the corresponding ellipse, with $b = 2$, $p = 0.1$, $\omega = 30$, $\alpha = \frac{\pi}{6}$, $\theta = \frac{\pi}{12}$ and $n = 2$.

As expected, the respective color ranges of these generated phasor noises are the same as those of the corresponding deterministic waves of Section 4.1.5, which illustrates how the elliptic model enables the generation of color stochastic oscillating textures with prescribed color content. Notice that the effect of the color parameters on the richness of the color content is consistent with the interpretation of the color covariances given in Section 4.3.1. While (Tricard et al. 2019) aims at building a purely procedural noise technique with a direct link between the parameters and the local oscillating behavior, this work goes further in this direction by including the color into the model rather than coloring greyscale textures *a posteriori*.

4.4 Conclusion

The main contribution of this chapter is the extension of the elliptic color model introduced in (Soulard & Carré 2015). Section 4.1 further studies the link between the color parameters, the color shades contained in the image and the shape of the ellipse, with both theoretical results and numerical illustrations. The linearity parameter, deeply investigated in Section 4.1.4, enables a numerical characterization of color richness, and is hence of great interest from a color texture description point of view.

Furthermore, by merging the elliptic color model and the phasor noise, this chapter generalizes both frameworks. Originally designed for deterministic oscillating color images, the elliptic model of (Soulard & Carré 2015) is extended to the stochastic case by being applied to phasor noise introduced in (Tricard et al. 2019), which in turn lacked a formal color extension. The direct link between the color parameters of the texture and the shape and position of an ellipse inside the RGB cube still provides a useful visual representation of color oscillations in a stochastic context, while being reinforced by their consistency with the color covariances. This enables a full control over the color content of the synthesized texture, in addition to the control over its frequency content which was already one of the main advantages of the phasor approach.

Because the color information is fully encoded in the parameters of the ellipse, it can be expected that these parameters would provide useful descriptors of the color content of real textures displaying oscillating patterns. In order to investigate this idea, a reliable estimation technique must be introduced to extract these parameters. This is exactly the topic of Chapter 5, which builds on the color phasor noise introduced in this chapter to further study both color texture analysis and synthesis, respectively.

APPENDIX C

Appendices

C.1 Proof of Theorem 8

The first step consists in expressing $|\Gamma^\top \Gamma|$ with the color parameters.

$$\begin{aligned}
|\Gamma^\top \Gamma|^2 &= \left| \sum_{C\in\{R,G,B\}} \left[\left(A^C\right)^2 \cos\left(2\varphi^C\right) \right] + \mathbf{i} \sum_{C\in\{R,G,B\}} \left[\left(A^C\right)^2 \sin\left(2\varphi^C\right) \right] \right|^2, \\
&= \sum_{C\in\{R,G,B\}} \left(A^C\right)^4 + \sum_{(C_1,C_2)\in\{R,G,B\}^2} \left(A^{C_1}\right)^2 \left(A^{C_2}\right)^2 \\
&\quad \times \left[\cos\left(2\varphi^{C_1}\right) \cos\left(2\varphi^{C_2}\right) + \sin\left(2\varphi^{C_1}\right) \sin\left(2\varphi^{C_2}\right) \right], \\
&= \left[\sum_{C\in\{R,G,B\}} \left(A^C\right)^2 \right]^2 + \sum_{(C_1,C_2)\in\{R,G,B\}^2} \left(A^{C_1}\right)^2 \left(A^{C_2}\right)^2 \\
&\quad \times \left[\cos\left(2\varphi^{C_1} - 2\varphi^{C_2}\right) - 1 \right], \\
&= A^4 - 2 \sum_{(C_1,C_2)\in\{R,G,B\}^2} \left(A^{C_1}\right)^2 \left(A^{C_2}\right)^2 \sin^2\left(\varphi^{C_1} - \varphi^{C_2}\right).
\end{aligned} \tag{C.1}$$

The special case $\lambda = 1$ is now characterized by using the color parameters.

$$\begin{aligned}
\lambda = 1 &\iff r_-^2 = 0, \\
&\iff \frac{A^2 - |\Gamma^\top \Gamma|}{2} = 0 \text{ (see Eq. (4.12))}, \\
&\iff A^2 = |\Gamma^\top \Gamma|, \\
&\iff A^4 = |\Gamma^\top \Gamma|^2, \\
&\iff A^4 = A^4 - 2 \sum_{(C_1,C_2)\in\{R,G,B\}^2} \left(A^{C_1}\right)^2 \left(A^{C_2}\right)^2 \sin^2\left(\varphi^{C_1} - \varphi^{C_2}\right), \\
&\iff \sum_{(C_1,C_2)\in\{R,G,B\}^2} \left(A^{C_1}\right)^2 \left(A^{C_2}\right)^2 \sin^2\left(\varphi^{C_1} - \varphi^{C_2}\right) = 0, \\
&\iff \forall (C_1,C_2) \in \{R,G,B\}^2, A^{C_1} A^{C_2} \sin\left(\varphi^{C_1} - \varphi^{C_2}\right) = 0.
\end{aligned} \tag{C.2}$$

This condition is fulfilled in three cases:

- $A^{C_1} = A^{C_2} = 0$ for at least two distinct color channels $(C_1, C_2) \in \{R,G,B\}^2$,

- $A^{C_1} = 0$ and $\varphi^{C_2} = \varphi^{C_3}$ $[\pi]$, with C_1, C_2 and C_3 being three distinct color channels of $\{R, G, B\}$,
- $\varphi^R = \varphi^G = \varphi^B$ $[\pi]$,

which is exactly what was to be proved. The special case $\lambda = 0$ is now studied.

$$
\begin{aligned}
\lambda = 0 &\iff r_-^2 = r_+^2, \\
&\iff \frac{A^2 - |\Gamma^\top \Gamma|}{2} = \frac{A^2 + |\Gamma^\top \Gamma|}{2}, \\
&\iff |\Gamma^\top \Gamma| = 0, \\
&\iff \Gamma^\top \Gamma = 0, \\
&\iff \sum_{C \in \{R,G,B\}} \left[\left(A^C\right)^2 \cos\left(2\varphi^C\right) \right] + \mathbf{i} \sum_{C \in \{R,G,B\}} \left[\left(A^C\right)^2 \sin\left(2\varphi^C\right) \right] = 0, \\
&\iff \begin{cases} \sum_{C \in \{R,G,B\}} \left(A^C\right)^2 \cos\left(2\varphi^C\right) = 0, \\ \sum_{C \in \{R,G,B\}} \left(A^C\right)^2 \sin\left(2\varphi^C\right) = 0. \end{cases}
\end{aligned}
\tag{C.3}
$$

C.2 Proof of Theorem 4.53

The proof uses a similar procedure as the proof of Theorem 5 in the greyscale case. Each of the scalar unidirectional Gabor noises s^C, $C \in \{R, G, B\}$, are stationary and zero-mean as stated in (Lagae & Drettakis 2011) and recalled in Section 3.2.3. Let $\mathbf{z} \in \mathbb{R}^2$ be a 2D spatial delay and $(C_1, C_2) \in \{R, G, B\}^2$ be a pair of colors. The delayed Gabor noise $s^{C_2}_{\mathbf{z}}$ is defined for all $\mathbf{x} \in \mathbb{R}^2$ as

$$s^{C_2}_{\mathbf{z}}(\mathbf{x}) = A^{C_2} \sum_i a(\mathbf{x} - \mathbf{z} - \mathbf{x}_i) \cos\left[b\omega \mathbf{u}^\top (\mathbf{x} - \mathbf{z} - \mathbf{x}_i) + \psi_i + \varphi^{C_2}\right]. \tag{C.4}$$

In order to calculate the covariance matrix of s, Proposition 3.1 of (Galerne 2010) is applied to the Gabor noises s^{C_1} and $s^{C_2}_{\mathbf{z}}$, *i.e.*,

$$\begin{aligned} \mathrm{Cov}\left(s^{C_1}, s^{C_2}_{\mathbf{z}}\right) &= \frac{\mu}{2\pi} A^{C_1} A^{C_2} \int_{-\pi}^{\pi} \int_{\mathbb{R}^2} a(\mathbf{y}) a(\mathbf{y} - \mathbf{z}) \\ &\times \cos\left(b\omega \mathbf{u}^\top \mathbf{y} + \psi + \varphi^{C1}\right) \cos\left[b\omega \mathbf{u}^\top (\mathbf{y} - \mathbf{z}) + \psi + \varphi^{C2}\right] d\mathbf{y} d\psi \end{aligned} \tag{C.5}$$

Using the trigonometric identity $\cos(a)\cos(b) = \frac{\cos(a+b)+\cos(a+b)}{2}$ leads to

$$\mathrm{Cov}\left(s^{C_1}, s^{C_2}_{\mathbf{z}}\right) = \frac{\mu}{4\pi} A^{C_1} A^{C_2} \left(I_1 + I_2\right), \tag{C.6}$$

where

$$\begin{aligned} I_1 = \int_{-\pi}^{\pi} \int_{\mathbb{R}^2} & e^{-\pi b^2 ||\mathbf{y}||^2} e^{-\pi b^2 ||\mathbf{y}-\mathbf{z}||^2} \\ & \times \cos\left[b\omega \mathbf{u}^\top (2\mathbf{y} - \mathbf{z}) + 2\psi + \varphi^{C_1} + \varphi^{C_2}\right] d\mathbf{y} d\psi, \end{aligned} \tag{C.7}$$

and

$$\begin{aligned} I_2 = \int_{-\pi}^{\pi} \int_{\mathbb{R}^2} & e^{-\pi b^2 ||\mathbf{y}||^2} e^{-\pi b^2 ||\mathbf{y}-\mathbf{z}||^2} \\ & \times \cos\left(b\omega \mathbf{u}^\top \mathbf{z} + \varphi^{C_1} - \varphi^{C_2}\right) d\mathbf{y} d\psi. \end{aligned} \tag{C.8}$$

Applying the same procedures as in the proof of Theorem 5 then yields $I_1 = 0$ and

$$I_2 = \frac{\pi}{b^2} \cos\left(b\omega \mathbf{u}^\top \mathbf{z} + \varphi^{C_1} - \varphi^{C_2}\right) e^{-\frac{1}{2}\pi b^2 ||\mathbf{z}||^2}. \tag{C.9}$$

Injecting this expression in Eq. (C.6) finally leads to

$$\begin{aligned} \mathrm{Cov}\left(s^{C_1}, s^{C_2}_{\mathbf{z}}\right) =& \frac{\mu}{4b^2} A^{C_1} A^{C_2} e^{-\frac{1}{2}\pi b^2 ||z||^2} \cos\left(b\omega \mathbf{u}^\top \mathbf{z} + \varphi^{C_1} - \varphi^{C_2}\right), \\ =& \frac{\mu}{4b^2} A^{C_1} A^{C_2} e^{-\frac{1}{2}\pi b^2 ||z||^2} \\ & \times \left[\cos\left(b\omega \mathbf{u}^\top \mathbf{z}\right) \cos\left(\varphi^{C_1} - \varphi^{C_2}\right)\right. \\ & \left. - \sin\left(b\omega \mathbf{u}^\top \mathbf{z}\right) \sin\left(\varphi^{C_1} - \varphi^{C_2}\right)\right], \end{aligned} \tag{C.10}$$

which is exactly what was to be proved.

CHAPTER 5

The color phasor noise

Chapter 3 has extended the scope of the monogenic signal by highlighting its ability to extract the local features of oscillating stochastic textures. However, only greyscale images were considered. A proper color model has then been introduced in Chapter 4 based on the elliptic approach of (Soulard & Carré 2015), which is then used to define color extensions of the Gabor and phasor noises. The results have pointed out the direct link between the color parameters, the color covariances and the color content of the synthesized textures, which is one the main advantages of this approach. This chapter thus aims at merging the results of Chapters 3 and 4, *i.e.*, extending the monogenic tool to color textures by using the elliptic color model.

Following the works of (Felsberg & Sommer 2001) in the greyscale case, a color extension has been introduced in (Demarcq et al. 2011) by use of Clifford algebras. While interesting for its purely vectorial treatment of the color channels, the generalized notion of local color phase lacks a clear physical interpretation, partly due to its use of 5-dimension spaces. Besides the generalization of the elliptic model to color textures already studied in Chapter 4, (Soulard & Carré 2015) has also introduced a proper color extension of the monogenic signal. This time, the physical interpretation of the defined local features, as well as the analogy with the greyscale case, were clearer. The features extracted by the color monogenic tool have then proved to be particularly useful in the field of image denoising (Gai 2018, Gai 2019). However, as for the elliptic model, these local features were only defined for deterministic color waves. Consequently, this chapter aims at extending them to stochastic textures and study the reliability of their estimations by use of the color phasor noise introduced in Chapter 4. The color monogenic signal is then applied to real color textures displaying oscillating patterns in order to characterize their color dynamics.

Focusing on the texture synthesis field, this chapter also aims at introducing a monogenic-based measure of local regularity in order to evaluate the quality of a synthesized color phasor noise. In the greyscale case, one of the most significant contributions of the phasor noise introduced in (Tricard et al. 2019) was the elimination of the local losses of contrast of the Gabor noise without modifying their oscillating behaviors. However, as noticed in Chapters 3 and 4, these synthesized phasor noises display local singularities, *i.e.*, local irregularities caused by abrupt phase jumps or changes of direction. Such singularities make the synthesized texture look artificial, hence the need to control their occurrences. While this issue is explicitly evoked in (Tricard et al. 2019), it was left as an open problem for future works. Given the fact that the singularities observed in the phasor noise are directly linked with its phase function (Tricard et al. 2019), one possible approach to bypass this difficulty is to use reliable phase extraction techniques in order to characterize their occurrence. One of the main ideas of this chapter is thus to use the quality of the monogenic

estimation of phase highlighted in the previous chapters, as well as in numerous works such as (Langley & Anderson 2010, Seelamantula et al. 2012, Alessandrini et al. 2013, Olhede et al. 2014), in order to evaluate the quality of the synthesis in terms of singularity occurrence.

The rest of the chapter is organized as follows. Section 5.1 studies the robustness of the monogenic extraction of the color parameters, with both theoretical and numerical results. Applications to real color textures are included. The singularity issue is then tackled in Section 5.2, in which the monogenic signal yields a numerical criterion that characterizes the local regularity of synthesized phasor noises. This technique is finally applied in Section 5.3, with a special focus on the influence of the model parameters on the quality of the synthesis.

5.1 Monogenic estimation of the color parameters

Chapter 4.1 has illustrated the benefits of the visual representation of color oscillation provided by the color phasor noise, making it a useful color texture synthesis tool. This section tackles the color texture analysis side of the model. This is performed by using the Riesz transform, which has already proved its relevance in extracting the local oscillating features of 2D signals in the previous chapters, as well as in works such as (Seelamantula et al. 2012, Olhede et al. 2014, Kaseb et al. 2019).

5.1.1 Effect of a constant phase-shift on the three color components

Let Φ be a color phasor noise as defined in Eq. (4.44). In order to extract the exact values of the color phase-shifts φ^C, $C \in \{R, G, B\}$, from the three components of Φ, a first idea consists in applying the Riesz transform to each channels. However, this would yield an estimation of the sum $\varphi(\mathbf{x}) + \varphi^C$, $\mathbf{x} \in \mathbb{R}^2$, with no obvious means to separate the two terms. This implies that the exact values of the color phase-shifts cannot be extracted through this technique. However, this does not prevent the monogenic tool to characterize the color oscillations of the image. Indeed, this section aims at showing how knowing the phase differences rather than the phase values themselves is enough to characterize the ellipse associated with the texture. For any angular value $\psi \in]-\pi, \pi[$, let Φ_ψ denote the phase-shifted image defined for all $\mathbf{x} \in \mathbb{R}^2$ by

$$\Phi_\psi(\mathbf{x}) = \begin{pmatrix} \Phi_0^R + A^R \cos\left(\varphi(\mathbf{x}) + \varphi^R + \psi\right) \\ \Phi_0^G + A^G \cos\left(\varphi(\mathbf{x}) + \varphi^G + \psi\right) \\ \Phi_0^B + A^B \cos\left(\varphi(\mathbf{x}) + \varphi^B + \psi\right) \end{pmatrix}. \tag{5.1}$$

Then, the Euclidian distance between each point of the texture and the offset Φ_0 can be expressed by applying the same technique as in Eq. (4.10), *i.e*, for all $\mathbf{x} \in \mathbb{R}^2$,

$$\|\Phi_\psi(\mathbf{x}) - \Phi_0\|^2 = \frac{A^2 - |\Gamma^\top_\psi \Gamma_\psi|}{2} + |\Gamma^\top_\psi \Gamma_\psi| \cos^2\left[\varphi(\mathbf{x}) + \frac{1}{2}\arg\left(\Gamma^\top_\psi \Gamma_\psi\right)\right], \tag{5.2}$$

where Γ_ψ denotes the ψ-shifted version of the complex vector Γ defined in Eq. (4.8), *i.e.*,

$$\Gamma_\psi = \begin{pmatrix} A^R e^{\mathbf{i}(\varphi^R + \psi)} \\ A^G e^{\mathbf{i}(\varphi^G + \psi)} \\ A^B e^{\mathbf{i}(\varphi^B + \psi)} \end{pmatrix} = \Gamma e^{\mathbf{i}\psi}. \tag{5.3}$$

It is clear that the complex numbers $\Gamma_\psi^\top \Gamma_\psi$ and $\Gamma^\top \Gamma$ have the same modulus. Furthermore,

$$\begin{aligned}\frac{1}{2}\arg\left(\Gamma_\psi^\top \Gamma_\psi\right) &= \frac{1}{2}\arg\left(\Gamma^\top \Gamma e^{2\mathbf{i}\psi}\right) \ [2\pi], \\ &= \frac{1}{2}\arg\left(\Gamma^\top \Gamma\right) + \frac{1}{2}\arg\left(e^{2\mathbf{i}\psi}\right) \ [2\pi], \\ &= \widehat{\varphi} + \psi \ [2\pi],\end{aligned} \tag{5.4}$$

where $\widehat{\varphi}$ denoted the unified phase defined in Eq. (4.13). Eq. (5.2) hence becomes

$$\|\Phi_\psi(\mathbf{x}) - \Phi_0\|^2 = \frac{A^2 - |\Gamma^\top \Gamma|}{2} + |\Gamma^\top \Gamma| \cos^2\left[\varphi(\mathbf{x}) + \widehat{\varphi} + \psi\right]. \tag{5.5}$$

This expression has the same extreme values as its non-shifted counterpart, which implies that the ellipse associated with the phase-shifted image Φ_ψ has the same shape as the original ellipse associated with Φ. Furthermore, if the maximal and minimal values are reached, they correspond to $\varphi(\mathbf{x}) = -\varphi - \psi$ and $\varphi(\mathbf{x}) = -\varphi - \psi - \frac{\pi}{2}$, respectively. If Φ_+^ψ and Φ_+^ψ denote the vertexes of the shifted ellipse, then, Eq. (4.58) becomes

$$\Phi_+^\psi = \Phi_0 + \begin{pmatrix} A^R \cos\left(\varphi^R + \psi - \varphi - \psi\right) \\ A^G \cos\left(\varphi^G + \psi - \varphi - \psi\right) \\ A^B \cos\left(\varphi^B + \psi - \varphi - \psi\right) \end{pmatrix} = \Phi_+, \tag{5.6}$$

and

$$\Phi_-^\psi = \Phi_0 + \begin{pmatrix} A^R \sin\left(\varphi^R + \psi - \varphi - \psi\right) \\ A^G \sin\left(\varphi^G + \psi - \varphi - \psi\right) \\ A^B \sin\left(\varphi^B + \psi - \varphi - \psi\right) \end{pmatrix} = \Phi_-, \tag{5.7}$$

where Φ_+ and Φ_- denote the vertexes of the non-shifted ellipse. This shows that phase-shifting the image with an angle ψ not only preserves the shape of the ellipse, but also the position of its vertexes. In other words, the phase-shift has no impact on the ellipse at all, the only difference being that the points of the ellipse are not reached at the same pixels. The impact of ψ is thus analogous to that of the classical phase-shift in the case of 1D signals. This is of particularly great interest when parameter estimation comes into play, which is the subject of Section 5.1.2.

5.1.2 Estimation of the color parameters

Chapter 4 has already illustrated the direct link between the color parameters of the elliptic model and the color content of the synthesized image, with both theoretical and numerical results. The ability of the linearity parameter λ, defined in Eq. (4.21), to characterize the color content of real textures has also been highlighted in (Soulard & Carré 2015). Though the Riesz transform was used to extract the color parameters of the studied images, no formal study of how the Riesz transform deals with stochastic textures has been performed yet. This section aims at studying formally and numerically how the Riesz transform manages to extract the color parameters of a stochastic texture displaying oscillating patterns. Similarly to what is done in Chapter 3 in the greyscale case, the Riesz transform is first applied to synthesized color phasor noises. This class of oscillating stochastic textures is used for the direct control over the frequency and color content it provides, respectively.

Let Φ be a color phasor noise as defined in Eq. (4.44), and let Φ^C denote the color components of Φ for all $C \in \{R, G, B\}$. Because each component of Φ is a greyscale phasor noise (up to an offset), the results established in Chapter 3 can be used. Indeed, for all $C \in \{R, G, B\}$, if A_M^C and ϕ^C denote the monogenic amplitude and phase of the centered color component $\Phi^C - s_0^C$ as defined in Eq. (2.44), respectively, then for all $\mathbf{x} \in \mathbb{R}^2$, it can be expected that

$$\begin{cases} A_M^C(\mathbf{x}) \approx A^C, \\ \phi^C(\mathbf{x}) \approx \omega \mathbf{u}^\top \mathbf{x} + \varphi^C \ [2\pi]. \end{cases} \tag{5.8}$$

Because the color components are assumed to share the same wave vector, this implies that, for all $\mathbf{x} \in \mathbb{R}^2$ and $(C_1, C_2) \in \{R, G, B\}^2$,

$$\phi^{C_1}(\mathbf{x}) - \phi^{C_2}(\mathbf{x}) \approx \varphi^{C_1} - \varphi^{C_2} \ [2\pi]. \tag{5.9}$$

Eq. (5.8) and Eq. (5.9) hence provide techniques to extract the color amplitudes and phase differences of oscillating color textures. Though the exact values of the phase-shifts φ^C ($C \in \{R, G, B\}$) cannot be estimated through this technique, Section 5.1.1 shows that applying a constant shift to all phase values does not affect the shape of the ellipse, *i.e.*, the nature of the color oscillations. As highlighted in the synthetic tests of Section 4.1.5, the difference between the phase parameters matters more than their proper values. Therefore, fixing $\varphi^R = 0$ and estimating the other two phase values φ^G and φ^B, respectively, from the phase differences extracted by Eq. (5.9) implies no loss of information in terms of color oscillations. The ellipse can then be fully parametrized by applying the equations established in Section 4.1. Though the statistical behavior of these estimators has not been formally studied yet, the synthetic tests performed in Section 5.1.3 show that they give consistent results when applied to color phasor noises.

5.1.3 Synthetic tests

The color parameter extraction technique introduced in Section 5.1.2 is now applied on synthesized color phasor noises to study its reliability. A discrete color phasor is first generated by using the procedure described in Section 4.2.4. After removing the offset, the Riesz transform is applied to each color channel, which yields monogenic measures of amplitude and phase at each pixel and for each channel, respectively. For each color $C \in \{R, G, B\}$, let A_M^C and ϕ^C denote the discrete amplitude and phase signals extracted from the image, respectively. Focusing on the green channel, the amplitude signal A_M^G is expected to be constantly equal to A^G, while the difference between the green and red phase signals, $\phi^G - \phi^R$ is expected to be constantly equal to $\varphi^G - \varphi^R$. Figure 5.1 shows the absolute error at each pixel for both the green amplitude and the green phase-shift, *i.e.*, $|A_M^G - A^G|$ and $|\phi^G - \phi^R - \varphi^G + \varphi^R|$ $[2\pi]$, respectively. The parameters are $M = N = 1000$, $T_x = T_y = 0.002$, $b = 2$, $\omega = 30$, $\alpha = \frac{\pi}{6}$, $n = 1$, $A^R = 0.1$, $A^G = 0.5$, $A^B = 0.25$, $\varphi^R = 0$, $\varphi^G = \frac{2\pi}{3}$, $\varphi^B = -\frac{2\pi}{3}$ and $\Phi_0 = \begin{pmatrix} 0.1 & 0.5 & 0.25 \end{pmatrix}^\top$. As expected, aside from border effects, the absolute error is close to 0 in both cases. Focusing on the red or blue channels yields the same results. Notice that, similarly to what was observed in Section 3.3.2 in the greyscale case, the estimation diverges where singularities appear, *i.e.*, where abrupt phase jumps occur. This is further discussed in Section 5.3. This confirms the theoretical results of Section 5.1.2, *i.e.*, the color parameters are well extracted by the monogenic signal.

For each color $C \in \{R, G, B\}$, the estimators of A^C and φ^C, denoted by $\widehat{A^C}$ and $\widehat{\varphi^C}$, respectively, are then computed as

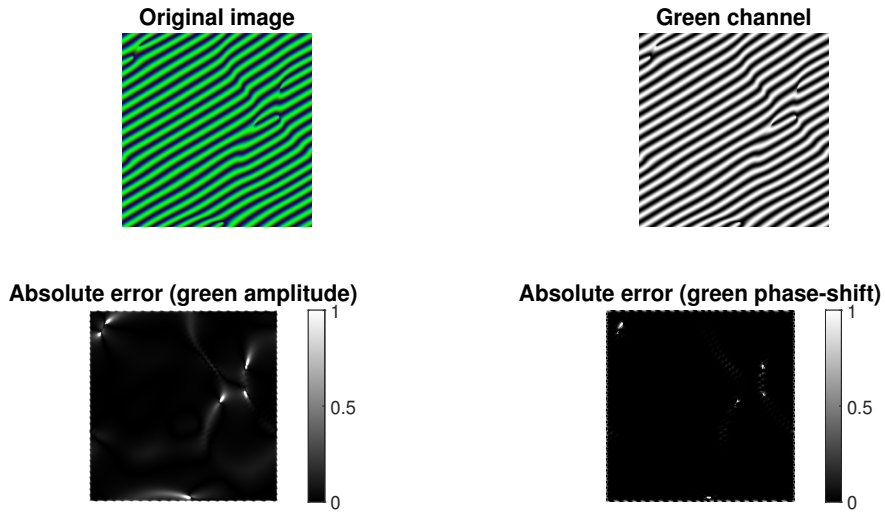

Figure 5.1: Original color phasor noise (top left), green channel (top right), absolute error of the green amplitude estimator (bottom left) and absolute error of the green phase-shift estimator (bottom right), with $b = 2$, $p = 0.1$, $\omega = 30$, $\alpha = \frac{\pi}{6}$, $n = 1$, $A^R = 0.1$, $A^G = 0.5$, $A^B = 0.25$, $\varphi^R = 0$, $\varphi^G = \frac{2\pi}{3}$, $\varphi^B = -\frac{2\pi}{3}$ and $\Phi_0 = \begin{pmatrix} 0.1 & 0.5 & 0.25 \end{pmatrix}^\top$.

$$\begin{array}{rl} \widehat{A^C} & = \frac{1}{(M-2m_0)(N-2n_0)} \sum_{j=m_0}^{M-1-m_0} \sum_{k=n_0}^{N-1-n_0} \left(A_M^C\right)_{j,k}, \\ \widehat{\varphi^C} & = \frac{1}{(M-2m_0)(N-2n_0)} \sum_{j=m_0}^{M-1-m_0} \sum_{k=n_0}^{N-1-n_0} \left(\phi_{j,k}^C - \phi_{j,k}^R\right) \ [2\pi] \quad (C \in \{G, B\}), \end{array} \tag{5.10}$$

where m_0 and n_0 are integers chosen to avoid the border effect. In the subsequent tests, $m_0 = n_0 = 30$, which is enough to eliminate the problematic pixels. Thanks to Eq. (4.6) and Eq. (4.13), these estimates can then be used to calculate the unified amplitude A and phase-shift $\widehat{\varphi}$, respectively. This yields the reconstruction the ellipse by applying the results established in Sections 4.1.2 and 4.1.3, respectively. Though applying the Riesz transform to each color channel marginally may not be the best solution from a color image processing point of view, it is necessary to extract the parameters of the ellipse, which then provides a non-marginal description of the color oscillations. Table 5.1 gives the results obtained from two color phasor noises generated with different sets of color parameters, the other parameters being $b = 2$, $\omega = 30$, $\alpha = \frac{\pi}{6}$ and $n = 1$ for both images. The estimated parameters are very close to the real values, which further confirms what was expected in Section 5.1.2. This yields a reconstructed ellipse that looks very close to the real one, which is reflected in its linearity parameter as well as its color shades. Remember that the color phase-shifts are all known up to a translation, as seen in Section 5.1.1.

Focusing on the unified parameters A and $\widehat{\varphi}$, as well as the linearity parameter λ, the same technique is applied to $m = 50$ color phasor noises generated with the same set of parameters as in Figure 5.1. The results are given as boxplots in Figure 5.2. Though a bias is observed for all three parameters A, $\widehat{\varphi}$ and λ, the estimated values remain close to the corresponding real values (marked with a big black dot).

Because this estimation technique relies heavily on Theorem 6, it is not surprising that increasing b and ω makes the color parameter extraction more efficient, as can be seen on the

Name	s_1		s_2	
	Real	Estimated	Real	Estimated
s_0^R	0.5	0.5006	0.1	0.0998
s_0^G	0.5	0.5003	0.5	0.4995
s_0^B	0.5	0.5	0.25	0.2506
A^R	0.5	0.498	0.1	0.1038
A^G	0.5	0.4984	0.5	0.5187
A^B	0.5	0.4987	0.25	0.259
A	0.866	0.8632	0.5679	0.589
φ^R	0	-	0	-
φ^G	$\frac{\pi}{3}$	1.0472	$\frac{2\pi}{3}$	2.0784
φ^B	$\frac{\pi}{2}$	1.5708	$-\frac{2\pi}{3}$	-2.0787
$\widehat{\varphi}$	$\frac{\pi}{3}$	1.0484	$-\frac{2\pi}{3}$	-1.1706
Ellipse				
λ	0.33	0.3338	0.6776	0.6891

Table 5.1: Comparison between the real and estimated parameters of a color phasor noise, with $b = 2$, $p = 0.1$, $\omega = 30$, $\alpha = \frac{\pi}{6}$ and $n = 1$.

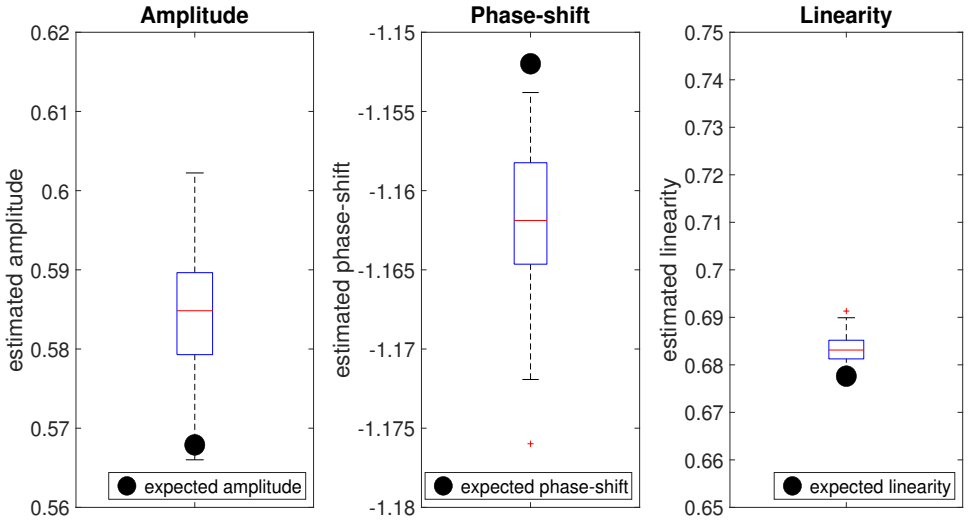

Figure 5.2: Boxplots of the unified amplitude A (left), unified phase-shift $\widehat{\varphi}$ (middle) and linearity parameter (right) estimated from $m = 50$ color phasor noises, with $b = 2$, $p = 0.1$, $\omega = 30$, $\alpha = \frac{\pi}{6}$, $n = 1$, $A^R = 0.1$, $A^G = 0.5$, $A^B = 0.25$, $\varphi^R = 0$, $\varphi^G = \frac{2\pi}{3}$, $\varphi^B = -\frac{2\pi}{3}$ and $\Phi_0 = \begin{pmatrix} 0.1 & 0.5 & 0.25 \end{pmatrix}^\top$.

boxplots displayed in Figure 5.3 and 5.4 in the case of the unified phase-shift estimation. Similar results can be observed for the other color parameters. This illustrates how the monogenic tool requires clear oscillating patterns in the image to yield a relevant measure of the color dynamic.

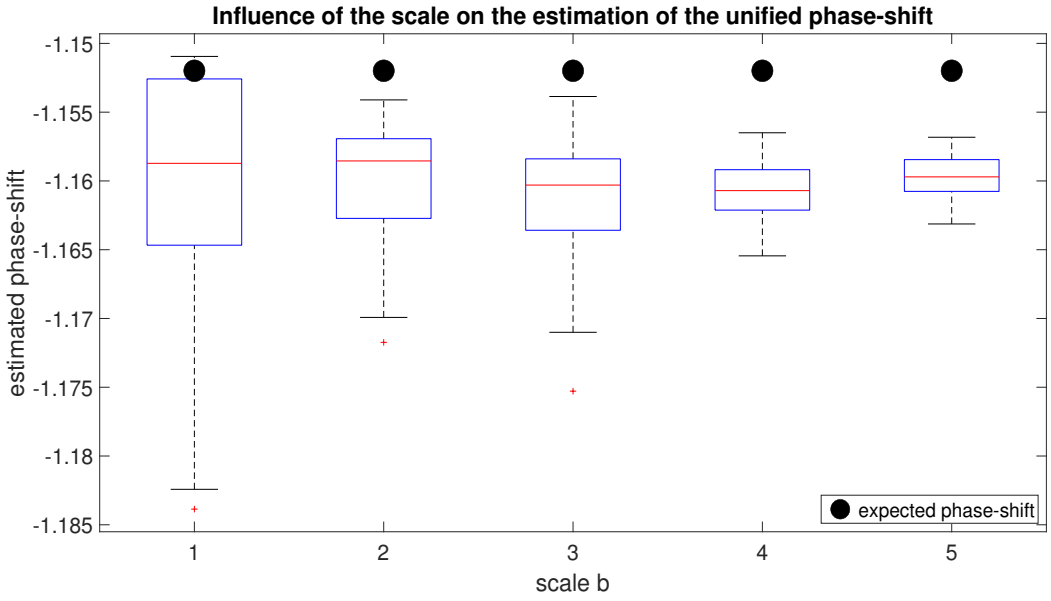

Figure 5.3: Boxplots of the unified phase-shift measured from $m = 50$ color phasor noises, $b \in \{1, \dots, 5\}$, $M = N = 1000$, $T_x = T_y = 0.002$, $p = 0.1$, $\omega = 30$, $\alpha = \frac{\pi}{6}$, $n = 1$, $A^R = 0.1$, $A^G = 0.5$, $A^B = 0.25$, $\varphi^R = 0$, $\varphi^G = \frac{2\pi}{3}$, $\varphi^B = -\frac{2\pi}{3}$ and $\Phi_0 = \begin{pmatrix} 0.1 & 0.5 & 0.25 \end{pmatrix}^\top$.

5.1.4 Case of a multidirectional phasor noise

In all former examples, the number of Gabor noises, denoted by n, is always equal to 1, which implies that the synthesized phasor noise is unidirectional. However, the color phasor noise introduced in Section 4.2.3 is more general, as it involves a sum of independent Gabor noises rather than a single Gabor noise. In order to increase the degree of complexity of the texture, a second Gabor noise with a different orientation can be independently added, yielding a bidirectional phasor noise, similarly to what is done in the greyscale case in (Tricard et al. 2019). The color noise Φ is now assumed to result from the sum of two independent color Gabor noises whose orientations are equal to α and $\alpha + \theta$, respectively, with $(\alpha, \alpha + \theta) \in]-\frac{\pi}{2}, \frac{\pi}{2}]^2$. The other parameters are assumed to be the same for both Gabor noises. Though no formal study of how the Riesz transform deals with such a noise, it can be expected that increasing the difference between the two orientations, *i.e.*, increasing θ, damages the estimation of the color parameters. Indeed, as highlighted in Section 4.2.4, if noises of significantly different orientations are combined, the oscillating patterns of the resulting image are obscured due to the conflicts between the two underlying waves. Figure 5.5 confirms this conjecture by estimating the green phase-shift from $m = 50$ color phasor noises generated from two Gabor noises of increasingly different orientations. As θ increases, the monogenic extraction of amplitude and phase loses quality, which is reflected by the loss of reliability of the green phase-shift estimation.

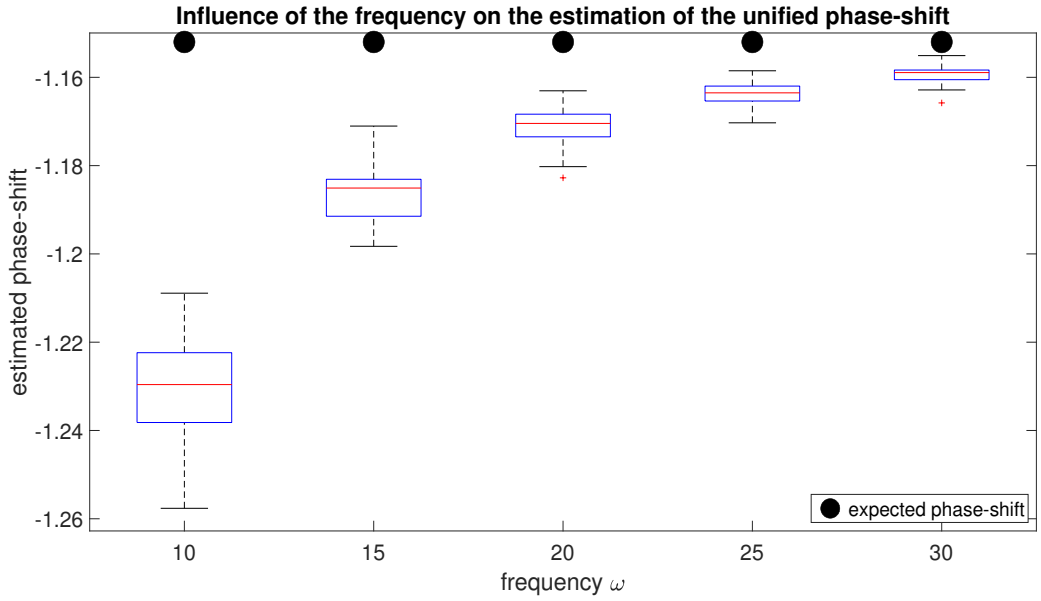

Figure 5.4: Boxplots of the unified phase-shift measured from $m = 50$ color phasor noises, $\omega \in \{10 + 5k, k = 0, \ldots, 4\}$, $M = N = 1000$, $T_x = T_y = 0.002$, $b = 5$, $p = 0.1$, $\alpha = \frac{\pi}{6}$, $n = 1$, $A^R = 0.1$, $A^G = 0.5$, $A^B = 0.25$, $\varphi^R = 0$, $\varphi^G = \frac{2\pi}{3}$, $\varphi^B = -\frac{2\pi}{3}$ and $\Phi_0 = \begin{pmatrix} 0.1 & 0.5 & 0.25 \end{pmatrix}^\top$.

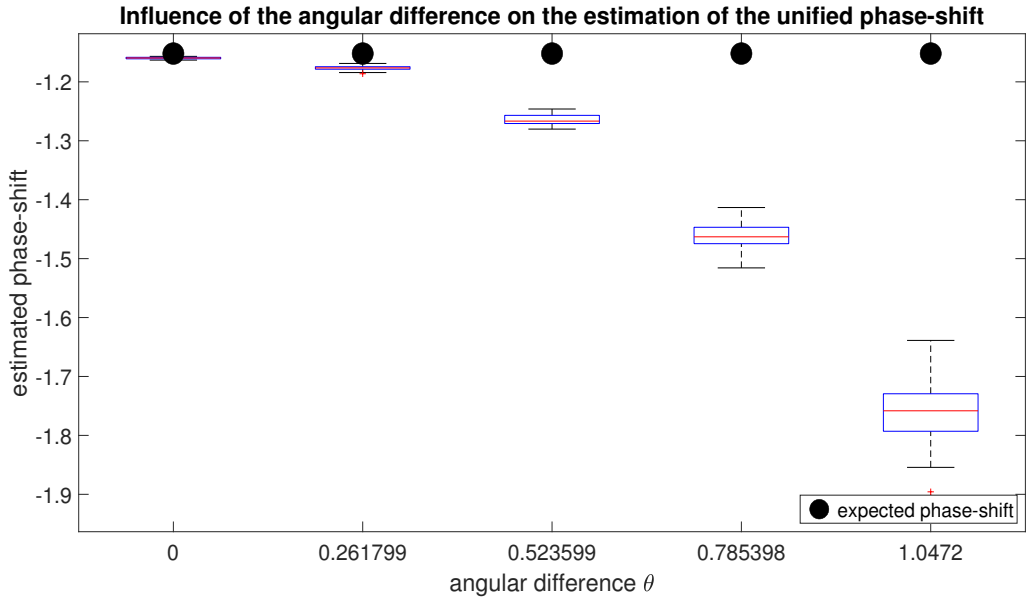

Figure 5.5: Boxplots of the unified phase-shift measured from $m = 50$ color phasor noises, $\theta \in \{\frac{\pi}{12}k, k = 0, \ldots, 4\}$, $M = N = 1000$, $T_x = T_y = 0.002$, $b = 5$, $p = 0.1$, $\omega = 30$, $\alpha = \frac{\pi}{6}$, $n = 2$, $A^R = 0.1$, $A^G = 0.5$, $A^B = 0.25$, $\varphi^R = 0$, $\varphi^G = \frac{2\pi}{3}$, $\varphi^B = -\frac{2\pi}{3}$ and $\Phi_0 = \begin{pmatrix} 0.1 & 0.5 & 0.25 \end{pmatrix}^\top$.

The number of independent Gabor noises in the sum is now raised to $n = 5$. For $\ell \in \{1, \dots, 5\}$, let α_ℓ denote the orientation of each Gabor noise s_ℓ. These orientations are randomly drawn following a normal distribution with mean $\frac{\pi}{6}$ and variance $v \in \mathbb{R}_+^*$. It can then be expected that the variance v has to be small enough to ensure that the image displays enough local regularity. This is confirmed by the synthesized noises shown in Figure 5.6. Increasing the variance v implies the occurring of more singularities, *i.e.*, discontinuities in the oscillations, which can then damage the color parameter extraction.

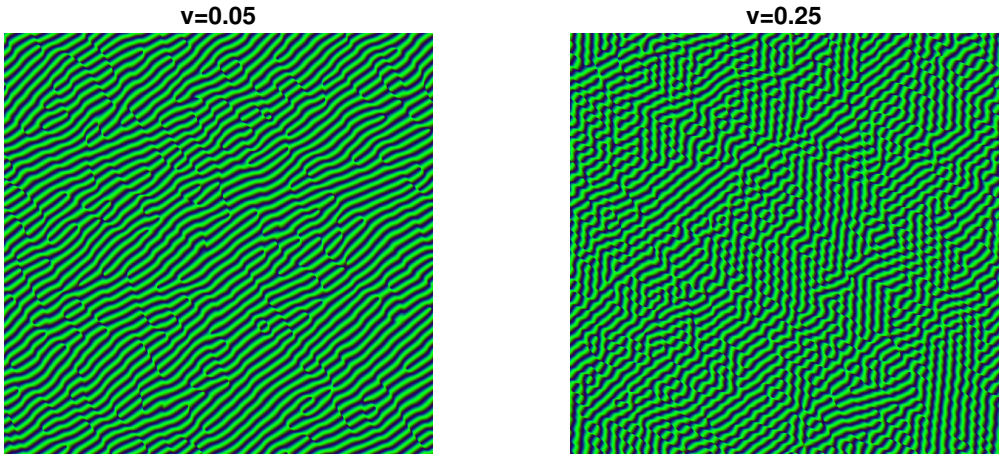

Figure 5.6: Color phasor noises generated from the independent sum of 5 Gabor noises with random orientations, $v = 0.05$ (left), $v = 0.25$ (right), $M = N = 1000$, $T_x = T_y = 0.002$, $b = 5$, $p = 0.1$, $\omega = 30$, $\alpha_\ell \sim \mathcal{N}\left(\frac{\pi}{6}, v\right)$ for each $\ell \in \{1, \dots, 5\}$, $n = 5$, $A^R = 0.1$, $A^G = 0.5$, $A^B = 0.25$, $\varphi^R = 0$, $\varphi^G = \frac{2\pi}{3}$, $\varphi^B = -\frac{2\pi}{3}$ and $\Phi_0 = \begin{pmatrix} 0.1 & 0.5 & 0.25 \end{pmatrix}^\top$.

The boxplots displayed in Figure 5.7 further confirm these expectations. The estimation of the green phase-shift is more consistent when the orientations of the 5 Gabor noises are close to each other, *i.e.*, when the image displays more regular oscillating patterns.

5.1.5 Application to real color textures

The color parameter estimation technique described in the previous sections is now applied to real color textures. After the parameters are extracted by using the Riesz transform, the ellipse can be drawn, yielding a visual representation of the color oscillation inside the RGB cube. The results are given in Table 5.2. As suggested by the synthetic tests, the most homogenous texture in terms of color content, *i.e.*, the grass texture, yields a flat ellipse ($\lambda = 1$). The fabric texture displays more color variations, which is reflected in the lower value of λ and the shape of the ellipse. In both cases, the color content of the texture is consistent with the color range of the ellipse. The results are less convincing in the case of the sand texture. Though the value of λ is consistent with the color content of the image, which oscillates between light brown and blue, the color range of the ellipse does not contain any shade of blue, suggesting that the estimation does not work well.

In order to further illustrate these results, color phasor noises are generated from the estimated color parameters for each image, while the other parameters are $b = 2$, $p = 0.1$, $\omega = 20$ $n = 1$. The orientation α is extracted by applying the stochastic structure tensor described in Section 3.4 to the greyscale version of each image. The results displayed

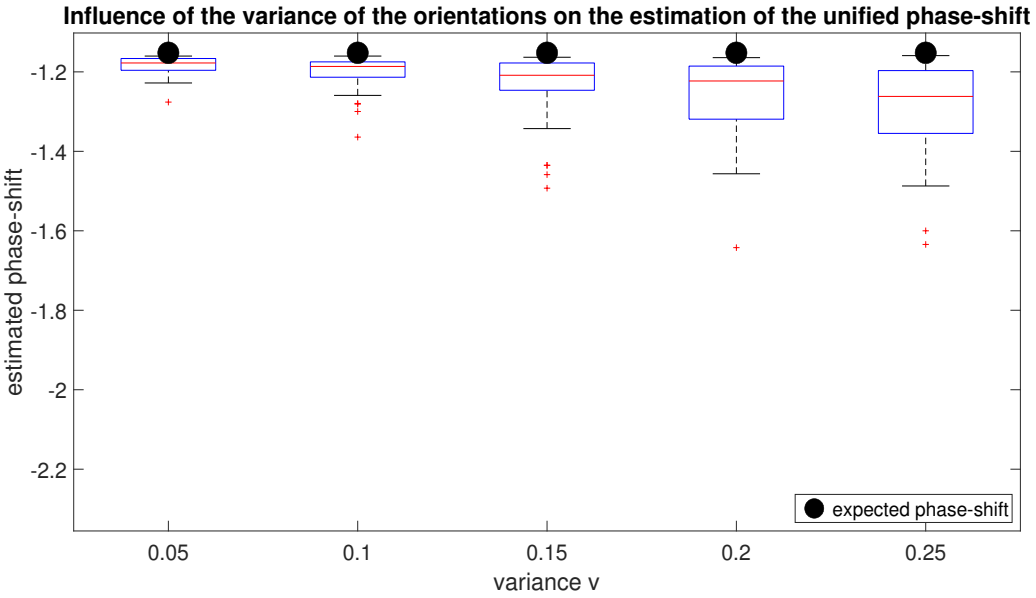

Figure 5.7: Boxplots of the unified phase-shift measured from $m = 50$ color phasor noises, $v \in \{0.05(1+k), k = 0, \dots, 4\}$, $M = N = 1000$, $T_x = T_y = 0.002$, $b = 5$, $p = 0.1$, $\omega = 30$, $\alpha_\ell \sim \mathcal{N}\left(\frac{\pi}{6}, v\right)$ for each $\ell \in \{1, \dots, 5\}$, $n = 5$, $A^R = 0.1$, $A^G = 0.5$, $A^B = 0.25$, $\varphi^R = 0$, $\varphi^G = \frac{2\pi}{3}$, $\varphi^B = -\frac{2\pi}{3}$ and $\Phi_0 = \begin{pmatrix} 0.1 & 0.5 & 0.25 \end{pmatrix}^\top$.

in Figure 5.8 confirm the previous observations. Indeed, the color information is well extracted from the grass and the fabric textures, respectively, while it struggles more with the sand texture. As for the orientation, the value obtained from the grass texture is difficult to interpret due to the lack of clear directional patterns. The sand texture is much more suitable for this technique, hence the more intuitive value of α. The stochastic structure tensor seems to struggle with the fabric texture, probably because of the presence of both horizontal and vertical directional patterns. Notice that the synthesis only focuses on reconstructing the color content and the directionality of the image, respectively. A proper reconstruction of the image would require more complex phasor noises involving terms of different frequencies and orientations, which should be possible by generalizing existing exemplar approaches such as (Galerne et al. 2012, Guehl et al. 2020). Another possibility would be to make the color parameters space-dependent in order to add more richness in the color content. This is further discussed in the conclusion.

5.2 Monogenic-based detection of singularities

5.2.1 Phasor noise and singularities

Section 5.1 highlights the ability of the monogenic signal to extract the color parameters of an oscillating stochastic texture. This section focuses on the use of the monogenic signal as a tool to evaluate the quality of the synthesized noise. As said in (Tricard et al. 2019), though the phasor noise eliminates the local losses of contrast of the Gabor noise, it displays singularities, *i.e.*, local irregularities that make it look artificial. They occur randomly in the texture, though Section 5.3 shows that the parameters of the noise directly impact their occurrence. Figure 5.9 shows an example of a greyscale phasor noise displaying singularities. Because these singularities are due to abrupt jumps in the phase function

Texture	grass	sand	fabric
s_0^R	0.28	0.57	0.54
s_0^G	0.54	0.51	0.56
s_0^B	0.09	0.46	0.29
A^R	0.09	0.22	0.16
A^G	0.09	0.11	0.15
A^B	0.09	0.15	0.14
φ^R	0	0	0
φ^G	0	0.15	0.24
φ^B	0.01	0.17	0.22
Image			
Ellipse			
λ	1	0.99	0.97

Table 5.2: Examples of real color textures and their estimated color parameters.

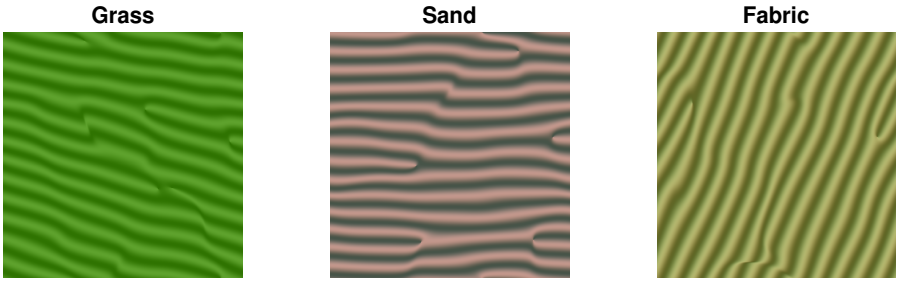

Figure 5.8: Color phasor noises generated from the color parameters of the grass (left), sand (center) and fabric (right) textures, respectively, with $b = 2$, $p = 0.1$, $\omega = 20$, $\alpha = \frac{\pi}{6}$, $n = 1$.

φ of the phasor noise (Tricard et al. 2019), it can be expected that these singularities have a measurable impact on the monogenic phase function ϕ. In the next sections, this assumption is investigated by applying the Riesz transform to the color phasor noise, from which a measure of local phase can be extracted.

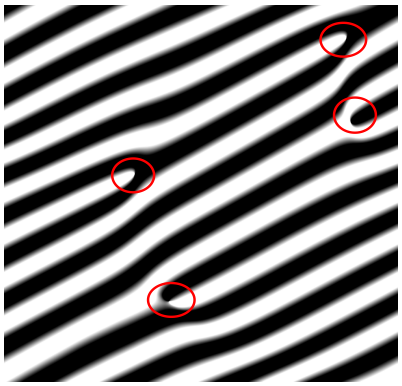

Figure 5.9: Example of a greyscale phasor noise displaying singularities (marked by red circles).

5.2.2 Fusion of the three color channels

In Section 5.1, the Riesz transform has to be applied to the three color channels marginally in order to get estimates of the color parameters. When tackling the singularity detection issue, it is possible to avoid marginal analysis by fusing the color channels before applying the Riesz transform. Thus, let Φ be a color phasor noise generated from a sum of color Gabor noises as defined in Eq. (4.44), *i.e.*, for all $\mathbf{x} \in \Omega \subset \mathbb{R}^2$,

$$s(\mathbf{x}) = I(\mathbf{x}) \begin{pmatrix} A^R \cos\left[\varphi(\mathbf{x}) + \varphi^R\right] \\ A^G \cos\left[\varphi(\mathbf{x}) + \varphi^G\right] \\ A^B \cos\left[\varphi(\mathbf{x}) + \varphi^B\right] \end{pmatrix}. \tag{5.11}$$

Before applying the Riesz transform to Φ, these components are fused to get a single noise involving the color parameters. Similarly to what is done in Section 4.2, the noise Φ can be seen as the real part of a $\mathbb{C}^3$-valued signal $\widetilde{\Phi}$ defined for all $\mathbf{x} \in \Omega \subset \mathbb{R}^2$ by

$$\widetilde{\Phi}(\mathbf{x}) = \begin{pmatrix} A^R e^{\mathbf{i}\left[\varphi(\mathbf{x}) + \varphi^R\right]} \\ A^G e^{\mathbf{i}\left[\varphi(\mathbf{x}) + \varphi^G\right]} \\ A^B e^{\mathbf{i}\left[\varphi(\mathbf{x}) + \varphi^B\right]} \end{pmatrix}. \tag{5.12}$$

Then, $\widetilde{\Phi}$ can be expressed for all $\mathbf{x} \in \Omega$ as

$$\widetilde{\Phi}(\mathbf{x}) = e^{\mathbf{i}[\varphi(\mathbf{x})]}\Gamma, \tag{5.13}$$

where Γ denotes the color Fourier atom defined in Eq. (4.8). The three color channels are now fused to get a unified complex noise $\widetilde{\Phi}^u$ defined for all $\mathbf{x} \in \Omega$ as

$$\widetilde{\Phi}^u(\mathbf{x}) = \left[\widetilde{\Phi}(\mathbf{x})^\top \widetilde{\Phi}(\mathbf{x})\right]^{\frac{1}{2}} = |\Gamma^\top \Gamma|^{\frac{1}{2}} e^{\mathbf{i}[\varphi(\mathbf{x}) + \widehat{\varphi}]}, \tag{5.14}$$

where $\widehat{\varphi}$ denotes the unified color phase shift defined in Eq. (4.13). The unified noise Φ^u is finally obtained by taking the real part of $\widetilde{\Phi}^u$, hence for all $\mathbf{x} \in \Omega$,

$$\Phi^u(\mathbf{x}) = |\Gamma^\top \Gamma|^{\frac{1}{2}} \cos\left[\varphi(\mathbf{x}) + \widehat{\varphi}\right]. \tag{5.15}$$

In the further developments, the Riesz transform is applied to this unified noise Φ^u rather than the three color channels separately. This is done in order to avoid marginal analysis.

5.2.3 Phase comparison and cosine difference

In the special case of $n = 1$, *i.e.*, if only one Gabor noise is used to generate the phasor noise, then Theorem 6 implies that the monogenic phase ϕ estimated from $\Phi^u(\mathbf{x})$ through the Riesz transform is expected to be close to the function inside the cosine in Eq. (5.15). If $n \geq 2$, then no theoretical guarantee has been established so far. However, the literature suggests that, if the original amplitude and phase functions are slowly varying, their respective monogenic estimations are reliable (Larkin et al. 2001, Seelamantula et al. 2012, Kaseb et al. 2019). Therefore, if Φ^u denotes the unified noise obtained from a sum of Gabor noises as defined in Eq. (5.15), it can be expected that the phase function inside the cosine, *i.e.*, $\varphi + \widehat{\varphi}$, and the monogenic phase ϕ extracted through the Riesz transform, are close to each other as long as the texture is regular enough. The pixels at which these two phase functions diverge would then correspond to the occurrence of singularities. In order to quantify the similarity between these two phase functions, a first approach consists in comparing them through the cosine of their difference at each pixel $\mathbf{x} \in \Omega$, *i.e.*,

$$\cos\left[\varphi(\mathbf{x}) + \widehat{\varphi} - \phi(\mathbf{x})\right] \tag{5.16}$$

The closer to 1 this cosine difference is, the more regular the texture is at the pixel $\mathbf{x}$. Conversely, pixels at which the cosine difference is close to -1 are expected to display visual singularities. Calculating the mean of these cosine differences in the whole image then yields a quality criterion for the synthesized texture. This mean cosine difference between $\varphi + \widehat{\varphi}$ and ϕ is now denoted by $\mathrm{MCD}(\Phi)$ and can be expressed as

$$\mathrm{MCD}(\Phi) = \frac{1}{|\Omega|} \int_{\mathbf{x} \in \Omega} \cos\left[\varphi(\mathbf{x}) + \widehat{\varphi} - \phi(\mathbf{x})\right] d\mathbf{x}. \tag{5.17}$$

These tools are now applied to synthesized phasor noise in order to illustrate their relevance in detecting the singularities and evaluate the global regularity of the texture.

5.3 Application of the monogenic-based detection of singularities to synthesized color phasor noises

5.3.1 Discrete mean cosine difference

Let s be a sum of discrete color Gabor noises as defined in Section 4.2.4, and let Φ denote the associated color phasor noise. The discrete unified noise associated with Φ is denoted by Φ^u and is defined for all $(j,k) \in \{0 \dots M-1\} \times \{0 \dots N-1\}$ as

$$\Phi^u_{j,k} = |\Gamma^\top \Gamma|^{\frac{1}{2}} \cos\left(\varphi_{j,k} + \widehat{\varphi}\right), \tag{5.18}$$

where Γ and $\widehat{\varphi}$ denote the color Fourier atom and unified phase shift defined in Eq. (4.8) and Eq. (4.13), respectively. Assuming that the discrete monogenic signal of Φ^u, denoted by M^u_Φ, can be approximated for all $(j,k) \in \{0 \dots M-1\} \times \{0 \dots N-1\}$ as

$$\left(M^u_\Phi\right)_{j,k} \approx |\Gamma^\top \Gamma|^{\frac{1}{2}} e^{\mathbf{i}\left(\varphi_{j,k} + \widehat{\varphi}\right)}, \tag{5.19}$$

then it can be expected that the monogenic phase ϕ of the signal Φ^u is close to the phase function inside the complex exponential, *i.e.*, for all $(j,k) \in \{0 \dots M-1\} \times \{0 \dots N-1\}$,

$$\phi_{j,k} \approx \varphi_{j,k} + \widehat{\varphi} \quad [2\pi]. \tag{5.20}$$

The two phase functions are then compared by using the discrete mean cosine difference, *i.e.*,

$$\mathrm{MCD}(\Phi) = \frac{1}{MN} \sum_{j=0}^{M-1} \sum_{k=0}^{N-1} \cos\left[\varphi_{j,k} + \widehat{\varphi} - \phi_{j,k}\right]. \tag{5.21}$$

Areas where the two phase functions do not coincide should then correspond to singularities. In the next sections, this process is applied to detect the singularities in synthesized phasor noises and illustrate the impact of the parameters on their occurrence.

5.3.2 Impact of the scale and the frequency on the occurrence of singularities

As shown in Section 4.2.4, the discrete phase function φ of a single Gabor noise is given for all $(j,k) \in \{0 \dots M-1\} \times \{0 \dots N-1\}$ by

$$\varphi_{j,k} = b\omega \left(t_j \cos\alpha + t_k \sin\alpha\right) + \Psi_{j,k} \quad [2\pi]. \tag{5.22}$$

In order to illustrate how comparing the original and monogenic phase functions highlights the singularities occurring when b changes, five color phasor noises are synthesized with $b \in \{1, \dots, 5\}$, the other parameters being $M = N = 500$, $T_x = T_y = 0.002$, $p = 0.1$, $\omega = 30$, $\alpha = \frac{\pi}{6}$, $n = 1$, $A^R = 0.3$, $A^G = 0.2$, $A^B = 0.1$, $\varphi^R = 0$, $\varphi^G = \frac{\pi}{3}$, $\varphi^B = \frac{\pi}{2}$ and $\Phi_0 = \begin{pmatrix} 0.7 & 0.6 & 0.3 \end{pmatrix}^\top$. For each value of b, the synthesized phasor noise, the MCD criterion and the cosine difference at each pixel are all given in Table 5.3. The white areas correspond to cosine difference values close to 1, *i.e.*, areas where the expected and monogenic phase functions are close, while the black areas correspond to cosine difference values close to -1, *i.e.*, areas where the expected and monogenic phase functions differ from π. As b increases, more singularities occur, which is reflected in an increase of the number of black areas at the corresponding pixels. However, the local rate of singularities do not vary, which is reflected in the high values of MCD and the stability of the overall aspect of the image apart from the scale.

Of course, the MCD value varies randomly depending on the underlying Poisson and phase shift processes. Generating $m = 50$ images for each bandwidth value gives an idea of how the distribution of the MCD values changes when b increases. As can be seen in Figure 5.10, the MCD values may vary greatly for small values of b, but stabilize around 0.98 for higher values of b. This can be explained by the fact that singularities occurring in a zoomed-in image (small value of b) have a higher impact on the overall regularity than singularities occurring in a zoomed-out image (high value of b).

The impact of the frequency parameter ω is now studied. Table 5.4 shows the results obtained from five color phasor noises synthesized with $\omega \in \{10 + 5m, m \in \{0, \dots, 4\}\}$, the other parameters being $M = N = 500$, $T_x = T_y = 0.002$, $p = 0.1$, $b = 2$, $\alpha = \frac{\pi}{6}$, $n = 1$, $A^R = 0.3$, $A^G = 0.2$, $A^B = 0.4$, $\varphi^R = 0$, $\varphi^G = \frac{\pi}{3}$, $\varphi^B = \frac{\pi}{2}$ and $\Phi_0 = \begin{pmatrix} 0.7 & 0.2 & 0.6 \end{pmatrix}^\top$. It can be observed that singularities are more likely to occur in low frequency images than in high frequency ones, which is reflected in the reduction of the number of black areas as

b	1	2	3	4	5
phasor				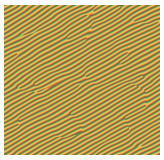	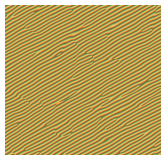
MCD	0.99	0.97	0.98	0.98	0.98
cosine diff.	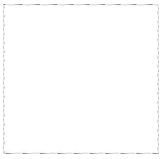				

Table 5.3: Link between the occurrence of singularities and the cosine difference for increasing values of the scale parameter b, with $M = N = 500$, $T_x = T_y = 0.002$, $p = 0.1$, $\omega = 30$, $\alpha = \frac{\pi}{6}$, $n = 1$, $A^R = 0.3$, $A^G = 0.2$, $A^B = 0.1$, $\varphi^R = 0$, $\varphi^G = \frac{\pi}{3}$, $\varphi^B = \frac{\pi}{2}$ and $\Phi_0 = \begin{pmatrix} 0.7 & 0.6 & 0.3 \end{pmatrix}^\top$.

well as the increase of the MCD parameter. Notice how the reformulation of the Gabor kernel enables a clear separation of scale and frequency aspects.

ω	10	15	20	25	30
phasor	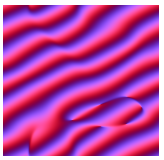	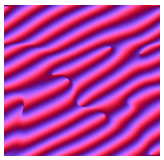	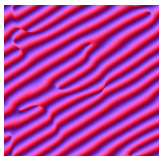		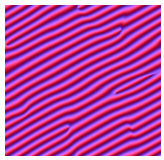
MCD	0.87	0.92	0.95	0.96	0.98
cosine diff.			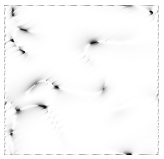		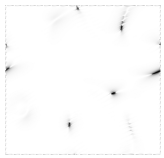

Table 5.4: Link between the occurrence of singularities and the cosine difference for increasing values of the frequency ω, with $M = N = 500$, $T_x = T_y = 0.002$, $p = 0.1$, $b = 2$, $\alpha = \frac{\pi}{6}$, $n = 1$, $A^R = 0.3$, $A^G = 0.2$, $A^B = 0.4$, $\varphi^R = 0$, $\varphi^G = \frac{\pi}{3}$, $\varphi^B = \frac{\pi}{2}$ and $\Phi_0 = \begin{pmatrix} 0.7 & 0.2 & 0.6 \end{pmatrix}^\top$.

Generating $m = 50$ noises for each value of ω confirms these observations. As the frequency ω increases, fewer singularities occur, hence the steady increase of the MCD, as well as a slight decrease of its variability. Notice that, in all these tests, the MCD criterion decreases rapidly when the number of singularities rises. Even for MCD values between 0.9 and 0.95, the image already looks damaged, which makes this criterion difficult to interpret. Future works should focus on bypassing this difficulty by introducing a more relevant criterion.

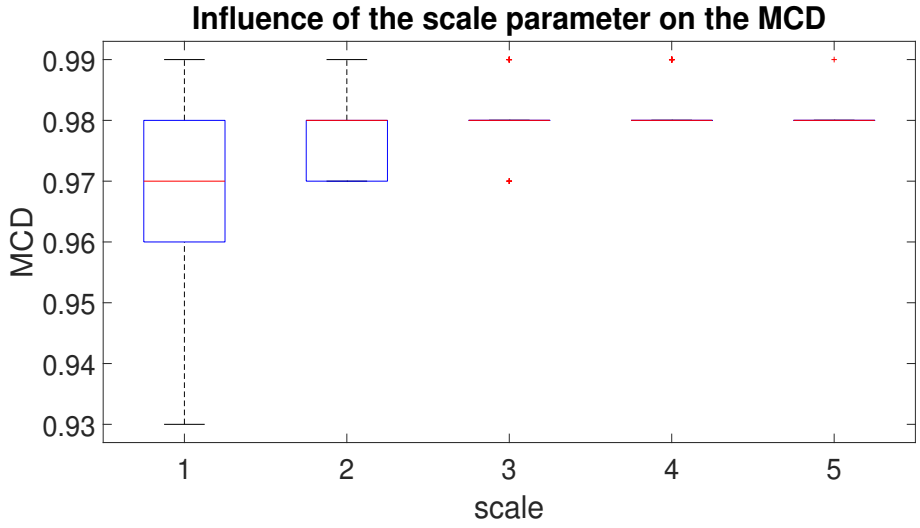

Figure 5.10: Boxplots of the MCD values for different scale parameters.

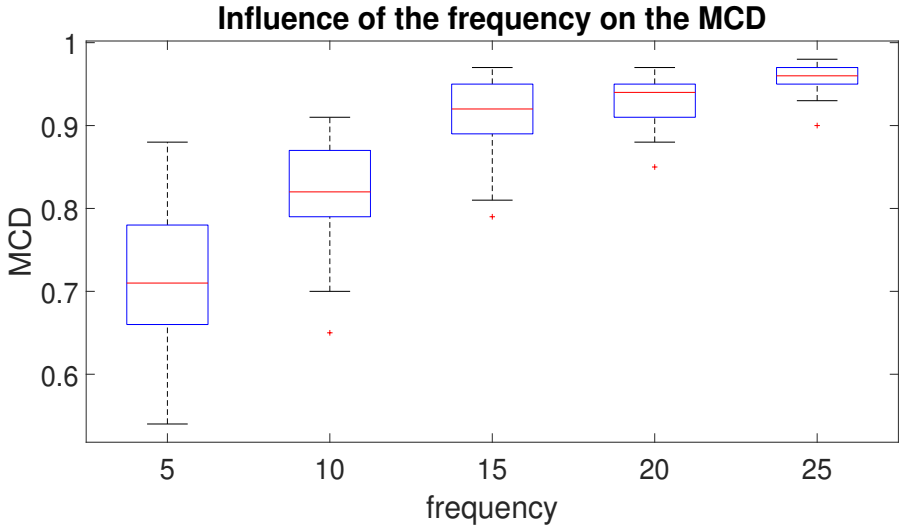

Figure 5.11: Boxplots of the MCD values for different frequencies.

5.3.3 Case of a bidirectional phasor noise

Small values of θ imply fewer singularities occurring in the bidirectional Gabor noise and a better estimation of the phase function by the monogenic tool, while the regularity of the noise and the monogenic estimation of the phase both lose quality as θ increases. In order to illustrate this, five color bidirectional phasor noises are synthesized with $\theta \in \left\{m\frac{\pi}{12}, m \in \{0,\dots,4\}\right\}$, the other parameters being $M = N = 500$, $T_x = T_y = 0.002$, $b = 2$, $p = 0.1$, $\omega = 30$, $\alpha = \frac{\pi}{6}$, $n = 2$, $A^R = 0.3$, $A^G = 0.2$, $A^B = 0.1$, $\varphi^R = 0$, $\varphi^G = \frac{\pi}{3}$, $\varphi^B = \frac{\pi}{2}$ and $\Phi_0 = \begin{pmatrix}0.3 & 0.5 & 0.7\end{pmatrix}^\top$. For each value of θ, the synthesized phasor noise, the MCD criterion and the cosine difference at each pixel are all given in Table 5.5. As θ increases, the two underlying waves become more and more divergent, which rapidly increases the number of singularities and makes the MCD drop. Notice that the cosine differences only decrease in areas where singularities occur, which further confirm the direct link between the occurrence of singularities and the monogenic estimation of the phase

function.

θ	0	$\frac{\pi}{12}$	$\frac{\pi}{6}$	$\frac{\pi}{4}$	$\frac{\pi}{3}$
phasor	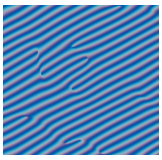	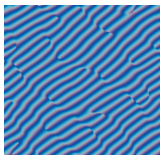	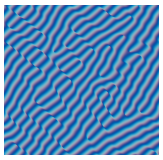	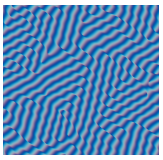	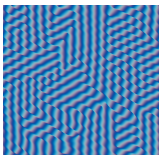
MCD	0.98	0.96	0.93	0.84	0.73
cosine diff.			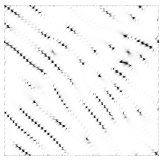	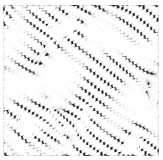	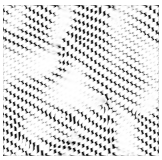

Table 5.5: Link between the occurrence of singularities and the cosine difference for increasing values of the angular difference θ, with $M = N = 500$, $T_x = T_y = 0.002$, $b = 2$, $p = 0.1$, $\omega = 30$, $\alpha = \frac{\pi}{6}$, $n = 2$, $A^R = 0.3$, $A^G = 0.2$, $A^B = 0.1$, $\varphi^R = 0$, $\varphi^G = \frac{\pi}{3}$, $\varphi^B = \frac{\pi}{2}$ and $\Phi_0 = \begin{pmatrix} 0.3 & 0.5 & 0.7 \end{pmatrix}^\top$.

Like the scale parameter b, the angular difference θ not only impacts the MCD values, but also their distribution, as can be seen in Figure 5.12 which displays the boxplots of $m = 50$ bidirectional phasor noises for each value of θ. As θ increases, the MCD values drop, while their variability strongly increases. This variability implies that even for higher values of θ, the synthesized phasor noise may display few singularities. This is what happens in Figure 5.13. Despite being synthesized with $\theta = \frac{\pi}{3}$, this phasor noise has a regular structure, which is reflected in the high value of MCD (MCD = 0.98). Therefore, by providing an efficient measure of local and global regularity, the monogenic signal can be used to choose the noise that displays enough local variability to look realistic, with a reduced number of singularities.

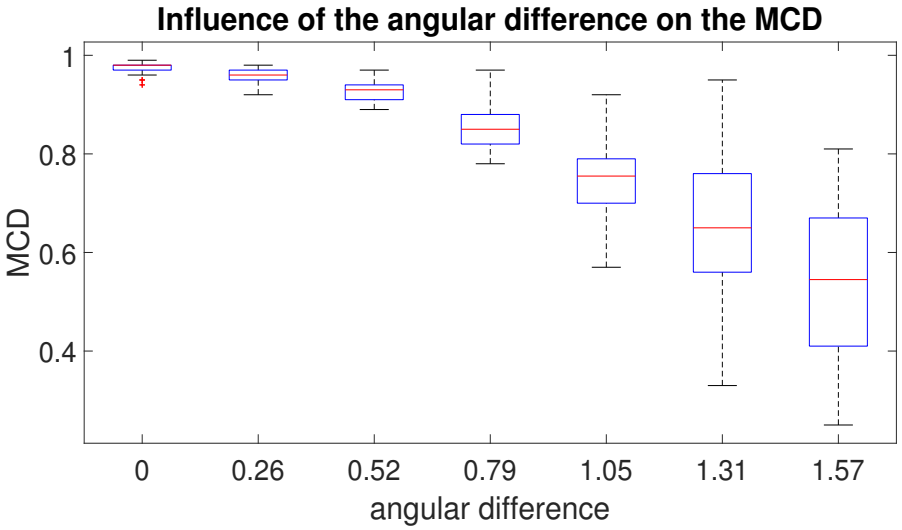

Figure 5.12: Boxplots of the MCD values for different angular difference.

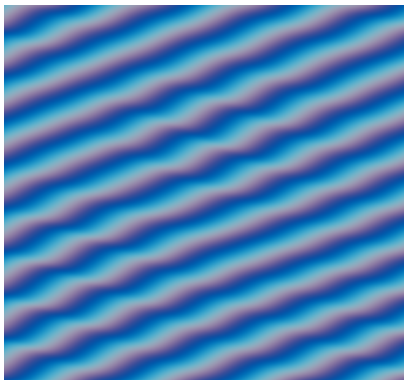

Figure 5.13: A bidirectional phasor noise displaying few singularities with $\theta = \frac{\pi}{3}$.

5.4 Conclusion

While Chapter 4 highlights the direct link between the color parameters of the elliptic model and the color content of the generated texture, this chapter goes further by introducing a monogenic-based technique to extract these parameters from a color image. Though further studies would be necessary to improve this technique, the tests performed on real color texture show that these elliptic color parameters can accurately describe color oscillations. Similarly to the greyscale case tackled in Chapter 3, theoretical conditions on the frequency content of the image are given to ensure the reliability of the monogenic estimation.

Furthermore, this chapter makes substantial progress regarding the issue of local singularities raised in (Tricard et al. 2019) thanks to the Riesz-based monogenic signal introduced in (Larkin et al. 2001). While the occurrence of these singularities still cannot be avoided, the monogenic signal provides an efficient tool to measure the local regularity of the synthesized noise, detect the singularities and hence quantify the global regularity of the image. This technique is essentially based on the reliable estimation of local phase enabled by the Riesz transform, whose relevance is supported both theoretically and numerically. This further illustrates the importance of the phase function in analyzing the local structure of the texture, which was already highlighted in (Kaseb et al. 2019).

The elliptic color model and monogenic-based detection of irregularities could now be applied to more general procedural noises. In (Tricard et al. 2019), sums of Gabor noises with randomly generated frequencies and orientations are considered, which enables a greater array of textures though still displaying singularities. Outside the field of pure procedural texture synthesis, this technique could also be applied to semi-procedural noises, *i.e.*, data-driven texture synthesis techniques as found in, *e.g.*, (Galerne et al. 2012, Guehl et al. 2020). The ability of the monogenic signal to extract local features such as phase and orientation would then be used not only after the synthesis as an evaluation tool, but also in the analysis of the exemplar texture.

While this chapter focuses on marked Poisson processes, determinantal point processes have become particularly used in machine learning (Kulesza & Taskar 2012) and image processing (Launay, Desolneux & Galerne 2021) in the last decade due to the richer interactions between the generated points they offer. It could hence be interesting to generalize

the results presented here to noises synthesized through more complex processes, and discuss the impact of the underlying point process on the generated texture.

Finally, this chapter only considers the case of constant color parameters A^C and φ^C, $C \in \{R, G, B\}$. However, when dealing with real color textures, such parameters are more likely to evolve along the pixels rather than remaining constant, hence the introduction of dynamic color parameters in both the 1D and the 2D cases (Lilly 2011, Soulard & Carré 2015). Applying the monogenic extraction of the color parameters described in Section 5.1.2 to a real color texture clearly shows that these parameters are space-dependent and cannot be considered constant global descriptors anymore, as can be seen in Figure 5.14. The histograms are only shown for the green channel but the other channels give similar results. This probably explains why the color parameter extraction fails in the case of the sand texture, as seen in Section 5.1.5.

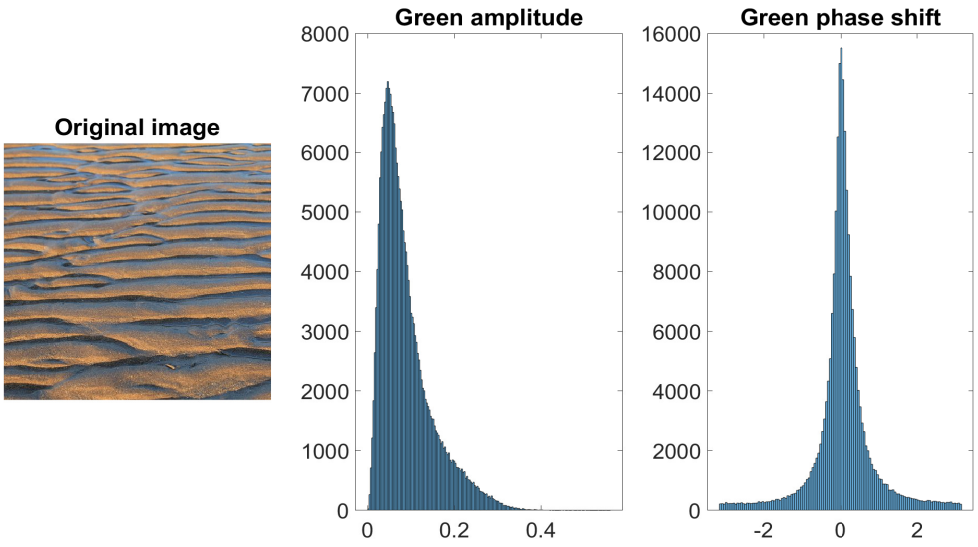

Figure 5.14: Original image (left), green amplitude (middle) and green phase-shift (right).

Conclusion and perspectives

Conclusion

The main objective of this thesis was the introduction and extension of numerical descriptors for color images, which can then be directly linked to their visual features. This was done by merging image processing techniques from the fields of signal processing, probabilities and system identification. The developments performed in the previous chapters have studied the reliability of the parameters extracted through these techniques, as well as their interpretation in terms of local feature characterization. Because the color content of a texture is an inherently vectorial information (Soulard & Carré 2015), a particular attention has also been paid on the non-marginal treatment of the color channels.

Widely used in 2D system identification, the Roesser model is deeply studied from a color image modeling point of view in Chapter 1, with a special focus on the subspace-based estimation algorithm of the Roesser parameters introduced in (Ramos & Mercère 2018). Besides its robustness, this algorithm is noteworthy for its purely vectorial treatment of the color channels of the handled image, which provides a great advantage over marginal techniques. Indeed, many works such as (Xu et al. 2015, Hosono et al. 2019) highlight the crucial information contained in the correlations between the color channels, hence the need to include them in the estimation process. Chapter 1 provides a brand-new interpretation of the subspace-based estimation in terms of color covariance matrices, which places it more clearly within the color texture framework.

This thesis also distances itself from the 2D ARMA models handled in, *e.g.*, (Kokaram 2004, Köppel et al. 2015) in the way the innovation sequence is treated. As stated in (Kailath et al. 2000), describing the innovation sequence as a white noise characterized by its second-order statistics is not enough to fully describe its structural information. Besides the colorimetric study of the subspace-based estimation algorithm, Chapter 1 shows how some of the structural information of the image subsists in the innovation after the model has been identified. A direct consequence of this fact is that replacing the innovation with a white noise sharing the same second-order statistics implies losing an important part of the original structure in the reconstructed image. Such results suggest that properly characterizing the innovation is as crucial as reliably estimating the parameters of the model.

The limits of the Roesser model in terms of local structure characterization is what has motivated the use of other tools taken from the field of signal processing in Chapter 2. Indeed, one of the biggest contributions of the monogenic signal (introduced in (Larkin et al. 2001, Felsberg & Sommer 2001)) is the proper definition of a local phase function to characterize the structural information of 2D images. Although this information was already extracted by the Fourier phase (Oppenheim & Lim 1981), the fact that the monogenic phase is defined in the spatial domain rather than the frequency domain makes it

easier to connect with the local features of the image. While, in theory, the monogenic measures of phase and orientation are optimal for pure cosine waves only, Chapter 2 goes further by studying the reliability of the monogenic phase and orientation extraction in the case of more complex 2D deterministic waves. The theoretical and numerical results provided in this chapter show how both functions are still well estimated when the oscillations contain more curves, under the condition that the oscillating patterns are explicit enough. These results are then illustrated by extracting the phase function from real interferometric fringes, which extends the previous works dealing with the use of the Riesz transform in field of interferometry such as (Larkin et al. 2001, Seelamantula et al. 2012, Kaseb et al. 2019).

While Chapter 2 focuses on deterministic images only, Chapter 3 generalizes the reliability of the monogenic phase extraction to random fields displaying oscillating patterns, in order to further enlarge its application scope. This extends the application of the monogenic framework to stochastic images performed in (Olhede et al. 2014), though it focuses on the characterization of directionality only. Because the phase function contains crucial structural information that is not encoded in any other signal extracted by the monogenic signal (Felsberg & Sommer 2001), this motivates the study of the monogenic phase extraction in the case of random fields. Thus, Chapter 3 shows how the monogenic signal still provides a reliable measure of both phase and orientation in this case, with numerical results to illustrate the theoretical study. Chapter 3 also further studies the use of the Riesz transform to measure directionality. Introduced in (Olhede et al. 2014), the Riesz-based stochastic structure tensor provides a reliable technique to extract the preferred orientation from random fields, but its original quaternionic formulation was masking some of its geometrical aspects. In Chapter 3, the quaternionic formalism of (Olhede et al. 2014) is reformulated in $\mathbb{R}^3$, which yields a more visual interpretation of the measure of directionality. The link with more classical structure tensors is also made more explicit.

After highlighting the ability of the monogenic tool to extract the local features of greyscale images in Chapters 2 and 3, Chapter 4 tackles color image characterization. The main contribution of this chapter is the merging of the elliptic color model and the phasor noise frameworks, respectively. While the 2D elliptic model (introduced in (Soulard & Carré 2015)) provides a useful color generalization of the notions of amplitude and phase, its theoretical developments only deal with deterministic color waves. Meanwhile, the phasor noise (introduced in (Tricard et al. 2019)) enables the synthesis of a wide variety of textures with prescribed frequency content, but no color model is included. Chapter 4 generalizes both models by defining a proper color phasor noise based on the elliptic model, which allows the synthesis of stochastic color textures with both prescribed frequency and color content, respectively. The ability of the model to encode the whole color information of the texture in a small set of parameters is of particularly great interest for fields such as parametric texture characterization and texture synthesis.

The use of the elliptic parameters as descriptors for oscillating color textures is then investigated in Chapter 5. These parameters are estimated thanks to the monogenic signal, and are then used to characterize the color content of the image. This technique hence provides a fully spatial description of the color oscillations inside the RGB cube with a compact set of parameters. Chapter 5 also tackles the occurrence of singularities in the phasor noise, which was left for further studies in (Tricard et al. 2019). Because the structural information of the noise is contained in its phase function, the key idea is to characterize the

singularities as jumps of π between the physical phase function and the estimated phase measured by the monogenic signal. Synthetic tests show how this technique manages to detect the singularities in the synthesized image, which yields a characterization of the quality of its overall appearance. The effect of the parameters on the number of singularities in the image is also deeply studied, which opens the door for a better understanding of their occurrence.

Perspectives

As stated in (Felsberg & Sommer 2001), the split of information between amplitude and phase provided by the Riesz transform is orthogonal, which implies that the energy and structure of the image are strictly separated. This ensures that the whole structural information is encoded in the phase function, without interference from the energy. This local measure is of particular interest in fields such as interferometry, where the phase value at each pixel can be linked to physical quantities (Robin et al. 2005, Kaseb et al. 2019). However, being a 2D signal of the same size as the original image, the monogenic phase is still difficult to interpret. While this thesis deeply investigates the quality of the phase extraction, no further analysis of the estimated phase is performed. An interesting perspective would hence be the definition of parameters to characterize the phase function, similarly to the various indexes designed for the Fourier phase in (Kovesi 2000, Leclaire & Moisan 2015). In these works, the local behavior of the Fourier phase is characterized by a small set of indexes, and is then directly linked to the blurry aspect of the image, as well as the detection of edges. Defining similar tools for the local phase measured by the monogenic signal would constitute an important step in the parametric characterization of images.

Like the phase function in the case of oscillating textures, the innovation sequence of the Roesser model is reliably extracted, and its structural information is heavily emphasized in this thesis, but there still lacks a proper modeling of its content. The texture completion detailed in Chapter 1 provides interesting results, but the innovation in the masked area still has to be copied from available data, which is an important limitation. Future works should hence focus on defining efficient techniques to reconstruct the unknown parts of the innovation sequence without relying on copy-pastes from the available innovation terms. The use of the monogenic signal to characterize the structural and directional behavior of this sequence could be a particularly interesting perspective.

The monogenic-based color texture analysis described in Chapter 5 also has to be further developed. When applied to phasor noises, the color parameters and the ellipse are well estimated by the monogenic signal, and provide a precise description of the richness of the color content. However, the link between the ellipse and the color content is not as explicit when real color textures are considered. Because such textures contain more complex patterns, a possible solution is to make the color parameters space-dependent, as suggested in (Soulard & Carré 2015). Assuming that the richness of the color content is not constant in the whole image, this would yield an ellipse and a linearity value at each pixel, making it more suitable for complex color patterns.

In the field of texture synthesis, the monogenic-based detection of singularities in the phasor noise could also be further improved. Though the monogenic signal manages to characterize the occurrence of singularities thanks to its measure of local phase, the overall

regularity of the synthesized image is still difficult to quantify. The MCD used in Chapter 5 gives a very partial idea of how the image actually looks, which suggests the introduction of more relevant criteria. In (Tricard et al. 2020), the singularities of the phasor noise are classified by using a local measure involving the gradient of the phase function. Given the strong links between the gradient and the Riesz transform (Felsberg & Sommer 2001), it would hence be interesting to formally compare both approaches.

While the color generalization of the phase is widely discussed in Chapters 4 and 5, respectively, no notion of color orientation is introduced in this work. Because the monogenic signal provides a clear separation between energetical, structural and directional information (Felsberg & Sommer 2001), this implies that parts of the information contained in the image are still left unmodeled. A color extension of the Riesz-based structure tensor can be found in (Soulard & Carré 2015), in which the three tensors of each color channels are summed to form a single tensor, from which a unified notion of orientation is extracted. However, numerical tests suggest that it is equivalent to converting the color image into a grey image and extracting the orientation from the corresponding scalar structure tensor. A possible solution is to rely on Clifford algebras, as is done in (Demarcq et al. 2011). This article goes back to the formal definition of the monogenic signal in (Felsberg & Sommer 2001), which leads to the introduction of an $\mathbb{R}^5$-valued monogenic signal designed for color images. A formal generalization of the angular signals such as the local phase can then be performed by using this 5-dimensional vector. As already said in (Soulard & Carré 2015) and recalled in Chapter 4, the main drawback of this approach is that the local measures that it yields lack a clear physical interpretation. Future works could hence focus on either introducing a proper notion of color orientation, or studying how the 5-dimensional monogenic signal can be used to describe the local features of a color image.

Finally, though this thesis introduces numerical descriptors for color textures, it does not tackle the use of these quantities for image classification. In the field of greyscale medical imaging, (Alessandrini et al. 2013) have already used the monogenic signal and the phase extraction that it provdes to analyze heart motion, with convincing results. However, as stated in (Badano, Revie & Casertano 2015), the treatment of color information in medical images is still an open question, and many widely used techniques lack proper standardization. Subsequent works could hence focus on the application of the monogenic-based extraction of structural and color features to medical image analysis. Because color plays a significant role in fields such as digital microscopy, telemedicine and medical photography (Badano et al. 2015), this would be a particularly interesting perspective.

Bibliography

Abramowitz, M. & Segun, I. (1964), *Handbook of mathematical functions with formulas, graphs, and mathematical tables*, Dover, New York.

Alessandrini, M., Basarab, A., Liebgott, H. & Bernard, O. (2013), 'Myocardial motion estimation from medical images using the monogenic signal', *IEEE Transactions on Image Processing* **22**, 1084–1095.

Arevallilo-Herráez, M., Burton, D. R., Lalor, M. J. & Gdeisat, M. A. (2002), 'Fast two-dimensional phase-unwrapping algorithm based on sorting by reliability following a noncontinuous path', *Applied Optics* **41**, 7437–7444.

Badano, A., Revie, C. & Casertano, A. (2015), 'Consistency and standardization of color in medical imaging: a consensus report', *Journal of Digital Imaging* **28**, 41–52.

Ballard, D. H. & Brown, C. M. (1982), *Computer vision*, Prentice Hall Professional Technical Reference, Upper Saddle River, NJ, US.

Berger, M., Pansu, P., Berry, J. P. & Saint-Raymond, X. (1984), *Problems in geometry*, Springer-Verlag, New York City, NY, USA.

Biermé, H. & Desolneux, A. (2020), 'Mean geometry for 2d random fields: level perimeter and level total curvature integrals', *Annals of applied probability* **30**, 561–607.

Bracewell, R. N. (1965), *The Fourier transform and its applications*, McGraw Hill, New York City, NY, US.

Bruning, J. M., Herriott, D. R., Gallagher, J. E., Rosenfeld, D. P., White, A. D. & Bragaccio, D. J. (1974), 'Digital wavefront measuring interferometer for testing optical surfaces and lenses', *Applied Optics* **13**, 2693–2703.

Brémand, F. (1994), 'A phase unwrapping technique for object relief determination', *Optics and Lasers Engineering* **21**, 49–60.

Burger, W. & Burge, M. J. (2008), *Digital image processing: an algorithmic introduction using Java*, Springer, London.

Chierchia, G., Pustelnik, N., Pesquet-Popescu, B. & Pesquet, J. C. (2014), 'A nonlocal structure tensor-based approach for multicomponent image recovery problems', *IEEE Transactions on Image Processing* **23**, 5531–5544.

Chiu, S. N., Stoyan, D., Kendall, W. S. & Mecke, J. (2013), *Stochastic geometry and its applications*, John Wiley And Sons Inc., New York City, NY, USA.

Demarcq, G., Mascarilla, L., Berthier, M. & Courtellemont, P. (2011), 'The color monogenic signal: application to color edge detection and color optical flow', *Journal of Mathematical Imaging and Vision* **40**, 269–284.

Diallo, M., Kulesh, M., Holschneider, M., Scherbaum, F. & Adler, F. (2006), 'Characterization of polarization attributes of seismic waves using continuous wavelet transforms', *Geophysics* **71**, V67–V77.

Edwards, S. F. & Parrent, G. B. (1959), 'The form of the general unimodular analytic signal', *Optica Acta* **6**, 367–371.

Evans, L. C. & Gariepy, R. F. (2015), *Measure theory and fine properties of functions, revised edition*, CRC Press, Boca Raton, FL, USA.

Feller, W. (1968), *An introduction to probability theory and its applications*, Vol. 1, John Wiley And Sons Inc., New York City, NY, USA.

Felsberg, M. (2002), Low-level image processing with the structure multivector, PhD thesis, University of Kiel.

Felsberg, M. & Sommer, G. (2001), 'The monogenic signal', *IEEE Transactions on Signal Processing* **49**, 3136–3144.

Field, D. J., Hayes, A. & Hess, R. F. (2000), 'The roles of polarity and symmetry in the perceptual grouping of contour fragments', *Spatial Vision* **13**, 51–66.

Fubini, F. (1907), 'Sugli integrali multipli', *Accademia dei Lincei, Rendiconti, V. Serie* **16**, 608–614.

Gai, S. (2018), 'Multichannel image denoising using color monogenic curvelet transform', *Soft Computing* **22**, 635–644.

Gai, S. (2019), 'Color image denoising via monogenic matrix-based sparse representation', *The Visual Computer* **35**, 109–122.

Galerne, B. (2010), Stochastic image models and texture synthesis, PhD thesis, ENS Cachan.

Galerne, B., Lagae, A., Lefebvre, S. & Drettakis, G. (2012), 'Gabor noise by example', *ACM Transactions on Graphics* **31**, Art. 73.

Gilet, G., Sauvage, B., Vanhoey, K., Dischler, J. & Ghazanfarpour, D. (2014), 'Local random-phase noise for procedural texturing', *ACM Transactions on Graphics* **33**, Art. 195.

Guehl, P., Allègre, R., Dischler, J., Benes, B. & Galin, E. (2020), 'Semi-procedural textures using point process texture basis functions', *Computer Graphics Forum* **39**, 159–171.

Hansen, B. C. & Hess, R. F. (2006), 'The role of spatial phase in texture segmentation and contour integration', *Journal of Vision* **6**, 594–615.

Hilbert, D. (1912), *Grundzüge einer allgemeinen Theorie der linearen Integralgleichungen*, B. G. Teubner, Leipzig, Berlin, GER.

Horn, R. & Johnson, C. (1990), *Matrix analysis*, Cambridge University Press, Cambridge, UK.

Hosono, K., Ono, S. & Miyata, T. (2019), 'Weighted tensor nuclear norm minimization for color image restoration', *IEEE Access* **7**, 88768–88776.

Jahne, B. (2004), *Practical handbook on image processing for scientific and technical applications*, CRC Press, Boca Raton, FL, USA.

Johnson, R. A. & Wichern, D. W. (2002), *Applied multivariate statistical analysis*, Prentice Hall, Upper Saddle River, NJ, USA.

Kailath, T., Sayed, A. H. & Hassibi, B. (2000), *Linear Estimation*, Prentice Hall, Upper Saddle River, NJ, USA.

Kallenberg, O. (2002), *Foundations of modern probability*, Springer-Verlag, New York City, NY, USA.

Kaseb, M., Mercère, G., Biermé, H., Brémand, F. & Carré, P. (2019), 'Phase estimation of a 2d fringe pattern using a monogenic-based multiscale analysis', *Journal of the Optical Society of America* **36**, C143–C153.

Katayama, T. (2005), *Subspace methods for system identification*, Springer-Verlag, New York City, NY, USA.

Kokaram, A. (2004), 'A statistical framework for picture reconstruction using 2D AR models', *Image and Vision Computing* **22**, 165–171.

Kovesi, P. (2000), 'Phase congruency: a low-level image invariant', *Psychological research* **64**, 136–148.

Kulesza, A. & Taskar, B. (2012), 'Determinantal point processes for machine learning', *Foundations and Trends in Machine Learning* **5**, 123–286.

Köppel, M., Doshkov, D., Racape, F., Ndjiki-Nyab, P. & Wiegand, T. (2015), 'On the usage of the 2D-AR-model in texture completion scenarios with causal boundary conditions: A tutorial', *Signal Processing: Image Communication* **32**, 106–120.

Köthe, U. & Felsberg, M. (2005), 'Riesz-transforms vs. derivatives : on the relationship between the boundary tensor and the energy tensor', *Proc. Scale Space Conference, LNCS 3459* pp. 179–191.

Lagae, A. & Drettakis, G. (2011), 'Filtering solid gabor noise', *ACM Transactions on Graphics* **30**, Art. 51.

Lagae, A., Lefebvre, S., Drettakis, G. & Dutré, P. (2009), 'Procedural noise using sparse gabor convolution', *ACM Transactions on Graphics* **28**, Art. 54.

Langley, K. & Anderson, S. J. (2010), 'The riesz transform and simultaneous representations of phase, energy and orientation in spatial vision', *Vision Research* **50**, 1748–1765.

Larkin, K. G., Bone, D. J. & Oldfield, M. A. (2001), 'Natural demodulation of two-dimensional fringe patterns', *Journal of the Optical Society of America* **18**, 1862–1881.

Launay, C., Desolneux, A. & Galerne, B. (2021), 'Determinantal point processes for image processing', *SIAM Journal on Imaging Sciences* **14**, 304–348.

Leclaire, A. & Moisan, L. (2015), 'No-reference image quality assessment and blind deblurring with sharpness metrics exploiting fourier phase information', *Journal of Mathematical Imaging and Vision* **52**, 145–172.

Lewis, J. P. (1989), 'Algorithms for solide noise synthesis', *ACM SIGGRAPH Computer Graphics* **23**, 263–270.

Li, Z., He, H., Tai, H. M., Yin, Z. & Chen, F. (2015), 'Color-direction patch-sparsity-based image inpainting using multidirection features', *IEEE Transactions on Image Processing* **24**, 1138–1152.

Lilly, J. (2011), 'Modulated oscillations in three dimensions', *IEEE Transactions on Signal Processing* **59**, 5930–5943.

Lilly, J. & Gascard, J. C. (2006), 'Wavelet ridge diagnosis of time-varying elliptical signals with application to an oceanic eddy', *Nonlinear Processes in Geophysics* **13**, 467–483.

Lilly, J. & Olhede, S. (2010), 'Bivariate instantaneous frequency and bandwidth', *IEEE Transactions on Signal Processing* **58**, 591–603.

Loève, M. (1978), *Probability theory II*, Springer-Verlag, New York City, NY, USA.

Mairal, J., Elad, M. & Sapiro, G. (2008), 'Sparse representation for color image restoration', *IEEE Transactions on Image Processing* **17**, 53–69.

Marks, R. J. (1991), *Introduction to Shannon sampling and interpolation theory*, Springer-Verlag, New York City, NY, USA.

Milkereit, B. & Spencer, C. (1990), 'Multiattribute processing of seismic data: application to dip displays', *Canadian Journal of Exploration Geophysics* **26**, 44–53.

Morimoto, Y., Seguchi, Y. & Higashi, T. (1989), 'Two-dimensional moiré method and grid method using Fourier transform', *Experimental mechanics* **29**, 399–404.

Olhede, S. (2013), 'Modulated oscillations in many dimensions', *Philosophical transactions of the royal society A* **371**.

Olhede, S., Ramirez, D. & Schreier, P. (2014), 'Detecting directionality in random fields using the monogenic signal', *IEEE Transactions on Information Theory* **60**, 6491–6510.

Ono, S. & Yamada, I. (2016), 'Color-line regularization for color artifact removal', *IEEE Transactions on Computational Imaging* **2**, 204–217.

Oppenheim, A. & Lim, J. (1981), 'The importance of phase in signals', *Proceedings of the IEEE* **69**, 529–541.

Oppenheim, A. V. (1996), *Signals and systems*, Pearson Education Limited, Harlow, Essex, England.

Oswald, J. (1956), 'The theory of analytic band-limited signals applied to carrier systems', *IRE Transactions on Circuit Theory* **3**, 244–251.

Overschee, P. V. & Moor, B. D. (1996), *Subspace identification for linear systems. Theory, implementation, applications*, Kluwer Academic Publishers, Dordrecht, NL.

Papoulis, A. & Pillai, S. (2002), *Probability, random variables and stochastic processes*, McGraw Hill, New York City, NY, USA.

Peternell, K., Sherrer, W. & Deistler, M. (1996), 'Statistical analysis of novel subspace identification methods', *Signal Processing* **52**, 161–177.

Picinbono, B. (1997), 'On instantaneous amplitude and phase of signals', *IEEE Transactions on Signal Processing* **45**, 552–560.

Picinbono, B. (2008), *Time-frequency analysis*, ISTE Ltd and John Wiley & Sons, Inc, New York City, NY, USA.

Polisano, K. (2017), Modélisation de textures anisotropes par la transformée en ondelettes monogènes et super-résolution de lignes 2D, PhD thesis, Université de Grenoble Alpes.

Ramos, J. & Mercère, G. (2016), 'Image modeling based on a 2-D stochastic subspace system identification algorithm.', *Multidimensional Systems and Signal Processing* **28**, 1133–1165.

Ramos, J. & Mercère, G. (2018), 'A stochastic subspace system identification algorithm for state space systems in the general 2-D Roesser model form', *International Journal of Control* **91**, 2743–2771.

René, R. M., Fitter, L., Forsyth, P. M., Kim, K. Y., Murray, D. J., Walters, J. K. & Westerman, J. D. (1986), 'Multicomponent seismic studies using complex trace analysis', *Geophysics* **51**, 1235–1251.

Riesz, M. (1928), 'Sur les fonctions conjuguées', *Mathematische Zeitschrift* **27**, 218–244.

Robin, E., Valle, V. & Brémand, F. (2005), 'Phase demodulation method from a single fringe pattern based on correlation with a polynomial form', *Applied Optics* **44**, 7261–7269.

Robinson, D. W. & Reid, G. T. (1993), *Interferogram analysis, digital fringe pattern measurement techniques*, CRC Press, Boca Raton, FL, USA.

Roesser, R. (1975), 'A discrete-state-space model for linear image processing', *IEEE Transactions on Automatic Control* **20**, 1–10.

Seelamantula, C. S., Pavillon, N., Depeursinge, C. & Unser, M. (2012), 'Local demodulation of holograms using the riesz transform with application to microscopy', *Journal of the Optical Society of America* **29**, 2118–2129.

Smith, W. (1995), *Handbook of real-time Fast Fourier Transforms: algorithms to product testing*, John Wiley And Sons Inc., IEEE Press, New York City, NY, USA.

Soulard, R. (2012), Ondelettes analytiques et monogènes pour la représentation des images couleur, PhD thesis, Université de Poitiers.

Soulard, R. & Carré, P. (2015), 'Elliptical monogenic wavelets for the analysis and processing of color images', *IEEE Transactions on Signal Processing* **64**, 1535–1549.

Soulard, R. & Carré, P. (2017), 'Characterization of color images with multiscale monogenic maxima', *IEEE Transactions on Pattern Analysis and Machine Intelligence* **40**, 2289–2302.

Steel, W. H. (1986), *Interferometry, second Edition: Cambridge Studies in Modern Optics 1*, Cambridge University Press, Eds., New York City, NY, USA.

T. D. Carozzi, A. M. B. & Gough, M. P. (2004), 'Instantaneous local wave vector estimation from multi-space craft measurements using few spatial points', *Annales Geophysicae* **22**, 2633–2641.

Tong, Y. L. (1989), *The multivariate normal distribution*, Springer-Verlag, New York City, NY, USA.

Tricard, T., Efremov, S., Zanni, C., Neyret, F., Martinez, J. & Lefebvre, S. (2019), 'Procedural phasor noise', *ACM Transactions on Graphics* **38**, Art. 57.

Tricard, T., Tavernier, V., Zanni, C., Martinez, J., Hugron, P. A., Neyret, F. & Lefebvre, S. (2020), 'Freely orientable microstructures for designing deformable 3d prints', *ACM Transactions on Graphics* **39**, Art. 211.

Tóth, R. (2007), *Modeling and identification of linear parameter-varying systems*, Cambridge University Press, Eds., New York City, NY, USA.

Via, J., Ramirez, D. & Santamaría, I. (2010), 'Properness and widely linear processing of quaternion random vectors', *IEEE Transactions on Information Theory* **56**, 3502–3515.

Ville, J. (1948), 'Théorie et applications de la notion de signal analytique', *Câbles et Transmissions* **2D**, 61–74.

Xu, Y., Yu, L., Xu, H., Zhang, H. & Nguyen, T. (2015), 'Vector sparse representation of color image using quaternion matrix analysis', *IEEE Transactions on Image Processing* **24**, 1315–1329.

Yin, Q., Wang, J., Luo, X., Zhai, J., Jha, S. K. & Shi, Y. Q. (2019), 'Quaternion convolutional neural network for color image classification and forensics', *IEEE Access* **7**, 20293–20301.

Zhang, K., Zuo, W., Chen, Y., Meng, D. & Zhang, L. (2017), 'Beyond a Gaussian denoiser: residual learning of deep CNN for image denoising', *IEEE Transactions on Image Processing* **26**, 3142–3155.

Zhao, Z., Zhang, H., Xiao, Z., Du, H., Zhuang, Y., Fan, C. & Zhao, H. (2018), 'Robust 2D phase unwrapping algorithm based on the transport of intensity equation', *IOP Publishing* **30**, 015201.

Zhuang, H., Low, K. S. & Yau, W. Y. (2012), 'Multichannel pulse-coupled-neural-network-based color image segmentation for object detection', *IEEE Transactions on Industrial Electronics* **59**, 3299–3308.

Zujovic, J., Pappas, T. N. & Neuhoff, D. L. (2013), 'Structural texture similarity metrics for image analysis and retrieval', *IEEE Transactions on Image Processing* **22**, 2545–2558.